# Loss of protamine 1 and actin-like 7b – Investigating genes relevant for male fertility

Dissertation

zur

Erlangung des Doktorgrades (Dr. rer. nat.)

der

Mathematisch-Naturwissenschaftlichen Fakultät

der

Rheinischen Friedrich-Wilhelms-Universität Bonn

vorgelegt von

**Gina Esther Merges**

aus

Köln

Bonn, 2023

Angefertigt mit Genehmigung der Mathematisch-Naturwissenschaftlichen Fakultät
der Rheinischen Friedrich-Wilhelms-Universität Bonn

1. Gutachter: Prof. Dr. Hubert Schorle
2. Gutachter: Prof. Dr. Oliver Gruß

Tag der Promotion: 21.12.2023

Erscheinungsjahr: 2024

Teile dieser Arbeit wurden bereits in folgenden Originalpublikationen/Pre-prints veröffentlicht:

Gina Esther Merges, Julia Meier, Simon Schneider, Alexander Kruse, Andreas Christian Fröbius, Klaus Steger, Lena Arévalo, Hubert Schorle (2022) Loss of *Prm1* leads to defective chromatin protamination, impaired PRM2 processing, reduced sperm motility and subfertility in male mice. *Development.* DOI: 10.1242/dev.200330

Gina Esther Merges, Lena Arévalo, Keerthika Lohanadan, Dirk G. de Rooij, Melanie Jokwitz, Walter Witke, Hubert Schorle (2022) *Actl7b*-deficiency leads to mislocalization of LC8 type dynein light chains and disruption of murine spermatogenesis. *BioRxiv.* DOI: 10.1101/2022.12.19.520998

# List of Abbreviations

| Abbreviation | Meaning |
|---|---|
| 8-OHdG | 8-hydroxydesoxyguanosine |
| Actl7a | actin-like 7a |
| Actl7b | actin-like 7b |
| ART | assisted reproductive technology |
| ATP | adenosine triphosphate |
| BRDT | testis-specific bromodomain-containing protein |
| CAMK4 | Ca2+/calmodulin-dependent protein kinase IV |
| cAMP | cyclic adenosine monophosphate |
| Cas9 | CRISPR-associated 9 |
| cDNA | complementary DNA |
| CMA3 | Chromomycin A3 |
| cP2 | cleaved PRM2 |
| CRISPR | clustered regularly interspaced short palindromic repeats |
| CTSB | cathepsin B |
| DAPI | 4',6-diamidin-2-phenylindol |
| DEPC | diethyl pyrocarbonat |
| DNA | deoxyribonucleic acid |
| dpc | days post coitum |
| DTT | 1,4-dithiothreit |
| Dynll1 | LC8 dynein light chain 1 |
| Dynll2 | LC8 dynein light chain 2 |
| e.g. | *exempli gratia*; latin: for example |
| EDTA | ethylenediaminetetraacetic acid |
| EN | eosin-nigrosin |
| ES cell | embryonic stem cell |
| *et al.* | *et alii, aliae, alia*; latin: and others |
| EtBr | ethidium bromide |
| EtOH | ethanol |
| F-actin | filamentous actin |
| FCS | fetal calf serum |
| fwd | forward |
| g | gram |
| G-actin | globular actin |
| GFP | green fluorescent protein |
| GO | gene ontology |
| GPX4 | glutathione peroxidase 4 |
| HEK cell | human embryonic kidney cell |
| HEPES | 4-(2-hydroxyethyl)-1-piperazineethanesulfonic acid |
| HOS test | hypoosmotic swelling test |

| Abbreviation | Meaning |
|---|---|
| HPLC | high performance liquid chromatography |
| HRP | horseradish peroxidase |
| i.e. | *id est*; latin: that is |
| i.u. | international unit |
| ICSI | intracytoplasmic sperm injection |
| IF | immunofluorescence |
| IHC | immunohistochemistry |
| IP | immunoprecipitation |
| IVF | in vitro fertilization |
| kb | kilobase pairs |
| KCl | potassium chloride |
| kDA | kilo Dalton |
| KO | knockout |
| LB | lysogeny broth |
| LC-MS/MS | liquid chromatography – tandem mass spectrometry |
| M | molar |
| MeOH | methanol |
| MEF | murine embryonic fibroblast |
| min | minute(s) |
| ml | milliliter |
| mM | millimolar |
| mP2 | mature PRM2 |
| mRNA | messenger RNA |
| NaCl | sodium chloride |
| NLS | nuclear localization signal |
| ns | not significant |
| ODF2 | outer dense fiber protein 2 |
| PAGE | polyacrylamide gel electrophoresis |
| PAS | periodic acid Schiff |
| PBS | phosphate-buffered saline |
| PCA | principal component analysis |
| PCR | polymerase chain reaction |
| PRDX5 | peroxiredoxin 5 |
| Prm1 | protamine 1 |
| Prm2 | protamine 2 |
| PRND | prion like protein doppel |
| rev | reverse |
| RIPA | radioimmunoprecipitation assay buffer |
| RNA | ribonucleic acid |
| ROS | reactive oxygen species |
| s.d. | standard deviation |
| SDS | sodium dodecyl sulfate |

| Abbreviation | Meaning |
|---|---|
| sec | second(s) |
| Ser | Serine |
| SNP | single nucleotide polymorphism |
| SOD1 | superoxide dismutase 1 |
| SPAG8 | sperm associated antigen 8 |
| SRPK1 | SRSF protein kinase 1 |
| SSC | spermatogonial stem cells |
| TEM | transmission electron microscopy |
| Thr | Threonine |
| Tnp1 | transition protein 1 |
| Tnp2 | transition protein 2 |
| TUNEL | terminal deoxynucleotidyl transferase dUTP nick end labeling |
| UTR | untranslated region |
| UV | ultraviolet |
| v/v | volume solute per volume of total solution |
| WT | wild type |
| X-Gal | 5-bromo-4-chloro-3-indoxyl-β-d-galactopyranoside |
| µl | microliter |
| µm | micrometer |

# Table of Contents

# List of Figures

## List of Tables

## Summary

Sperm express a suite of genes specific to the testis. While they likely play essential roles in sperm function and male fertility we still lack fundamental knowledge about many of these genes.

One of the key events during spermatogenesis is the replacement of histones by protamines. This leads to hypercondensation of the chromatin, reduction of sperm nucleus size and protection of the paternal genome. In human and mice, two protamines, protamine-1 (*Prm1*) and protamine-2 (*Prm2*) are expressed in a species-specific ratio. Alterations of this ratio are associated to male sub- and infertility. Unlike PRM1, PRM2 is a precursor protein, containing a mature domain (mP2) and a cleaved domain (cP2), which is sequentially cleaved off upon DNA binding. To decipher common and unique roles of both protamines, *Prm1*-deficient mice were analyzed and compared to previously described *Prm2*-deficient mice. Whereas, loss of one allele of *Prm1* (*Prm1+/-*) rendered male mice subfertile, *Prm2+/-* mice were fertile. Mice lacking *Prm1* or *Prm2* were infertile, showing severe DNA damage and increased histone retention. *Prm1+/-* mice displayed only slight DNA damage. However, they contained high levels of unprocessed PRM2 and the species-specific protamine ratio was skewed. In comparison, the protamine ratio was maintained in *Prm2+/-* sperm, suggesting that the ratio needs to be precisely controlled to retain full fertility.

Additionally, a mouse model carrying a *Prm1-Prm2* fusion gene was analyzed. Here most of the *Prm1* coding sequence was fused to *mP2*, lacking the cP2 domain. By comparing this model to a previously described cP2-deficient mouse model we were able to narrow down the specific functions of the protamine domains and PRM1-PRM2 interaction. cP2-deficient mice were infertile, demonstrating that the cP2 domain is essential. Surprisingly, mice carrying one or two copies of the fusion allele partially retained sperm function and fertility. This suggests, that cP2 is necessary for PRM1-PRM2 interaction and that loss of cP2 might be compensated by fusing PRM1 to the mP2 domain.

Moreover, Actin-like 7b (*Actl7b)*-deficient mice were generated and phenotypically characterized. The function of ACTL7B in spermatogenesis was unknown to date. *Actl7b-/-* mice were infertile, showed reduced sperm numbers and severe sperm malformations. *Actl7b+/-* mice appear phenotypically inconspicuous and remain fertile. First, co-immunoprecipitation and subsequent mass spectrometric analyses, imply that ACTL7B functions in the microtubule network during spermiogenesis.

Together the results of this project present an important step forward in understanding the function and essentiality of a key set of sperm specific genes and their potential importance in male infertility.

# 1. Introduction

Results presented in this study were generated based on gene-edited mouse models, in which genes were targeted coding for proteins important in spermatogenesis. Hence, in the following murine spermatogenesis, with specific focus on spermiogenesis, as well as the genes targeted will be introduced.

## 1.1. Spermatogenesis

Spermatogenesis describes the developmental process from diploid spermatogonial stem cells to haploid sperm (Figure 1). It takes place in the seminiferous tubules of the testis, where germ cells transit from the basal compartment of the epithelium towards the lumen. In mice, the epithelial cycle is divided into 12 stages (roman numbers), depending on the composition

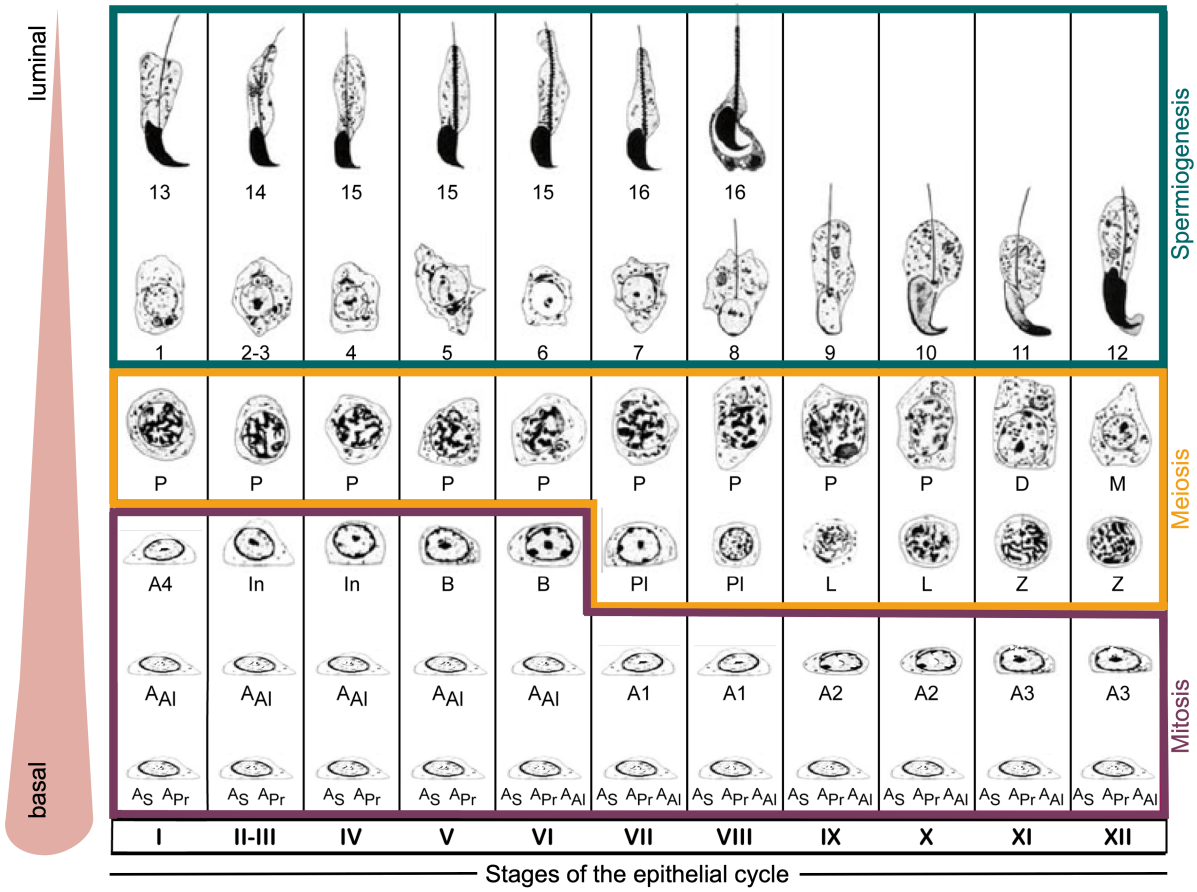


**Figure 1: Graphical presentation of murine spermatogenesis.** Germ cell development is depicted from left to right, starting in the bottom row. Mitotic phase (purple): A-single- (AS), A-paired- (APr), A-aligned- (AAl), A1-4-, intermediate- (In) and B-spermatogonia (B). Meiotic phase (yellow): Preleptotene (Pl), Leptotene (L), Zygotene (Z), Pachytene (P), Diplotene (D), Meiotic divisions I/II (M). Spermiogenesis (turquoise): steps are numbered. The stages of the seminiferous epithelium, depending on the composition of cells present, are marked in roman numbers. Direction of germ cell development from basal to luminal compartment is marked on the left side. Modified from (Russell et al., 1990).

of germ cells present. One cycle lasts 8.6 days in mice and has to be passed through four times (34.5 days in total) for mature sperm to develop (Oakberg, 1956b). Spermatogenesis can be divided into three phases; the mitotic phase, the meiotic phase and spermiogenesis.
In human, the duration of one epithelial cycle has been described to last ~16 days and spermatogenesis lasts approx. 64 days in total (Heller and Clermont, 1963). Later, this value has been corrected to approx. 74 days in studies using tritium-labelled testicular biopsies (Amann, 2008, Griswold, 2016, Heller and Clermont, 1964). Further, a new classification of the spermatogenic stages, increasing the number from 6 to 12 distinguishable stages, has been proposed (Muciaccia et al., 2013). Still, a definitive classification of the cycle in humans is lacking and urgently needed for even better comparison to murine spermatogenesis.

### 1.1.1. Mitosis

The spermatogonial stem cell (SSC) pool derives from primordial germ cells (PGCs) during embryonic development (Phillips et al., 2010). PGCs residing in the genital ridges give rise to gonocytes, which later give rise to the first round of cells entering spermatogenesis and establish the initial SSC pool for the maintenance. Undifferentiated type A spermatogonia can be differentiated based on their topological arrangement along the basement membrane of the seminiferous tubules. Single type A spermatogonia ($A_S$) divide mitotically to produce paired tape A spermatogonia ($A_{pr}$) (Figure 1) (Oakberg, 1971b, a, 1956b, a). These eventually complete cytokinesis and give rise to new $A_S$ for self-renewal. Part of $A_{pr}$, however, produce a chain of aligned type A spermatogonia ($A_{al}$), which remain connected via cytoplasmic bridges and are destined to enter the differentiation process. Larger $A_{al}$ chains differentiate into A1 spermatogonia, which start dividing in a synchronized manner giving rise to A2, A3, A4, intermediate and B spermatogonia at specific stages of the epithelial cycle. Type B spermatogonia finally divide mitotically to produce primary diploid spermatocytes, which enter meiosis.

### 1.1.2. Meiosis

During meiosis I, diploid (2n, 4c) primary spermatocytes first enter leptotene phase, in which sister chromatids become individualized and double strand DNA breaks are formed to allow for crossing over (Baudat and de Massy, 2007). In zygotene and pachytene phase, chromosomes are stably paired, crossing over takes place and DNA strand breaks are repaired (Snustad and Simmons, 2016). Homologous chromosomes start to separate in diplotene phase followed by the first meiotic division. The resulting haploid (1n, 2c) secondary spermatids undergo an equational division to separate the sister chromatids in meiosis II.

Finally, four haploid (1n, 1c) spermatids are produced from one primary spermatocyte, which enter the differentiation process.

### 1.1.3. Spermiogenesis

During spermiogenesis haploid spermatids undergo dramatic morphological changes and can be categorized into 16 steps (Figure 2). These can be divided into four major phases depending on acrosome biogenesis (Azhar et al., 2021). In the first phase, the Golgi phase, proacrosomal vesicles fuse to form the acrosomal vacuole. Golgi-derived vesicles accumulate and fuse to form the acrosomal sac. Simultaneously, the centrioles migrate to the other pole of the cell, attach to the cell membrane and form the primary cilium, which starts to form the axoneme (Avidor-Reiss et al., 2020). During cap phase, the axoneme elongates (Azhar et al., 2021). The distal centrioles start forming the flagella, while the proximal centrioles, together with the pericentriolar matrix start forming the head-tail coupling apparatus. While the proximal centriole persists in the sperm, the distal centriole disintegrates and is no longer present in mature murine sperm (Fawcett and Phillips, 1969). In step 4-7 spermatids the acrosomal sac grows to form a cap-like structure, which adheres to the anterior nuclear envelope through the F-actin-containing acroplaxome (Azhar et al., 2021). While the nucleus starts to elongate, the acrosome-acroplaxome complex descends caudally. In the third phase, the acrosome phase, the manchette is formed. The manchette is a transient structure, present in step 8-14 spermatids. This microtubular structure surrounds the posterior part of the nucleus as supportive structure. It aids in sperm head shaping, flagella assembly and nucleocytoplasmic exchange, both through intra-manchette transport of molecules and microtubular dynamics (Lehti and Sironen, 2017). While the manchette aids in spermatid elongation the acrosome further descends to finally line the anterior nuclear envelope (Azhar et al., 2021). At the same time, outer dense fibers start to align along the axoneme and mitochondria accumulate around the midpiece of the sperm tail. Chromosome remodeling is initiated, in which the majority of somatic histones is replaced by protamines and the chromatin intensely condensates. During maturation phase, the anterior part of the acrosome becomes the acrosome apex, which later bursts during the fertilization process, while the posterior part covers the majority of the nucleus (Khawar et al., 2019). Chromatin remodeling and tail formation continue. DNA in mammalian sperm is condensed into an almost crystalline state, reducing the size of nuclei considerably and rendering mature sperm transcriptionally/metabolically inert (Chandley and Kofman-Alfaro, 1971, Kierszenbaum and Tres, 1975, Pogany et al., 1981, Balhorn, 1982). Lastly, excess cytoplasm is evicted as residual bodies, which become phagocytosed by Sertoli cells. Step 16 spermatids are finally released into the lumen of the seminiferous tubules in a process

called spermiation. These, however still need to mature during transit through the epididymis to gain capacitation competence and motility.

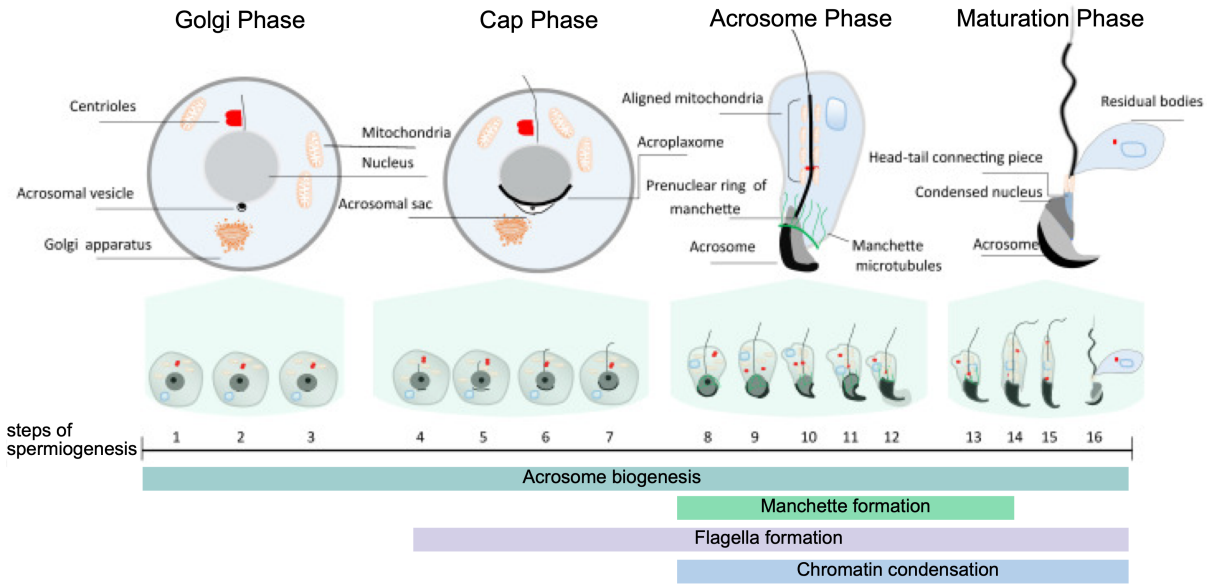


**Figure 2: Phases of murine spermiogenesis.** Graphical representation of the four phases of spermiogenesis (Golgi phase, Cap phase, Acrosome Phase and Maturation phase). Spermatids can be divided into 16 steps. The duration of major events is depicted as bars. Modified from (Azhar et al., 2021)

## 1.2. Sperm maturation

In mammals, spermatozoa gain their fertilization ability during epididymal transit. This post-gonadal differentiation process involves modifications to transcriptionally silent sperm orchestrated by epididymal tissue secretions and milieu changes.

Already in the efferent ducts (Figure 3), connecting the testis with the caput epididymis, the majority of water is reabsorbed, leading to an increase in sperm and protein concentration as well as changes in the ionic composition of the luminal fluid (Dacheux and Dacheux, 2014). In epididymides, proteins are secreted into the lumen dependent on the epididymal section. Protein concentration depends on both secretion and reabsorption. Proteins important for sperm motility, capacitation, acrosome reaction, sperm-egg fusion and fertilization are transferred to sperm by so-called epididymosomes released

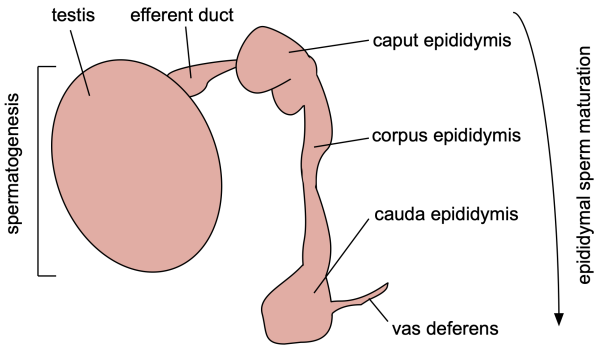


**Figure 3: Schematic of male murine reproductive organs.** Testis and epididymis are depicted. The graphic has been created using Graphic.

from the epidydimal epithelium (Gervasi and Visconti, 2017). The most commonly secreted protein identified in mammals is clusterin, but species-specific proteins have been identified (Dacheux and Dacheux, 2014). One major function of the secretome is reactive oxygen species (ROS) reduction to protect sperm form oxidative damage. Further, proteins with binding activity (e.g. clusterin) seem to be involved in the protection of active sites of sperm surface proteins during the transit. Additional to sperm cell protection, sperm are continuously modified. Several sperm membrane proteins important for sperm-oocyte binding and fusion are processed. Moreover, sperm gain motility during epididymal transit. ATP production, metabolic capacity and intracellular cAMP levels increase gradually.

## 1.3. Male fertility problems and models

According to the World Health Organization (WHO), infertility is defined as the failure to achieve pregnancy after one year of unprotected sexual intercourse (World Health Organization, 2023). It is estimated that one third of infertility cases is caused by female factors, one third by male factors and one third by a combination of both or remain unresolved (Agarwal et al., 2015). Hence, males contribute to around 50% of all infertility cases. Male infertility can be caused by a wide variety of factors. Besides lifestyle factors (e.g. smoking) and environmental factors (e.g. pollutants), male infertility might be explained by obstruction of the reproductive tract, endocrine disorders and primary testicular defects. These can be caused by a variety of etiologies, such as malignancies, medications, anatomical abnormalities, immunological disorders or genetic factors (Leslie et al., 2023). 10-20% of cases are idiopathic (Leslie et al., 2023), while 6-27 % of cases are defined as ´unexplained male infertility´ cases, where the origin of male infertility is unknown and female infertility factors have been ruled out (Hamada et al., 2012).

The fact that male-factor infertility can originate at every stage of spermatogenesis, sperm maturation, during transit through the female reproductive tract, at or even after fertilization, makes studying male infertility challenging. *In vitro* models addressing molecular origins of male infertility are still scarce and inefficient, never reflecting the whole developmental process. Human tissue samples on the other hand, might provide crucial insights, but are limited. Therefore, targeted mutagenesis or treatment of model organisms – first and foremost mice - have been the model of choice for decades and have considerably advanced our knowledge to be able to provide new screening, diagnostic and treatment options.

## 1.4. Protamines

During chromatin remodeling, sperm chromatin is hypercondensed to an almost crystalline state to protect the paternal genome on its way to the fertilization site. This is achieved by the substitution of the majority of somatic histones by protamines. The sperm nucleus is elongated and reduced in size into hydrodynamic shape.

### 1.4.1. Protamine structure and DNA binding capacity

Whereas most mammals achieve DNA compaction in sperm using only one protamine (protamine-1, *PRM1*), primates and most rodents express two protamines; *PRM1* and protamine-2 (*PRM2)* (Chauviere et al., 1992, Retief and Dixon, 1993). In human and mice, *PRM1* and *PRM2* are encoded in a tightly regulated gene cluster together with transition protein 2 (*TNP2*) on chromosome 16 (Wykes and Krawetz, 2003). Transcriptional control of protamines has been shown to be conferred by 5´-UTR regions of *Prm1* and *Prm2* (Braun et al., 1989, Peschon et al., 1987, Stewart et al., 1988, Johnson et al., 1988, Bunick et al., 1990). Translational control of protamines has on the other hand been pinpointed to 3´-UTR regions (Braun et al., 1989, Lee et al., 1995, Braun, 1990). Different germ cell-specific proteins binding sequences of the 3´ -UTR regions of *Prm1* and *Prm2* mRNA have been identified, suggesting active translational repression and activation (Kwon and Hecht, 1993, 1991, Lee et al., 1996, Fajardo et al., 1997, Giorgini et al., 2002, Fukuda et al., 2013). Mice harbouring a transgene encoding the human *PRM1-PRM2-TNP2* locus maintain temporal expression, suggesting that all elements necessary for transcriptional and translational control are encoded within this fragment (Stewart et al., 1999). Of note, Kleene and Bagarova applied comparative genomics and found conserved regulatory sequences of *Prm1* and *Prm2* in different mammalian species (Kleene and Bagarova 2008).

After transcription in step 7-9 round spermatids, *Prm mRNAs* are stored as cytoplasmic ribonucleoprotein particles until translation (Hecht et al., 1986b, Hecht et al., 1986a, Kleene et al., 1984, Kleene, 1989). In mice, PRM1 is translated first in step 12 elongating spermatids, followed by translation of PRM2 in step 14-15 elongating spermatids (Klaus et al., 2016). While PRM1 is translated in its mature from, PRM2 is translated as precursor protein, which is proteolytically cleaved upon DNA binding. Cleavage of the N-terminal PRM2 cleaved domain (cP2) occurs sequentially (cleavage sites marked in Figure 4) (Yelick et al., 1987, Balhorn, 2007, Balhorn et al., 2018). The mature part of PRM2 (mP2) is highly similar to PRM1. PRM1 and mP2 are small, highly basic proteins containing arginine-rich DNA binding domains (blue R´s). Cysteine residues (green C´s) allow for inter- and intra-protamine disulfide bridge formation during epididymal transit, further stabilizing DNA condensation (Balhorn et al., 1992).

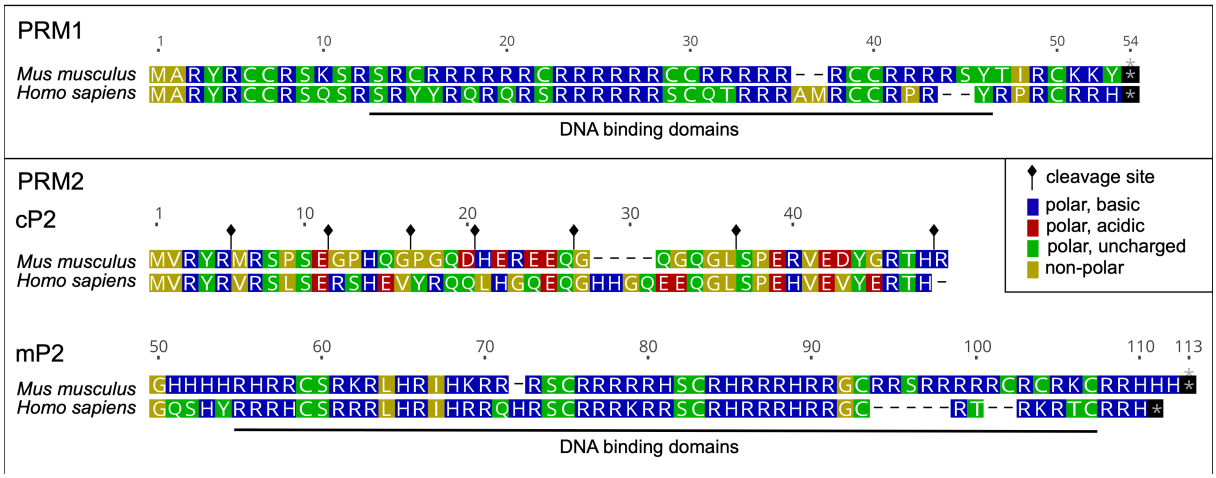


**Figure 4: Amino acid sequences of PRM1 and PRM2 in human and mice.** Sequences of PRM1, cP2 and mP2 are displayed. Amino acids are color coded according to polarity. Cleavage sites in the N-terminal mP2 domain are indicated as described (Balhorn, 2007). Arginine-rich DNA binding domains are marked. The figure was constructed using Geneious Prime and Graphic, adapted from (Arévalo et al., 2022b).

Evolutionary analysis revealed that *Prm1* is under purifying and positive selection. More precisely, arginine-rich DNA binding domains seem to be maintained, but their location seem variable. *Prm2* codes for two domains, the cleaved *Prm2* domain (cP2), which is under purifying selection, and the mature *Prm2* domain (*mP2*), which evolves more freely. *mP2* was proposed to have originated from a gene duplication of *PRM1* (Krawetz and Dixon, 1988).

Incorporation of basic protamines neutralizes the negative charge of the phosphodiester backbone of DNA (Pogany et al., 1981, Bench et al., 1996) providing protamine-bound DNA with a rather insoluble state. Mimicking DNA compaction by protamines and arginine-rich peptides *in vitro*, showed that the rate of DNA condensation depends on the amount of protamine binding to the chromatin (Brewer et al., 1999) and that the stability of the DNA-protamine complex is dependent on the arginine content of the protamine or peptide used (Balhorn et al., 2000, Brewer et al., 1999). Since DNA compaction in (mammalian) sperm is highly stable, early methods used to release DNA from sperm were very harsh, which caused decondensation of the chromatin and did not allow for thorough structural studies (Henricks and Mayer, 1965, Lung, 1972, Mahi and Yanagimachi, 1975, Balhorn, 1982). Advances in imaging techniques (atomic force microscopy) allowed to visualize DNA-protamine complexes isolated from mammalian sperm (Allen et al., 1993, Hud et al., 1993, Hud et al., 1995, Allen et al., 1996). Protamine-bound DNA was shown to be organized in toroidal structures, containing up to 60 kb of DNA per toroid (Hud et al., 1993, Allen et al., 1997). The current model of protamine-mediated chromatin condensation states that protamines bind DNA sequence-independent in the major groove. One protamine molecule binds to each turn of DNA, neutralizing the charge and causing the DNA to coil into toroidal structures (Balhorn, 2007).

The amino- and carboxyl-termini of protamines contain serine and threonine (Ser and Thr) residues, which are subject to phosphorylation. Analysis of trout sperm revealed that protamines are subjected to phosphorylation after transport to the nucleus and before binding to DNA (Louie and Dixon, 1972). This process reduces their net positive charge and

supposedly provides the protamines more freedom to bind DNA correctly. Once bound to DNA protamines become dephosphorylated, thereby “locking” the protamines in place. In sperm from human, stallion, bull, boar and ram ejaculates however, remaining phosphorylated protamines have been identified (Gusse et al., 1986, Pirhonen et al., 1994).
Moreover, it was shown that PRM2 can bind one zinc atom per molecule (Bench et al., 2000). The formation of zinc bridges during epididymal transit further stabilizes protamine-DNA complexes. *In vitro* experiments using Syrian hamster protamines determined that the condensation and decondensation rates of PRM1 and PRM2 are similar (Brewer et al., 2002). Addition of zinc, however, increased the DNA condensation rate of PRM2 nearly 3-fold, while it did not influence PRM1-mediated DNA condensation.

### 1.4.2. The role of protamines in nuclear remodeling

DNA in haploid round spermatids is organized in nucleosomes. To initiate chromatin remodeling, somatic histones are modified (Figure 5). Histone acetylation promotes accessibility of the chromatin (Luense et al., 2019). Next, canonical histones are replaced by sperm-specific histone variants, which pack the DNA less stably compared to canonical histones (Montellier et al., 2013, Govin et al., 2007, Yan et al., 2003, Shinagawa et al., 2015, Tachiwana et al., 2010). Nucleosome eviction may cause DNA supercoiling. Tension is released by DNA double strand breaks and subsequent repair (McPherson and Longo, 1993, Marcon and Boissonneault, 2004, Leduc et al., 2008). Binding of the testis-specific bromodomain-containing protein (BRDT) to acetylated histones allows for histone removal by transition-proteins 1 and 2 (TNP1 and TNP2) (Goudarzi et al., 2014). The incorporation of sperm-specific histone variants, like H2A.L.2, allows for TNP loading onto DNA (Govin et al., 2007, Barral et al., 2017). TNPs then recruit protamines, which in turn evict histones and histone-TNP complexes. PRM2 is processed upon DNA binding by sequential proteolytic cleavage of the N-terminal cP2 domain, leaving only the mP2 domain bound to DNA. cP2 might help in regulating the speed of DNA hypercondensation. However, it has been shown that large amounts of PRM2 are not processed in WT mice and evicted in residual bodies (Arévalo et al., 2022a). This suggests, that PRM2 (and maybe PRM1) are produced in overabundant levels ensuring proper protamination and hence hypercondensation.
During protamine incorporation, Ca2+/calmodulin-dependent protein kinase IV (CAMK4) and SRSF protein kinase 1 (SRPK1) are involved in protamine phosphorylation (Wu et al., 2000, Gou et al., 2020), while the testis- and sperm-specific phosphatase PPP1CC2 was shown to be involved in dephosphorylation of deposited protamines (Itoh et al., 2019).
Noteworthy, part of the paternal chromatin remains histone-bound. Studies showed that these histone-bound regions are not randomly located throughout the chromatin, but seem to be important for early embryonic development and paternal imprinting (Hammoud et al., 2011,

Brykczynska et al., 2010, Yamaguchi et al., 2018, Jung et al., 2017, Erkek et al., 2013). In mice 1-10% of the genome remains histone-bound, whereas in human 10-15% of the sperm chromatin is organized in nucleosomes (Yamaguchi et al., 2018, Jung et al., 2017, Erkek et al., 2013).

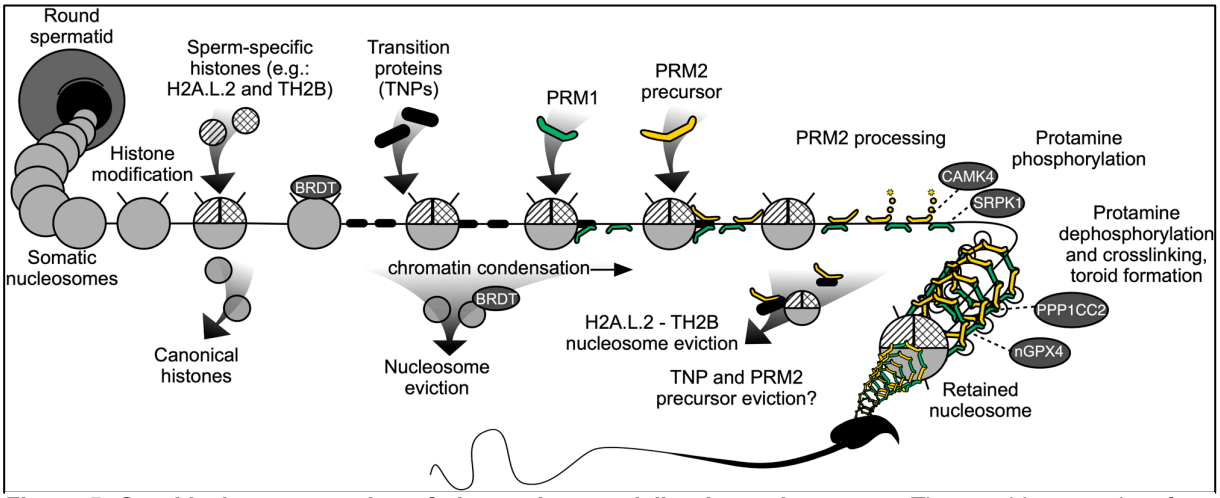


**Figure 5: Graphical representation of chromatin remodeling in murine sperm.** The graphic was taken from (Arévalo et al., 2022b) and is based on current knowledge as we have discussed in the respective review article.

### 1.4.3. The protamine ratio

Protamine expression varies widely between different species. Whereas, in most mammals, chromatin compaction in sperm is accomplished by incorporation of PRM1 alone, those species which express two protamines, express them in a species-specific ratio (Chauviere et al., 1992, Retief and Dixon, 1993). In human, PRM1 and PRM2 levels are almost identical (1:1) (Corzett et al., 2002), although a recent study using liquid chromatography-mass spectrometry (LC-MS) to measure intensities of PRM1 proteoforms and mature PRM2 proteoforms (as opposed to standard gel band intensity measurements) detected a much higher ratio of approximately 1.8 (Soler-Ventura et al., 2020). In mice, PRM2 accounts for around 65% of the total protamine (1:2) (de Mateo et al., 2009). Interestingly, a recent study demonstrated that the protamine expression ratio in different rodent clades, under the selective pressure of sperm competition, appears to adapt towards a 1:1 proportion (Arévalo et al., 2021).

### 1.4.4. Protamines and male fertility

Various correlative studies have been published, associating protamination problems with male sub- or infertility in human. Aberrant protamination has been correlated to decreased sperm DNA integrity in infertile men (Aoki et al., 2005a, Torregrosa et al., 2006, Garcia-Peiro et al., 2011, Ni et al., 2016, Aoki et al., 2006a, Simon et al., 2011). Further, mutations and

single nucleotide polymorphisms (SNPs) in the protamine coding sequence (CDS) have been associated with male sub- or infertility (Gazquez et al., 2008, Tuttelmann et al., 2010, Jodar et al., 2011, Yu et al., 2012, Imken et al., 2009, Aoki et al., 2006b, Ravel et al., 2007, He et al., 2012). These were described to induce conformational changes in protamines thereby hindering correct incorporation into the chromatin. Additionally, increased and decreased protamine ratios both on mRNA and protein level have been correlated to male sub- and infertility (Balhorn et al., 1988, Belokopytova et al., 1993, de Yebra and Oliva, 1993, Khara et al., 1997, de Yebra et al., 1998, Carrell and Liu, 2001, Oliva, 2006, Torregrosa et al., 2006, Rogenhofer et al., 2013, Ni et al., 2016, Steger et al., 2008, Bench et al., 1998, Mengual et al., 2003, Francis et al., 2014). Consequently, the protamine ratio has been proposed as diagnostic marker in infertile men (Ni et al., 2016, Steger et al., 2008). Moreover, it has been reported that infertile men with aberrant protamine ratios show lower success rates in assisted reproductive technology (ART) treatments (Rogenhofer et al., 2013, Nasr-Esfahani et al., 2004, Aoki et al., 2006c). Besides rare mutations, defects in transcriptional and/or translational regulation as well as environmental factors (e.g. smoking) have been correlated to defective protamination (Hammadeh et al., 2010, Hamad et al., 2019, Yu et al., 2014, Carrell et al., 2007).

### 1.4.5. Protamine-deficient and protamine-modified mouse models

Various protamine-deficient and protamine-modified mouse models have been published in the last decades.

First, it has been shown that transgenic mice lacking the 3´-UTR of *Prm1* loose translational control of *Prm1* (Lee et al., 1995). Premature *Prm1* translation let to premature DNA condensation, abnormal spermatid head shapes, spermatogenic arrest and, interestingly defects in PRM2 processing. Later, a specific translational control element within the 3´-UTR of *Prm1* was identified (Zhong et al., 2001). This sequence is highly conserved among the 3´-UTRs of *Prm1* and *Prm2* in several different species and seems to be required for translational regulation in mice. These results clearly demonstrate, that correct timing and control of protamine expression is crucial for correct chromatin remodeling in sperm.

Next, Cho *et al.* generated protamine-deficient chimeras (Cho et al., 2003, Cho et al., 2001). Classical gene targeting was applied to insert a construct encoding for PGK-neo cassette into the *Prm1* and *Prm2* coding sequence in embryonic stem (ES) cells. *Prm1+/-* and *Prm2+/-* ES cells were injected into murine blastocysts. Neither male nor female chimeras were able to generate ES-derived offspring, but it was shown that ES cells have contributed to the germ line. Males were reported to produce varying amounts of ES-cell derived sperm. Those showing higher amounts of ES-cell derived sperm, showed increased numbers of morphologically abnormal sperm, lower sperm DNA integrity and increased amounts of

unprocessed PRM2. Since no ES-cell derived offspring was produced, the authors concluded that deletion of one allele of *Prm1* or *Prm2* renders male mice infertile.

Following introduction of gene editing (CRISPR-Cas9), Schneider *et al.* generated *Prm2+/-* mice (Schneider et al., 2016), which were fertile, enabling the generation and analysis of *Prm2-/-* mice. The researchers hypothesized that the expression of the neo-cassette in the mouse model published by Cho *et al.* resulted in trans-silencing of *Prm1*. This hypothesis was supported by the fact that Cho *et al.* reported significant reductions in PRM1 levels in *Prm2*-deficient chimeras (Cho et al., 2003, Cho et al., 2001). *Prm2-/-* mice generated by Schneider *et al.* were infertile, displaying severe sperm damage (Schneider et al., 2016). *Prm2-/-* sperm were inviable and showed fragmented DNA, disintegrated membranes, reduced sperm head sizes, disrupted acrosomes and complete immotility. In a follow-up study Schneider *et al.* showed that *Prm2-/-* mice displayed increased levels of reactive oxygen species (ROS)-induced DNA damages in epididymal sperm. Further, *Prm2-/-* sperm showed lower levels of ROS scavenger proteins SOD1 (superoxide dismutase 1) and PRDX5 (peroxiredoxin 5). Defects in chromatin condensation initiated a ROS-mediated destruction cascade during epididymal transit. *Prm2+/-* and *Prm2-/-* mice produced by Dr. Schneider were used in this thesis.

Also, *Prm1*-deficient mouse models have been published. First, Mashiko *et al.* generated *Prm1+/-* mice utilizing CRISPR-Cas (Mashiko et al., 2013). The study was a CRISPR/Cas9 methodology-focused study in which several genes, which have been described in earlier studies, were targeted to compare CRISPR/Cas efficiency. Mashiko *et al.* reported *Prm1+/-* males to be infertile. *Prm1+/-* sperm showed abnormalities and reduced motility. Noteworthy, fertility analysis was performed by mating male *Prm1+/-* founder animals to superovulated WT females. Oocytes were isolated and the formation of pronuclei was considered a successful fertilization. Hence, fertility testing was very limited.

Next, Takeda *et al.* targeted *Prm1* in TT2-XO ES cells (Takeda et al., 2016). Female founder animals were generated, which passed the mutated allele to the germline enabling to generate *Prm1+/-* mice. *Prm1+/-* sperm displayed defective protamination, reduced DNA integrity, elevated levels of unprocessed PRM2, accelerated acrosome reactions, head deformities and tail malformations, which were linked to disorganized microtubules and a reduced mitochondrial membrane potential. *Prm1+/-* males were infertile, averting the generation of *Prm1-/-* males. *In vitro* fertilization (IVF) on zona-free oocytes with *Prm1+/-* sperm generated viable *Prm1+/-* offspring. These results demonstrated that DNA integrity of *Prm1+/-* sperm is sufficient to produce viable offspring and fertilization failure seems to be connected to secondary effects.

For the present work, *Prm1+/-* mice were generated utilizing CRISPR/Cas9. *Prm1+/-* mice were subfertile allowing the generation of *Prm1-/-* males.

A recent study describes a mouse model were lysine 49 of PRM1, which is conserved in the mouse lineage and acetylated in sperm, has been substituted with alanine (Moritz et al., 2023). Homozygous mice (*Prm1*$^{K49A/K49A}$) were subfertile, showing reduced sperm motility. Whereas spermatogenesis appeared overtly unaffected, sperm showed malformations in the head and tail regions. Additionally, sperm contained increased levels of unprocessed PRM2, while the overall PRM1 and PRM2 levels was unaffected. Due to accumulation of unprocessed PRM2, the PRM1/PRM2 ratio shifted towards 1:1, opposed to the expected 1:2 ratio. Moreover, nucleosome eviction was disturbed, as histones were retained in *Prm1*$^{K49A/K49A}$ sperm. Of note, TNP eviction appeared unaffected. *In vitro*, the substitution led to decreased binding of protamines to DNA. Therefore, Moritz *et al.* concluded that this single posttranslational modification affects protamine binding and nucleosome eviction, demonstrating that the effectiveness of protamine-DNA binding does not solely rely on arginine-rich binding domains. Another study, addressed the role of the cP2 domain of PRM2 (Arévalo et al., 2022a). Staining with a cP2-specific antibody on murine testis sections revealed that full-length PRM2 is detected in sperm cytoplasm and residual bodies, while mature PRM2 is detected in the nuclei of condensed sperm only. Hence, a certain amount of PRM2 remains unprocessed, is not associated with DNA and evicted from sperm prior to spermiation. The presence of unprocessed PRM2 in sperm nuclei was reported in various mouse models carrying a deletion of genes important in chromatin remodeling (Takeda et al., 2016, Barral et al., 2017, Zhao et al., 2001, Shirley et al., 2004, Merges et al., 2022b, Arévalo et al., 2022a). This has been interpreted as defects in the processing of PRM2. New results by Arévalo *et al.* however imply that full-length PRM2 observed sperm nuclei, indicate failed full-length PRM2 eviction as opposed to failed PRM2 processing. Further, it has been shown *in vitro*, that the cP2 domain alone does not locate to the nucleus, but needs to be attached to the mP2 domain or a nuclear localization signal (NLS).

Utilizing CRISPR/Cas9, Arévalo *et al*. deleted the cP2 domain in mice, so that only the mP2 domain was expressed. Heterozygous mice (*Prm2*$^{+/\Delta c}$) were infertile. So surprisingly, while loss of one cP2 domain leads to male mice infertility, *Prm2*+/- males were shown to be fertile (Arévalo et al., 2022a, Schneider et al., 2016). To exclude interfering effects of the mP2 domain with the full-length PRM2, *Prm2*$^{-/\Delta c}$ mice were bred. However, also these males were infertile demonstrating that the cP2 domain is essential. Upon loss of the cP2 domain, PRM1 and PRM2 amounts were severely reduced in sperm and the PRM1/PRM2 ratio was shifted to 2:1-5:1 (*Prm2*$^{+/\Delta}$ and *Prm2*$^{-/\Delta c}$ sperm respectively). Large amounts of retained full-length PRM2 were detected and sperm DNA was degraded already in testicular sperm. Hence, the cP2 domain or full-length PRM2 seem to be essential for correct protamine incorporation. Additionally, TNP1 was retained in cP2-deficient sperm, while H2A.L.2 levels were reduced.

This indicates that the cP2 domain is involved in TNP eviction and H2A.L.2 retention. Of note, direct interaction of the cP2 domain with TNP1 has been demonstrated *in vitro*.

## 1.5. Actin-related proteins (Arps)

The actin-related protein (Arp) superfamily comprises proteins functioning in a wide variety of cellular processes including vesicle trafficking, chromatin modulation, microtubule motility and actin filament dynamics (Schafer and Schroer, 1999). Arps share 17-60% amino acid identity with conventional actins and usually form stable macromolecular complexes with other proteins.

### 1.5.1. Actin-like 7b (*Actl7b*) and Actin-like 7a (*Actl7a*)

*ACTL7A/ T-ACTIN 2* and *ACTL7B/ T-ACTIN 1* have been identified by Chadwick *et al.* in 1999 (Chadwick et al., 1999). The novel actin-like genes showed a high level of identity between them and a larger than 40% predicted amino acid identity to other actin proteins. *ACTL7A* and *ACTL7B* are intronless single copy genes encoded in head-to-head orientation on chromosome 9q31 in human (Chadwick et al., 1999, Hisano et al., 2003b). The murine homologues (*Actl7a, Actl7b*) were mapped to murine chromosome 4. Due to their structure, it has been proposed that these genes arose by retroposition of a spliced mRNA transcribed from an actin progenitor gene prior to the divergence of rodents and primates. It was shown that methylation of CpG dinucleotides in the open reading frame of *Actl7b*, suppresses its expression in somatic cells (Hisano et al., 2003a). Both, *ACTL7A* and *ACTL7B*, are expressed specifically in testis in mice and human (Tanaka et al., 2003).

In murine sperm, ACTL7A is immunolocalized in both the acrosome and the tail, but only in the acrosome in human sperm (Fu et al., 2012). After finding anti-ACTL7A antibodies in vasectomized men's serum, it has been proposed to include anti-ACTL7A in anti-sperm antibody (ASA) testing in clinic. Active immunization of mice with ACTL7A reduced litter sizes, and direct injection of anti-ACTL7A into mice testis prevented the production of mature spermatids. Additionally, it was found that ACTL7A is present in the entire sperm head in murine sperm following *in vitro* capacitation, implying an involvement in the capacitation process (Fu et al., 2013). Identification of a homozygous missense variant showed that disruption of ACTL7A causes sperm acrosomal defects and infertility in human and mice (Xin et al., 2020). ACTL7A-deficient sperm had lower levels of PLCζ, a sperm-borne oocyte activation factor and infertility induced by ACTL7A deficiency was overcome with artificial oocyte activation. ACTL9-deficient human and murine sperm show a similar phenotype and,

indeed, it has been shown that ACTL9 appears to interact with ACTL7A (Dai et al., 2021). Both proteins are mislocated, when ACTL9 is absent. In another study Dai et al. reported a teratozoospermic patient with a homozygous missense variation of ACTL7A (Dai et al., 2022). The acrosome and acroplaxome become detached during spermiogenesis, according to the analysis of a mouse model with an identical mutation. The acroplaxome, ACTL7A and PLCζ are shed of and evicted in cytoplasmic droplets and sperm failed to activate the oocyte. Supporting previous findings, *Actl7a*-mutation-caused infertility was overcome with artificial oocyte activation. Moreover, ACTL7A and ACTL7B were found to be significantly lower expressed in teratozoospermic males in a study comparing the expression of testis-enriched genes in fertile men and patients (Ahn et al., 2017).

*ACTL7B* has been shown to be expressed post-meiotically in round and elongating spermatids in mice and humans (Hisano et al., 2003b, Guo et al., 2018). The protein is detected in the cytoplasm of round and elongating spermatids and, unlike ACTL7A, is evicted with excess cytoplasm at the end of spermiogenesis (Tanaka et al., 2003). Of note, a study comparing two groups of Luzhong mutton sheep with varied fecundity found nine genes, including ACTL7B and ACTL7A, that were associated with reduced litter size (Tao et al., 2021). Furthermore, proteomic and phosphoproteomic studies of swamp buffalo prepubertal and pubertal testis revealed that ACTL7B was more abundant and phosphorylated in pubertal testis, indicating that it plays a vital function in spermatogenesis (Huang et al., 2020). Interestingly, 5 polymorphisms in *ACTL7B* (and 6 in *ACTL7A*) were found in a cohort of Japanese infertile male patients, implying that also in human *ACTL7B* plays an important role in fertility (Tanaka et al., 2019). Moreover, ACTL7B was recently described as one of the six proteins/transcripts with the highest discriminating capacity between obstructive and non-obstructive azoospermia subtypes applying comparative proteomics on human testicular tissue (Davalieva et al., 2022). Taken together these studies imply, that *ACTL7B* plays a crucial role in male fertility in various species.

Recently, Clement et al. discussed the creation and analysis of *Actl7b*-null mice (Clement et al., 2023). Male *Actl7b*-null mice are infertile and displayed severe oligoteratozoospermia with sperm tail and head abnormalities.

During my PhD time, I have generated *Actl7a*- and *Actl7b*-deficient mice. The results from the analysis of the *Actl7b*-deficient mice were published in a pre-print and are presented in this thesis.

A pre-print has been published, describing our results of *Actl7b*-deficiency in mice:
Gina Esther Merges, Lena Arévalo, Keerthika Lohanadan, Dirk G. de Rooij, Melanie Jokwitz, Walter Witke, Hubert Schorle (2022) *Actl7b*-deficiency leads to mislocalization of LC8 type dynein light chains and disruption of murine spermatogenesis. *BioRxiv.* DOI: 10.1101/2022.12.19.520998

## 1.6. Aim of this research project

For this thesis different mouse models were generated and analyzed, which are deficient for sperm-specific genes. First, I have analyzed *Prm1*-deficient mice and compared them to *Prm2*-deficient and protamine-modified mice to decipher common and unique roles of *Prm1* and *Prm2*. Phenotypical differences are elaborated and discussed. Additionally, I have analyzed a mouse model carrying a *Prm1-Prm2* fusion gene. Here 5' of the *Prm1* CDS is fused in frame to the *mP2* part of *Prm2*. These mice lack 3' *Prm1* and the *cP2* domain and express one large fusion transcript. Initial results are compared to data from *Prm1*-, *Prm2*- and *cP2*-deficient mice generated in the laboratory. Aim was to learn more about PRM1-PRM2 interaction and the role of the cP2 domain.
Second, I have generated *Actl7a*- and *Actl7b*-deficient mice. Aim was to phenotypically characterize defects during spermatogenesis of these mice and understand the molecular roles of the genes targeted. Compared to the recently published *Actl7b*-null mice by Clement *et al.*, our study deepens the understanding about the consequences of loss of *Actl7b.* Evolutionary analysis of the *ACTL7B* coding sequence across various species should help to examine sequence conservation and selective pressures. This facilitates the interpretation on whether a gene is free to evolve or highly conserved, indicating great essentiality. Next, co-immunoprecipitation and subsequent mass spectrometric analyses were performed to determine potential interaction partners, taking an important step towards understanding the molecular role of ACTL7B and uncovering its interactome.

# 2. Materials

## 2.1. Equipment

| Description | Model | Supplier |
|---|---|---|
| Adjustable micro pipettes | Research | Eppendorf AG, Hamburg, Germany |
| Amicon® Ultra 30K – 0.5 Centrifugal Filter Device | UFC503008 | Merck Millipore Ltd., Burlington, MA, USA |
| Bacterial incubator | | Memmert, Schwabach, Germany |
| Balances | JE 120 | Ohaus Corporation, USA |
| | BP211S | Sartorius, Göttingen, Germany |
| | CP3202P | Sartorius, Göttingen, Germany |
| | PT 120 | Sartorius, Göttingen, Germany |
| Blot imaging system | ChemiDoc™ MP | Bio-rad, Hercules, USA |
| Cell culture incubators | Heracell 240i CO2 incubator | Hera Safe |
| Centrifuges | Multifuge 3 S-R | Kendro, Hanau, Germany |
| | 5417R | Eppendorf AG, Hamburg, Germany |
| | 5415D | Eppendorf AG, Hamburg, Germany |
| | Galaxy mini | Merck, Darmstadt, Germany |
| Confocal microscopes | LSM 710 | Zeiss, Oberkochen, Germany |
| | VisiScope | Vistron Systems, Puchheim, Germany |
| Cooling plate | Microm CP 60 | Microm GmbH, Walldorf, Germany |
| Counting chamber | Neubauer-improved | Marienfeld, Lauda-Königshofen, Germany |
| DNA SpeedVac | DNA110 | Savant, Farmingdale, USA |

| Description | Model | Supplier |
|---|---|---|
| Electrophoresis power supply | Consort EV243 | Peqlab, Erlangen, Germany |
| Electroporator | Gene Pulser II | Bio-rad, Hercules, USA |
| Gel electrophoresis chambers | 40-1214 | Peqlab, Erlangen, Germany |
| | B1 | Peqlab, Erlangen, Germany |
| Heating plate | OTS 40.2025 | Medite, Burgdorf, Germany |
| High speed camera | acA1920-155ucMED | Basler AG, Ahrensburg, Germany |
| HPLC system | Dionex Ultimate 3000 RSLC nano | Dionex GmbH, Idstein, Germany |
| Magnetic stirrer | MR3001 | Heidolph, Schwabach, Germany |
| Mass spectrometer | Orbitrap Fusion Lumos | ThermoFisher Scientific, Bremen, Germany |
| Microcentrifuge | 1-15P | Sigma Laborzentrifugen, Osterode am Harz, Germany |
| Microplate shaker | 980121EU | VWR, Radnor, USA |
| Microscopes | DM IRB | Leica, Wetzlar, Germany |
| | IX71 | Olympus, Tokio, Japan |
| | DM5500 B | Leica Microsystems, Wetzlar, Germany |
| Microtome | Microm HM 325 | Microm GmbH, Walldorf, Germany |
| Orbital shaker and incubator | Innova 4000 | New Brunswick Scientific, New Jersey, USA |
| PAGE Handcast System | Mini-PROTEAN® Tetra Handcast Syytem | Bio-rad, Hercules, USA |
| PCR cyclers | 2720 Thermal Cycler | Applied Biosystems |
| | FlexCycler | Jena Analytik, Jena, Germany |
| pH meter | FiveEasyTMFE20 | Mettler Toledo AG, Schwerzenbach, Switzerland |
| Pipette controller | Accu-jet® pro | BRAND, Wertheim, Germany |
| Polyacrylamide gel electrophoresis (PAGE) chamber | Mini-PROTEAN® Tetra Cell | Bio-rad, Hercules, USA |

| Description | Model | Supplier |
|---|---|---|
| Repetitive pipette | HandyStep® | BRAND, Wertheim, Germany |
| RNA Sequencing system | HiSeq 2500 V4 platform | Illumina, San Diego, USA |
| Sample mixer | HulaMixer™ | Thermo Fisher, Waltham, USA |
| Scanning electron microscope | Verios 460L with STEM3 detector | FEI Company, Hillsboro, Oregon, USA |
| | Crossbeam 550 FIB SEM equipped with a retractable STEM detector | Zeiss, Oberkochen, Germany |
| Spectrophotometer | NanoDrop™ 1000 | Peqlab, Erlangen, Germany |
| Thermomixer | Thermoblock compact | Eppendorf AG |
| Tissue embedding station | Tissue-Tek® | Sakura Finetek, Heppenheim, Germany |
| Tissue sample processor | Tissue-Tek® VIP | Sakura Finetek, Heppenheim, Germany |
| Trans-illuminating dissection microscope | SZ61 | Olympus Corporation, Tokyo, Japan |
| | SZX2-ILLTS | Olympus Corporation, Tokyo, Japan |
| | MS 5 | Leica, Microsystems, Wetzlar, Germany |
| Transmission electron microscope | CM 10 | Philips, Amsterdam, Netherlands |
| Ultramicrotome | Ultracut R | Leica, Wetzlar, Germany |
| UV imaging system | GEL iX20 | INTAS Science Imaging Instruments GmbH, Göttingen, Germany |
| Vortexer | Vortex-Genie® 2 | Scientific Industries, New York, USA |
| Water bath | TW8 | Julabo, Seelbach, Germany |

## 2.2. Consumables

| Product | Manufacturer |
|---|---|
| 1.5 ml / 2 ml reaction tubes | Sarstedt, Nümbrecht, Germany |
| 1.5 ml low bindng tubes | Sarstedt, Nümbrecht, Germany |
| 15 ml / 50 ml centrifuge tubes | Greiner, Kremsmuenster, Austria |
| 5 ml reaction tubes | Eppendorf AG, Hamburg, Germany |
| Amicon® Ultra 30K – 0.5 Centrifugal Filter Device | Merck, Darmstadt, Germany |
| Axygen® PCR® strip tubes | Corning Inc., New York, USA |
| Cover slips (18 x18 mm, 24 x 40 mm, 24 x 60 mm) | Medite, Burgdorf, Germany |
| Cryo tubes | Thermo Fisher Scientific, Waltham, MA, USA |
| Filter tips | Nerbe plus GmbH, Winsen, Germany |
| Microscope slides | Marienfeld GmbH, Lauda-Königshofen, Germany |
| Multiwell dishes, cell culture grade | TPP, Trasadingen, Switzerland |
| Paraplast Plus | McCormick Scientific, St. Louis, MO, USA |
| Pipette tips | Greiner, Kremsmuenster, Austria |
| Roti® PVDF 0.45 µm pore size | Carl Roth, Karlsruhe, Germany |
| Serological pipettes | Corning Incorporated, Corning, NY, USA |
| Sterile filters, 0.45 µm surfactant-free cellulose acetate membrane (SFCA) | Corning Incorporated, Corning, NY, USA |
| Whatman paper | Macherey-Nagel, Düren, Germany |

## 2.3. Chemicals and Reagents

| Product | CAS-No. | Manufacturer |
|---|---|---|
| 1,4-dithiothreit (DTT) | 3483-12-3 | Carl Roth, Karlsruhe, Germany |

| Product | CAS-No. | Manufacturer |
|---|---|---|
| 2-Dodecenylsuccinic acid anhydride | 26544-38-7 | Serva, Heidelberg, Germany |
| 2-Mercaptoethanol | 60-24-2 | Carl Roth, Karlsruhe, Germany |
| 2-propanol | 67-63-0 | VWR, Radnor, USA |
| 2,4,6-Tris-(dimethylaminomethyl)phenol | 90-72-2 | Serva, Heidelberg, Germany |
| Aceton | 67-64-1 | VWR, Radnor, USA |
| Albumin fraction V (BSA) | 9048-46-8 | AppliChem, Darmstadt, Germany |
| Ammonium persulfate (APS) | 7727-54-0 | Carl Roth, Karlsruhe, Germany |
| Ampicillin (Amp) | 69-52-3 | AppliChem, Darmstadt, Germany |
| Calcium chloride | 10043-52-4 | Merck, Darmstadt, Germany |
| Chloroform | 67-66-3 | Sigma-Aldrich, St. Louis, USA |
| Chromomycin A3 | 7059-24-7 | Merck, Darmstadt, Germany |
| cOmplete™ ULTRA Tablets, Mini Protease Inhibitor Cocktail | - | Roche, Basel, Suisse |
| Coomassie Brillant Blue G250 | 6104-58-1 | Biomol, Hamburg, Germany |
| Diethyl pyrocarbonat (DEPC) | 1609-47-8 | Sigma-Aldrich, St. Louis, USA |
| Entellan® new | - | Merck, Darmstadt, Germany |
| Eosin Y | - | Merck, Darmstadt, Germany |
| Eosin Y solution 0.5 % in H2O | 17372-87-1 | Carl Roth, Karlsruhe, Germany |
| Epon 812 | 90529-77-4 | Serva, Heidelberg, Germany |

| **Product** | **CAS-No.** | **Manufacturer** |
|---|---|---|
| Ethanol (EtOH) absolute | 64-17-5 | VWR, Radnor, USA |
| Ethidium bromide (EtBr) solution 1% | 1239-45-8 | Carl Roth, Karlsruhe, Germany |
| Ethylenediaminetetraacetic acid (EDTA) | 60-00-4 | AppliChem, Darmstadt, Germany |
| Glacial acetic acid | 64-19-7 | AppliChem, Darmstadt, Germany |
| Glucose | 50-99-7 | AppliChem, Darmstadt, Germany |
| Glycine | 56-40-6 | Carl Roth, Karlsruhe, Germany |
| Guanidine hydrochloride | 50-01-1 | Carl Roth, Karlsruhe, Germany |
| Heparin | | Braun, Melsungen, Germany |
| HEPES | 7365-45-9 | Sigma-Aldrich, St. Louis, USA |
| Hydrochloric acid | 7647-01-0 | VWR, Radnor, USA |
| Isofluran-Piramal | - | Piramal healthcare, Northumberland, UK |
| Lead citrate | | |
| Lipofectamine™ 2000 | - | Thermo Fisher, Waltham, USA |
| L-lactate | 867-56-1 | AppliChem, Darmstadt, Germany |
| Magnesiumsulphat heptahydrate | 10034-99-8 | Carl Roth, Karlsruhe, Germany |
| Methanol (MeOH) | 67-56-1 | VWR, Radnor, USA |
| Methylnadicanhydrid | 25134-21-8 | Serva, Heidelberg, Germany |
| Mineral oil GM-501 | | GYNEMED, Lensahn, Germany |

| Product | CAS-No. | Manufacturer |
|---|---|---|
| MitoTracker Red CMXRos (#9082) | | Cell Signaling Technology, Cambridge, UK |
| Nigrosin | 8005-03-6 | Carl Roth, Karlsruhe, Germany |
| Osmium tetroxide | 20816-12-0 | EMS, Hatfield, USA |
| Peanut agglutinin (PNA)-fluorescein isothiocyanite (FITC) Alexa 615 Fluor 488 conjugate | - | Molecular Probes, Invitrogen, Waltham, USA |
| Phenol Chloroform isoamylalcohol (PCI) | 13611 2-00-0 | AppliChem, Darmstadt, Germany |
| phenylmethylsulfonyl fluoride (PMSF) | 329-98-6 | |
| PBS tablets | - | AppliChem, Darmstadt, Germany |
| Potassium acetate | 127-08-2 | AppliChem, Darmstadt, Germany |
| Potassium dihydrogen phosphate (KH2PO4) | 7778-77-0 | Carl Roth, Karlsruhe, Germany |
| Propylenoxide | 75-56-9 | Merck, Darmstadt, Germany |
| Rotiphorese | - | Carl Roth, Karlsruhe, Germany |
| Skim milk powder | 99999 9-99-4 | Merck, Darmstadt, Germany |
| Sodium chloride (NaCl) | 7647-14-5 | AppliChem, Darmstadt, Germany |
| Sodium dodecyl sulphate (SDS) | 151-21-3 | VWR, Radnor, USA |
| Sodium hydrogen carbonate ($NaHCO_3$) | 144-55-8 | Carl Roth, Karlsruhe, Germany |
| Sodium hydroxide | 1310-73-2 | VWR, Radnor, USA |
| Sodiumacetate (NaAc) | 127-09-3 | Carl Roth, Karlsruhe, Germany |

| Product | CAS-No. | Manufacturer |
|---|---|---|
| Tetramethylethylendiamine (TEMED) | 110-18-9 | Carl Roth, Karlsruhe, Germany |
| tri-sodium citrate (dihydrate) | 6132-04-3 | Merck, Darmstadt, Germany |
| Trichloroacetic acid | 76-03-9 | VWR, Radnor, USA |
| Tris hydrochloride | 1185-53-1 | Carl Roth, Karlsruhe, Germany |
| Tris(hydroxymethyl)aminomethane | 77-86-1 | VWR, Radnor, USA |
| Triton® X-100 | 9036-19-5 | AppliChem, Darmstadt, Germany |
| TRIzol™ | - | Invitrogen™, Thermo Fisher Scientific, Waltham, USA |
| Tryptone/peptone | 91079-40-2 | Carl Roth, Karlsruhe, Germany |
| Tween® 20 | 9005-64-5 | AppliChem, Darmstadt, Germany |
| UltraPure™ agarose | - | Invitrogen™, Thermo Fisher Scientific, Waltham, USA |
| Uranyl acetate | 541-09-3 | EMS, Hatfield, USA |
| Urea | 57-13-6 | Merck, Darmstadt, Germany |
| Xylene | 1330-20-7 | VMP Chemiekontor, Siegburg, Germany |
| Yeast extract | 8013-01-2 | Merck, Darmstadt, Germany |
| β-mercaptoethanol | 60-24-2 | Carl Roth, Karlsruhe, Germany |

## 2.4. Buffers and solutions

| Buffer/Solution | Recipe/Supplier |
|---|---|
| Alkaline lysis buffer (HotShot) | 25 mM NaOH, 0.2 mM EDTA; pH 12 |
| Annealing buffer (10x) | 100 mM NaCl, 50 mM HEPES pH7.4 |
| Bouin fixation solution | Carl Roth, Karlsruhe, Germany |
| Carnoy´s solution | 3:1 (v/v) methanol-acetic acid |
| Coomassie Brilliant Blue staining solution | 1 g CBB, 500 ml MeOH, 100 ml glacial acetic acid, 400 ml $_{dd}H_2O$ |
| Daily sperm production (DSP) buffer | 0.15 M NaCl, 0.1 M $NaN_3$ 0.05% Triton-X 100 in water |
| Decondensing mix | 0.385 g DTT, 0.2% (v/v) Triton x-100, 200 i.u./ml, heparin, PBS ad 100 ml |
| Destaining solution (Coomassie Brilliant Blue) | 40% MeOH, 10% acetic acid in $_{dd}H_2O$ |
| DNA lysis buffer | 2 ml 5 M NaCl, 1 ml 1 M Tris-HCl, pH 8.0, 5 ml 0.5 M EDTA, pH 8.0, 5 ml 10% (m/v) SDS, $_{dd}H_2O$ ad 100 ml |
| Eosin-Nigrosin stain | 0.67 g eosin Y (color index 45380), 0.9 g sodium chloride, 10 g nigrosin (color index 50420), 100 ml $_{dd}H_2O$ |
| Epon A | 62 ml Epon 812, 100 ml 2-Dodecenylsuccinic acid anhydride |
| Epon B | 100 ml Epon 812, 89 ml Methylnadicanhydrid |
| Epon C | 20 ml Epon A, 20 ml Epon B, 0.6 ml 2,4,6-Tris (dimethylaminomethyl)phenol |
| Fixation solution for TEM | 3% (v/v) glutaraldehyde in 0.1 M cacodylate buffer, pH 7.4 |
| Fixing solution (Coomassie Brilliant Blue) | 50% MeOH, 10% acetic acid in $_{dd}H_2O$ |
| Heamalum, acididc (Mayer) | Waldeck, Münster, Germany |

| Buffer/Solution | Recipe/Supplier |
|---|---|
| HOS solution | 1.375 g D-fructose, 0.75 g sodium citrate dihydrate, 100 ml $_{dd}H_2O$ |
| LB medium (x5) | 25 g tryptone/peptone, 12.5 g yeast extract, 12.5 g NaCl, ddH2O ad 500 ml |
| Lysogeny broth (LB) agar | 5 g tryptone/peptone, 2.5 g yeast extract, 2.5 g sodium chloride, 8 g agar, $_{dd}H_2O$ ad 500 ml |
| Miniprep buffer P1 | 50 mM glucose, 25 mM Tris-HCl pH 8.0, 10 mM EDTA |
| Miniprep buffer P2 | 0.2 M NaOH, 1% (m/v) SDS |
| Miniprep buffer P3 | 60 ml 5 M potassium acetate, 11.5 ml acetic acid, 28.5 ml $_{dd}H_2O$ |
| Mouse anesthesia | 8.5 ml 0.9% NaCl, 1 ml 10% Ketamine, 0.5 ml 2% Xylazine |
| Neutralizing buffer (HotShot) | 40 mM Tris-HCl; pH 4 |
| PageRuler™ prestained protein ladder | 26616, Thermo Fisher, Waltham, USA |
| PHEM bufffer | 600 mM PIPES-Na, 250 mM HEPES-Na, 100 mM EGTA, 20 mM $MgCl_2$, pH 6.9 |
| Radioimmunoprecipitation assay (RIPA) buffer (10x) | Cell Signaling Technology, Cambridge, UK |
| Roti®-Load 1, reducing, 4x conc. | Carl Roth, Karlsruhe, Germany |
| Sample buffer (basic sperm proteins) | 5.5 M urea, 20% 2-mercaptoethanol, 5% acetic acid |
| SDS loading buffer 5x | 110 mM Tris/HCl pH 6.8, 20% Glycerol, 3.8% SDS, 8% β-mercaptoethanol, 0.05% bromophenol blue |
| SDS running buffer x10 | VWR, Radnor, USA |
| Solution 1 (basic sperm proteins) | 10 mM PMSF, 2 mM EDTA, 100 mM Tris, pH 8 |
| Solution 2 (basic sperm proteins) | 0.04435 g DTT in 0.5 ml 6 M GuHCl |
| Sperm DNA lysis buffer | 1 M Tris-HCl pH 8.0, 3 M NaCl, 0.5 M EDTA, 20% (m/v) SDS; 21 µl 1 M DTT, 2.5 µl 0.5% Triton X-100, 40 µl 10 mg/ml proteinase K |

| Buffer/Solution | Recipe/Supplier |
|---|---|
| Storage solution (Coomassie Brilliant Blue) | 5% acetic acid in $_{dd}H_2O$ |
| Transfer buffer (x10) | 24.2 g Tris(hydroxymethyl)aminomethane, 144.1 g glycine, 5 ml SDS 20%, $_{dd}H_2O$ ad 1 l |
| Tris-acetate-EDTA (TAE) buffer (50x) | 292 g Tris(hydroxymethyl)aminomethane, 18.6 g EDTA, 57.1 ml glacial acetic acid, $_{dd}H_2O$ ad 1 l |
| UranyLess | Electron Microscopy Sciences, Hatfield, PA, USA |

## 2.5. Media and cell culture reagents

| Medium | Recipe/supplier |
|---|---|
| DMEM | Gibco®/Life Technologies, Carlsbad, USA |
| ESC medium | DMEM+GlutaMAX; 15% (v/v) FCS; 50 U/ml penicillin/streptomycin; 2 mM L-glutamine; 1x nonessential amino acids; 1x essential amino acids; 0.1 mM β-mercaptoethanol; 1000 U/ml LIF; 3 µM CHIR-99021; 1 µM PD0325901 |
| Fetal calf serum (FCS) | Sigma-Aldrich, St. Louis, USA |
| Freezing medium (2x) | FCS; 20% (v/v) DMSO |
| HEK cell medium | DMEM+GlutaMAX; 15% (v/v) FCS; 50 U/ml penicillin/streptomycin; 2 mM L-glutamine |
| KSOM | GYNEMED, Lensahn, Germany |
| M16 | Sigma-Aldrich, St. Louis, US |
| M2 | Sigma-Aldrich, St. Louis, US |
| MEM Amino Acids Solution 50x | Gibco®/Life Technologies, Carlsbad, USA |
| MEM Non-Essential Amino Acids 100x | Gibco®/Life Technologies, Carlsbad, USA |
| OPTI-MEM | Thermo Fisher, Waltham, USA |
| TYH medium | 138 mM NaCl, 4.8 mM KCl, 2 mM CaCl2, 1.2 mM KH2PO4, 1 mM MgSO4, 5.6 mM glucose, 10 mM HEPES, 0.5 mM sodium pyruvate, 10 mM L-lactate, pH 7.4, 310-320 mOsm |

## 2.6. Kits

| Description | Manufacturer |
|---|---|
| Dako AEC+ High Sensitivity Substrate Chromogen Ready-to-Use | Dako, Agilent Technologies, Santa Clara, USA |
| Dynabeads™ Antibody Coupling Kit | Thermo Fisher, Waltham, USA |
| Dynabeads™ Co-Immunoprecipitation Kit | Thermo Fisher, Waltham, USA |
| GeneRuler™ 1 kb DNA ladder | Thermo Fisher, Waltham, USA |
| GeneRuler™ 100 bp plus DNA ladder | Thermo Fisher, Waltham, USA |
| GFP-Trap Magnetic Particles Kit | Chromotek GmbH, Munich, Germany |
| ImmPACT® Vector® Red alkaline phosphatase substrate- (SK-5105) | Vector Laboratories, Newark, CA, USA |
| Maxima H Minus Reverse Transcriptase | Thermo Fisher, Waltham, USA |
| NucleoBond® Xtra Maxi kit | Thermo Fisher, Waltham, USA |
| NucleoSpin® Gel and PCR Clean-up | Thermo Fisher, Waltham, USA |
| Pierce™ BCA protein assay kit | Thermo Fisher, Waltham, USA |
| SuperSignal™ West Femto Maximum Sensitivity Substrate | Thermo Fisher, Waltham, USA |
| TOPO™ TA Cloning™ Kit, with pCR™2.1-TOPO™ | Thermo Fisher, Waltham, USA |
| TUNEL Assay Kit- HRP-DAB (ab206386) | Abcam, Cambridge, UK |
| VectaFluor™ Anti-Mouse IgG, DyLight® 594 Kit, R.T.U- (DI-2794) | Vector Laboratories, Newark, CA, USA |
| VectaFluor™ Duet Double Labeling Kit, DyLight® 594 Anti-Rabbit IgG, DyLight® 488 Anti-Mouse IgG- (DK-8828) | Vector Laboratories, Newark, CA, USA |
| VectaFluor™ Horse Anti-Rabbit IgG, DyLight® 488 Antibody Kit- (DI-1788) | Vector Laboratories, Newark, CA, USA |
| VECTASTAIN® ABC-AP Kit, Alkaline Phosphatase (Rabbit IgG)- (AK-5001) | Vector Laboratories, Newark, CA, USA |
| VECTASTAIN® Elite® ABC-HRP Kit, Peroxidase (Standard)- (PK-6100) | Vector Laboratories, Newark, CA, USA |
| WESTAR NOVA 2.0 Western Blot Substrate | Cyanagen s.r.l., Bologna, Italy |

## 2.7. Plasmids

| Name | Source |
|---|---|
| DYNLL1_mCherry | Cloning was performed by Lena Arévalo |
| DYNLL2_mCherry | |
| Envelope (pMD2G) | Addgene, Watertown, MA, USA (#12259) |
| GAG-POL (pspax2) | Addgene, Watertown, MA, USA (#12260) |
| pCR®2.1 | Thermo Fisher, Waltham, USA |
| pCW57.1 | Addgene, Watertown, MA, USA (#41393) |
| pEGFP_N3 | Clontech (#6080-1) |
| Prm_trunc-EGFP | Cloning was performed together with Lena Arévalo |
| Prm1-EGFP | |
| Prm1KO-EGFP | |
| pVLmCherry | Addgene, Watertown, MA, USA (#36084) |
| pX330-U6-Chimeric_BB-CBh-hSpCas9 | Addgene, Watertown, MA, USA ( #42230) |

## 2.8. Oligonucleotides

| sgRNAs | | |
|---|---|---|
| **Name** | **Sequence (5´->3´)** | **Reference** |
| Actl7b_sg1_ts | CACCCGGACACGGCGTGTCGCAT | (Merges et al., 2022a) |
| Actl7b_sg1_bs | AAACCATGCGACACGCCGTGTCC | |
| Actl7b_sg2_ts | CACCAATACGGAAGATCAAGGCG | |
| Actl7b_sg2_bs | AAACGCGCCTTGATCTTCCGTAT | |
| Prm1_sg1_ts | CACCGCGAAGATGTCGCAGACGG | (Schneider, 2015) |
| Prm1_sg1_bs | AAACCCGTCTGCGACATCTTCGC | |
| Prm1_sg2_ts | CACCGTGTATGAGCGGCGGCGA | |
| Prm1_sg2_bs | AAACTCGCCGCCGCTCATACAC | |
| Prm2_sg1_ts | CACCATGGTTCGCTACCGAATG | |
| Prm2_sg1_bs | AAACCATTCGGTAGCGAACCAT | |
| Prm2_sg2_ts | CACCATAGTCCTCTACGCGCTC | |
| Prm2_sg2_bs | AAACGAGCGCGTAGAGGACTAT | |

| crRNAs | |
|---|---|
| **Name** | **Sequence (5´->3´)** |
| Actl7b_guide1 | CGGACACGGCGUGUCGCAUG |
| Actl7b_guide2 | AAUACGGAAGAUCAAGGCGC |

| cloning primers | |
|---|---|
| **Name** | **Sequence (5´->3´)** |
| Dynll1_fw | AAAAGAATTCATGTGCGACCGGAAGGC |
| Dynll1_fw | AAAAGAATTCATGTCTGACCGGAAGGCAG |
| Dynll1_rv | TTTTGGATCCTTACCAGATTTGAACAGAAGAATG |
| Dynll1_rv | TTTTGGATCCTTGCCCGACTTGAGAGGAG |
| EGFP_AgeI_rev | TTTTACCGGTTTACTTGTACAGCTCGTCCATGC |
| Dynll1_OV_fwd | AAAAGAATTCATGTGCGACCGGAAGGC |
| Dynll1_OV_rev | TTTTGGATCCTTACCAGATTTGAACAGAAGAATG |
| Dynll2_OV_fwd | AAAAGAATTCATGTCTGACCGGAAGGCAG |
| Dynll2_OV_rev | TTTTGGATCCTTGCCCGACTTGAAAGAGGAG |
| Prm1_NheI_fwd | AAAAGCTAGCGCCACCATGGCCAGATACCGATGCTG |
| Prm1_BamHI_rev | TTTTGGATCCGTATTTTTTACACCTTATGGTG |
| Prm1_EcoRI_fwd | AAAAGAATTCATGGCCAGATACCGATG |

| ES cell PCR | | | |
|---|---|---|---|
| **Gene/Locus** | **Direction** | **Sequence (5´->3´)** | **Reference** |
| *Actl7a* | fwd | CTCCAAACCGCCTCCCTAAA | this study |
| | rev | GTGAGAGACTTTCTGAGCCGT | |
| *Actl7b* | fwd | GGACACAGGTTCCACTCAACT | this study |
| | rev | CACTGATGTCTTCCTCTCGGG | |

| genotyping primer | | | | |
|---|---|---|---|---|
| **Gene/Locus** | **Direction** | **Sequence (5´->3´)** | **Mouseline** | **Reference** |
| *Actl7b* | fwd | GGGACACAGGTTCCACTCAAC | B6-Actl7bΔ | (Merges et al., 2022a) |
| | rev | AGGTAGTTGGTGAGGTCGCA | | |
| *Prm1* | fwd | CCACAGCCCACAAAATTCCAC | B6-Prm1Δ | (Schneider, 2015) |
| | rev | TCGGACGGTGGCATTTTTCA | | |

| genotyping primer | | | | |
|---|---|---|---|---|
| **Gene/Locus** | **Direction** | **Sequence (5´->3´)** | **Mouseline** | **Reference** |
| | | | | (Merges et al., 2022a) |
| *Prm2* | fwd | TGCAGCCTCAATCCAGAACC | B6-Prm2Δ | (Schneider et al., 2016) |
| | rev | TGTAGCCTCTTACGAGAGCAG | | |
| $Prm^{mut}$ | fwd | CCAGATACCGATGCTGCCG | B6-$Prm^{mut}$ | (Merges, 2018) |
| $Prm^{mut}$ | rev | CCCCTGTGTGTCCTCCCATA | | |
| $Prm^{mut}$ | rev | GTCTCCCCTATGCCTTTCTGG | | |

| sequencing primer | | |
|---|---|---|
| **Name** | **Sequence (5´->3´)** | **Targeted plasmid** |
| CMV_prom_fwd | CGCAAATGGGCGGTAGGCGTG | pVLmCherry |
| EGFP_seq_rev | ACGCTGAACTTGTGGCC | pEGFP_N3, Prm1-EGFP, Prm1KO-EGFP, Prm_trunc-EGFP |
| M13 fwd | TGTAAAACGACGGCCAGT | pCR®2.1 |
| M13 rev | CAGGAAACAGCTATGACC | |
| mCherry_N_rev | CTCCTTGATGATGGCCATGTTATC | pVLmCherry |
| pX330_seq | TTGCATATACGATACAAGGCTG | pX330-U6-Chimeric_BB-CBh-hSpCas9 |

## 2.9. Enzymes

| **Enzyme** | **Supplier** |
|---|---|
| DNase I, RNase free | Thermo Fisher, Waltham, USA |
| DreamTaq DNA Polymerase | Thermo Fisher, Waltham, USA |
| Platinum™ Taq DNA Polymerase | Thermo Fisher, Waltham, USA |
| Proteinase K | Merck, Darmstadt, Germany |
| Restriction enzyme AgeI | Thermo Fisher, Waltham, USA |
| Restriction enzyme BamHI | Thermo Fisher, Waltham, USA |
| Restriction enzyme BbsI | Thermo Fisher, Waltham, USA |
| Restriction enzyme EcoRI | Thermo Fisher, Waltham, USA |
| Restriction enzyme NheI | Thermo Fisher, Waltham, USA |

| Enzyme | Supplier |
|---|---|
| RNase A, DNase free | AppliChem, Darmstadt, Germany |
| T4 DNA ligase | Thermo Fisher, Waltham, USA |

## 2.10. Antibodies

| Antibody | Manufacturer | Order No. | Dilution IHC/IF | Dilution WB |
|---|---|---|---|---|
| anti-8-OHdG | Santa Cruz Biotechnology Inc., Dallas, USA | sc-66036 | 1:200 pH 6 | |
| anti-ACTIN | Abcam, Cambridge, UK | ab179467 | 1:500 pH 9 | |
| anti-ACTL7A | Proteintech, Rosemont, IL, USA | 17355-1-AP | | 1:1000 |
| anti-ACTL7B | Proteintech, Rosemont, IL, USA | 13537-1-AP | 1:750 pH 6 | 1:1000 |
| anti-alpha-tubulin | Santa Cruz Biotechnology Inc., Dallas, USA | sc-8035 | | 1:1000 |
| anti-β-actin | MP Biomedicals, Santa Ana, CA, USA | 08-691002 | | 1:5000 |
| anti-cP2 | custom-made, Davids Biotechnologie GmbH | - | 1:500 - 1:2500 pH 6 | |
| anti-CTSB | Abcam, Cambridge, UK | ab214428 | | 1:1000 |
| anti-DYNLL1 | Invitrogen, Waltham, MA, USA | SD08-04 | 1:1500 pH 6 | 1:1000 |
| anti-DYNLL2 | Proteintech, Rosemont, IL, USA | 16811-1-AP | 1:1500 pH 6 | 1:1000 |
| anti-Ezrin | Santa Cruz Biotechnology Inc., Dallas, USA | sc-58758 | 1:100 pH 6 | |
| anti-GPX4 | Abcam, Cambridge, UK | ab125066 | | 1:1000 |
| anti-H2A.L.2 | Govin *et al*., 2007 | - | | 1:1000 |

| Antibody | Manufacturer | Order No. | Dilution IHC/IF | Dilution WB |
|---|---|---|---|---|
| anti-H3 | Abcam, Cambridge, UK | ab1791 | 1:1500 pH 6 | 1:1000 |
| anti-H4 | Abcam, Cambridge, UK | ab177840 | 1:2000 pH 6 | |
| anti-HOOK1 | Proteintech, Rosemont, IL, USA | 10871-1-AP | | 1:1000 |
| anti-LC3A/B | Abcam, Cambridge, UK | ab128025 | | 1:1000 |
| anti-ODF2 | Proteintech, Rosemont, IL, USA | 12058-1-AP | 1:500 pH 6 | 1:1000 |
| anti-PRM1 (Hup1N) | Briar Patch Biosciences, Livermore, CA, USA | HupN1 | 1:200 pH 6 | 1:1000 |
| anti-PRM2 (Hup2B) | Briar Patch Biosciences, Livermore, CA, USA | Hup2B | 1:200 pH 6 | 1:1000 |
| anti-PRND | Proteintech, Rosemont, IL, USA | 26947-1-AP | 1:500 pH 9 | |
| anti-SPAG8 | Proteintech, Rosemont, IL, USA | 13915-1-AP | | 1:500 |
| anti-TNP1 | Abcam, Cambridge, UK | ab73135 | 1:1000 pH 6 | |
| anti-TNP2 | Santa Cruz Biotechnology Inc., Dallas, USA | sc-393843 | 1:100 pH 6 | |
| Biotinylated goat-anti-mouse | Dako, Agilent Technologies, Santa Clara, USA | E0433 | 1:200 | |
| goat anti-rabbit IgG/HRP | Dako, Agilent Technologies, Santa Clara, USA | P044801-2 | | 1:2000 |
| goat-anti-mouse Alexa Fluor 488 antibodies | Thermo Fisher Scientific | A-11001 | 1:500 | |
| rabbit anti-mouse IgG/HRP | Dako, Agilent Technologies, Santa Clara, USA | P026002-2 | | 1:1000 |

## 2.11. Bacteria

| Name | Genotype/Supplier |
|---|---|
| *E.cloni* 10G Chemically Competent | Lucigen Corporation, Middelton, WI, USA |
| TOP10 | F– mcrA Δ(mrr-hsdRMS-mcrBC) φ80lacZΔM15 ΔlacX74 recA1 araD139 Δ(ara-leu)7697 galU galK λ– rpsL(StrR) endA1 nupG |

## 2.12. Cell lines

| Cell line | Reference |
|---|---|
| E14TG2A (mES cells) | Prof. Dr. Christof Niehrs, IMB Mainz, Germany |
| HEK-293T | Dr. Michael Peitz, Bonn University, Institute of Reconstructive Neurobiology, Bonn, Germany |
| HEK$^{Actl7b\text{-}eGFP}$ | Prof. Dr. Walter Witke, Bonn University, Institute of Genetics, Bonn, Germany |

## 2.13. Animals

| Strain | Description | Mouseline ID | Variant description | Reference |
|---|---|---|---|---|
| B6-*Actl7bΔ* | endonuclease-mediated mutation of *Actl7b* | Actl7b$^{em1Hsc}$ ID:671828 | NM_025271.2: c.159_631del | this study |
| B6-*Prm1Δ* | endonuclease-mediated mutation of *Prm1* | | NM_013637.5: c.51_125del | (Schneider, 2015) (Merges et al., 2022a) |
| B6-*Prm2Δ* | endonuclease-mediated mutation of *Prm2* | Prm2$^{em1Hsc}$ ID:5760133 | NM_008933.2: c.13_109del | (Schneider et al., 2016) |

| Strain | Description | Mouseline ID | Variant description | Reference |
|---|---|---|---|---|
| B6-*Prm*$^{mut}$ | endonuclease-mediated mutation of Prm1-Prm2 locus | | c.[NM_013637.5:72_74del; NM_013637.5:75_NM_008933.2:106inv; NM_013637.5:111_NM_008933.2:107del] | (Schneider, 2019) |
| B6D2F1 | hybrid mouse strain derived from a cross between female C57BL/6 and male DBA/2, black coat color | | | Charles River, Erkrath, Germany |
| C57BL/6 J (B6) | imbred mouse strain, black coat color | | | Charles River, Erkrath, Germany |
| CD-1 | outbred mouse stain, albino | | | Charles River, Erkrath, Germany |

## 2.14. Software

| Name | Description | Source |
|---|---|---|
| analySiS | TEM imaging software | Olympus Soft Imaging Solutions GmbH, Münster, Germany |
| Endnote | reference management software | https://www.endnote.com |
| Ensembl | genome database | http://www.ensembl.org |

| Name | Description | Source |
|---|---|---|
| Gene ontology | enrichment analysis on gene/protein sets | www.geneontology.org |
| Geneious Prime | Bioinformatic platform for sequence analysis | https://www.geneious.com |
| Graphic for Mac | Vector graphics software | https://www.graphic.com |
| ImageJ | Vector graphics software | http://imagej.nih.gov/ij/ |
| Mascot server version 2.8.1 | peptide identification | Matrix Science Ltd, London, UK |
| NCBI | collection of databases; National Center for Biotechnology Information (NCBI) | http://www.ncbi.nlm.nih.gov/ |
| Nuclear_Morphology_Analysis_1.18.1_standalone | Plug-in for ImageJ | (Skinner et al., 2019) |
| Office for Mac | word processor, spreadsheet and a presentation program | Microsoft, Redmond, USA |
| PAML4.9 | phylogenetic analysis | (Yang, 1997, 2007) |
| Percolator algorithm version 3.02.1 | Mascot data evaluation | The et al., 2016 |
| Proteome Discoverer software 2.5.0.400 | mass spectrometry raw data processing | Thermo Fisher, Waltham, USA |
| R | statistical computing software | https://www.r-project.org |
| STRING | Protein-Protein Interaction Networks search tool | https://string-db.org |

| Name | Description | Source |
|---|---|---|
| SwissProt database | annotated protein sequence database | https://www.sib.swiss/swiss-prot |
| Tree of Life web project | phylogeny database | www.tolweb.org |
| VisiView software | imaging software | Vistron Systems GmbH, Puchheim, Germany |
| webPRANK software | codon-based phylogeny-aware alignment of orthologous gene sequences | Loytynoja and Goldman, 2010 |
| White balance correction_1.0 | Plug-in for ImageJ | written by Vytas Bindokas (2006, University of Chicago, USA) and modified by Patrice Mascalchi (2014, University of Cambridge, UK) |

# 3. Methods

## 3.1. CRISPR/Cas-mediated gene editing

### 3.1.1. Guide RNA design

Single guide RNAs for the generation of Actl7b-deficient mice were designed using the Benchling CRISPR Guide RNA design tool https://www.benchling.com/crispr/; ENSMUSG00000070980), aiming for maximum on-target and minimum off-target effects. Potential off-targets were additionally checked utilizing the "CRISPR-Cas9 guide RNA design checker" from IDT (https://eu.idtdna.com/site/order/designtool/index/CRISPR_SEQUENCE). The two guides selected after testing in murine embryonic stem (mES) cells (see next section), had off-target scores of 91/100 and 86/100, respectively. For guide 2, there were only two potential off-targets found on chromosome 4, both of which are located in non-coding regions. Guides used for the generation of *Prm1*-deficient mice were designed by Dr. Simon Schneider, who used the "CRISPR Design Tool" of the Massachusetts Institute of Technology (MIT) (Hsu et al., 2013) as described (Schneider, 2015).

### 3.1.2. Guide RNA testing

Guides were tested in mES cells as described (Schneider, 2015). Top and bottom strand oligonucleotides were annealed, digested with BbsI restriction enzyme and cloned into the expression plasmid px330. After transformation into chemically competent *E.cloni* via heat shock according to manufacturer's instructions, plasmids were isolated and sent to GATC/Eurofins (Cologne, Germany) for sequencing.

mES cells were transfected with 1 µg of plasmid and the transfection agent Lipofectamine™ 2000 following the manufacturer's instructions. Control cells were transfected with 1 µg of pEGFP_N3 plasmid. Subsequently, DNA was isolated from transfected cells and the targeted genomic region was amplified by PCR. PCR products were separated on agarose gels and editing-positive guide combinations were chosen for the use in murine zygotes.

For the generation of *Actl7b*-deficient mice, guides were ordered as crRNAs (IDT, Leuven, Belgium), annealed to tracRNA (IDT) (50nM) and mixed with Cas9 endonuclease (IDT) in OPTI-MEM medium.

*Prm1* and *Prm2* targeting guides were generated via *in vitro* transcription (Schneider, 2015).

## 3.2. Animals

### 3.2.1. Ethics statement

Animal experiments were performed according to the German law of animal protection and with the approval of the local institutional animal care committees Landesamt für Natur, Umwelt und Verbraucherschutz, North Rhine-Westphalia (approval IDs: AZ84-02.04.2013.A429, AZ81-0204.2018.A369).

### 3.2.2. Animal keeping

Animals were housed with 12 hours day/night rhythm and fed *ad libitum*. For organ dissection animals were sacrificed by cervical dislocation after euthanasia by isoflurane inhalation. Mice and testis were weight and the testis/body weight ratio was calculated. Mice aged between 8 and 13 weeks (starting in generation N3 for *Actl7b*-deficient mice and N4 for *Prm1*-deficient mice) were used for analysis.

### 3.2.3. Generation of gene-edited mice

Intraperitoneal injections of 5 i.u. of pregnant mare's serum and 5 i.u. of human chorionic gonadotropin were used to superovulate 6–8-week-old B6D2F1 females. 0.5 days after copulation (dpc) with B6D2F1 males, zygotes were isolated.
For the generation of *Prm1*-deficient mice and $Prm^{mut}$ mice (performed by Dr. Simon Schneider), sgRNAs (50 ng/l each) and Cas9 mRNA (100 ng/l) were microinjected into zygotes simultaneously. For the generation of $Prm^{mut}$ mice both guide combinations targeting the *Prm1* and the *Prm2* coding sequence were injected. After culturing in KSOM medium for 3 days, developing blastocysts were transferred into the uteri of pseudopregnant CB6F1 foster mice (Angela Egert and Andrea Jäger pers.commun.).
For the generation of *Actl7b*-deficient mice, zygotes were electroporated using a BioRad Gene Pulser in OPTI-MEM containing the guide RNA mix. Zygotes were washed and recovered before incubation in KSOM overlaid with mineral oil at 37°C overnight. Developing 2-cell stage embryos were transferred into the fallopian tube of pseudo-pregnant CD1 foster mice (Angela Egert and Andrea Jäger pers.commun.).
Offspring was genotyped by PCR and selected alleles were sequenced. The F1 generation was sequenced following initial backcrossing to C57BL/6J mice. Mice were selected for mouse line establishment and further backcrossed to C57BL/6J mice.

### 3.2.4. Fertility assessment

Male mice, aged between 8-12 weeks, were mated 1:1/1:2 to C57BL/6J females. Daily, plug-positive females were separated from males and later monitored for pregnancies and litters. Minimal five plugs per male were assessed and the proportion of plugs that resulted in live born litter was calculated.

## 3.3. Nucleic acid analysis

### 3.3.1. DNA isolation from ear punches

DNA from ear punches was isolated by alkaline lysis for 30 min at 95°C, cool-down on ice and subsequent neutralization with neutralization buffer (HotShot method; (Truett et al., 2000)).

### 3.3.2. DNA isolation from eukaryotic cells

For genotyping cells were pelleted at 3,000 rpm for 3 min and resuspended in 300 µl DNA lysis buffer supplemented with 12.5 µl Proteinase K (10 mg/ml) and 40 µl 10 % SDS. After incubation at 45°C for 1 h, 300 µl PCI was added to the solution and samples were shaken at RT for 10 min. Next, samples were centrifuged at 10°C, 10,000 rpm for 10 min and the aqueous phase was transferred to a threefold volume of EtOH containing 10% 3 M sodium acetate. Precipitated DNA was washed with 70% EtOH, dried and dissolved in TE low buffer.

### 3.3.3. DNA isolation from sperm

Sperm genomic DNA was isolated by incubation in sperm lysis buffer at 50°C over night (Weyrich, 2012). After centrifugation at 15,500 g for 10 min, 1 µl 20 mg/ml glycogen and 1/10 volume 3 M NaAc were added to the supernatant. DNA was precipitated with EtOH for 2 h at -80°C for 2 h followed by -20°C at 45 min, dried in a speed vac and dissolved in 30 µl TE buffer. DNA was analyzed on 0.8% agarose gels.

### 3.3.4. Genotyping polymerase chain reactions and agarose gel electrophoresis

For genotyping 1-2 µl of HotShot lysate/ 20 ng purified DNA was used mixed with 0.2 µl DreamTaq Polymerase, 5 µl 10x DreamTaq buffer, 2 µl dNTP mix (10 mM), 1 µl primer each (10 mM) adjusted to a final volume of 50 µl with $_{dd}H_2O$.

Cycling conditions:
*Actl7b* genotyping: 95°C, 5 min; 35x (95°C, 30 sec; 60°C, 30 sec; 72°C, 45 sec); 72°, 7 min; expected product sizes: WT: 607 bp, *Actl7b-:* 134 bp
*Prm1* genotyping: 95°C, 2 min; 35x (95°C, 30 sec; 64°C, 30 sec; 72°C, 35 sec); 72°, 5 min; expected product sizes: WT: 552 bp, $Prm^{mut}$*:* 225 bp
$Prm^{mut}$ genotyping: 95°C, 2 min; 35x (95°C, 30 sec; 60°C, 30 sec; 72°C, 40 sec); 72°, 5 min; expected product sizes: WT: 437 bp, *Prm1-:* 270 bp
*Actl7b* genotyping mES cells: 95°C, 5 min; 45x (95°C, 30 sec; 60°C, 30 sec; 72°C, 100 sec; 72°, 10 min; expected product size WT: 1048 bp
*Actl7a* genotyping mES cells: 95°C, 5 min; 45x (95°C, 30 sec; 60°C, 30 sec; 72°C, 100 sec; 72°, 10 min; 72°, 10 min; expected product size WT: 1451 bp
PCR products were separated on 1% agarose gels.

### 3.3.5. RNA isolation from testis

RNA from testis from 3 individuals per genotype were isolated in TRIzol according to manufactures instructions. After homogenization in 0.5 ml TRIzol, 100 µl chloroform was added to each sample and incubated for 3 min at room temperature. Samples were pelleted at 10,600 rpm for 15 min at 4°C and the supernatant was mixed with 250 µl isopropanol, incubated 10 min at RT and again pelleted at 10,600 for 10 min at 4°C. RNA was washed with 75% EtOH in DEPC $H_2O$ and air-dried. RNA was dissolved in 100 µl DEPC $H_2O$ at 55°C and stored at -80°C until use. RNA integrity (RIN) was determined using the RNA Nano 6000 Assay Kit with the Agilent Bioanalyzer 2100 system (AgilentTechnologies). RIN values were >7 for all samples.

### 3.3.6. DNase digestion and cDNA synthesis

1 µg RNA per sample was DNase I digested according to manufacturer's instructions and whole reaction mix was used for cDNA synthesis. For cDNA synthesis the Maxima H Minus Reverse Transcriptase Kit and oligo(dT) primers were used according to manufacturer's instructions.

### 3.3.7. 3´-mRNA sequencing

Sample quality control, library preparation and RNA-sequencing were performed by the University of Bonn Core Facility for Next Generation Sequencing (NGS). QuantSeq 3′-mRNA Library Prep (Lexogen) was used for library preparation and the Illumina HiSeq 2500 V4

platform for sequencing, producing >10 million, 50 bp 3′-end reads per sample. HiSAT2 2.1 was utilized to map reads to the mouse genome (GRCm38.89) (Kim et al., 2015) and quantification and annotation of transcripts was performed using StringTie 1.3.3 (Pertea et al., 2015) with annotations retrieved from Ensembl genome database. Differential gene expression (DE) was analyzed by Dr. Lena Arévalo. For the analysis, the Phython script (preDE.py) including the StringTie package was used to prepare DEseq2-compatible gene-level count matrices. Visualization of *Prm1*, *Prm2* and *Tnp2* genomic region mapping was done using the Integrative Genomics Viewer (IGV) (Robinson et al., 2011). DE was analyzed with DESeq2 1.16.1 (Love et al., 2014) and the adjusted *P*-value cut-off was determined using the Benjamini–Hochberg method and set to <0.05. Further, the log2-fold change (LFC) in expression cut-off was set at >1. Gene Ontology (GO) term and pathway overrepresentation analyses were performed using the PANTHER gene list analysis tool with Fisher's exact test and false discovery rate (FDR) correction (Mi et al., 2017).

## 3.4. Cloning

### 3.4.1. Ligation

Ligation of PCR products for sequencing was performed utilizing the TOPO™ TA Cloning™ Kit, with pCR™2.1-TOPO™ according to manufacturers instructions.

### 3.4.2. Transformation

Chemically competent *E.coli* safety strain TOP10 or chemically competent *E.cloni* (50 µl aliquots) were thawed on ice and 5 µl ligation product was added. After incubation on ice for 30 min, cells were heat shocked at 42°C for 1 min and again cooled down on ice. 400 µl of LB medium was added and suspension was shaken at 37°C for 1 h. Next, bacteria were plated onto LB agar plates containing 100 µg/ml ampicillin or kanamycin for selection. Additionally, X-Gal was used for blue-white screening. After incubation at 37°C overnight, clones were picked and transferred to 2 ml LB medium containing 100 µg/ml ampicillin or kanamycin and again incubated at 37°C overnight.

### 3.4.3. Plasmid isolation

1.5 ml of the 2 ml bacteria solution was used for plasmid isolation, while 0.5 ml were stored for Maxiprep. Bacteria were pelleted at 14,000 rpm for 30 sec and resuspended in 150 µl P1 buffer

supplemented with RNase A (1:1000). Next, 300 µl P2 buffer was added to the solution and mixed, followed by addition of 150 µl P3 buffer. After vigorous mixing, the samples were centrifuged at 14,000 rpm for 5 min and the supernatant was transferred to a tube containing 1 ml EtOH. DNA was pelleted at 13,000 rpm for 10 min at 4°C, washed twice with 80% EtOH, air-dried and dissolved in 40 µl TE low buffer or $_{dd}H_2O$.

#### 3.4.4. Sequencing

DNA sequencing was performed by GATC/Eurofins (Cologne, Germany) utilizing standard M13 primers or specific primers provided by us.

#### 3.4.5. Maxiprep

Bacteria were enriched in 150 ml LB medium containing 100 µg/ml ampicillin or kanamycin. Isolation of plasmids was performed using the Nucleobond Xtra Maxi Plus Kit according to manufacturers instructions. Plasmids used in transfections, were additionally sterile precipitated with EtOH at -80°C.

## 3.5. Evolutionary Analysis

Evolutionary analysis was performed by Dr. Lena Arévalo according to Lüke *et al.* (Lüke et al., 2016). The Ensembl genome browser and NCBI Genbank were used to find the *ACTL7B* coding sequences. The "Tree of Life web project" was used to construct the phylogenetic trees of the species under consideration (Letunic and Bork, 2021). Codon-based, phylogeny-aware alignment of orthologous gene sequences was performed using the webPRANK software (Loytynoja and Goldman, 2010). The ETE toolkit was used to visualize the tree and alignment (Huerta-Cepas et al., 2016). Using codeML implemented in PAML4.9, evolutionary rates and selective pressures were calculated (Yang, 1997, 2007). The calculation of the nonsynonymous/synonymous substitution rate ratio (ω = dN/dS) served as the foundation for calculating the evolutionary rate. Positive selection (ω >1), neutral evolution (ω =1), and purifying selection (ω <1) were differentiated. Different null and alternative models (M) were applied. All analyses that were done used the M0 model as their foundational model. For each gene's M0 model, various codon frequency settings were tested, and the setting with the best likelihood was selected. Likelyhood-ratio-tests (LRT) were used to determine whether alternative models described the selection constrains present in a dataset more accurately than the null models. We used two models to calculate the overall evolutionary rate and the

selective pressure on the coding sequence across all included species: M0 "one ratio" required that all branches evolve at the same freely estimated evolutionary rate; M0fix (fixed ratio) required that all branches' evolutionary rates be limited to 1. The overall evolutionary rate was calculated using the M0 model. To see if the computed evolutionary rate significantly deviates from 1 (neutral), an LRT between M0 and M0fix was conducted. Additionally, we used two models, the M0 "one ratio" and MCfree "two-ratio", which allow the calculation of a free and independent ω for the two designated clades, to ascertain whether the selective pressures differ between rodents and primates. The model log likelihood values were compared by LRT to see if the alternative MCfree model provides a better fit for the data. LRT was applied to compare the alternative model M2a "selection," which permits sites with ω >1, with the null model M1a "nearly neutral," which does not, in order to assess evolution along coding sequences and infer codon sites under positive or purifying selection. The models classify the codon sites into three groups: Sites in Class 0 are subject to purifying selection (0> ω >1); sites in Class 1 are evolving in a neutral fashion (ω = 1); and sites in Class 2a (only M2a) are under positive selection (ω <1). Codons that have undergone purifying selection (if the null model is the better match) or positive selection (if the alternative model is the better fit) were found using Bayesian statistics. Only sites with posterior probabilities (Bayes Empirical Bayes) higher than 0.95 classified to belong to class 0 or class 2a were determined to be subject to purifying or positive selection respectively.

## 3.6. Histology

### 3.6.1. Preparation of paraffin-embedded tissue sections

Murine tissue was fixed in Bouin´s solution or 4% paraformaldehyde at 4°C overnight. Next, tissue was processed in paraffin using an automated tissue sample processor and a tissue embedding station. Sections of 3 µm thickness were prepared utilizing a microtome.
For all downstream applications slides were deparaffinized and rehydrated by immersion into Xylene 2 times for 10 min followed by immersion into 100%, 96%, 80% and 70% EtOH for 5 min each and stored in PBS until use.

### 3.6.2. Hematoxylin and Eosin (HE) staining

Deparaffinized tissue sections were stained with Hemalum solution acid and Eosin Y solution, dehydrated by immersion into 70%, 80%, 96% and 100% EtOH for 5 min each, cleared in Xylene and mounted with Entellan.

### 3.6.3. Periodic acid Schiff (PAS) staining

Deparaffinized tissue sections were incubated in periodic acid solution (0.5%) for 10 min, rinsed in $H_2O$ and incubated in Schiff´s reagent for 20 min. Next, sections were rinsed in $H_2O$, counterstained with hematoxylin, dehydrated, cleared and mounted with Entellan.

### 3.6.4. TUNEL staining

TUNEL staining was performed utilizing a TUNEL Assay Kit according to manufacturers instructions. As recommended by the manufacturer, positive control slides were treated with 1 µg/µl DNase I in TBS/ 1 mM $MgSO_4$ for 20 min at RT.

### 3.6.5. Tissue preparation for transmission electron microscopy (TEM)

Tissue was fixed in TEM fixation solution at 4°C overnight, washed, fixed in 2% osmium tetroxide at 4°C for 2 h and washed again. The samples are dehydrated in increasing EtOH concentrations and contrasted in 70% (v/v) ethanol 0.5% (m/v) uranyl acetate for 1-1.5 h at 4°C. Next samples were washed with propylenoxid and incubated in decreasing ratios of propylenoxid:Epon C. Samples were embedded in 100% Epon C and Epon C was polymerized at 70°C for 48 h. Ultrathin sections were prepared and contrasted with UranyLess and lead citrate (Irina Kosterin, pers. commun.)

### 3.6.6. Transmission electron microscopy

TEM images were taken with the Philips CM10 transmission electron microscope equipped with analySiS imaging software, the scanning electron microscope Crossbeam 550 FIB SEM equipped with a retractable STEM detector and the scanning electron microscope Verios 460L with STEM3 detector. Part of the images were taken by the Microscopy Core Facility of the University Hospital Bonn.

## 3.7. Protein biochemistry

### 3.7.1. Immunohistochemical/Immunofluorescent staining

Deparaffinized tissue sections were subjected to heat mediated antigen retrieval in Tris-EDTA buffer (pH 9) or Citrate buffer (pH6) in the microwave at 500 W for 15 min (pH values given in

Antibody Table). Sections, which were stained against chromatin condensing proteins (PRM1, PRM2, cP2, TNP1, TNP2) were additionally treated with decondensing buffer for 5 min at 37°C. Sections stained against ACTIN, PRND, PRM1, PRM2 were additionally blocked with 3-6% $H_2O_2$ for 10-20 min. Next, slides were blocked with 5% BSA in PBS or Tris-HCl buffer and, if used, additionally with the blocking solution contained in the secondary antibody kit. Slides were incubated with primary antibodies (diluted in 1% BSA in PBS) at 4°C overnight. After washing with PBS, slides were treated with secondary antibodies.

Slides stained against PRM1 and PRM2 were treated either with a Vectastain Elite ABC-HRP Kit or the VectaFluor Duet Double Labeling Kit or the DyLight® 488 Anti-Mouse kit. Slides stained against 8-OHdG were processed using goat-anti-mouse Alexa Fluor 488 antibodies. Slides stained with anti-DYNLL1, anti-DYNLL2, anti-TNP1, anti-cP2, anti-PRND, anti-ODF2 and anti-ACTIN were processed using the VectaFluor™ Horse Anti-Rabbit IgG, DyLight® 488 Antibody Kit. Slides stained against Ezrin were processed with the VectaFluor™ Anti-Mouse IgG, DyLight® 594 Kit. Slides stained with anti-ACTL7B were processed using the Vectastain® ABC-AP Kit and ImmPACT® Vector® Red alkaline phosphatase substrate.

Slides stained with HRP were counterstained with hematoxylin and mounted with Entellan. IF stained slides were mounted with ProLong™ Gold antifade reagent (Thermo Fisher Scientific) or ROTI Mount FluorCare DAPI (Carl Roth).

For immunofluorescent staining of the acrosome, deparaffinized slides were permeabilized with 0.1% Triton-X 100 for 5 min at RT, blocked for 1 h with 1% BSA in PBS incubated for 1 h with Peanut agglutinin (PNA)-fluorescein isothiocyanite (FITC) Alexa 615 Fluor 488 conjugate and mounted with ROTI Mount FluorCare DAPI (Carl Roth).

### 3.7.2. Immunocytochemical staining of eukaryotic cells

Staining of HEK cells was performed by Dr. Lena Arévalo. Cells were fixed in 4% PFA under gentle agitation for 10 min at RT, washed 2 times with PBS and permeabilized with 0.5% Triton-X 100 for 5 min at RT. After two washing steps with PBS, cells were blocked in 2% BSA for 1 h at RT and incubated overnight at 4°C in primary antibody diluted in blocking solution. Cells were washed two times with PBS and incubated with Alexa Flour secondary antibody diluted in blocking solution for 2 h at RT. After two washing steps in PBS, cells were counterstained with Hoechst.

### 3.7.3. Immunocytochemical staining of sperm

Epididymal sperm were fixed in 4% PFA for 20 min at RT, incubated 5 µg/ml Peanut agglutinin (PNA)-fluorescein isothiocyanite (FITC) Alexa 615 Fluor 488 conjugate and 20 nm MitoTracker Red CMXRos for 45 min at RT, washed in PBS and smeared on slides. Slides were mounted with ROTI Mount FluorCare DAPI (Carl Roth).
Testicular sperm were fixed on slides and permeabilized with 0.1% Triton-X 100 for 15 min at RT, blocked 1 h with 5% BSA in PBS and incubated for 1 h with anti-$\alpha$-tubulin. Slides were counterstained with DyLight 488 antibody and mounted with ROTI Mount FluorCare DAPI (Carl Roth).

### 3.7.4. Isolation of testicular proteins

For western blot analysis and MassSpec analysis from whole testis protein, testes were homogenized in 1 ml per 100 mg tissue 1:10 RIPA buffer. After incubation on ice for 15 min, samples were sonicated for 5 min, centrifuged for 30 min at 14,000 rpm at 4°C and the supernatant was used for downstream applications.
For Co-IP experiments from whole testis protein the T-PER$^{TM}$ Tissue Protein Extraction Reagent (Thermo Fisher Scientific) supplemented with Halt Protease Inhibitor Single-Use Cocktail EDTA-Free (Thermo Fisher Scientific) was used according to the manufacturer's instructions.

### 3.7.5. Isolation of basic, nuclear-enriched sperm proteins

Isolation of basic, nuclear-enriched proteins from sperm was performed as described by Soler-Ventura *et al.* (Soler-Ventura et al., 2018). Sperm isolated from the cauda were counted, washed in PBS, pelleted resuspended in 200 µl buffer containing 4 µl 1 M Tris pH 8, 0.8 µl 0.5 M MgCl2 and 5 µl Triton X-100. Next, cells were pelleted at 8940 g for 5 min at 4°C and mixed with 1 mM phenylmethylsulfonyl fluoride (PMSF). Depending on the number of cells used, appropriate amounts of solution 1, solution 2 and vinylpyridine (0.8%) were added to the lysed cells and incubated for 30 min at 37°C. DNA was precipitated with 5x ice-cold 100% EtOH. Next, proteins were dissolved in 0.5 M HCl with 100% trichloroacetic acid at 4°C. Proteins were washed twice with acetone, lyophilized and resuspended in sample buffer.

### 3.7.6. Isolation of proteins from eukaryotic cells

Proteins isolated for Co-IP experiments were isolated utilizing the M-PER™ Mammalian Protein Extraction Reagent (Thermo Fisher Scientific) supplemented with Halt Protease Inhibitor Single-Use Cocktail EDTA-Free (Thermo Fisher Scientific) according to the manufacturers' instructions.

### 3.7.7. SDS-PAGE

Protein extracts were run on a 12% SDS gel with a 5% stacking gel and transferred to methanol-activated PVDF membranes using the Trans-Blot Turbo System (Bio-Rad).

### 3.7.8. Acid-Urea-PAGE

Basic proteins were separated on a pre-electrophorized 15% AU-PAGE (2.5 M urea, 0.9 M acetic acid, 15% acrylamide/0.1% *N,N'*-methylene *bis*-acrylamide, tetramethylethylenediamine (TEMED) and ammonium persulfate (APS)) and transferred to methanol-activated PVDF membranes using the Trans-Blot Turbo System (Bio-Rad). Protein extract volumes equivalent to 1.5 million sperm per well were loaded.

### 3.7.9. Western Blot

Membranes were blocked using 5% milk or 1:1 TBST (1% Tween 20): ChemiBLOCKER for 1 h at room temperature and incubated with primary antibody diluted in blocking buffer at 4°C overnight. Membranes were washed in TBST and incubated with secondary antibodies in TBS for 1 h at RT. Following washing in TBST, the signals were detected with WESTARNOVA2.0 chemiluminescent substrate or SuperSignalTM West Femto Maximum Sensitivity Substrate and the ChemiDoc MP Imaging system.

### 3.7.10. Coomassie staining and band size quantification

AU-gels were fixed in Fixing solution for 1 h – overnight under gentle agitation on a microplate shaker. Next, gels were incubated 20 min in Coomassie Brilliant Blue staining solution. Background staining was removed by incubation in Destaining solution for 1 h, while exchanging the solution once. Gels were stored in Storage solution until use. The density of Coomassie stained bands were analyzed utilizing ImageJ (Schneider et al., 2012, Arévalo et al., 2022a).

### 3.7.11. Antibody purification

Antibodies used for antibody coupling were purified using Amicon® Ultra 30K – 0.5 Centrifugal Filter Devices according to the manufacturer's instructions. Buffer exchange with PBS reduced Sodium Azide and Glycerol concentrations in antibody preservation buffers, which might have negatively affected antibody coupling.

### 3.7.12. Antibody coupling

Purified antibodies were coupled to beads using the Dynabeads™ Antibody Coupling Kit according to the manufacturer's instructions. For anti-ACTL7B beads were coupled with 7 µg antibody per mg beads, for anti-DYNLL1 and anti-DYNLL2 10 µg antibody per mg beads were used.

### 3.7.13. Co-immunoprecipitation (Co-IP)

For Co-IP experiments on whole WT testis protein 7.5 mg of anti-ACTL7B-coupled beads and 5 mg empty beads were used with the Dynabeads™ Co-Immunoprecipitation Kit according to the manufacturer's instructions. Proteins were eluted in in 1 ml HPH EB buffer and lyophilized in portions. 700 µl sent for mass spec analysis, 300 µl solubilized in SDS-PAGE sample loading buffer for western blot analysis.
1.5 mg of anti-DYNLL1-coupled, anti-DYNLL2-coupled and empty beads were used with the Dynabeads™ Co-Immunoprecipitation Kit for Western Blot applications according to the manufacturer's instructions.
For Co-IP on proteins isolated from eukaryotic cells, GFP pull-down assay was performed using GFP nanobody-coupled magnetic beads according to the manufacturer's instructions. Proteins were eluted in Roti®-Load 1 and analyzed in western blot.

### 3.7.14. Mass Spectrometry

Peptide preparation, liquid chromatography (LC)-mass spectrometry (MS) and data analysis were performed at the University of Bonn Core Facility Mass Spectrometry. Differential abundance analysis was performed by Lena Arévalo.
Peptide preparation from basic sperm protein extractions:
Proteins were dissolved in 50 mM acrylamide solution (Tris-HCl, pH = 8), alkylated for 30 min at RT. Next, 1 µg of Trypsin was added for proteolysis at 37˚C overnight. Dried peptides were dissolved in 10 µl 0.1% trifluoro acetic acid (TFA) and desalted with ZipTips (Waters

GmbH,Eschborn, Germany). Equilibration and binding were performed in presence of 0.1% TFA, followed by washing with 0.1% formic acid (FA). Eluates were dried and stored at -20˚C.

Preparation of Co-IP samples:

Protein samples (50 µg per sample) were subjected to in solution preparation of peptides with the iST 96x sample preparation kit (Preomics GmbH, Martinsried, Germany) according to manufacturer's instructions.

Preparation of whole testis proteomic samples:

Protein lysates containing 200 µg protein were mixed with a 4-fold volume of chilled acetone and incubated for 1 h at -20°C. After centrifugation for 15 min at 14,000 g, the supernatant was discarded, pellets were air-dried and dissolved in 20 µL Lyse buffer (Preomics iST-NHS kit). Protein amounts were determined by BCA assay and 40 µg of protein per sample was mixed with 50 µL of the kit's DIGEST solution. Next, 0.25 mg of TMTpro isobaric Mass Tag Labeling reagent (15plex) was added and incubated at RT for 1 h. Quenching was performed by using 10 µL of 5% hydroxylamine. After following the rest of the iST-NHS kit instructions, pooled peptides were dried in a vacuum concentrator, dissolved in 20 mM ammonium formate (pH=10) and fractionated by reversed phase chromatography at elevated pH with a Reprosil 100 C18 column (3 µm 125 x 4 mm, Dr. Maisch GmbH, Ammerbuch-Entringen, Germany). 6 pools were formed by combining 60 fractions and air-dried in a vacuum concentrator. Next, peptides were purified by solid phase extraction (Oasis HLB cartridges, Waters GmbH, Eschborn, Germany).

Prepared peptides were re-dissolved in 0.1% formic acid (FA) and separated on a Dionex Ultimate 3000 RSLC nano HPLC system (Dionex GmbH, Idstein, Germany). The autosampler was operated in µL-pickup mode. 1 µL was injected onto a C18 analytical column (self-packed 300/400 mm length, 75 µm inner diameter, ReproSil-Pur 120 C18-AQ, 1.9 µm, Dr. Maisch). Peptides were separated during a linear gradient from 2%/5% to 35% solvent B (90% acetonitrile, 0.1% FA) at 300 nL/min. The nanoHPLC was coupled online to an Orbitrap Fusion Lumos mass spectrometer (ThermoFisher Scientific, Bremen, Germany).

LC-MS measurement of basic sperm proteins and peptides from Co-IP experiments:

Every 3 seconds, peptide ions between 300 and 1600 m/z were scanned in the Orbitrap detector with R = 120,000 (maximum fill time 50 ms, AGC target 400,000). For internal calibration, Polysiloxane (445.12002 Da) was used (typical mass error ≤1.5 ppm). The gradient length was 90 min. In a top-speed method, peptides were subjected to higher energy collision induced dissociation (HCD: 1.0 Da isolation, threshold intensity 25,000, normalized energy 27%) and fragments were analyzed with target 50,000 and maximum injection time of 22 ms, R = 15,000. Fragmented peptide ions were excluded from repeat analysis for 20 s.

LC-MS measurement of TMT-labelled fractions (peptides from whole testis):

The gradient length was 150 min and peptide ions between 300 and 1600 m/z were scanned in the Orbitrap detector with R = 120,000 (maximum fill time 50 ms, AGC target 400,000). Peptides were subjected to collision induced dissociation for identification (CID: 0.7 Da isolation, normalized energy 30%) and fragments analyzed in the linear ion trap with AGC target 50% and maximum fill time 35 ms, rapid mode. Here, fragmented peptide ions were excluded from repeat analysis for 30 s. Top 10 fragment ions were chosen for synchronous precursor selection and fragmented with higher energy CID (HCD: 3 Da MS2 isolation, 65% collision energy) for detection of reporter ions in the Orbitrap analyzer (range 100-180 m/z, resolution 50,000, maximum fill time 86 ms, AGC target 200%).

Raw data was analyzed with Proteome Discoverer software 2.5.0.400 (Thermo Fisher Scientific) and peptide identification was done with an in-house (University of Bonn Core Facility Mass Spectrometry) Mascot server version 2.8.1 (Matrix Science Ltd, London, UK). Data was compared to Mus musculus sequences from the SwissProt database including isoforms (2022/03, 17132 murine sequences) and contaminants database (cRA (Mellacheruvu et al., 2013)). The precursor Ion m/z tolerance was 10 ppm and the fragment ion tolerance 0.5 Da (CID). Tryptic peptides with up to two missed cleavages were searched.

Static modifications wer set to be $C_6H_{11}NO$-modification of cysteines (delta mass of 113.08406) and TMTpro on N-termini and lysines. Additionally, oxidation was allowed as dynamic modification of methionine. The Mascot results were evaluated by the Percolator algorithm version 3.02.1 (The et al., 2016)(*Actl7b*-deficient mice) or version 3.05 (Kall et al., 2008)(*Prm*-deficient mice), which was implemented in Proteome Discoverer. Spectra with identifications above 1% q-value were sent to a second round of database search with semi tryptic enzyme specificity, allowing for one missed cleavage. Next, dynamic modifications were set. For analysis of the *Actl7b*-deficient mice those were set to be N-terminal acetylation, methionine oxidation, TMTpro, and cysteine alkylation. For the analysis of basic sperm proteins (*Prm1*- and *Prm2*-deficient mice) these were set to protein N-terminal acetylation, methionine oxidation and carbamylation on lysine and N-termini. Actual FDR values for analysis of *Actl7b*-deficient samples were 0.7% (peptide spectrum matches) and 1.0% (peptides and proteins). Reporter ion intensities (most confident centroid) were extracted from the MS3 level, with SPS mass match >65%. For the analysis of basic sperm proteins, actual FDR values were typically ≤0.5% (peptide spectrum matches), ≤1.0% (peptides) and <1% (proteins) and proteins were accepted if at least two peptides with q-value <1% were identified. Summed abundances were used for relative quantification.

Differential abundance (DA) analysis performed using the Bioconductor package proDA (Ahlmann-Eltze and Anders, 2021). The peptide spectrum match (PSM)-level data was extracted from Protein Discoverer. For the analysis of basic sperm proteins and whole testis protein only proteins detected in all genotypes and all replicates with more than two peptides

were included in the analysis. Next, those proteins were log2 transformed and median normalized before DA analysis. Proteins with a LFC >1 and FDR adjusted P<0.05 were considered differentially abundant compared with WT. For the analysis of whole testis proteome also proteins with an LFC>0.5 (FDR adjusted p<0.05) compared to WT were analyzed. Data was visualized using the R-package ggplot2 (Wickham, 2011).

#### 3.7.15. F-/G-Actin ratio

Analysis of the F-/G-Actin ratio was performed by Melanie Jokwitz as described (Pilo Boyl et al., 2007). Testis tissue was homogenized in 500 µl 1.1x PHEM buffer supplemented with 1.2% TritonX-100. After incubation on ice for 15 min, the samples were centrifuged in a swing-out rotor for 10 min at 10000 g at 4°C. 400 µl of the (G-Actin containing) supernatant was mixed with 100 µl 5x SDS loading buffer for 10 min and cooled on ice. The pellet was dried and resuspended in 650 µl 1x SDS loading buffer, boiled and incubated on ice. Equal volumes of supernatant and pellet fraction were separated on a 10% acrylamide gel. After blotting, the membranes were stained with anti-β-actin and band quantification was performed using the GE FujiFilm ImageQuant LAS-4000 CH mini Imager (GE Healthcare, Chicago, IL, USA).

## 3.8. Spermatid and sperm analysis

#### 3.8.1. Isolation of testicular sperm

For IF staining testicular sperm were isolated as described by Kotaja *et al.*(Kotaja et al., 2004). Seminiferous tubules are immersed in PBS, inspected under trans-illuminating dissection microscope (Leica and Olympus Corporation) and sections of the tubules were selected based on the light absorption pattern. Small pieces of the selected regions were transferred to a microscopic slide and smashed by covering with a coverslip. Excess liquid was soaked up with a filter paper and slides were snap frozen in liquid nitrogen. After flipping of the cover slide, slides were fixed in 90% EtOH for 5 min at RT and stored at -80°C until use.

#### 3.8.2. Isolation of epididymal sperm

Sperm were isolated from the cauda epididymis via the swim-out method (Schneider et al., 2016). Cauda were dissected and immersed in M2 medium or PBS at 37°C. The tissue was incised multiple times and incubated at 37°C for 20-30 min. After flushing with the pipet multiple times sperm were collected.

### 3.8.3. Daily testicular sperm production

Testicular daily sperm production was determined according to Juma *et al.* (Juma et al., 2017) with adjustments. After removal of the tunica albuginea, testes were homogenized in 400 µL DSP buffer and subsequently diluted further in DSP buffer. WT and heterozygous samples were adjusted to 4 ml, KO samples to 2 ml final volume. Next, elongating spermatids were counted utilizing a Neubauer counting chamber. The result was divided by 4.84, which is the number of days murine spermatids are spend in steps 14-16 during sperm development.

### 3.8.4. Eosin-Nigrosin (EN) staining

Equal volumes of sperm swim-out solution and EN stain were mixed and incubated for 30 sec. 30 µl of the mix was pipetted onto a microscopic slide, smeared out, air-dried and mounted with Entellan. 200 sperm per animal were analyzed under a light microscope. While sperm with impaired membrane integrity stain pink (inviable), sperm with intact membranes exclude the stain and appear white (viable).

### 3.8.5. Hypoosmotic swelling test

100 µl of sperm swim-out solution was mixed with 1 ml pre-warmed HOS solution, incubated for 30 min at 37°C and dropped onto a microscopic slide. The sample is covered with a cover slip and 200 sperm per animal were analyzed under a light microscope within 1 h. Sperm with swellings and coiling of flagella were counted as viable.

### 3.8.6. Nuclear morphology analysis

To analyze sperm nuclear head morphology, sperm were fixed in Carnoy´s solution, dropped on microscopic slides and mounted with ROTI Mount FluorCare DAPI (Carl Roth). Next, images were collected at 100x magnification to analyze a minimum of 100 sperm heads per animal. Testicular sperm were prepared in the same manner, but images were collected at 63x magnification and a minimum of 120 sperm heads per animal were examined. Images were analyzed with the ImageJ plugin ‘Nuclear_Morphology_Analysis_1.18.1_standalone’ as described by Sinner *et al.* (Skinner et al., 2019).

### 3.8.7. Sperm motility analysis

Sperm swim-out was performed in 1 ml sterile filtered THY medium for 15 min at 37°C and diluted 1:20 - 1:50 in THY medium containing 3 mg/ml BSA. 30 µl of dilution were pipetted onto a microscopic slide equipped with a spacer, covered with a cover slip and evaluated under an inverted microscope equipped with a heated slide holder (37°C). Sperm were recorded with a high-speed camera at 100 frames/sec for 2 sec. Analysis of videos was performed with ImageJ by producing a ´z project´ to distinguish motile from immotile sperm. 100 sperm per animal were analyzed.

## 3.9. Cell culture

### 3.9.1. Generation of HEK$^{Actl7b\text{-}eGFP}$ cells

HEK$^{Actl7b\text{-}eGFP}$ cells were generated by Carla Simon with aid of Dr. Piedro Pilo Boyl. *Actl7b* cDNA was amplified using the Q5 high fidelity thermostable DNA polymerase (NEB) (primer: GFP-Actl7b_fw and GFP-Actl7b_rv: ctcgagctcaagcttcgatggcgacaaagaacag, ggtaccgtcgactgcagttagcacttgctgtagatgg) and ligated into the EcoRI (NEB)-digested pEGFP-C1 vector (Clontech) utilizing the NEBuilder HiFi DNA Assembly kit (NEB) according to the manufacturer's instructions. Cells were transfected using Lipofectamine™ 2000. After selecting cells for 3 weeks with 1 mg/ml geneticin™ (G418 sulfate, Gibco), cells were cultured for another 6 weeks and five clones with different degrees of fluorescence were selected and expanded. The clone with the highest fluorescence intensity was chosen for further experiments.

### 3.9.2. Transfection of cells

HEK cells were transfected at 80% confluency using 3 µg plasmid with FuGENE HD Transfection Reagent according to the manufacturer's instructions. Cells were imaged 12 h after transfection.

## 3.10. Statistical analysis

If not stated otherwise, data are presented as means ± standard deviation (s.d.). Statistical significance was calculated using a two-tailed, unpaired Student's t-test. A value of $P<0.05$ was considered significant and is indicated in the graphs (*$P<0.05$; **$P<0.005$; ***$P<0.001$)

## 3.11. Data presentation

Shown images (photomicrographs and transmission electron micrographs) represent raw images, except for adjustments in size, cropping and white balance. Graphs were prepared using Microsoft Excel for Mac or R. Visualizations of graphs and figures were prepared using Graphic for Mac.

# 4. Results

**Parts of the results sections have been published in:**

Gina Esther Merges, Julia Meier, Simon Schneider, Alexander Kruse, Andreas Christian Fröbius, Klaus Steger, Lena Arévalo, Hubert Schorle (2022) Loss of *Prm1* leads to defective chromatin protamination, impaired PRM2 processing, reduced sperm motility and subfertility in male mice. *Development.* DOI: 10.1242/dev.200330

Gina Esther Merges, Lena Arévalo, Keerthika Lohanadan, Dirk G. de Rooij, Melanie Jokwitz, Walter Witke, Hubert Schorle (2022) *Actl7b*-deficiency leads to mislocalization of LC8 type dynein light chains and disruption of murine spermatogenesis. *BioRxiv.* DOI: 10.1101/2022.12.19.520998

## 4.1. Establishment of a *Prm1*-null allele

### 4.1.1. CRISPR/Cas9-mediated gene editing for the generation of *Prm1*-deficient mice

*Prm1*-deficient mice were generated by Dr. S. Schneider using CRISPR/Cas9-mediated gene editing in zygotes (Schneider, 2019). Zygotes were microinjected with *in vitro* transcribed Cas9 mRNA and two guide RNAs targeting exon 1 and exon 2 of *Prm1* (Figure 6A, black arrow heads). Gene editing positive founder animals were mated to C57BL/6J mice. The offspring was sequenced and a mouse carrying a 167 bp in frame deletion (Δ167) was selected for

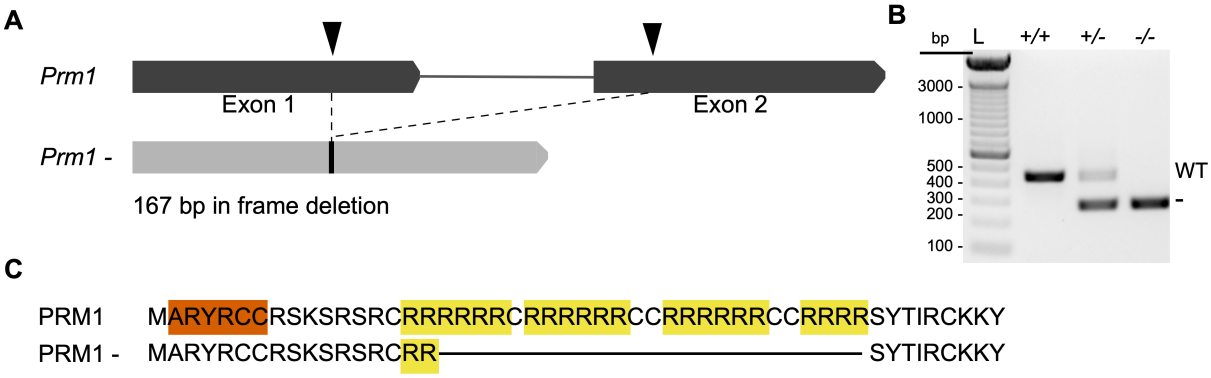


**Figure 6: Establishment of *Prm1*-deficient mice. (A)** Graphical representation of CRISPR/Cas9-mediated gene editing of the *Prm1* locus. sgRNA target sites in exon 1 and exon 2 of the *Prm1* coding sequence are marked with black arrowheads. A 167 bp in-frame deletion was generated. **(B)** Representative genotyping PCR of *Prm1+/+*, *Prm1+/-* and *Prm1-/-* mice. Amplification of WT *Prm1* or the *Prm1-* allele generated products of 437 bp or 270 bp, respectively. **(C)** Predicted amino acid sequence of the truncated PRM1. Arginine-rich DNA binding sites are marked in yellow. The epitope of the anti-PRM1 antibody used in this study is marked in vermillion. Modified from (Merges et al., 2022b). Gene editing was performed by Dr. Simon Schneider (Schneider, 2019).

further backcrossing and mouse line establishment. PCR-based genotyping was established using primers that flank the deleted region (Figure 6B). On protein level, the deletion has been predicted to cause loss of central arginine-rich DNA binding domains (Figure 6C, marked in yellow). The antibody used in the following experiments targets the N-terminal region of PRM1 (Figure 6C, marked in vermillion). Hence, if a truncated protein is synthesized, it should be detectable.

Transcripts and potential protein translated were evaluated by 3´-mRNA sequencing and transcript mapping as well as immunohistochemical (IHC) staining (Figure 7). While in wild-type mice transcripts mapped to the whole coding sequence of *Prm1* (WT; *Prm1*+/+), transcripts in the *Prm1*-deficient (*Prm1-/-*) mice mapped to the 3´- and 5´- region of *Prm1* only (Figure 7A). This indicated that truncated RNA lacking the central, deleted region is transcribed from the gene-edited *Prm1* allele. IHC using an antibody that targets the N-terminal region of PRM1 on testis sections showed, that a truncated PRM1 protein, however, is not produced in *Prm1-/-* mice (Figure 7B). This suggests that the transcripts are subjected to nonsense-mediated RNA decay. In testis sections from *Prm1*+/+ and *Prm1*+/- mice, PRM1 was detectable in step 12-16 elongating spermatids, as it has been described in literature (Klaus et al., 2016).

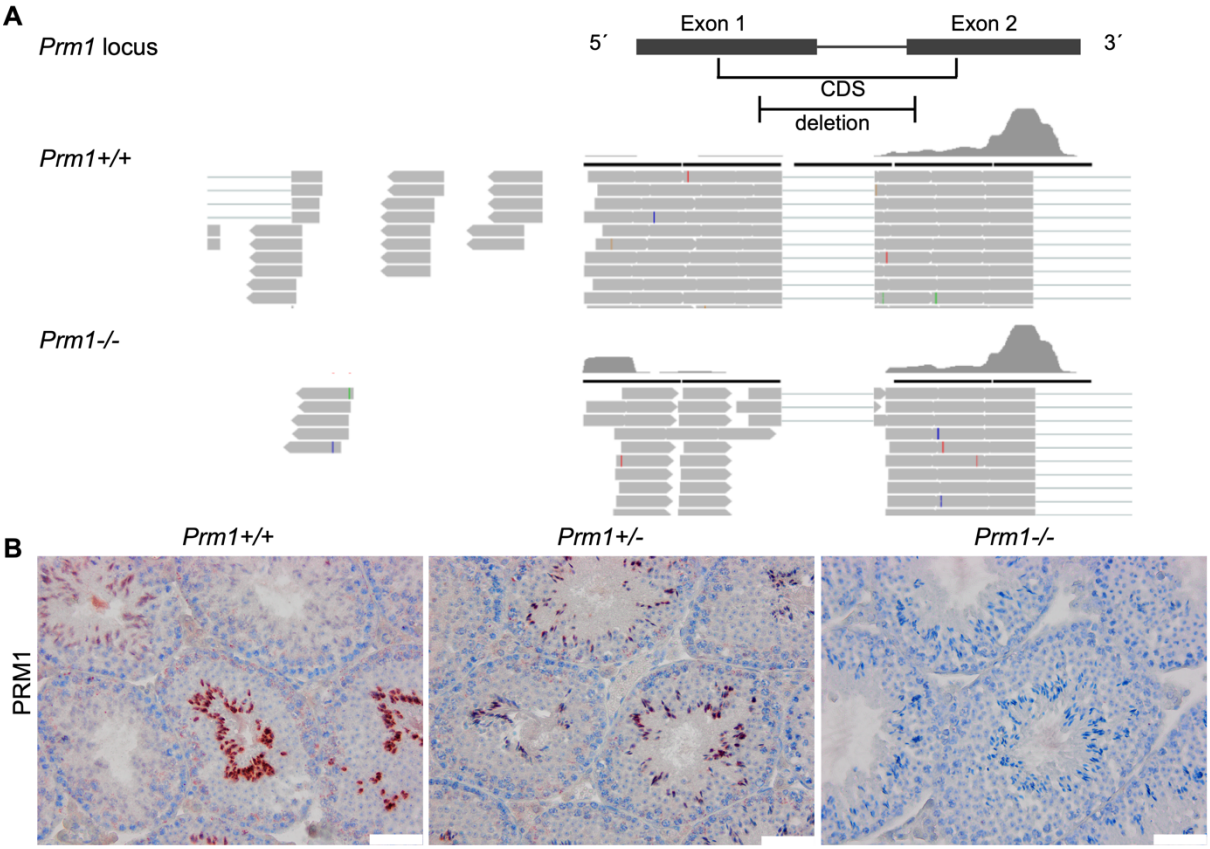


**Figure 7: Validation of *Prm1*-deficiency. (A)** Representative cut-out of RNAseq reads mapping to the *Prm1* locus from whole testis RNAseq of *Prm1*+/+ and *Prm1-/-* mice. **(B)** IHC staining against PRM1 on Bouin-fixed, paraffin-embedded testis sections of *Prm1*+/+, *Prm1*+/- and *Prm1-/-* mice (counterstain: Hematoxylin). Scale: 50 µm. Modified from (Merges et al., 2022b). RNAseq analysis was performed by Dr. Lena Arévalo. Immunohistochemical stainings were performed by Alexander Kruse and Andreas Christian Fröbius.

### 4.1.2. Functional analysis of *Prm1*-null allele *in vitro*

To analyze PRM1-protein interaction in a cell culture system, plasmids were constructed for transient PRM1 expression (Figure 8). Iuso *et al.* showed, that PRM1 is able to condense DNA when expressed in somatic cells *in vitro* (Iuso et al., 2015). Here we fused PRM1 to EGFP to visualize PRM1 expression and localization. 24 hours after transfection of murine embryonic fibroblasts, PRM1-EGFP was visible in foci in the nucleus (Figure 8A). Foci were DAPI bright, indicating beginning DNA condensation. These areas were enlarged and fused after 48 hours, in some cases leading to completely condensed chromatin, visualized by DAPI bright, small nuclei. Further the truncated PRM1 sequence as generated by the Δ167 allele detected *Prm1-/-* mice was fused to EGFP (*Prm1*KO-eGFP). Here, the EGFP signal was visible in the cytoplasm similar to the EGFP-only control suggesting that the Δ167 protein does not translocate to the nucleus and does not bind to chromatin. DAPI staining is even throughout the nuclei, suggesting that the Δ167 protein did not lead to chromatin condensation. This experiment again confirms that the Δ167 represents a *Prm1*-null allele. Moreover, it shows that the arginine-rich DNA binding domains deleted by gene editing in the Δ167 are crucial for protamine function. Interestingly, expression of a modified PRM1, carrying only one arginine-rich domain (*Prm_trunc*-EGFP), led to similar results as the full-length PRM1, suggesting that one DNA binding domain is sufficient to convey nuclear location and DNA condensation *in vitro* (Figure 8B-C).

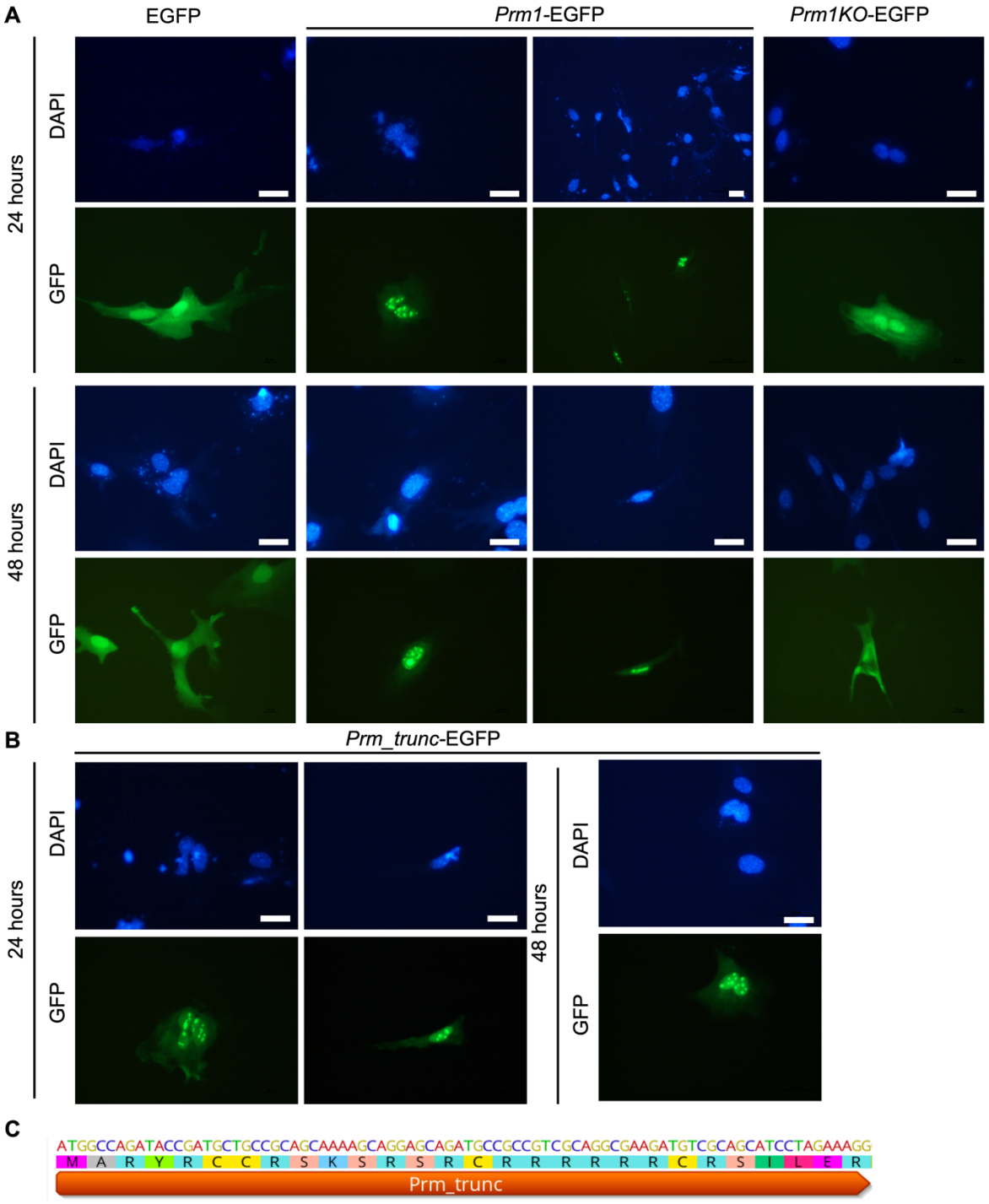


**Figure 8: Investigation of chromatin condensation potential of PRM1 *in vitro*. (A)** Representative images of murine embryonic fibroblasts (MEFs) transiently transfected with protamine expressing plasmids. *Prm1* and *Prm1KO* (mutated version of *Prm1* carrying the 167bp deletion generated in *Prm1-/-* mice) were fused to EGFP. An EGFP plasmid was used as control. **(B)** A modified Prm (*Prm_trunc*) was fused to EGFP and transfected into MEFs. DNA condensation was monitored after 24 and 48 hours. Scale: 20 µm. **(C)** Sequence of Prm_trunc and its predicted amino acid sequence. Cloning of plasmids was performed together with Dr. Lena Arévalo.

## 4.2. Characterization of *Prm1*-deficient mice

### 4.2.1. Fertility assessment and spermatogenesis in *Prm1*-deficient mice

After validating the *Prm1*-null allele, transcript mapping of surrounding gene locus was performed to analyze whether the deletion caused changes in expression of flanking *Prm2* and *Tnp2* coding sequences, (Figure 9A, Figure S1). No apparent off-targets were detected in *Prm1-/-* mice, as transcript reads mapped to the entire *Prm2* and *Tnp2* coding sequences. Further IHC staining against PRM2 on testis sections produced the expected spatiotemporal pattern comparable to *Prm1+/-* and *Prm1-/-* mice (Figure 9B). PRM2 was detected in elongating spermatids (steps 14-16; (Klaus et al., 2016)).

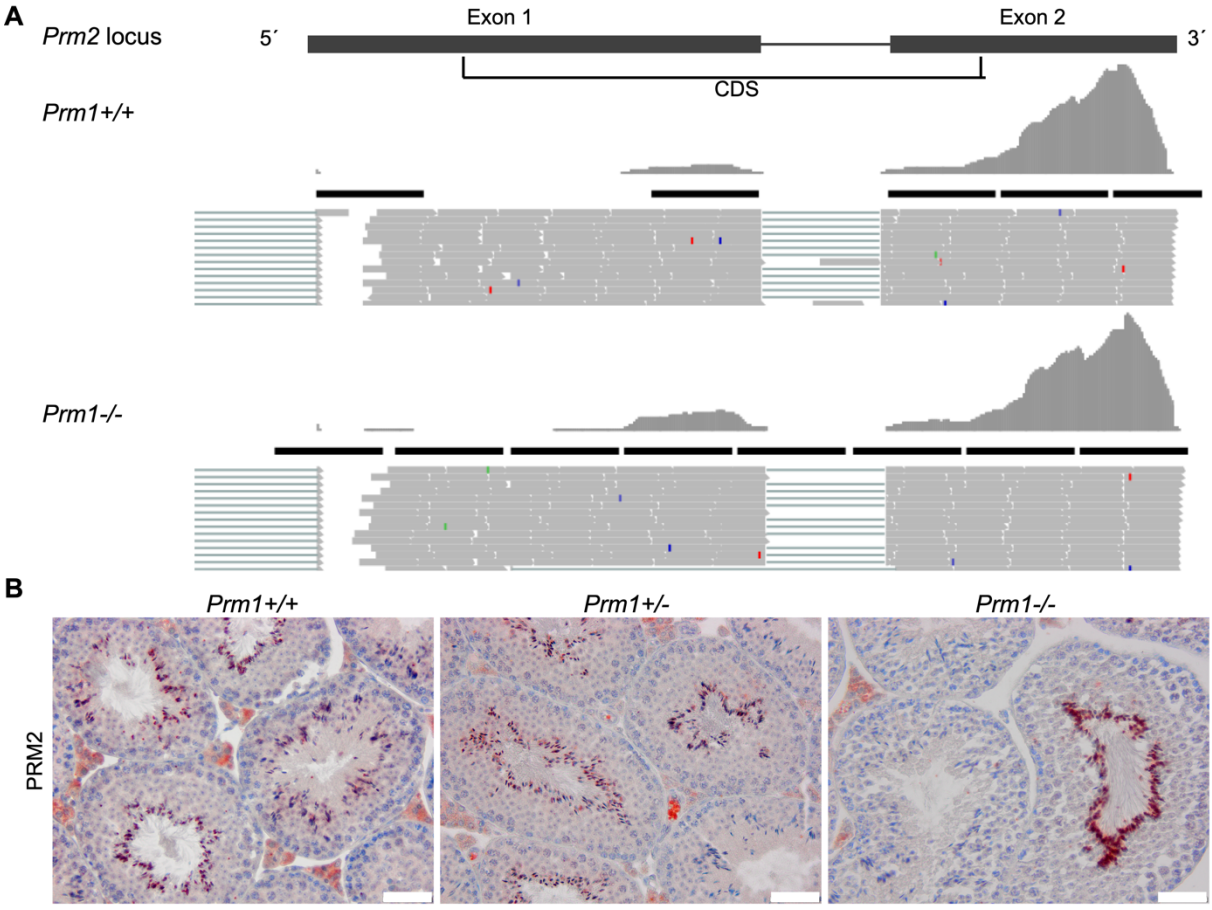


**Figure 9: Analysis of *Prm2* expression in *Prm1*-deficient mice. (A)** Representative cut-out of RNAseq reads mapping to the *Prm2* locus from whole testis RNAseq of *Prm1+/+* and *Prm1-/-* mice. **(B)** IHC staining against PRM2 on Bouin-fixed, paraffin-embedded testis sections of *Prm1+/+*, *Prm1+/-* and *Prm1/-* mice (counterstain: Hematoxylin). Scale: 50 µm. Modified from (Merges et al., 2022b). RNAseq analysis was performed by Dr. Lena Arévalo. Immunohistochemical stainings were performed by Alexander Kruse and Andreas Christian Fröbius.

Fertility testing revealed that *Prm1+/-* males are subfertile (Figure10). They showed significantly reduced litter sizes and pregnancy frequencies compared to *Prm1+/+* males. While on average 95% of copulations resulted in pregnancies for *Prm1+/+* males, only around

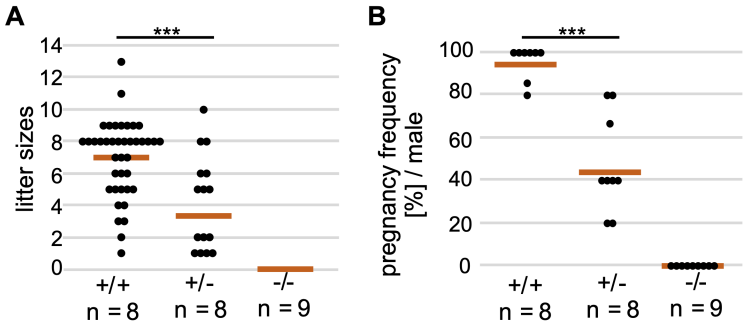


**Figure 10: Fertility analysis of *Prm1*-deficient mice. (A)** Scatter plot of litter sizes monitored for males after mating with female WT mice. The mean litter size per genotype is indicated by vermillion lines (n = number of males). **(B)** Pregnancy frequency (%) per male after mating with female WT mice. The mean pregnancy frequency per genotype is indicated by vermillion lines (n = number of males); data was analyzed using a two-tailed, unpaired Student's t-test (***p<0.001). Modified from (Merges et al., 2022b). Data obtained together with Julia Meier during her Master Thesis (Meier, 2020).

43% of copulations were successful for *Prm1+/-* males (Figure 10B). *Prm1-/-* males were infertile.

Next, basic spermatogenic parameters were evaluated. The average testis weight and seminiferous tubule diameter was not significantly different in *Prm1-/-* and *Prm1+/-* mice compared to *Prm1+/+* mice (Figure 11A-B). Additionally, the average number of elongating spermatids per tubule cross section was comparable (Figure 11C). Hence, sperm production appeared undisturbed in *Prm1+/-* and *Prm1-/-* mice compared to WT mice. Histologically, *Prm1+/-* and *Prm1-/-* testis appeared inconspicuous (Figure 11D). The spermatozoa lining the lumen of stage VII to VIII seminiferous tubules appear morphologically normal in all genotypes.

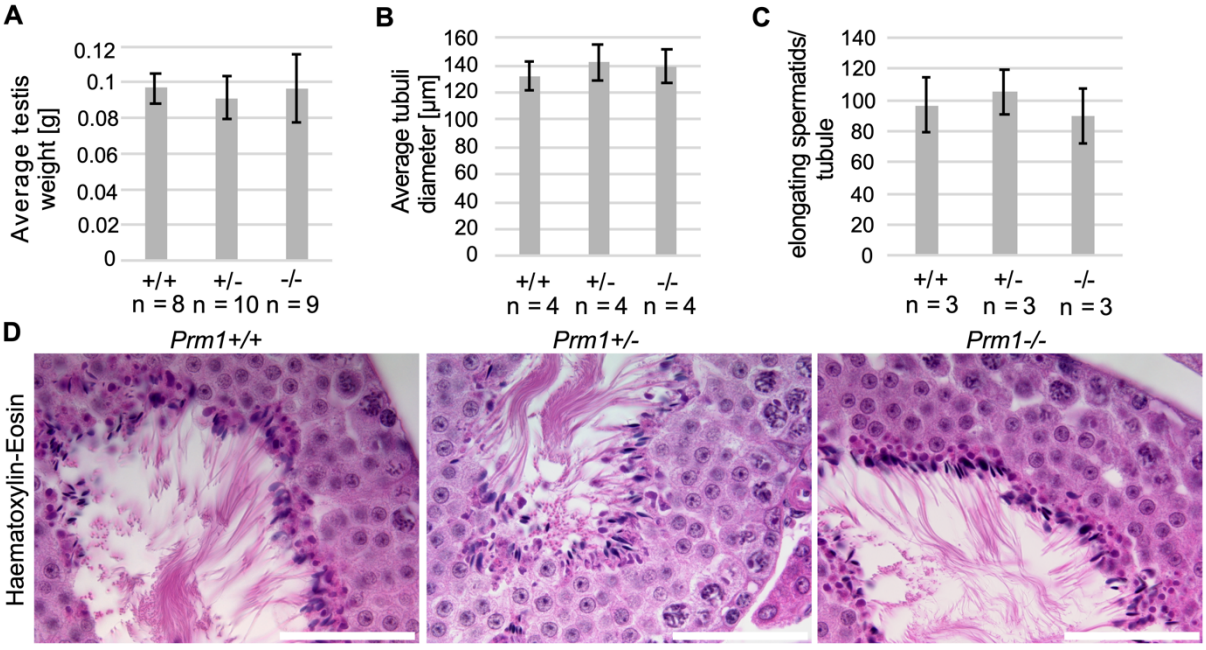


**Figure 11: Macro- and microscopic analysis of spermatogenesis of *Prm1*-deficient mice. (A)** Average testis weight of *Prm1+/+*, *Prm1+/-* and *Prm1-/-* males (n = number of males). **(B)** Average seminiferous tubule diameter of *Prm1+/+*, *Prm1+/-* and *Prm1-/-* males; 25 tubules per mouse were evaluated (n = number of males). **(C)** Number of elongating spermatids per seminiferous tubule cross section of *Prm1+/+, Prm1+/-* and *Prm1-/-* males; 5 tubules per male were analyzed (n = number of males); data are shown as mean ± s.d. and were analyzed using a two-tailed, unpaired Student's t-test. **(D)** Hematoxylin and Eosin staining of testis sections of *Prm1+/+, Prm1+/-* and *Prm1-/-* males. Stages VII to VIII of the epithelial cycle with spermatozoa lining up at the edge of tubule lumen are shown. Scale: 50 µm. Modified from (Merges et al., 2022b). Parts of the data obtained together with Julia Meier during her Master Thesis (Meier, 2020).

Next, periodic acid-Schiff (PAS) staining was used to visualize acrosomal structures (Figure 12A; vermillion arrow heads). Acrosome formation appeared normal in *Prm1+/-* and *Prm1-/-* mice. Acrosomal vesicles are formed, which later form a cap that continues to descend caudally along the elongating spermatid nucleus during the course of spermiogenesis. Lastly acrosomal structures line the anterior nuclear envelope of elongated spermatids. Additionally, transmission electron micrographs of testis revealed, that spermatid chromatin condensation appears normal in *Prm1*-deficient mice (Figure 12B). Further, spermatid flagella formation seemed undisturbed. Apparently, spermatogenesis is overtly normal in *Prm1*-deficient mice.

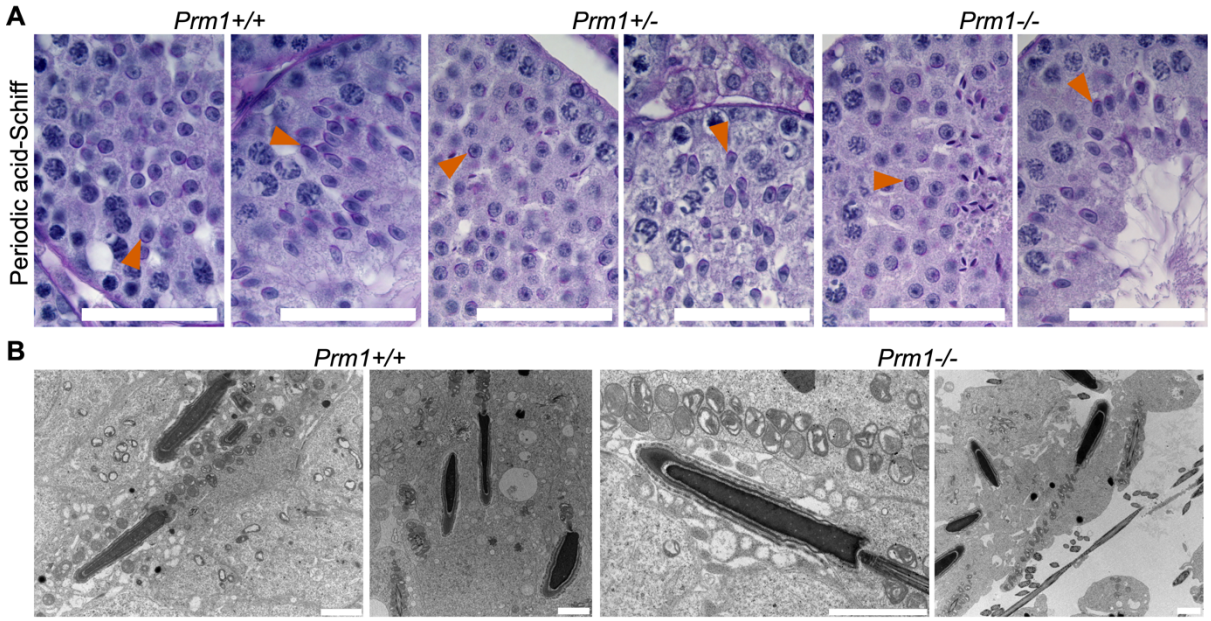


**Figure 12: Characterization of basic testicular sperm structures of *Prm1*-deficient mice. (A)** Periodic acid-Schiff staining of *Prm1+/+, Prm1+/-* and *Prm1-/-* testis sections (vermillion arrowheads mark acrosomal structures). Scale: 50 µm **(B)** Transmission electron micrographs of *Prm1+/+* and *Prm1-/-* testicular sperm. Scale: 2 µm. Modified from (Merges et al., 2022b).

### 4.2.2. Sperm DNA integrity in *Prm1*-deficient mice

Owing to the fact, that protamines play a central role in sperm chromatin compaction, the condensation of DNA in epididymal sperm after sperm maturation was evaluated (Figure 13A). *Prm1-/-* sperm showed defects in chromatin condensation, compared to *Prm1+/-* and *Prm1+/+* sperm. While around 80% of *Prm1+/-* and *Prm1+/+* sperm nuclei appear electron dense, indicative of highly condensed chromatin, less than 30% of *Prm1-/-* sperm nuclei were still condensed after epididymal transit (Figure 13B). Moreover, *Prm1-/-* epididymal sperm showed severe membrane damages and lacked acrosomal structures (Figure 13C).

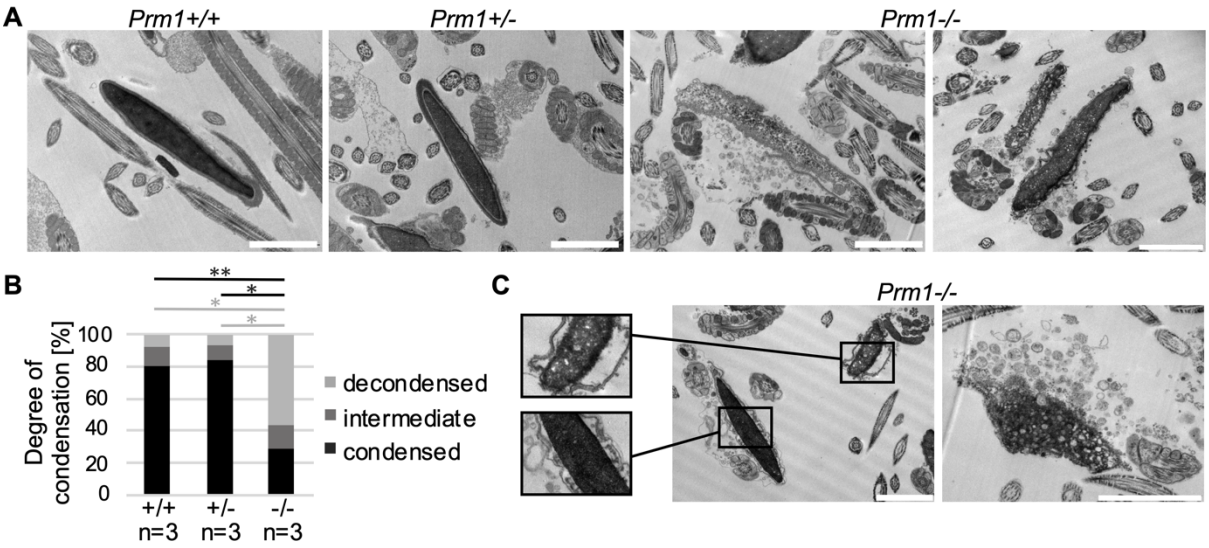


**Figure 13: Chromatin condensation status of epididymal *Prm1*-deficient sperm. (A)** Representative transmission electron micrographs of *Prm1+/+, Prm1+/-* and *Prm1-/-* epididymal sperm. Scale: 2 µm **(B)** Quantification of DNA condensation of *Prm1+/+, Prm1+/-* and *Prm1-/-* epididymal sperm; 100 sperm per male were analyzed (n = number of males). Data are means and were analyzed using a two-tailed, unpaired Student's t-test (*p<0.05; **p<0.005). **(C)** Transmission electron micrographs of *Prm1-/-* epididymal sperm. Scale: 2 µm. Modified from (Merges et al., 2022b). Data obtained together with Julia Meier during her Master Thesis (Meier, 2020).

To examine DNA integrity of epididymal sperm, DNA was isolated and run on an agarose gel (Figure 14). DNA isolated from WT sperm presented as a band of high molecular weight, suggestive of intact DNA. In contrast, DNA from *Prm1-/-* sperm was fragmented to around 100-500 bp in size. The majority of DNA isolated from *Prm1+/-* sperm appears to be intact. However, a weak smear of DNA of low molecular weight (100-600 bp) is suggestive of some DNA damage in *Prm1+/-* sperm. Of note, DNA from *Prm2-/-* sperm is completely degraded. *Prm2+/-* sperm DNA on the other hand presents as a single band of high molecular weight similar to WT. These results suggest that loss of one allele of *Prm1* cannot be fully compensated, while loss of one allele of *Prm2* did not lead to any pathomorphological effects.

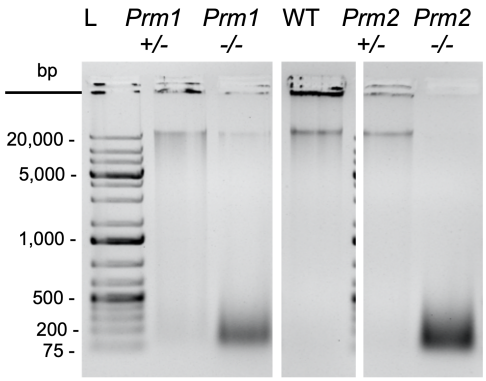


**Figure 14: Sperm DNA integrity in *Prm1*- and *Prm2*-deficient epididymal sperm.** Genomic DNA isolated from epididymal sperm of *Prm1+/-, Prm1-/-, Prm2+/-, Prm2-/-* and WT males separated by electrophoresis. Additional lanes loaded with the ladder were cut from the image. L = ladder. Modified from (Merges et al., 2022b).

### 4.2.3. Secondary defects in *Prm1*-deficient mice

Given that sperm DNA damage has been previously described for *Prm2-/-* sperm and correlated to oxidative stress, *Prm1*-deficient sperm were examined for oxidative stress-induced DNA lesions (Figure 15A) (Schneider et al., 2020). Immunofluorescent (IF) staining against 8-hydroxy-2'-deoxyguanosine (8-OHdG), a prevalent form of radical-induced DNA lesions, was performed on testis, caput and cauda epididymal tissue sections. *Prm1+/-* caput and cauda sections showed a few 8-OHdG positive sperm compared to none in the WT. However, around 60-65% of *Prm1-/-* caput and cauda sperm showed oxidative stress-induced DNA lesions (Figure 15B). Of note, 8-OHdG positive cells were already detectable in *Prm1-/-* testis (Figure 15C). This is in contrast to *Prm2-/-* mice, where oxidative stress-induced DNA damage and reactive oxygen species (ROS) accumulate after release from the testis during epididymal transit (Schneider et al., 2020).

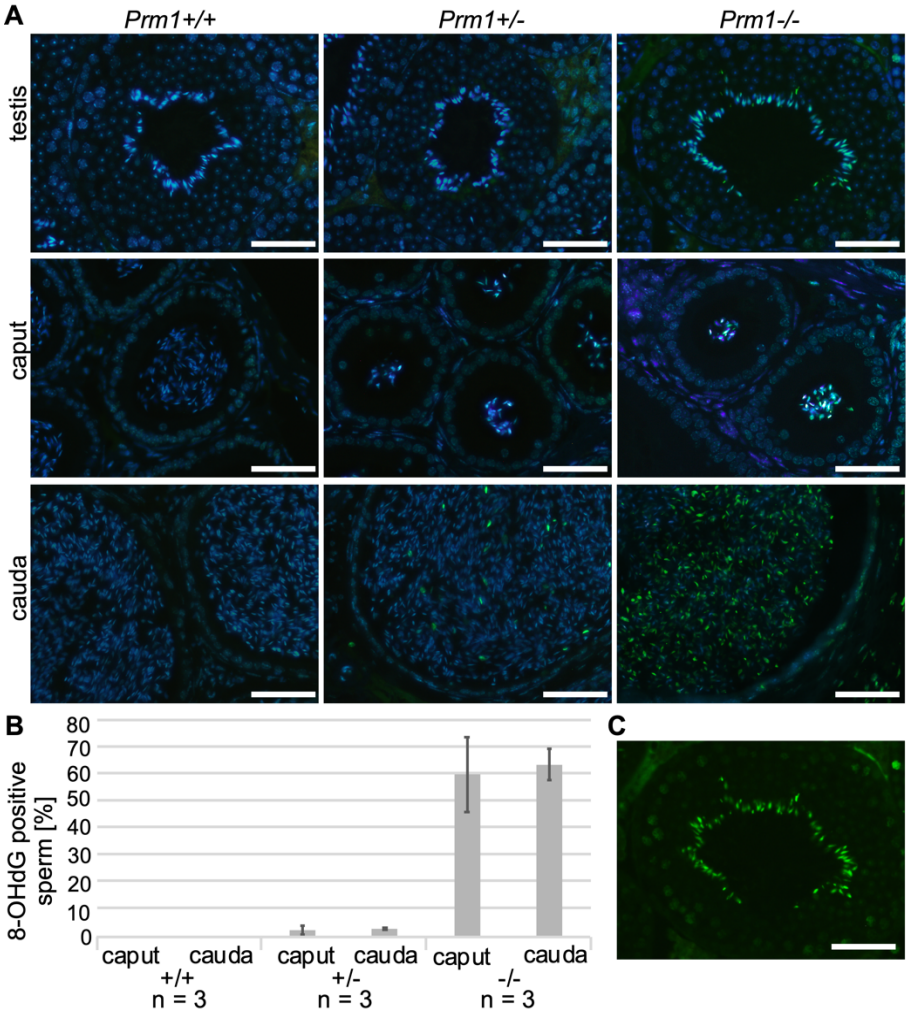


**Figure 15: Oxidative stress induced DNA damage in *Prm1*-deficient epididymal sperm.** **(A)** Representative IF staining against 8-OHdG in testis, caput epididymal and cauda epididymal tissue sections from *Prm1+/+*, *Prm1+/-* and *Prm1-/-* males (counterstain: DAPI). Scale: 50 µm. **(B)** Percentage of 8-OHdG-positive sperm on caput epididymal and cauda epididymal tissue sections of *Prm1+/+*, *Prm1+/-* and *Prm1-/-* mice. Data are mean ± s.d. **(C)** Representative IF staining against 8-OHdG in testis of *Prm1-/-* males without counterstain. Scale: 50 µm. Modified from (Merges et al., 2022b). These data were generated by Alexander Kruse and Andreas Christian Fröbius

Accumulation of ROS causes a wide range of damage to basic cell components, like nucleic acids, proteins or lipids. Therefore, the membrane integrity of *Prm1*-deficient epididymal sperm was analyzed utilizing Eosin-Nigrosin (EN) staining and a hypo-osmotic swelling test (HOS)

(Figure 16). While sperm with intact membranes exclude Eosin staining and show tail swellings in HOS solution, sperm with impaired membrane integrity stain EN-positive and show no swelling of the tail when exposed to hypo-osmotic conditions. *Prm1+/-* sperm did not show a significant increase in membrane damage compared to *Prm1+/+* sperm. *Prm1-/-* sperm presented with severe membrane damage (mean: approx. 98.5% EN-negative and 86% HOS-positive) indicating inviable sperm.

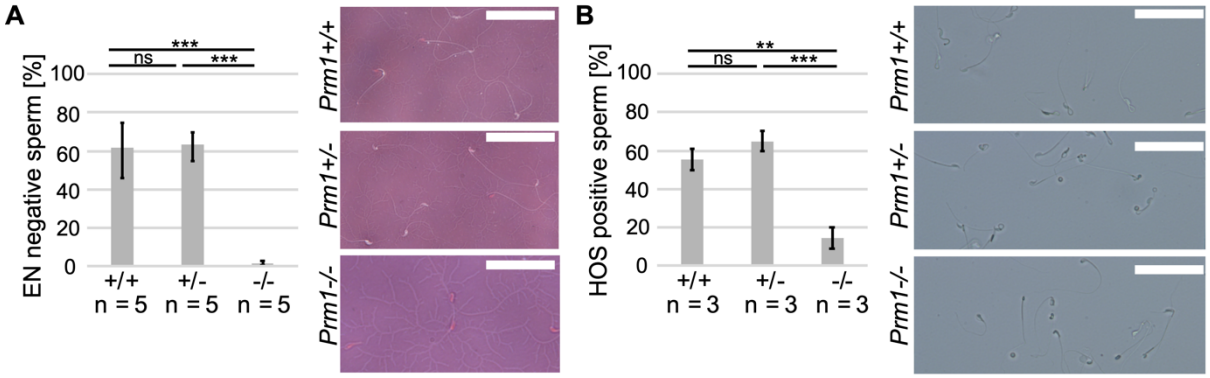


**Figure 16: Membrane integrity of *Prm1*-deficient epididymal sperm. (A)** Quantification of Eosin-Nigrosin (EN) negative epididymal sperm (%) from *Prm1+/+, Prm1+/-* and *Prm1-/-* males. **(B)** Quantification of hypo-osmotic swelling (HOS) test positive epididymal sperm (%) from *Prm1+/+, Prm1+/-* and *Prm1-/-* males. A minimum of 200 sperm per male was evaluated (n = number of males). Representative images are shown. Scale: 50 µm. Data are mean ± s.d. and were analyzed using a two-tailed, unpaired Student's t-test (**p<0.005; ***p<0.001). ns, not significant. Modified from (Merges et al., 2022b). Data obtained together with Julia Meier during her Master Thesis (Meier, 2020).

Given that protamines contribute to nuclear sperm head shape (Lüke et al., 2014), the nuclear head morphology of *Prm1*-deficient sperm was analyzed utilizing a high throughput ImageJ plugin (Skinner et al., 2019). To visualize the average head shape of each sperm population, consensus shapes were computed (Figure 17A). *Prm1-/-* sperm show a wide variety of shapes (Figure 17B) and are generally smaller compared to *Prm1+/-* and *Prm1+/+* sperm heads (mean area: 14.92 µm$^2$ (95% CI 14.92±0.26) compared to 19.82 µm$^2$ (95% CI 19.82±0.10) for *Prm+/+* and 19.47 µm$^2$ (95% CI 19.47±0.13) for *Prm+/-*)) (Figure 17C). Further, they are more elliptic and significantly thinner compared to *Prm1+/-* and *Prm1+/+* sperm heads (Figure 17D-E). They lose the typical hooked shape, which might be due to DNA fragmentation. *Prm1+/-* nuclear head shapes do not differ largely from *Prm1+/+* nuclear head shapes. They do, however show a slightly stronger hook curvature, which is reflected in a reduced maximum ferret (8.07 µm (95% CI 8.07±0.04) compared 8.38 µm (95% CI 8.38±0.04)) (Figure 17F).

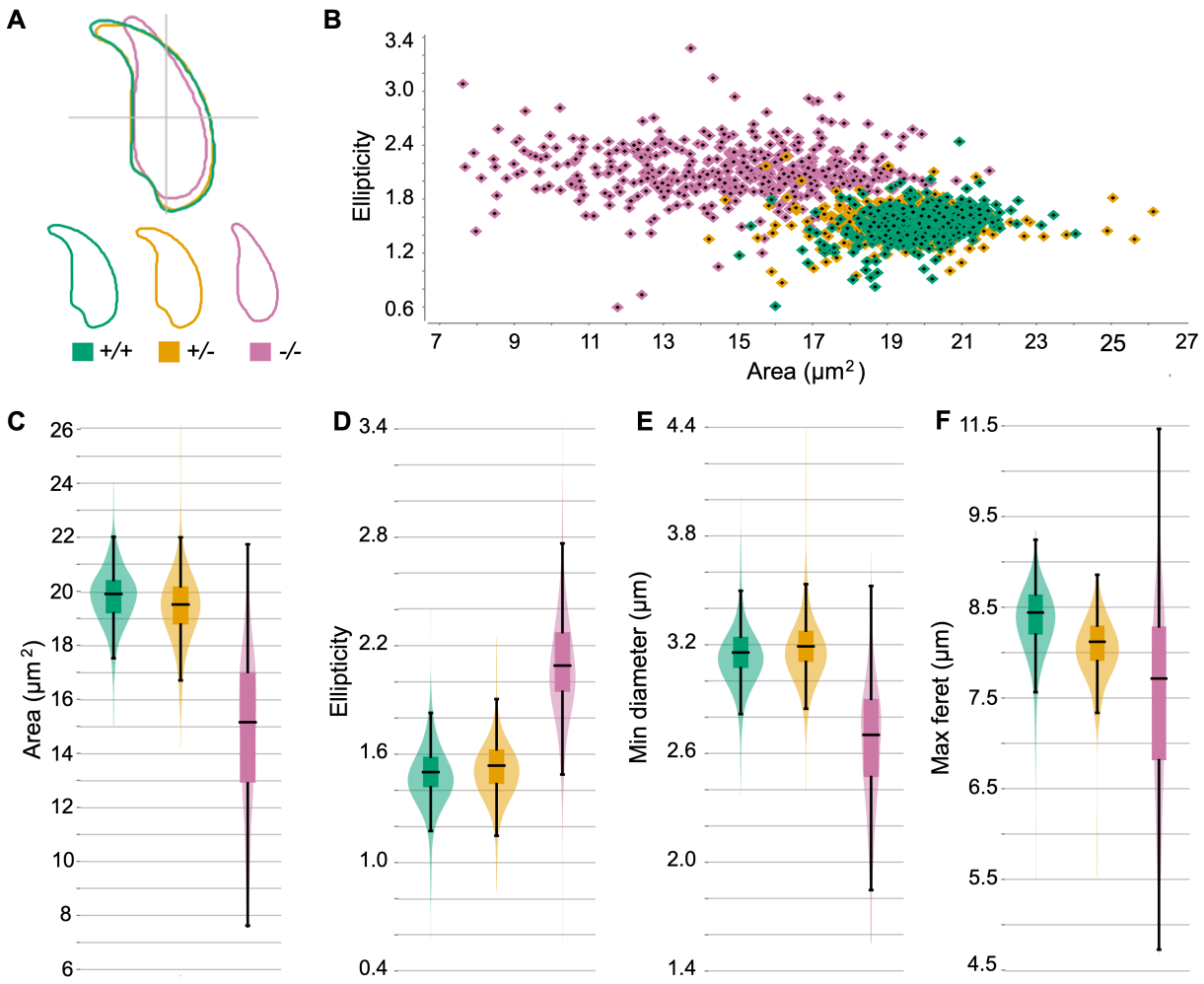


**Figure 17: Nuclear head morphology of *Prm1*-deficient epididymal sperm. (A)** Consensus shapes of *Prm1+/+*, *Prm1+/-* and *Prm1-/-* sperm heads are depicted. A minimum of 100 sperm per animal were analyzed (n = 4 males per genotype). Color code for this figure is given. **(B)** Scatter plot depicting the sperm head shapes of *Prm1+/+*, *Prm1+/-* and *Prm1-/-* mice by area (µm²) and ellipticity (bonding height/ bonding width). **(C-F)** Violin plots presenting the distribution of data measured for the area (µm²) **(C)**, ellipticity **(D)**, minimum diameter (µm) **(E)** and maximum ferret (µm) **(F)** of *Prm1+/+*, *Prm1+/-* and *Prm1-/-* sperm heads. Modified from (Merges et al., 2022b). Data obtained together with Julia Meier during her Master Thesis (Meier, 2020).

PAS staining of testicular tissue, showed that *Prm1-/-* sperm develop morphologically normal and from a hook during spermiogenesis comparable to *Prm1+/+* sperm (Figure 18A). The overall nuclear shape of step 14-16 spermatids isolated from testis did not differ significantly in *Prm1-/-* males compared to *Prm1+/-* and *Prm1+/+* males (Figure 18B). This suggests that *Prm1-/-* sperm heads lose their shape during epididymal transit. Epididymal *Prm1-/-* sperm nuclei appear DAPI-weak compared to *Prm1+/-* and *Prm1+/+* sperm nuclei most likely due to the high level of DNA fragmentation. Thus, changes in the nuclear head shape are likely caused by DNA degradation during epididymal transit.

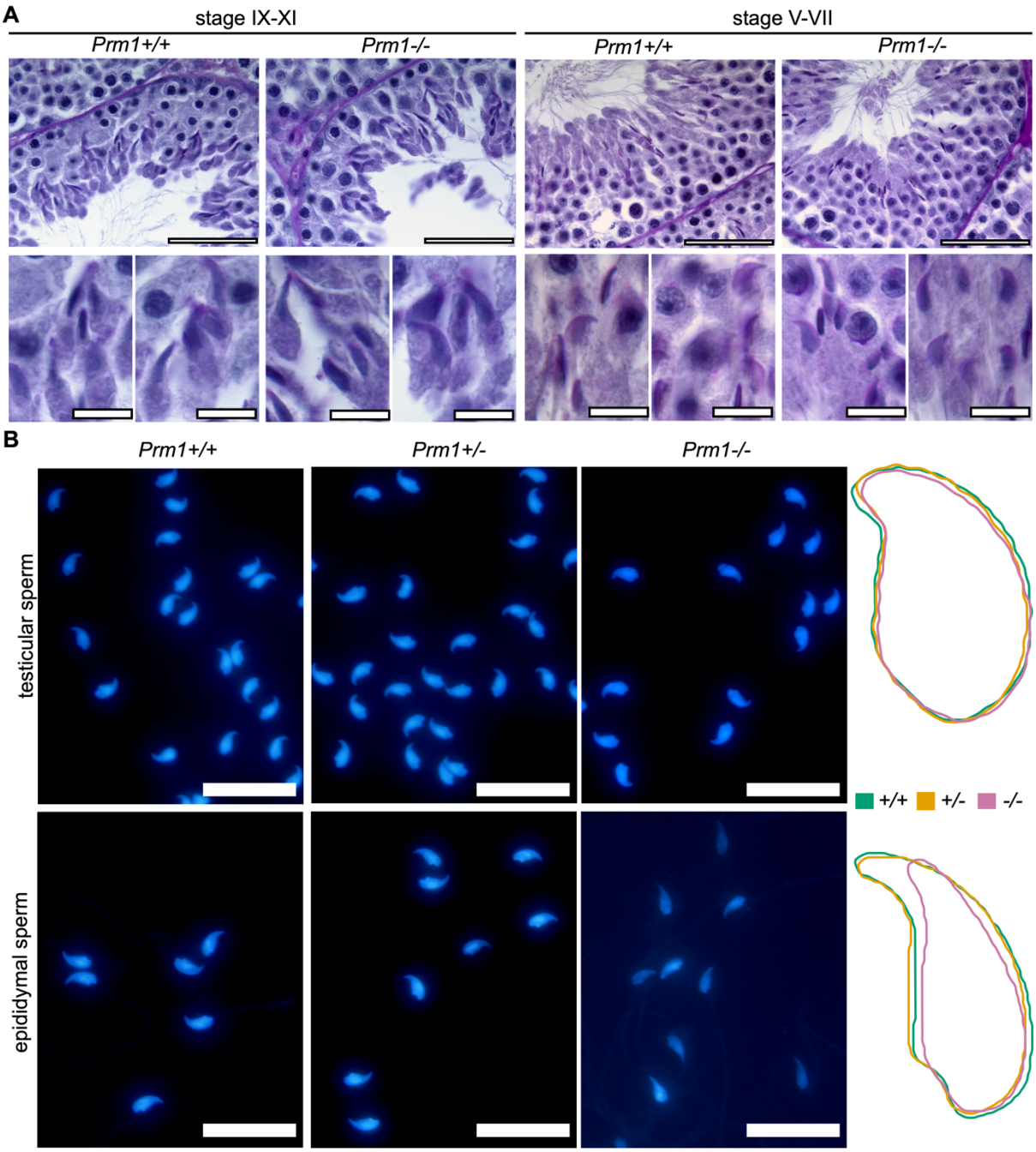


**Figure 18: Sperm head shape of testicular *Prm1*-deficient sperm. (A)** Representative Periodic acid-Schiff stainings of *Prm1+/+* and *Prm1-/-* seminiferous tubules. Scale: 50 µm (top) and 10 µm (bottom). **(B)** Fixed, DAPI-stained testicular and cauda epididymal sperm from *Prm1+/+, Prm1+/-* and *Prm1-/-* mice. Scale: 25 µm. The consensus shape for each population analyzed is depicted. Modified from (Merges et al., 2022b).

Next, sperm motility was analyzed by quantifying the percentage of mobile sperm after swim-out from the cauda epididymis. *Prm1-/-* sperm were immotile. Surprisingly, *Prm1+/-* sperm motility was drastically reduced compared to *Prm1+/+* sperm (Figure 19A). Sperm flagella show a 9+2 microtubule structure (Figure 19B). In *Prm1+/-* and *Prm1-/-* epididymal sperm, reduced numbers of proper microtubule arrangements were detected (Figure 19C). Moreover, *Prm1-/-* sperm showed severe flagella membrane disruptions. Since flagella

formation in the testis appeared normal, flagellar damages in *Prm1+/-* and *Prm1-/-* sperm seem to accumulate during epididymal maturation and might also result from oxidative stress.

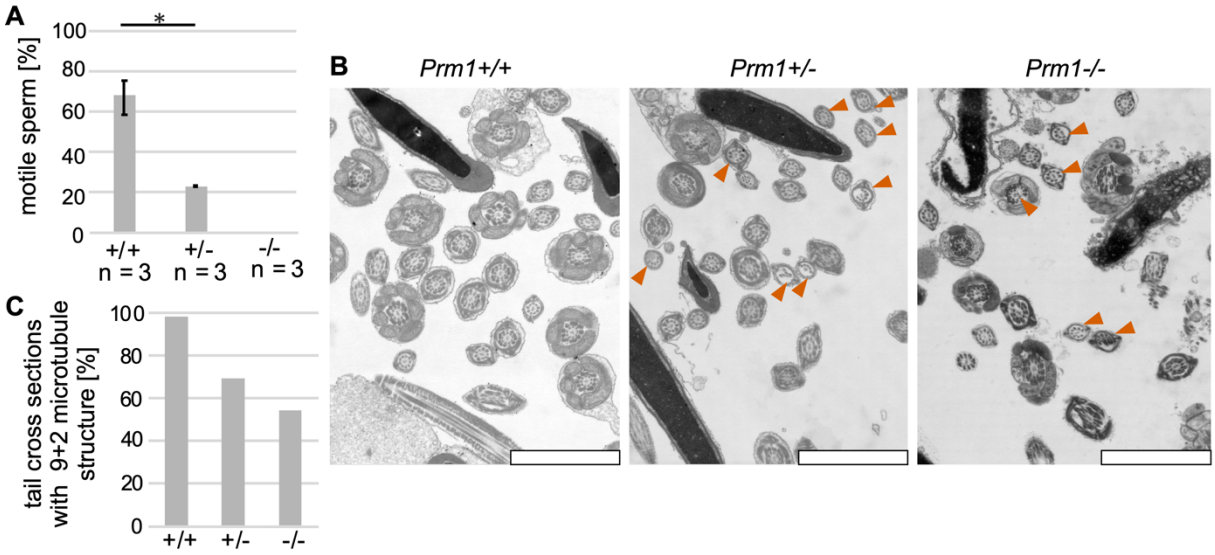


**Figure 19: Motility and flagella morphology of *Prm1*-deficient sperm. (A)** Quantification of motile sperm (%) from *Prm1+/+, Prm1+/-* and *Prm1-/-* males (n= number of males). 100 sperm per male were analyzed. Data are mean ± s.d. and were analyzed using a two tailed, unpaired Student's t-test (*p<0.05). **(B)** Representative transmission electron micrographs of *Prm1+/+, Prm1+/-* and *Prm1-/-* epididymal sperm. Abnormal flagella cross-sections are marked by vermillion arrow heads. Scale: 2 µm. **(C)** Quantification of sperm flagella cross-sections with correct 9+2 microtubule structure of *Prm1+/+, Prm1+/-* and *Prm1-/-* mice. A minimum of 400 tail cross-sections per genotype were evaluated. Modified from (Merges et al., 2022b). Parts of data obtained together with Julia Meier during her Master Thesis (Meier, 2020). Microscopic analysis was performed together with Dr. Gregor Kirfel.

### 4.2.4. Nuclear protein content in *Prm1*-deficient mice

To determine whether nuclear proteins are differentially abundant in *Prm1*-deficient and *Prm2*-deficient mature sperm, we used mass spectrometry to analyze basic nuclear protein extracts. Protein abundances from *Prm1+/-*, *Prm1-/-*, *Prm2-/-* and WT sperm were compared (Figure 20). In *Prm1-/-* samples, 31 proteins were differentially abundant compared with WT sperm, of which 21 were also differentially abundant in *Prm2-/-* compared to WT protein extracts. Here, proteins related to translation, mRNA splicing and

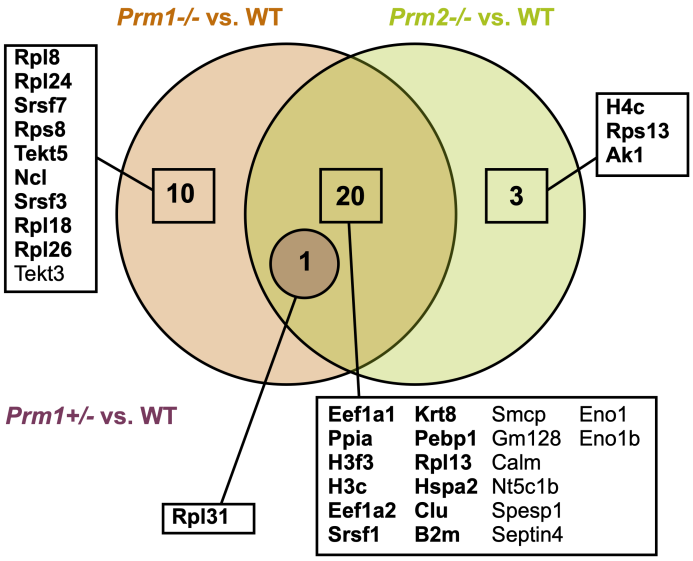


**Figure 20: Differentially abundant proteins in protamine-deficient sperm.** Venn diagram illustrating changes in abundances of basic sperm proteins from *Prm1-/-, Prm1+/-* and *Prm2-/-* males compared to WT sperm. Higher abundant proteins are in bold. Non-bold proteins showed lower abundances compared to WT sperm. Analysis was performed by Dr. Lena Arévalo. Modified from (Merges et al., 2022b).

protein folding (EEF1A1, EEF1A2, RPL13, RPL31, SRSF1 and PPIA) showed higher abundance. Further, histones H3F3 and H3C were higher abundant, suggesting increased histone retention in *Prm1-/-* and *Prm2-/-* sperm. *Prm2-/-* sperm additionally showed higher histone H4C abundance.

Immunofluorescence (IF) staining against H3 on caput epididymal tissue sections confirmed increased H3 histone retention in *Prm1-/-* and *Prm2-/-* sperm (Figure 21, Figure S2). *Prm1+/-*, *Prm2+/-* and WT sperm did not stain for histone H3. Histone H4 was detected in *Prm2-/-* and weakly in *Prm1-/-* sperm, but not in *Prm1+/-*, *Prm2+/-* or WT sperm (Figure S2).

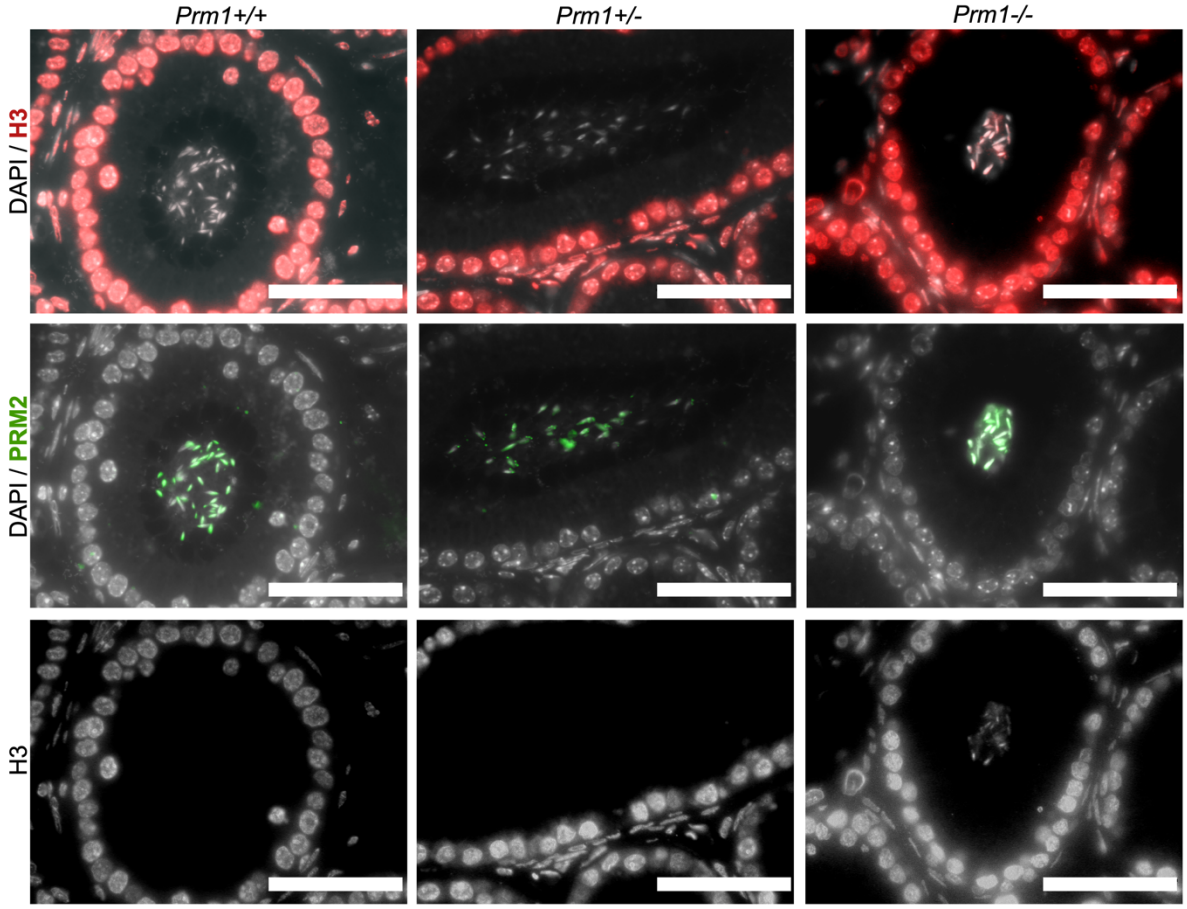


**Figure 21: Histone H3 retention in *Prm1*-deficient sperm.** IHC stainings against histone H3 (red) and PRM2 (green) on *Prm1+/+*, *Prm1+/-* and *Prm1-/-* caput epididymal tissue sections. DAPI (gray) was used as counterstain. H3 stainings are additionally shown as single gray channel pictures. Scale bars: 50 µm. Modified from (Merges et al., 2022b).

In *Prm1-/-* and *Prm2-/-* sperm, proteins related to stress response and apoptosis (B2M and CLU) were found to be more abundant compared to WT sperm (Figure 20). This might indicate a response to the increased oxidative stress-mediated sperm DNA, membrane and flagella damage detected. In contrast, proteins important for sperm motility and sperm-egg fusion (SMCP and SPESP1) were less abundant in both sperm populations lacking PRM1 or PRM2 compared to WT sperm. In *Prm1-/-* sperm nuclear protein extracts, additionally proteins related to translation and mRNA splicing were higher abundant (RPL8, RPS8, RPL18, RPL24, RPL26, SRSF3 and SRSF7). Only one non-protamine protein, the ribosomal protein RPL31, which

was also identified in *Prm1-/-* and *Prm2-/-* samples, was differentially abundant in *Prm1+/-* mature sperm compared to WT sperm. This suggests that the *Prm1+/-* sperm nuclear protein profile is not causative of the subfertility observed in these mice.

Next, we stained caput epididymal tissue sections for transition proteins (TNP1 and TNP2), which like protamines are not detected in mass spectrometry of basic nuclear extracts due to methodical limitations. Part of the caput sperm in *Prm1-/-* samples stained for TNP1 and TNP2, but not in *Prm1+/-* or *Prm1+/+* samples (Figure 22A). This indicated that lack of PRM1 leads to partial TNP retention. Co-IF staining against TNP1 and PRM2 showed that the majority of TNP1-positive *Prm1-/-* caput sperm stained for both proteins, proving that this partial TNP retention does not completely omit PRM loading onto DNA (Figure 22B).

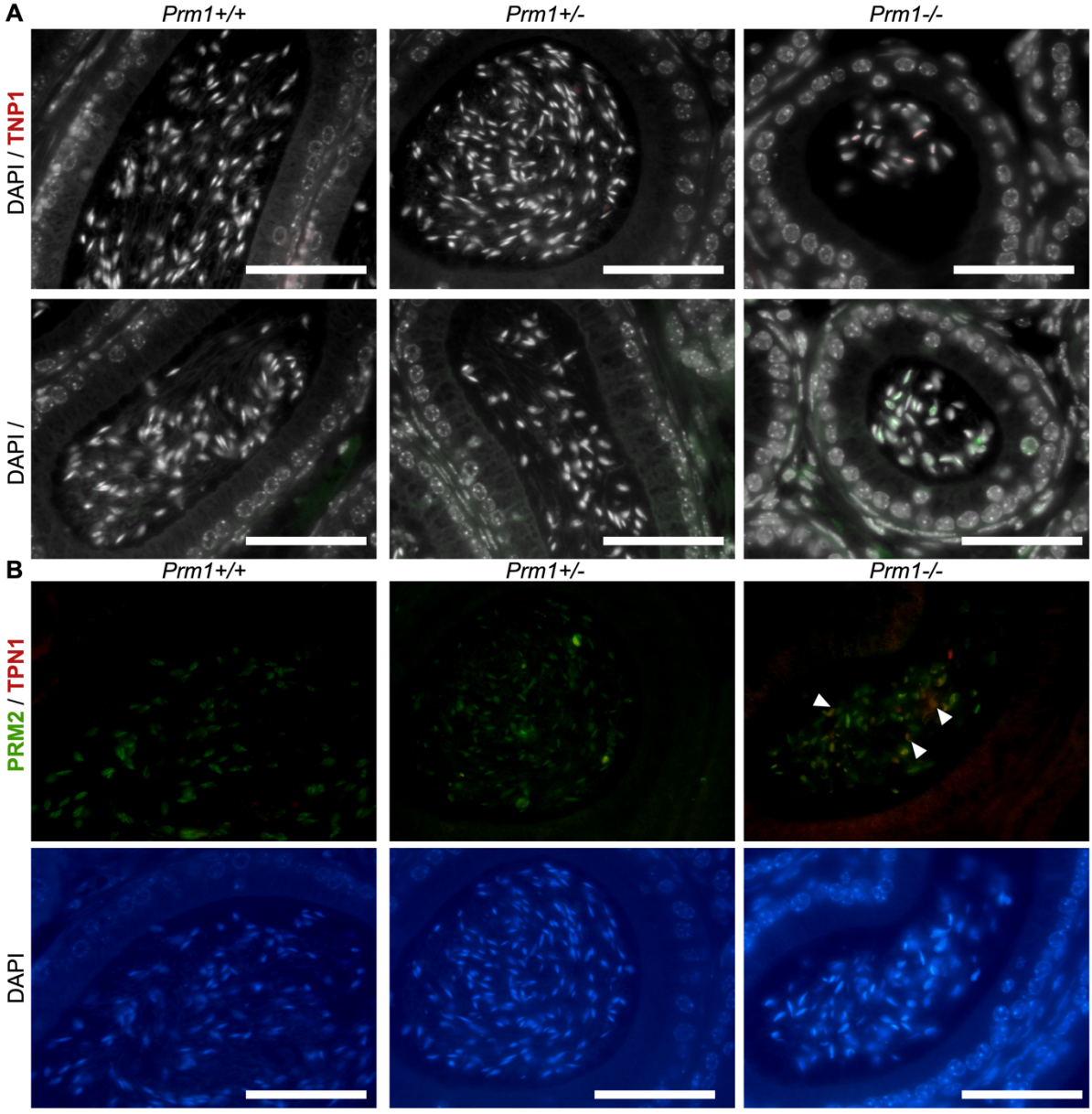


**Figure 22: Transition protein retention in *Prm1*-deficient sperm. (A)** IF stainings against TNP1 (red) and TNP2 (green) on *Prm1+/+*, *Prm1+/-* and *Prm1-/-* caput epididymal tissue sections (counterstaining: DAPI; gray). Scale bars: 50 µm. **(B)** Co-IF stainings of TNP1 (red) and PRM2 (green) on *Prm1+/+*, *Prm1+/-* and *Prm1-/-* caput epididymal tissue sections (counterstaining: DAPI; blue). Scale bars: 50 µm. Modified from (Merges et al., 2022b).

Of note, the heat shock-related 70 kDa protein 2 (HSPA2), was more abundant in both *Prm1-/-* and *Prm2-/-* basic nuclear extracts. This protein has been proposed to function as a TNP chaperone in condensing spermatids (Govin et al., 2006), and higher levels of HSPA2 could be indicative of HSPA2-TNP complexes which in turn might be the result of and impaired or incomplete TNP unloading.

To analyze nuclear remodeling in *Prm1*-deficient sperm in more detail, epididymal sperm were stained using Chromomycin A3 (CMA3). This dye binds, to CG-rich regions to the minor groove of DNA, allowing to indirectly monitor the level of protamination (Sadeghi et al., 2019). Of note, *Prm1-/-* and *Prm2-/-* sperm could not be analyzed since severe DNA fragmentation interfered with the staining procedure. *Prm1+/-* and *Prm2+/-* samples showed increased numbers of CMA3-positive sperm compared to WT samples, indicating not fully protaminated chromatin (Figure 23A). Interestingly, around 98% of *Prm1+/-* sperm showed CMA3 staining, while only around 29% of *Prm2+/-* sperm showed a CMA3 signal, showing that lack of *Prm1* causes more pronounced defects compared to *Prm2*. (Figure 23B). This indicates that loss of one allele of *Prm1* cannot be compensated leading to protamination defects throughout the whole sperm population, while one allele of *Prm2* is compensated for in the majority of sperm.

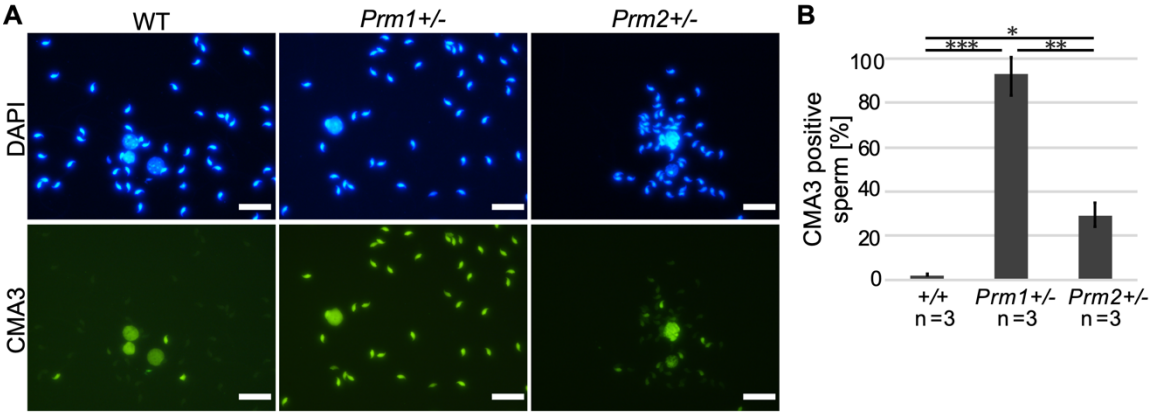


**Figure 23: Protamination of protamine-deficient sperm chromatin. (A)** Representative images of CMA3 stainings of *Prm1+/-, Prm2+/-* and WT epididymal sperm heads. (counterstain: DAPI). Scale: 20 µm **(B)** Mean percentage of CMA3-positive sperm in *Prm1+/-, Prm2+/-* and WT males (n = number of males). A minimum of 400 sperm per male were evaluated. Data are mean ± s.d. and were analyzed using a two-tailed, unpaired Student's t-test (*p<0.05; **p<0.005; ***p<0.001). Modified from (Merges et al., 2022b).

Next, basic, nuclear enriched proteins isolated from epididymal sperm from *Prm1+/-*, *Prm1-/-*, *Prm2+/-*, *Prm2-/-* and WT mice were separated on acid-urea polyacrylamide gels (AU-PAGE) to analyze the protamine content. Strikingly, in *Prm1+/-*, *Prm2+/-* and *Prm1-/-* extracts, PRM2 precursors (pre-PRM2) were detected, suggesting disturbed processing of PRM2 upon reduction or loss of PRM (Figure 24A, dashed vermillion box). To analyze the protamination and PRM2 processing in more detail, the relative amounts of basic proteins within individual

samples were quantified (Figure 24B-D). The relative amount of mature, processed PRM2 (mPRM2) to total protamine was not significantly different in *Prm1+/-* and *Prm2+/-* sperm compared with WT (Figure 24B). The total amount of PRM2 (mPRM2 + pre-PRM2), however, was significantly higher in *Prm1+/-* sperm (83%) (Figure 24C). While In *Prm2+/-* sperm the species-specific protamine ratio of 1:2 was maintained, the PRM1:PRM2 ratio in *Prm1+/-* sperm shifted to ~1:5. In addition, the pre-PRM2 content of total PRM2 was significantly larger in *Prm1+/-* and *Prm1-/-* sperm compared with *Prm2+/-* sperm (Figure 24D).

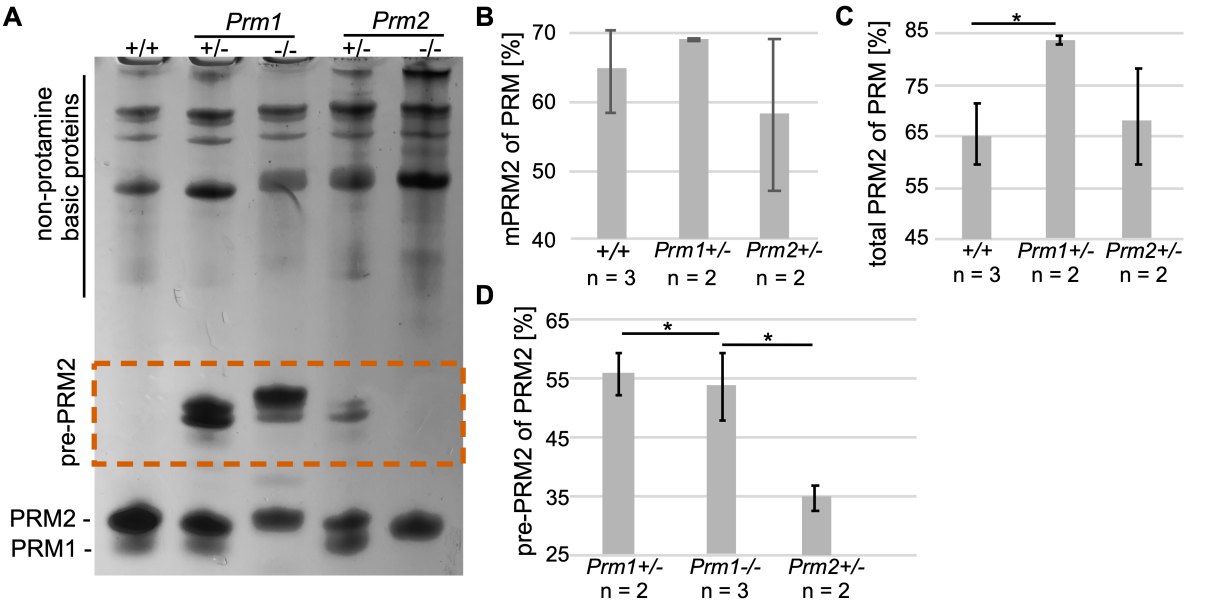


**Figure 24: Protamine ratios in protamine-deficient epididymal sperm. (A)** Representative AU-PAGE of basic protein extractions from WT, *Prm1+/-, Prm1-/-, Prm2+/-* and *Prm2-/-* epididymal sperm. Non-protamine basic proteins were detected at the top of gel. PRM1 and PRM2 ran at the bottom. Pre-PRM2 is marked with the dashed vermillion box. **(B)** Percentage of mPRM2 of PRM in basic protein extractions from *Prm1+/-, Prm2+/-* and WT epididymal sperm. **(C)** Percentage of total PRM2 (including pre-PRM2) of PRM in basic protein extractions from *Prm1+/-, Prm2+/-* and WT epididymal sperm. **(D)** Percentage of pre-PRM2 of PRM2 in basic protein extractions from *Prm1+/-, Prm1-/-* and *Prm2+/-* epididymal sperm. Data are mean ± s.d. and were analyzed using a two-tailed, unpaired Student's t-test (*p<0.05). Modified from (Merges et al., 2022b).

These data were published in:

Gina Esther Merges, Julia Meier, Simon Schneider, Alexander Kruse, Andreas Christian Fröbius, Klaus Steger, Lena Arévalo, Hubert Schorle (2022) Loss of *Prm1* leads to defective chromatin protamination, impaired PRM2 processing, reduced sperm motility and subfertility in male mice. *Development.* DOI: 10.1242/dev.200330

## 4.3. Characterization of *Prm1-Prm2*-fusion mice

In an attempt by Dr. Simon Schneider to generate a mouse line heterozygous for *Prm1* and *Prm2*, *Prm*-mutated mice have been generated. The two guides targeting *Prm1* and the two guides targeting *Prm2*, introduced earlier, were used for gene editing in zygotes (Schneider, 2019). Aim was to introduce multiple small deletions in the *Prm1* and *Prm2* coding sequence or one large deletion encompassing both coding sequences, to generate mice with a *Prm1-Prm2*-null allele. Founder animals were sequenced and selected for backcrossing and mouse line establishment. In the mouse line analyzed here, a large approx. 4.7 kb deletion spanning from the *Prm1* to the *Prm2* coding sequence was detected (Figure 25A). Additionally, part of the sequence is inverted. Sequencing of cDNA transcribed from mRNA isolated from testis of $Prm^{mut/mut}$ males revealed that a fusion-mRNA product consisting of the 5´-part of the *Prm1* coding sequence and the 3´-part of the *Prm2* coding sequence is transcribed (Figure 25B). The inversion represents an artificial intron, which is spliced out. Using the mRNA sequence for amino acid sequence prediction revealed, that the fusion protein should consist of the N-terminal part of PRM1 including the first DNA binding domain, followed by 9 amino acids (SILESIASS) of unknown function and ending with the C-terminal part of PRM2, encoding for the whole mPRM2 sequence. 5´ of the mPRM2 sequence 8 amino acids of cPRM2 remain, containing the last cleavage site of cPRM2. The allele was named $Prm^{mut}$.

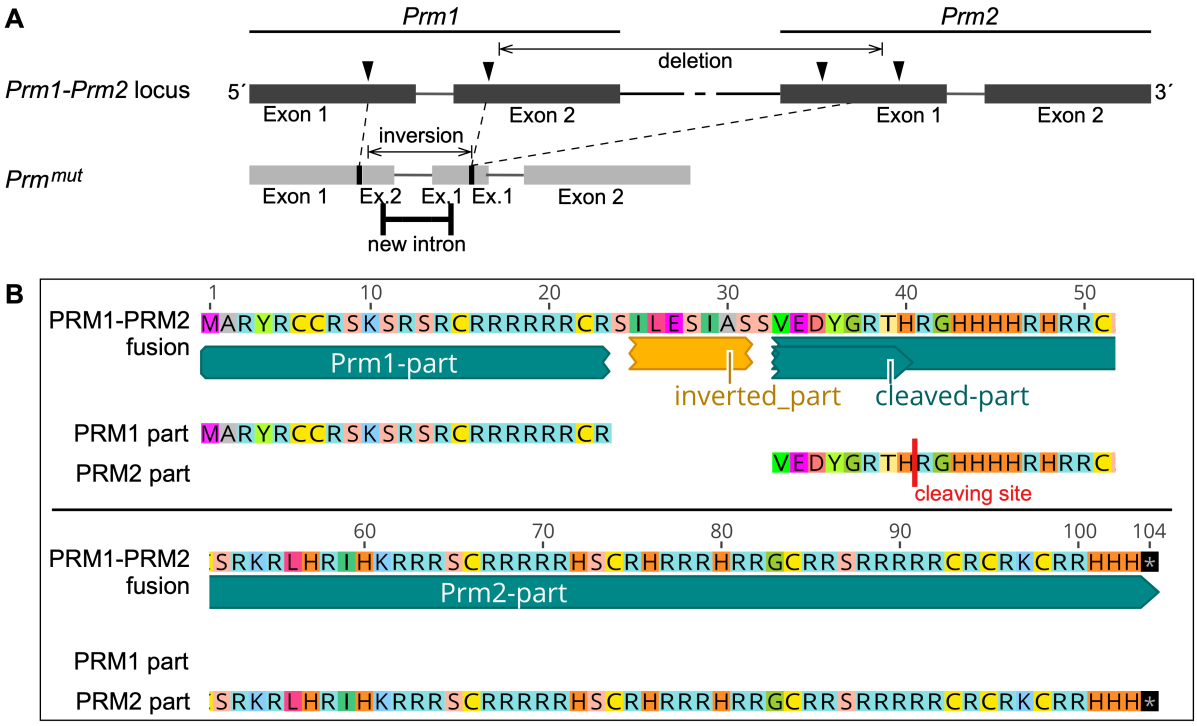


**Figure 25: Establishment of *Prm*-mutated mice. (A)** Graphical representation of CRISPR/Cas9-mediated gene editing of the *Prm1-Prm2* locus. sgRNA target sites in exon 1 and exon 2 of the *Prm1* and exon 1 of the *Prm2* coding sequence are marked with black arrowheads. An approximately 4.7 kb deletion in the *Prm1-Prm2* locus was generated. An additional inversion let to the generation of an artificial intron in the $Prm^{mut}$ allele. **(B)** Depiction of the amino acid sequence PRM1-PRM2 fusion protein generated. One cP2 cleaving site is preserved. Gene editing was performed by Dr. Simon Schneider (Schneider, 2019).

Next whole testis was used to isolate RNA in order to perform, 3´-mRNA sequencing with the aim to map the transcripts and get information about the RNA transcribed from the *Prm*$^{mut}$ allele (Figure 26A). In *Prm*$^{mut/mut}$ males transcripts map the 5´-part of *Prm1* and the 3´-part of *Prm2*, confirming the prediction based on the cDNA sequence. The transcripts predict a fusion protein 13.48 kDa in size. AU-PAGE of proteins isolated from *Prm*$^{mut/mut}$ sperm followed by Western blot against PRM1 (N-terminus of PRM1) and PRM2 (detecting mPRM2) were performed. Here, a band indicative of PRM1-PRM2 fusion protein could be detected (Figure 26B). *Prm*$^{mut/mut}$ sperm extracts show a higher running band. In *Prm*$^{+/mut}$ sperm, the fusion protein, as well as the endogenous PRM1 and PRM2 produced from the WT allele were detected. Interestingly, *Prm*$^{+/mut}$ sperm also displayed a band indicative for unprocessed pre-PRM2 suggesting that PRM2 processing is disturbed. So, the *Prm mut* locus produces a RNA which is translated into a larger fusion protein. This protein seems to be able to exert at least part of the function, since *Prm*$^{mut}$ mice retain some fertility. Lastly, a three-primer PCR for genotyping was developed as shown in Figure 26C. The *Prm*$^{mut}$ allele produces a 552 bp band, while the WT allele produces a 225 bp band (Figure 26D).

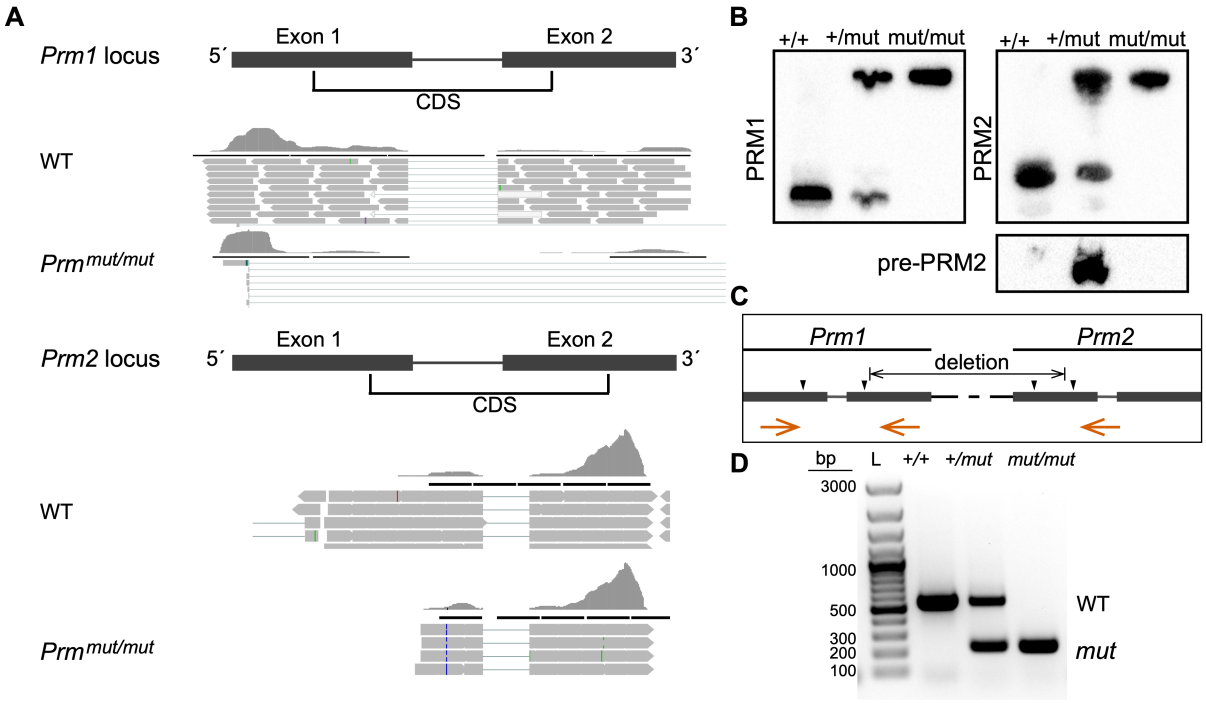


**Figure 26: Validation of *Prm*-mutated mice. (A)** Representative cut-out of RNAseq reads mapping to the *Prm1* and *Prm2* locus from whole testis RNAseq of WT and *Prm*$^{mut/mut}$ mice. **(B)** Western blots against PRM1, PRM2 and cP2 (pre-PRM2) on basic protein extracts from epididymal sperm from WT, *Prm*$^{+/mut}$ and *Prm*$^{mut/mut}$ mice. **(C)** Graphical representation of the 3 primer PCR is shown. The potential WT product of around 5000 bp is not amplified due to short elongation times. **(D)** Representative amplification of the WT and *Prm*$^{mut}$ allele generating products of 552 bp or 225 bp L=ladder. The three-primer PCR has been established during my Master thesis (Merges, 2018). Mapping of the *Prm1* and *Prm2* transcripts has been performed by Dr. Lena Arévalo.

Remarkably, fertility analysis of *Prm*-mutated males showed that both *Prm*$^{+/mut}$ and *Prm*$^{mut/mut}$ males are subfertile (Figure 27). *Prm*$^{+/mut}$ and *Prm*$^{mut/mut}$ show significantly reduced litter sizes and pregnancy frequencies. Further the pregnancy success rate, i.e. the pups born per visible pregnancy, is significantly reduced for pregnancies produced by *Prm*$^{mut/mut}$ males. The fact that life pups are born by matings with *Prm*$^{+/mut}$ and *Prm*$^{mut/mut}$ males suggests that the PRM1-PRM2 fusion protein is able to condense and protect the paternal chromatin sufficient to produce functional sperm.

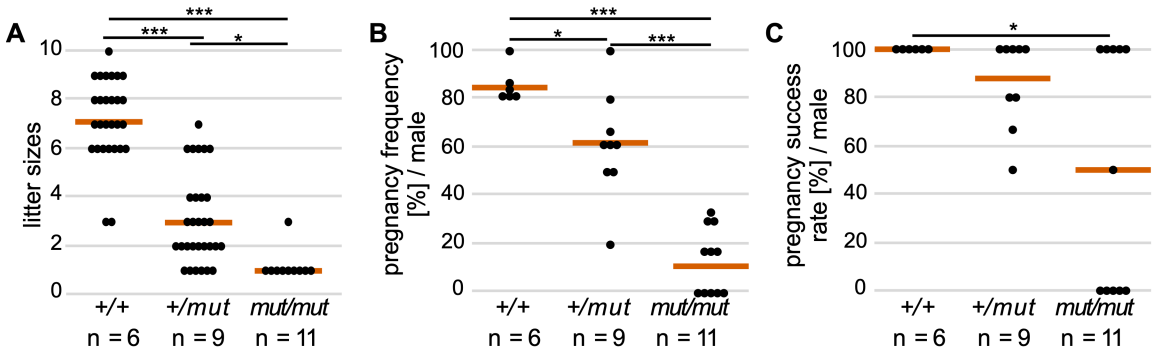


**Figure 27: Fertility analysis of *Prm*-mutated mice. (A)** Scatter plot of litter sizes monitored for males after mating with female WT mice. The mean litter size per genotype is indicated by vermillion lines (n = number of males). **(B)** Pregnancy frequency (%) per male after mating with female WT mice. The mean pregnancy frequency per genotype is indicated by vermillion lines (n = number of males). **(C)** Scatter plot of pregnancy success rate (%; life litter born/ visible pregnancy monitored) per male after mating with female WT mice. The mean pregnancy success rate per genotype is indicated by vermillion lines (n = number of males); data was analyzed using a two-tailed, unpaired Student's t-test (*p<0.05, ***p<0.001).

Next, macro- and microscopic analysis of *Prm*$^{mut}$ testis was performed. The average testis weight, mean testis/body weight ratio and the number of elongating spermatids per seminiferous tubule cross section did not significantly differ in *Prm*$^{+/mut}$ and *Prm*$^{mut/mut}$ compared to WT males (Figure 28A-C). Histological sections of testis from *Prm*-mutated males were examined. Sperm production appeared overtly normal (Figure 28D). However, upon closer inspection prominent residual bodies were visible in *Prm mut* seminiferous tubules. Especially in *Prm*$^{+/mut}$ testis, dark stained, enlarged residual bodies accumulated at the lumen of the tubules. Residual bodies contain excess cytoplasm and spermatid organelles no longer needed by the sperm. After detachment, these become phagocytosed by Sertoli cells and eliminated. The fact, that residual bodies appear enlarged in *Prm*$^{+/mut}$ mice suggests increased eviction of cellular components.

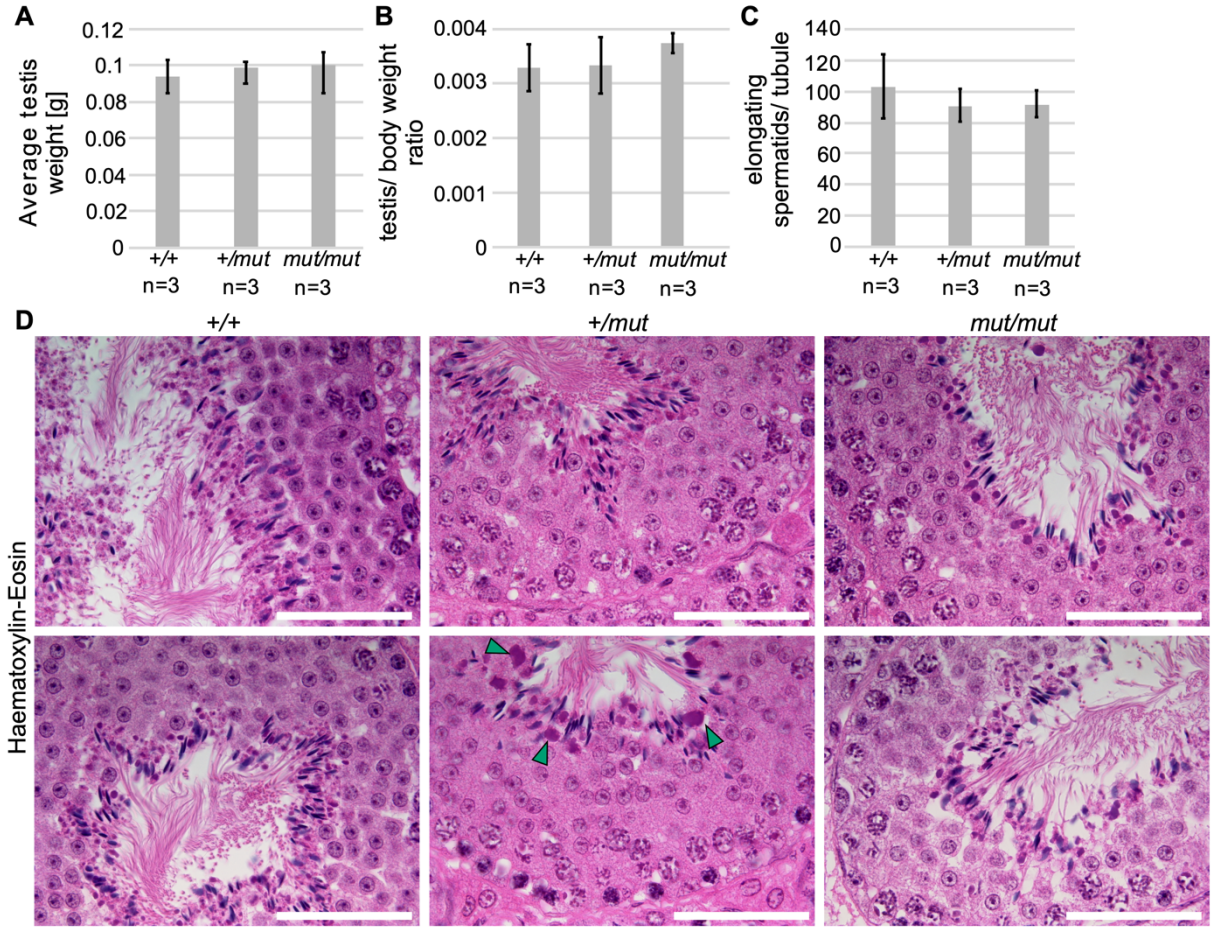


**Figure 28: Macro- and microscopic analysis of spermatogenesis of *Prm*-mutated mice. (A)** Average testis weight of WT, *Prm*$^{+/mut}$ and *Prm*$^{mut/mut}$ males (n = number of males). **(B)** Testis to body weight ratio of WT, *Prm*$^{+/mut}$ and *Prm*$^{mut/mut}$ males (n = number of males). **(C)** Number of elongating spermatids per seminiferous tubule cross section of WT, *Prm*$^{+/mut}$ and *Prm*$^{mut/mut}$ males; 5 tubules per male were analyzed (n = number of males); data are shown as mean ± s.d. and were analyzed using a two-tailed, unpaired Student's t-test. **(D)** Hematoxylin and Eosin staining of testis sections of WT, *Prm*$^{+/mut}$ and *Prm*$^{mut/mut}$ males. Stages VII to VIII of the epithelial cycle with spermatozoa lining up at the edge of tubule lumen are shown. Enlarged residual bodies are indicated by green arrow heads. Scale: 50 µm.

To examine chromatin condensation by the PRM1-PRM2 fusion protein, epididymal sperm were assessed using TEM. *Prm*$^{+/mut}$ and *Prm*$^{mut/mut}$ sperm present with condensed sperm nuclei comparable to WT (Figure 29A). In *Prm*$^{mut/mut}$ samples, however, part of the sperm was less condensed or degraded (Figure 29B). Some *Prm*$^{mut/mut}$ sperm showed decondensed areas in the central heterochromatin region of the nucleus (Figure 29A). However, DNA isolated from *Prm*$^{+/mut}$ and *Prm*$^{mut/mut}$ epididymal sperm did not reveal any fragmentation level (Figure 29C). So, any DNA fragmentation was below detection limit of an agarose gel. Additionally, membrane integrity of *Prm*$^{+/mut}$ and *Prm*$^{mut/mut}$ sperm was comparable to WT sperm (Figure 29D). This is in stark contrast to sperm lacking either PRM1 or PRM2 and *Prm2*$^{+/\Delta c}$ and *Prm2*$^{-/\Delta c}$ sperm (Arévalo et al., 2022a, Merges et al., 2022b, Schneider et al., 2016, Schneider et al., 2020). Sperm lacking either protamine or the cP2 domain show severe DNA fragmentation and sperm damage. Hence, both protamines are essential for proper chromatin remodeling and sperm function. The cP2 domain was shown to be crucial for proper chromatin remodeling,

however it seems that it is not essential when PRM1 and mP2 are fused together. This suggests that the cP2 domain is important for PRM1-PRM2 interaction or binding.

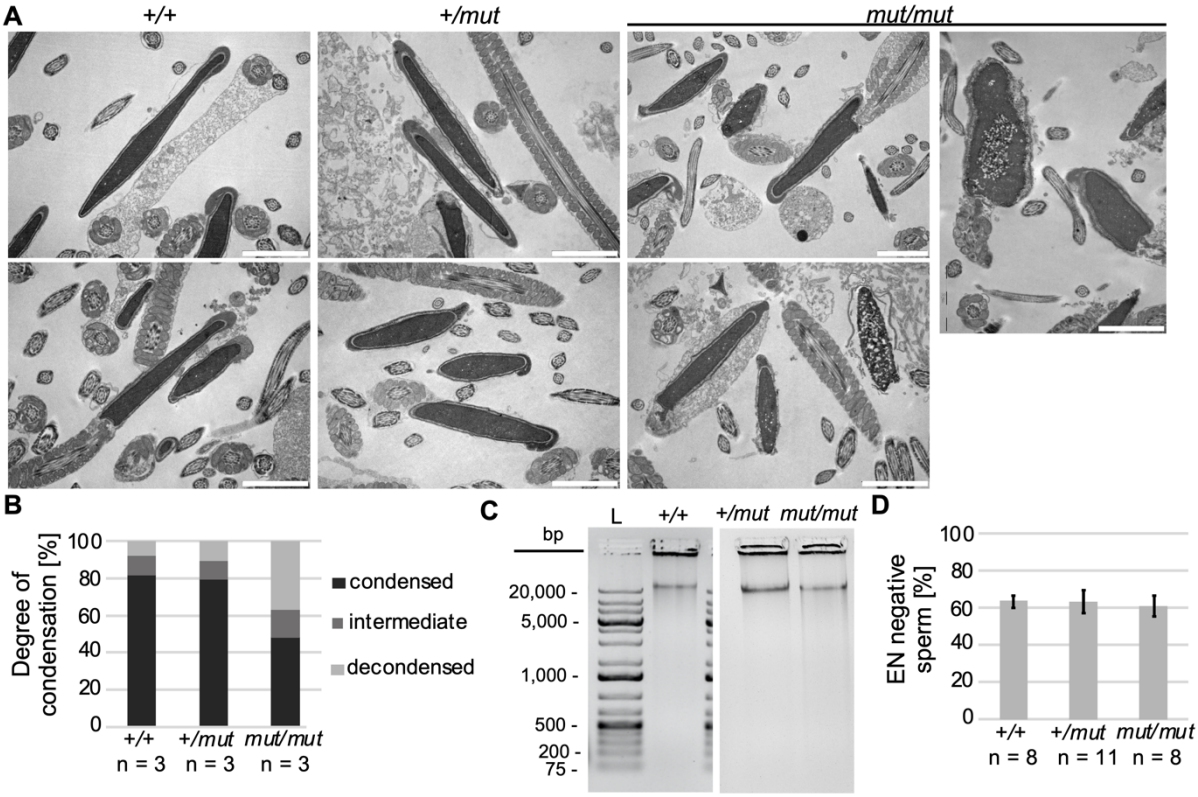


**Figure 29: Chromatin condensation, DNA degradation status and membrane integrity of *Prm*-mutated sperm. (A)** Representative transmission electron micrographs of WT, $Prm^{+/mut}$ and $Prm^{mut/mut}$ epididymal sperm. Scale: 2 µm **(B)** Quantification of DNA condensation of WT, $Prm^{+/mut}$ and $Prm^{mut/mut}$ epididymal sperm; 100 sperm per male were analyzed (n = number of males). Data are means and were analyzed using a two-tailed, unpaired Student's t-test. **(C)** Genomic DNA isolated from epididymal sperm of WT, $Prm^{+/mut}$ and $Prm^{mut/mut}$ males separated by electrophoresis. Additional lanes were cut from the image. L = ladder. **(D)** Quantification of Eosin-Nigrosin (EN) negative epididymal sperm (%) from WT, $Prm^{+/mut}$ and $Prm^{mut/mut}$ males. A minimum of 200 sperm per male was evaluated (n = number of males); data are shown as mean ± s.d. and were analyzed using a two-tailed, unpaired Student's t-test.

Sperm nuclear head shape was analyzed to examine if DNA condensation by the PRM1-PRM2 fusion protein influences the overall shape of sperm heads. Consensus shapes constructed for the different sperm populations did not differ greatly (Figure 30A). $Prm^{+/mut}$ and $Prm^{mut/mut}$ sperm show a gradual decrease in maximum ferret, reflecting a slight shortening of the sperm hook. The general scatter of sperm head shapes measured, however, show great overlap (Figure 30B), suggesting that the fusion protein does not lead to vast changes in sperm nuclear head shape.

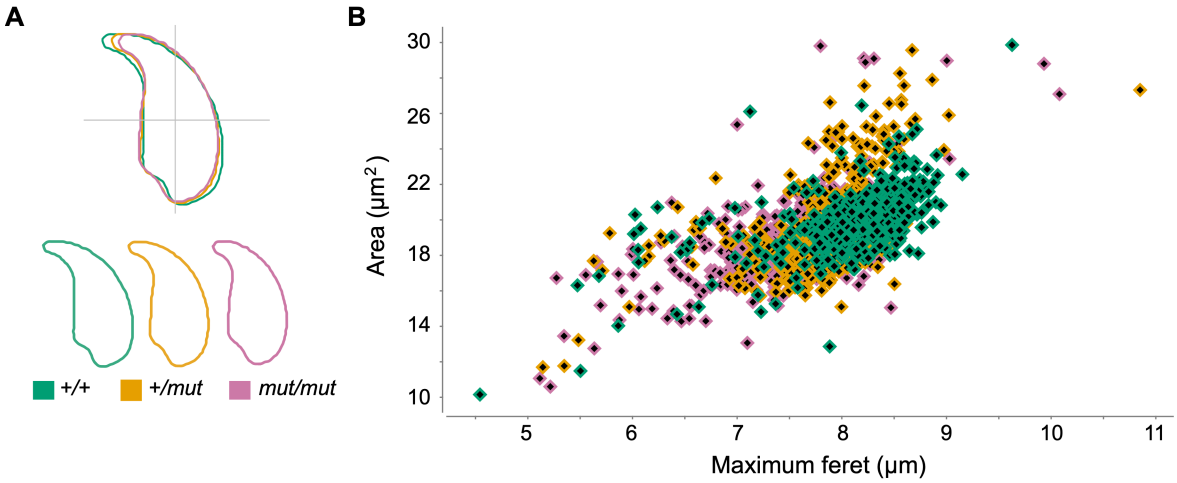


**Figure 30: Nuclear head morphology of *Prm*-mutated epididymal sperm. (A)** Consensus shapes of WT, *Prm*$^{+/mut}$ and *Prm*$^{mut/mut}$ sperm heads are depicted. A minimum of 100 sperm per animal were analyzed (n = 4 males per genotype). Color code for this figure is given. **(B)** Scatter plot depicting the sperm head shapes of WT, *Prm*$^{+/mut}$ and *Prm*$^{mut/mut}$ mice by area (µm2) and maximum feret (µm).

Next, epididymal sperm count after swim-out from cauda epididymis was performed (Figure 31A). Sperm count was reduced in *Prm*$^{mut/mut}$ mice compared to *Prm*$^{+/mut}$ and WT males. Of note, isolation of sperm via swim-out has the potential to bias the sperm count in favor of motile sperm, which is why I additionally quantified the elongating spermatids per seminiferous tubule cross section (Figure 31B). No significant differences in the number of sperm produced was detected. Hence, sperm are less motile and/or in part degraded during epididymal transit. Flagella cross sections of sperm isolated from cauda epididymis showed no apparent abnormalities (Figure 31C) and sperm appeared motile when inspected under the light microscope, suggesting partial sperm degradation during sperm maturation.

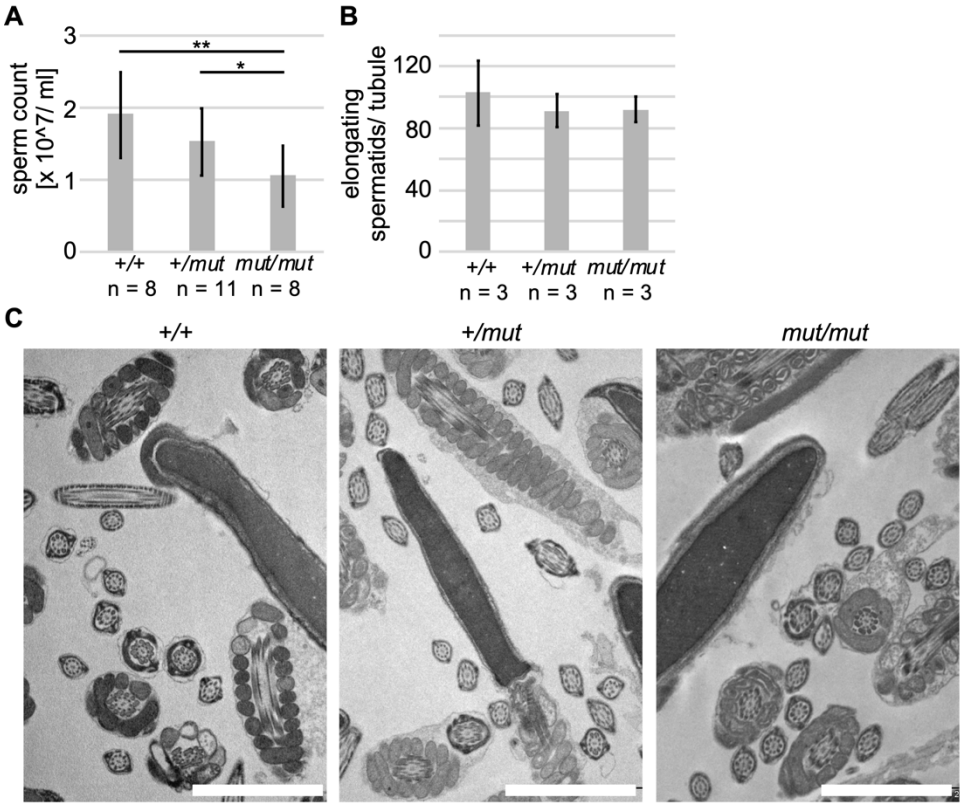


**Figure 31: Sperm production and sperm count in *Prm*-mutated mice. (A)** Average sperm count in swim-out from WT, $Prm^{+/mut}$ and $Prm^{mut/mut}$ cauda epididymides (n = number of males). **(B)** Number of elongating spermatids per seminiferous tubule cross section of WT, $Prm^{+/mut}$ and $Prm^{mut/mut}$ males; 5 tubules per male were analyzed (n = number of males). **(C)** Representative images of flagella cross sections of epididymal sperm isolated from WT, $Prm^{+/mut}$ and $Prm^{mut/mut}$ males; data are shown as mean ± s.d. and were analyzed using a two-tailed, unpaired Student's t-test. Scale: 2 µm

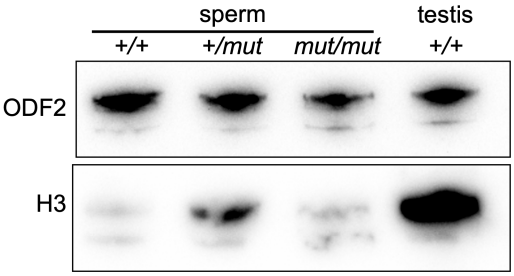


**Figure 32: Histone H3 retention in *Prm*-mutated sperm.** Western blot against histone H3 on basic protein extracts from epididymal sperm from WT, $Prm^{+/mut}$ and $Prm^{mut/mut}$ males. ODF2 was used as loading control. Protein extracts form WT testis tissue was used as positive control.

Previously, we have shown that lack of either PRM1 or PRM2 leads to increased histone retention (this thesis, (Merges et al., 2022b)). To address the question whether the PRM1-PRM2 fusion protein is able to evict histones, histone H3 contents in $Prm^{mut}$ sperm were analyzed. Interestingly, western blot analysis on nuclear protein extracts from mature sperm showed increased histone H3 retention in $Prm^{+/mut}$, but not $Prm^{mut/mut}$ sperm (Figure 32). This suggests that the PRM1-PRM2 fusion protein effectively evicts histones. However, the fact that $Prm^{+/mut}$ sperm display increased histone H3 levels suggest, that the $Prm^{mut}$ allele in itself interferes with proper histone-protamine exchange. Additionally, increased levels of unprocessed PRM2 in $Prm^{+/mut}$ sperm indicate that the $PRM^{MUT}$ protein interferes with regular PRM1-PRM2 dynamics (Figure 26B). Taken together, this indicates that aberrant interaction between the PRM1-PRM2 fusion protein and endogenous PRM1 and PRM2 in $Prm^{+/mut}$ sperm leads to defects in chromatin remodeling.

Detailed analysis of nuclear remodeling proteins in sperm and the PRM1-PRM2 fusion protein interaction with these in somatic cells *in vitro* has been taken over by Ilse Hamers during her

Master thesis and is still ongoing. Additionally, IHC stainings against nuclear remodelers on tissue sections and staining against 8-OHdG to detect sperm degradation are currently performed.

## 4.4. Establishment of an *Actl7b*-null allele

### 4.4.1. Evolutionary analysis of *ACTL7B* and its expression in male haploid germ cells

Since *ACTL7B* is a testis specific gene in both human and mouse and was proposed to have arisen prior to the divergence of rodents and primates by retroposition of a spliced mRNA transcribed from an actin progenitor gene (Hisano et al., 2003b), we decided to have a closer look at the *ACTL7B* coding sequence in both clades. Evolutionary analysis was performed to examine sequence conservation and selective pressures. To distinguish between purifying selection (codon sequence conservation) (ω < 1), neutral evolution (ω = 1) and positive selection (ω > 1), the nonsynonymous/synonymous substitution rate ratio (ω = dN/dS) was calculated (Table 1). The evolutionary rate (ω) of the whole sequences across all included species trees (Figure S3), was significantly lower than 1 (ω = 0.06, p > 0.001), showing that *ACTL7B* is under strong purifying selection. Next, selective pressures on *ACTL7B* in primates and rodents were compared. There was no significant difference in evolutionary rate between both clades (primates: ω = 0.06; rodents: ω = 0.06). Hence, *ACTL7B* is highly conserved and under purifying selection in both clades. When calculating the selective constrains acting on each codon site across the whole tree, we found that 97% of the *ACTL7B* codon sites were conserved. High purifying selection means that changes in the codon sequence are selected against, indicating that the gene and its protein product are essential. Additionally, human and

**Table 1: Evolutionary analysis of *ACTL7B*.** Values of selective constrains acting on *ACTL7B* across the whole phylogenetic tree, on the clades primates and rodentia, and the codon sites across the whole tree.

Results of the evolutionary analysis using CodeML (PAML4.9).

***ACTL7B***

| **Selection on:** | | **LnL null model** | **LnL alternative model** | **LRT** | **p** | **ω** | **interpretation** | | | |
|---|---|---|---|---|---|---|---|---|---|---|
| whole sequence, whole tree | | 12692.61 (M0fix) | 11332.97 (M0) | 2719.27 | >0.001 | 0.06 (M0) | ω sign. different from 1 | | overall conserved | |
| whole sequence, clades / lineages | Primates | 11332.97 (M0) | 11332.94 (MCfree) | 0.06 | n.s. | 0.06 (M0) | ω not group specific | | both lineages equally conserved | |
| | Rodentia | | | | | 0.06 (M0) | | | | |
| codon sites, whole tree | | 11273.60 (M1a) | 11273.60 (M2a) | 0.00 | n.s. | n.a. | purifying selection on sites | | sequence is 97% conserved | |
| | | | | | | | prop 0 | prop 1 | prop 2a | PSS |
| | | | | | | | 0.97 | 0.03 | n.a. | n.a. |

LnL = log Likelihood value of the model; LRT = Likelihood Ratio Test; p = p-value of the LRT; ω = evolutionary rate (dN/dS); sign. = sigificantly; prop = proportion of sites assigned to the respective site class; PSS = positively selected sites; for explanation of the models see M&M.

Modified from (Merges et al., 2022a). Analysis was performed by Dr. Lena Arévalo.

mouse ACTL7B show 85.9% pairwise amino acid identity, again suggesting a high essentiality of ACTL7B in spermatogenesis in both species.

Since *ACTL7A* and *ACTL7B* show 57% amino acid and 52% coding sequence identity in *Mus musculus*, we additionally analyzed the evolutionary rates for *ACTL7A*. *ACTL7A* is also highly conserved across primates and rodents (Table S1). The evolutionary rates of the whole sequences across all included species trees were significantly lower than 1 (*ACTL7A*: ω = 0.17, p > 0.001) and no significant difference in evolutionary rate between the clades was detected. 83% of the codon sites were conserved for *ACTL7A* (Figure S4). Although *ACTL7B* seems to be more strongly conserved than *ACTL7A, ACTL7A* is highly conserved, arguing for its essentiality.

ACTL7B has been described to be expressed exclusively in haploid male germ cells (Hisano et al., 2003a, Hisano et al., 2003b). Data extracted from the Human Testis Atlas published by *Guo et al.*, showed that expression of *ACTL7B* is detected in round and elongating spermatids in human (Guo et al., 2018) (Figure 33A). Additionally, RNA expression data published by

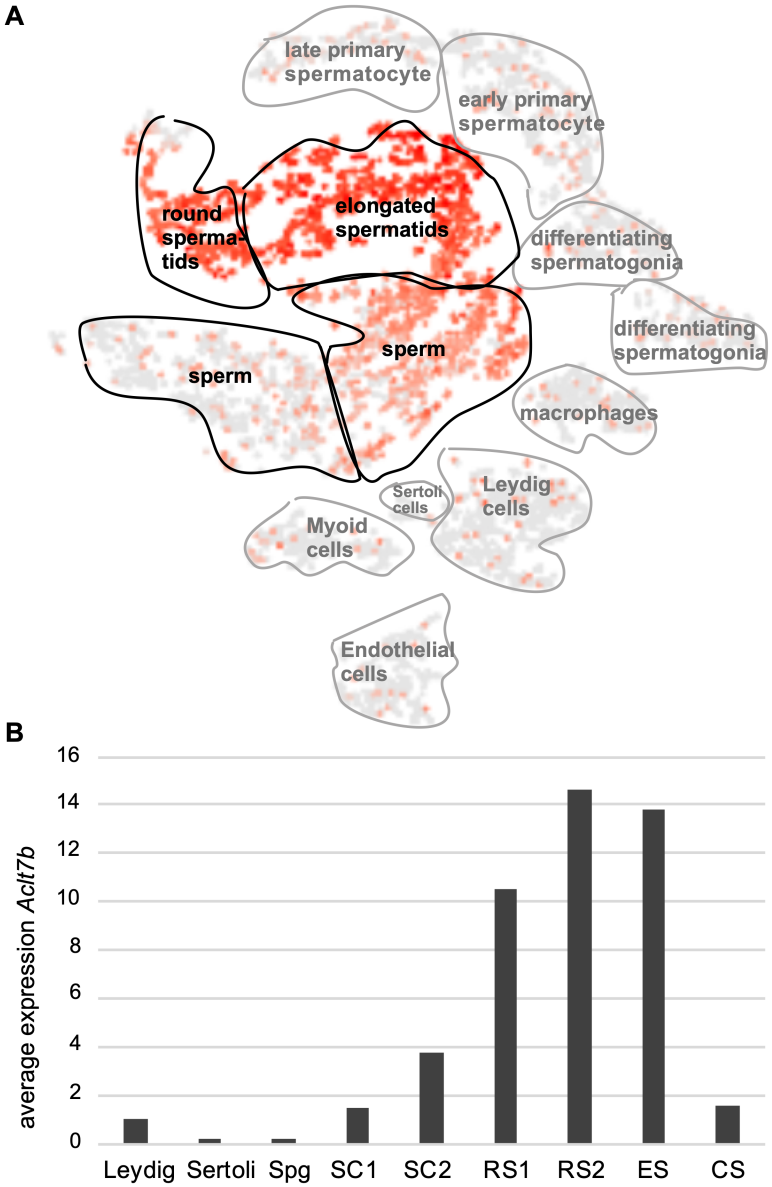


**Figure 33: *ACTL7B* expression in young adult human testicular tissue and murine testicular cells.** **(A)** Expression data of *ACTL7B* (indicated in red) in human testis extracted from the Human Testis Atlas adapted from Guo et al. (Guo et al., 2018). The clusters of cells are encircled. *ACTL7B* is expressed mainly in round and elongated spermatids (marked in red). **(B)** Average normalized expression of *Actl7b* in testicular cell populations of adult mouse testis adapted from Lukassen *et al.* (Lukassen et al., 2018). *Actl7b* is expressed mainly in round and elongated spermatids. Spg: spermatogonia, SC: spermatocytes, RS: round spermatids, ES: elongating spermatids, CS: condensing spermatids. Modified from (Merges et al., 2022a).

Lukassen et al. showed, that also in mice *Actl7b* transcripts are detected in round and elongating spermatids in testis (Figure 33B). Importantly, *ACTL7B* transcripts were not detected in other cell populations in the testis of human and mice.

### 4.4.2. CRISPR/Cas9-mediated gene editing for the generation of *Actl7b*-deficient mice

To characterize the role of ACTL7B in murine spermatogenesis, we decided to generate an *Actl7b*-null allele. Three different guide RNA pairs were designed and tested in murine ES cells *in vitro*. Guide RNAs were annealed and cloned into the pX330-U6-Chimeric_BB-CBh-hSpCas9 plasmid, which encodes for an optimized SpCas9 variant. ES cells were transfected and DNA isolated 48 hours later. *Actl7b* was amplified using PCR to identify gene editing positive ES cell populations (Figure 34A). Amplification of the WT allele produced an amplicon of 1048 bp. Amplification of DNA isolated from cells transfected with guide combination 1 produced additional bands of smaller size, indicating CRISPR/Cas9-mediated gene editing. Given that *Actl7b* and *Actl7a* show 52% coding sequence identity in *Mus musculus,* amplification of *Actl7a* was performed to exclude off-target effects (Figure 34B). ES cells transfected with guides targeting *Actl7b* showed no additional bands, suggesting that the guides used are specific. Additionally, potential off-targets of the guides selected were analyzed using "CRISPR/Cas9 guide RNA design checker" from IDT. Guide one had off-target scores of 91/100 and guide two of 86/100, meaning the guides are very specific to the target sequence. On chromosome 4 only two potential off-targets were detected for guide 2, both of which are localized in non-coding areas.

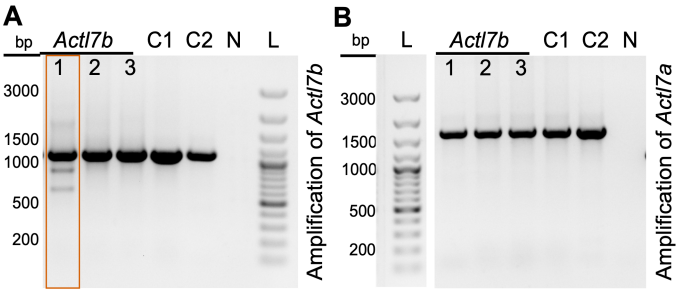


**Figure 34: Testing of sgRNAs targeting *Actl7b* in murine ES cells.**
**(A)** Amplification of the *Actl7b* coding sequence in ES cells transfected with the expression vector px330 containing guides targeting the *Actl7b* coding sequence. **(B)** Amplification of the *Actl7a* coding sequence in ES cells transfected with the expression vector px330 containing guides targeting the *Actl7b* coding sequence. C1 = DNA isolated from ES cells transfected with the control plasmid (pEGFP-N3); C2 = WT mouse DNA; N = water control; L = ladder. Selected guide combinations are marked with a vermillion box.

Hence, guide combination 1 was used to generate *Actl7b*-deficient mice (Figure 35A). A mouse carrying a 473 bp deletion in the *Actl7b* coding sequence, which leads to a frameshift and premature stop codon, was selected to establish an *Actl7b*-deficient mouse line. A genotyping PCR utilizing primers, which flank the deleted sequence, was established (Figure 35B). *ACTL7B* is expressed in round and elongating spermatids in mice and human and its protein localizes to the cytoplasm (Hisano et al., 2003b, Guo et al., 2018, Lukassen et al., 2018, Tanaka et al., 2003) (Figure 35C). IHC staining against ACTL7B on murine testis sections from

WT males (*Actl7b+/+*), confirmed ACTL7B immunolocalization (Figure 35D). Of note, the staining is most intense throughout the cytoplasm of round spermatids and weakly present in the cytoplasm of elongating spermatids. Round spermatids in testis sections from heterozygous mice (*Actl7b+/-*) showed a weaker ACTL7B signal suggestive of a gene-dosage effect. No ACTL7B was detected in homozygous samples (*Actl7b-/-*), validating the generation of an *Actl7b*-null allele.

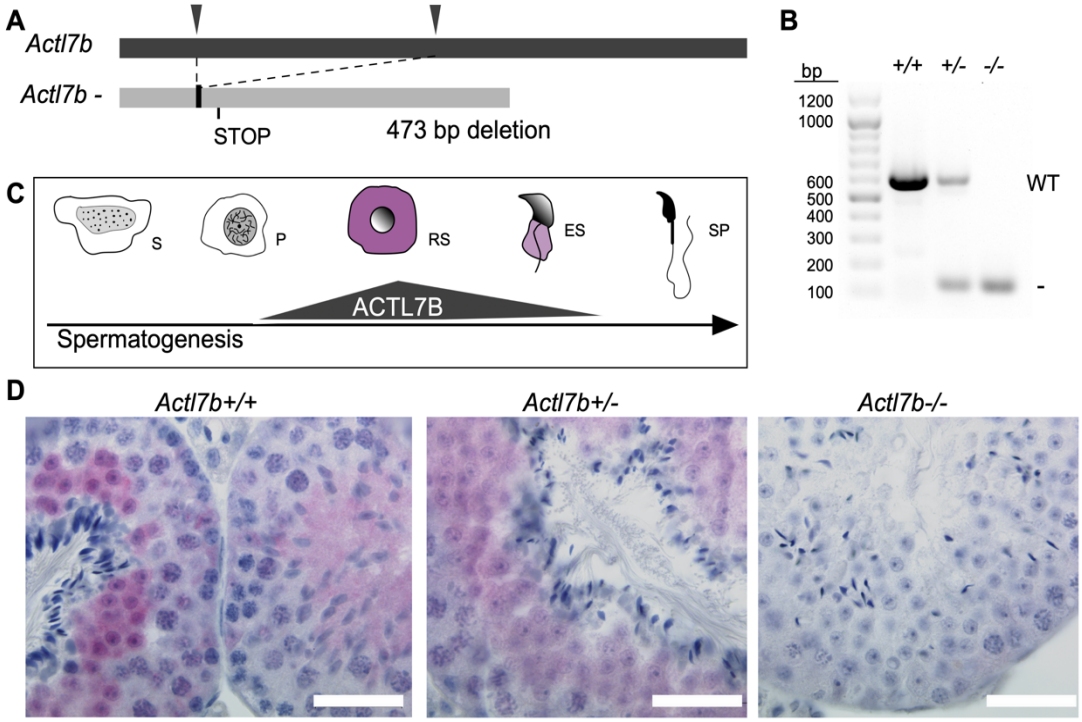


**Figure 35: Establishment of *Actl7b*-deficient mice. (A)** Graphical representation of CRISPR/Cas9-mediated gene editing of the *Actl7b* coding sequence. sgRNA target sites are marked with black arrowheads. A 473 bp deletion in the *Actl7b* coding sequence was generated, leading to a premature stop codon. **(B)** Representative amplification of WT *Actl7b* or the *Actl7b-* allele generating products of 607 bp or 134 bp. **(C)** Graphical representation of ACTL7B immunolocalization during spermiogenesis based on literature (Tanaka et al., 2003). **(D)** IHC staining of ACTL7B on *Actl7b+/+, Actl7b+/-* and *Actl7b-/-* testis sections (counterstain: Hematoxylin). Scale: 50 µm. Modified from (Merges et al., 2022a).

## 4.5. Characterization of *Actl7b*-deficient mice

### 4.5.1. Fertility assessment and spermatogenesis in *Actl7b*-deficient mice

First, the fertility of *Actl7b*-deficient mice was assessed. Fertility analysis revealed, that *Actl7b-/-* males are infertile (Figure 36). *Actl7b+/-* males showed similar litter sizes and pregnancy frequencies compared to *Actl7b+/+* males. Further, testis size and weight were significantly reduced in *Actl7b-/-* males, compared to *Actl7b+/-* and *Actl7b+/+* males, indicating defects in spermatogenesis (Figure 37).

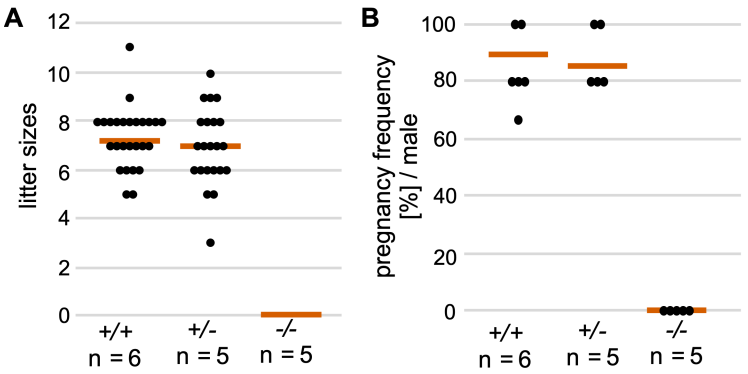


**Figure 36: Fertility analysis of *Actl7b*-deficient mice.** **(A)** Scatter plot of litter sizes monitored for males after mating with female WT mice. The mean litter size per genotype is indicated by vermillion lines (n = number of males). **(B)** Pregnancy frequency (%) per male after mating with female WT mice. The mean pregnancy frequency per genotype is indicated by vermillion lines (n = number of males). Modified from (Merges et al., 2022a).

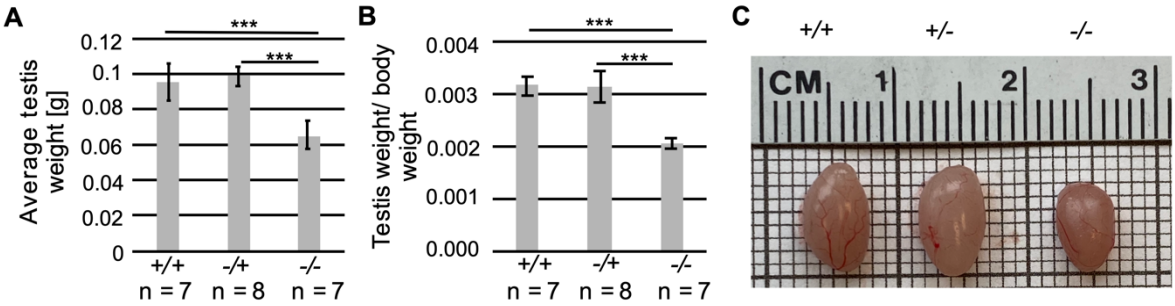


**Figure 37: Macroscopic analysis of spermatogenesis of *Actl7b*-deficient mice.** **(A)** Average testis weight of *Actl7b+/+*, *Actl7b+/-* and *Actl7b-/-* males (n = number of males). **(B)** Average testis to body weight ratio of *Actl7b+/+*, *Actl7b+/-* and *Actl7b-/-* males (n = number of males). **(C)** Representative picture of testis dissected from *Actl7b+/+*, *Actl7b+/-* and *Actl7b-/-* males with similar body weight. Data are shown as mean ± s.d. and were analyzed using a two-tailed, unpaired Student's t-test (***p<0.001). Modified from (Merges et al., 2022a).

Strikingly, the dissected cauda epididymides from *Actl7b-/-* males appeared more translucent compared to *Actl7b+/+* (Figure 38A). Cauda epididymides were generally smaller in *Actl7b-/-* males compared to *Actl7b+/+* and *Actl7b+/-* males. In the swim-out preparation to obtain sperm prepared from *Actl7b-/-* cauda epididymides mainly round cells and barely any sperm were detected (Figure 38B).

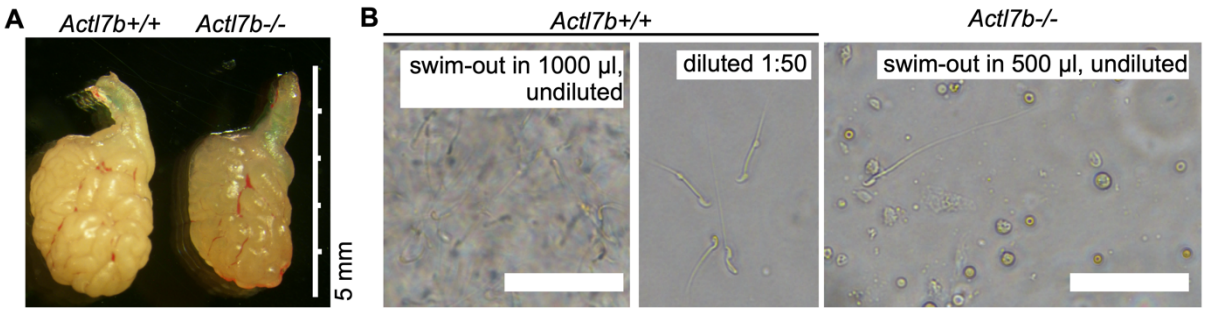


**Figure 38: Macroscopic analysis of cauda epididymis of *Actl7b*-deficient mice. (A)** Representative picture of cauda epididymides dissected from *Actl7b+/+* and *Actl7b-/-* littermates. **(B)** Representative images of cell suspension after swim-out from cauda epididymides from *Actl7b+/+* and *Actl7b-/-* mice. Scale: 50 µm

An average of 32,250 sperm were counted in the swim-out from both cauda epididymides from *Actl7b-/-* males compared to approximately 3.1-3.5 x $10^7$ sperm in *Actl7b+/+* and *Actl7b+/-* males, respectively (Table 2).

**Table 2: Sperm counts from both cauda epididymides.**

| | +/+ n = 3 | +/- n = 3 | -/- n = 3 |
|---|---|---|---|
| Individual 1 | 30500000 | 34000000 | 34500 |
| Individual 2 | 35375000 | 39750000 | 41250 |
| Individual 3 | 28125000 | 32875000 | 21000 |
| Average sperm count per genotype | 31333333.33 | 35541666.67 | 32250.00 |
| s.d. | 3696141.01 | 3687676.55 | 10310.80 |

Next, HE-stained tissue sections of testis, caput and cauda epididymis were prepared to examine the microanatomy of the reproductive organs. Sperm production appeared normal in *Actl7b+/-* and *Actl7b+/+* testis and caput and cauda are filled with mature sperm (Figure 39). *Actl7b-/-* seminiferous tubules appear disorganized and sperm production disturbed. Caput and cauda epididymides are filled with cell debris, morphologically abnormal spermatids and large amounts of roundish cells, which most likely represent immature germ cells.

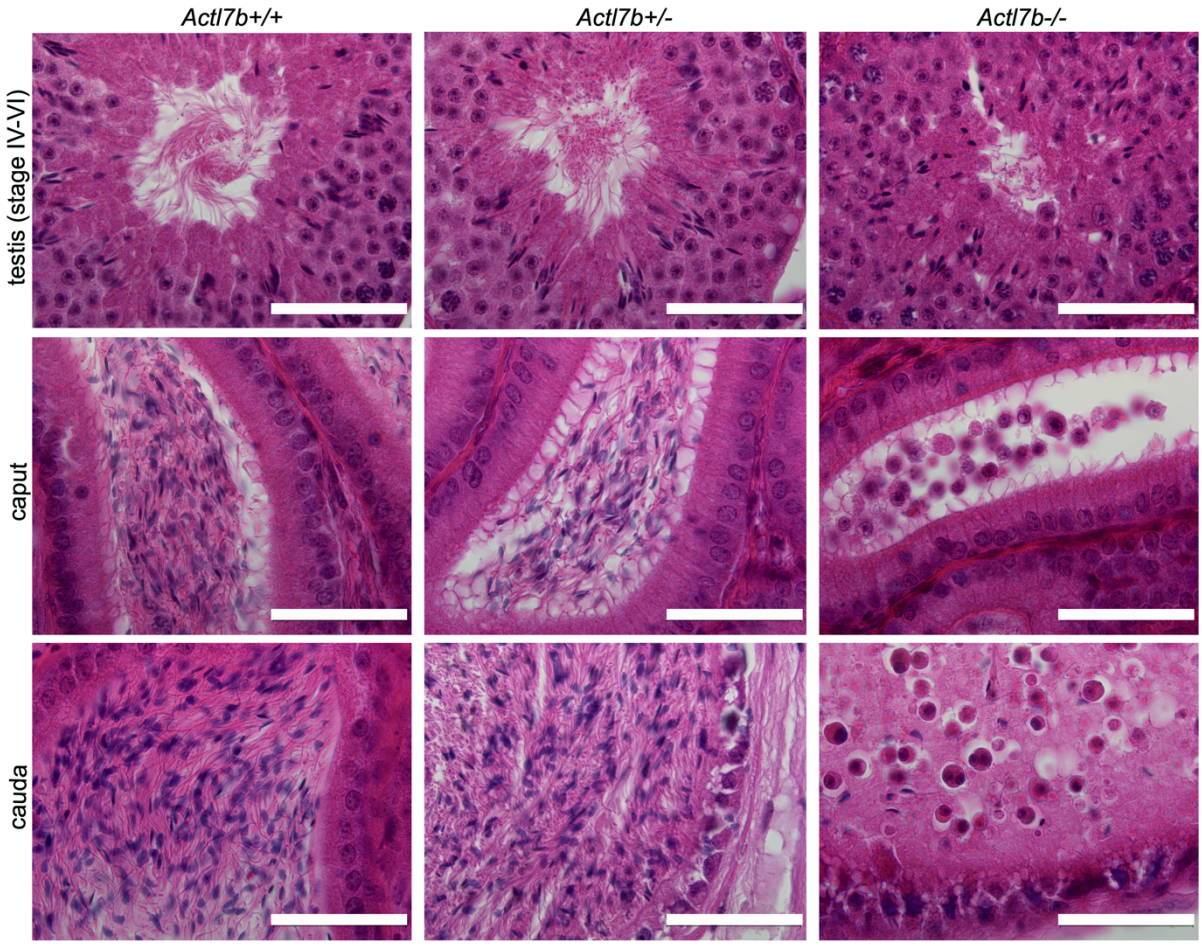


**Figure 39: Microscopic analysis of spermatogenesis and sperm maturation of *Actl7b*-deficient mice.** Representative images of Bouin-fixed paraffin-embedded testis (IV-VI of the epithelial cycle), caput epididymis and cauda epididymis of *Actl7b+/+*, *Actl7b+/-* and *Actl7b-/-* males stained with Hematoxylin-Eosin. Scale: 50 µm. Modified from (Merges et al., 2022a).

Upon closer examination of *Actl7b-/-* seminiferous tubule sections vacuolations in the tissue were detected (Figure 40). These localize mostly in the basal region of the seminiferous tubules, indicating recent loss of germ cells. In stage VIII seminiferous tubules, darkly stained, abnormally formed elongated spermatids were found, which reside deeper in the tissue. This suggests that they are retained and originate from the previous epithelial cycle. Additionally, round spermatids that present with dark cytoplasm, indicative for apoptosis/degradation, were detected. Seemingly these were blocked in development. Immature germ cells seem to be released into the lumen of seminiferous tubules. Late stage spermatids showed abnormal morphologies.

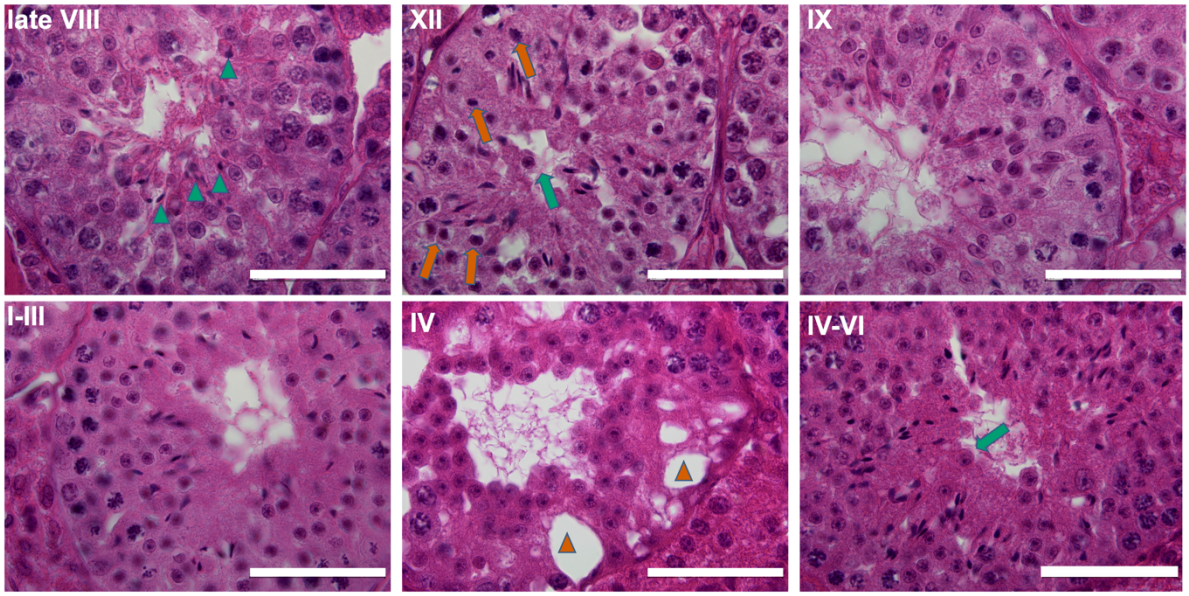


**Figure 40: Morphology of Actl7b-deficient seminiferous tubules.** Images of Bouin-fixed paraffin-embedded testis sections of *Actl7b-/-* mice stained with Hematoxylin-Eosin. Immature apoptotic germ cells about to be released into the lumen are marked by green arrows. In late stage VIII, elongated spermatids with an abnormal morphology, which were not spermiated, are marked by green arrow heads. Round spermatids blocked in development with dark cytoplasm are marked by vermillion arrows. Vacuolation of seminiferous tubules is marked by vermillion arrow heads. Scale: 50 µm Modified from (Merges et al., 2022a).

Next, we took a closer look at the synchronization of the epithelial cycle in *Actl7b-/-* mice. Inspection of transmission electron micrographs and PAS-stained testicular sections revealed disturbance in synchronization in *Actl7b*-deficient mice (Figure 41). In stage VI tubules elongation of spermatids appears non-synchronic, condensation of chromatin is delayed and irregular and spermatids are localized too close to the basal lamina (Figure 41A). Furthermore, already at stage IX cohorts of round spermatids appear abnormal and disorganized (Figure 41B). In comparison, WT stage IX tubules appear more synchronized and later, in stage X, all elongating spermatids appear morphologically normal and in the same developmental stage (Figure 41C). Opposed to that, morphologically abnormal elongating spermatids can be seen in *Actl7b-/-* stage X tubules. Lastly, in stage VII abnormal, elongating spermatids were localized unordered throughout the epithelium (Figure 41D), while in WT elongating spermatids align properly at the lumen. Substantial numbers of round spermatids are formed properly in *Actl7b-/-* testis, but only few elongated spermatids can be seen in later spermiogenic steps.

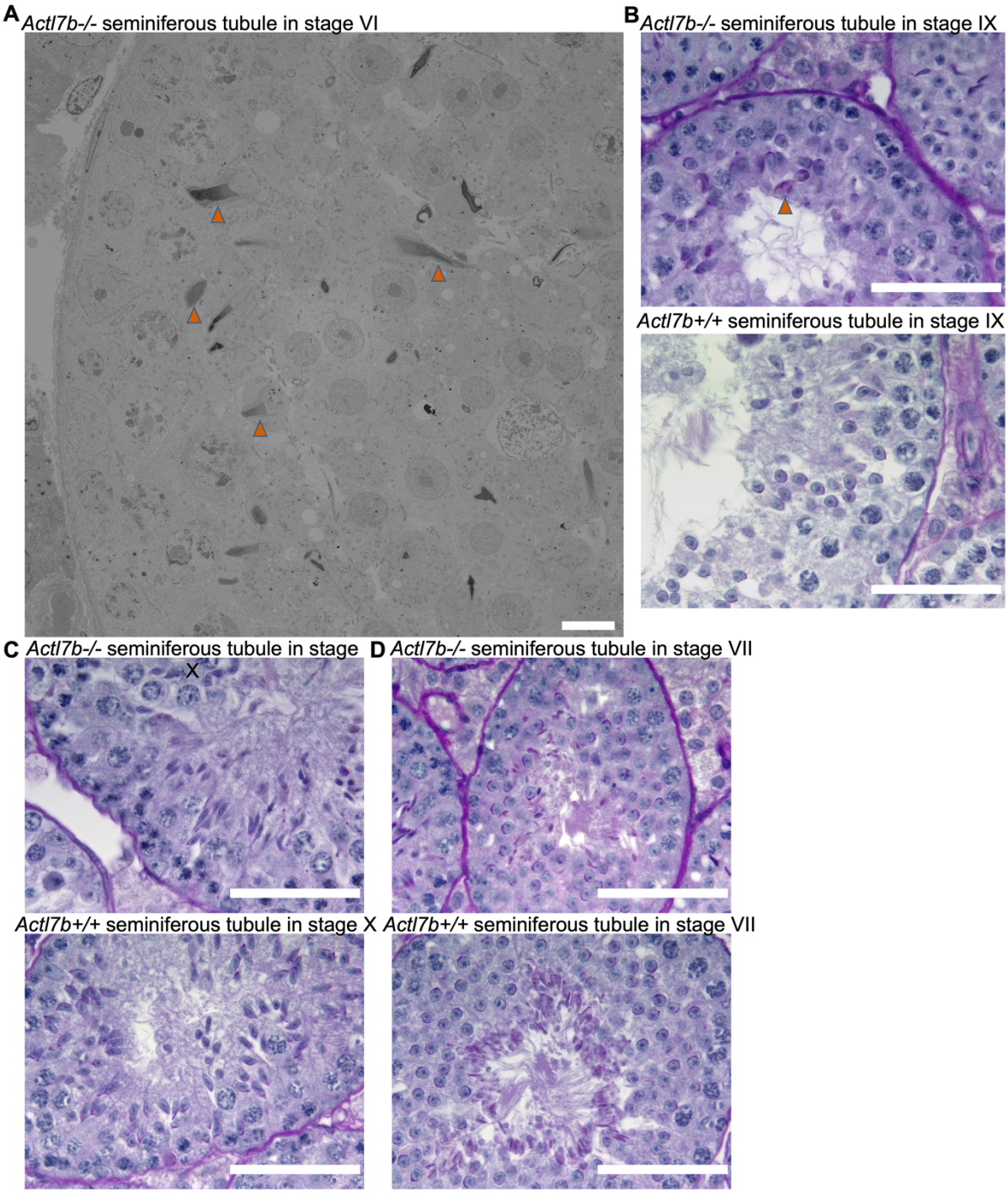


**Figure 41: The seminiferous cycle in *Actl7b*-deficient mice. (A)** Representative transmission electron micrograph of *Actl7b-/-* seminiferous tubule. Elongating spermatids are indicated by vermillion arrow heads. Scale: 5 µm **(B)** PAS staining of testis sections of stage VI seminiferous tubules of *Actl7b+/+* and *Actl7b-/-* mice. A double nucleated spermatid found is labeled with a vermillion arrow head. **(C)** PAS staining of testis sections of stage X seminiferous tubules of *Actl7b+/+* and *Actl7b-/-* mice. **(D)** PAS staining of testis sections of stage VII seminiferous tubules of *Actl7b+/+* and *Actl7b-/-* mice. Scales B-D: 50 µm

Since substantial numbers of round spermatids are produced in *Actl7b-/-* seminiferous tubules, we decided to analyze transmission electron micrographs of testes in more detail to find an indication as to why sperm numbers are drastically reduced in final stages of spermiogenesis and epididymides of *Actl7b-/-* mice. Interestingly, we found increased numbers of vesicle-like

structures containing degrading spermatids, suggestive of Sertoli cell-mediated degradation of abnormal spermatids, in *Actl7b-/-* testis (Figure 42A-B). Western blots on whole testis protein extractions from *Actl7b+/+*, *Actl7b+/-* and *Actl7b-/-* mice, revealed increased levels of the autophagy marker protein LC3 in *Actl7b-/-* testis (Figure 42C). Additionally, cathepsin B (CTSB) levels were elevated in *Actl7b-/-* testis. It has been shown that deletion of CTSB in mice leads to inhibition of autophagy and increased apoptosis (Wen et al., 2022). This might indicate that in *Actl7b-/-* mice, controlled sperm degradation rather than germ cell apoptosis is the cause of reduced elongating spermatid numbers. This was further validated by measuring daily elongating spermatid production and counting the average number of elongating spermatids in tubule cross sections (Figure 42D-E). The number of elongating spermatids was drastically reduced in *Actl7b-/-* testis compared to *Actl7b+/-* and *Actl7b+/+* testis.

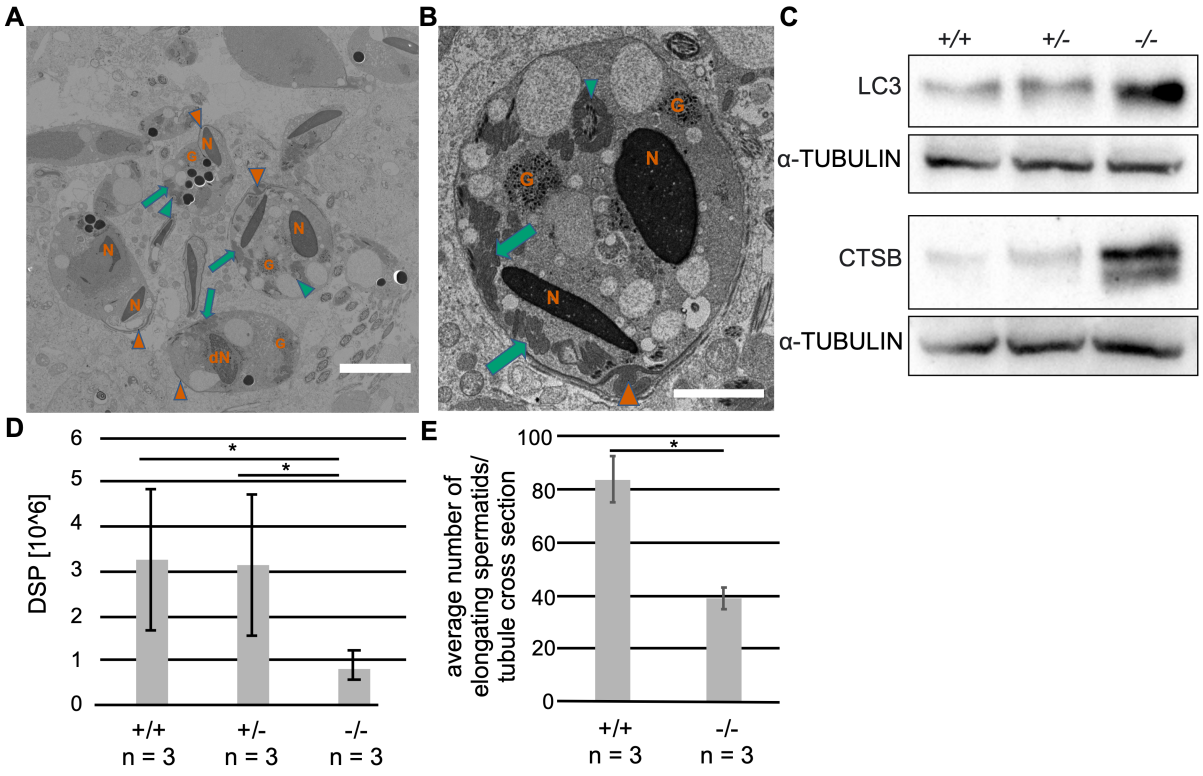


**Figure 42: Sperm degradation in *Actl7b*-deficient mice. (A-B)** Representative images of transmission electron micrographs of vesicles filled with degrading spermatids in *Actl7b-/-* seminiferous tubules. N = condensed nuclei, dN = degraded nucleus, G = granular material, vermillion arrow heads = acrosomal structures, green arrow heads = flagellar cross sections, green arrows = mitochondria. Scales: **(A)** 5 µm, **(B)** 2 µm. **(C)** Western blots on protein extractions from whole testis from *Actl7b+/+*, *Actl7b+/-* and *Actl7b-/-* mice. **(D)** Average daily sperm production in *Actl7b+/+*, *Actl7b+/-* and *Actl7b-/-* mice (n = number of males). **(E)** Average number of elongating spermatids counted per PAS-stained seminiferous tubule cross section of *Actl7b+/+*, *Actl7b+/-* and *Actl7b-/-* mice. Five tubule cross-sections per animal were analyzed (n = number of males). Data are mean ± s.d. and were analyzed using a two-tailed, unpaired Student's t-test (*p<0.05). Parts modified from (Merges et al., 2022a).

To examine apoptosis in *Actl7b*-deficient testis, TUNEL staining was performed (Figure S5). Indeed, no increase in TUNEL positive cells was seen in *Actl7b-/-* compared to *Actl7b+/+* and *Actl7b+/-* testis sections.

Abnormal spermatid morphologies were detected in later steps of spermiogenesis in *Actl7b-/-* males. Sperm membranes and acrosomal structures became detached (Figure 43A-B). Some condensed nuclei show inclusions (Figure 43C). All in all, elongating spermatid structures seem to fail to assemble correctly (Figure 43D).

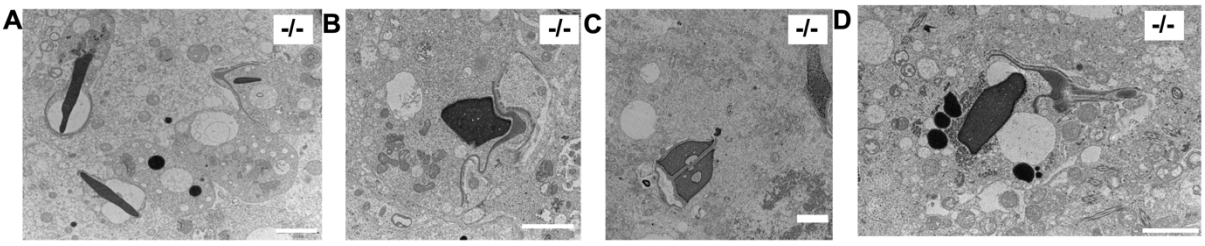


**Figure 43: Morphology of late step spermatids in *Actl7b-/-* testes. (A-D)** Representative transmission electron micrographs of *Actl7b-/-* late step spermatids. Scales: 2 µm. Modified from (Merges et al., 2022a).

To characterize spermatid malformations in more detail, we looked at different basic spermatogenic parameters including manchette formation, acrosome biogenesis, flagella formation and chromatin remodeling.

Manchette formation starts in early step 8 of spermiogenesis in *Actl7b+/+* and *Actl7b-/-* spermatids (Figure 44). In step 9 spermatids, manchette formation starts to look abnormal in part of *Actl7b-/-* spermatids and spermatid head shapes appear malformed compared to *Actl7b+/+* in later stages.

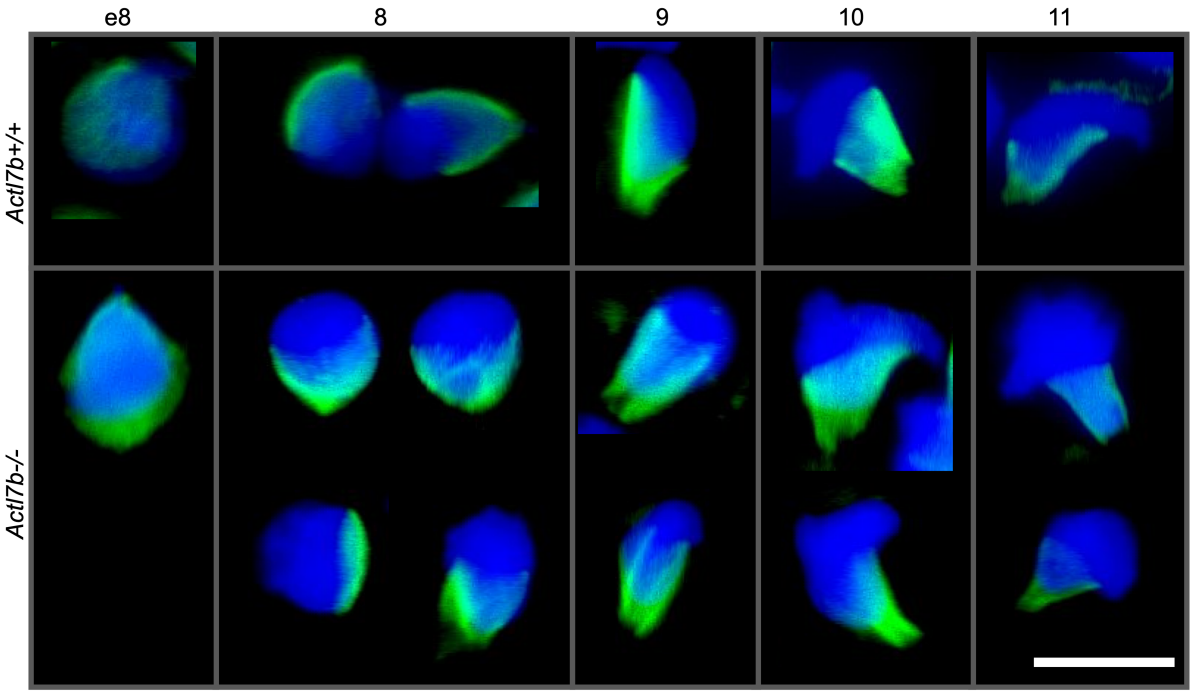


**Figure 44: Manchette formation in *Actl7b*-deficient mice.** Representative images of spermatids isolated from *Actl7b+/+* and *Actl7b-/-* testes. Manchette was stained with α-tubulin (counterstain: DAPI). e8 = early step 8 spermatids, 8-11 = step 8-11 spermatids. Scales: 10 µm. Staining and imaging was performed by Anđela Kovacevic.

Next, acrosome biogenesis was evaluated by using PNA staining on testis sections. Proacrosomal vesicles are formed in *Actl7b-/-* round spermatids (Figure 45). Again, it can be seen that substantial numbers of round spermatids are formed in *Actl7b-/-* mice, all of which start acrosome biogenesis (Figure S6A). Also, acrosomal caps appear similar in *Actl7b-/-* testis compared to *Actl7b+/-* and *Actl7b+/+* testis (Figure 45, Figure S6A). Malformed acrosomal structures are first detected in maturation phase of acrosome biogenesis. Acrosomal structures appear disorganized and disrupted in *Actl7b-/-* testis (Figure S6B).

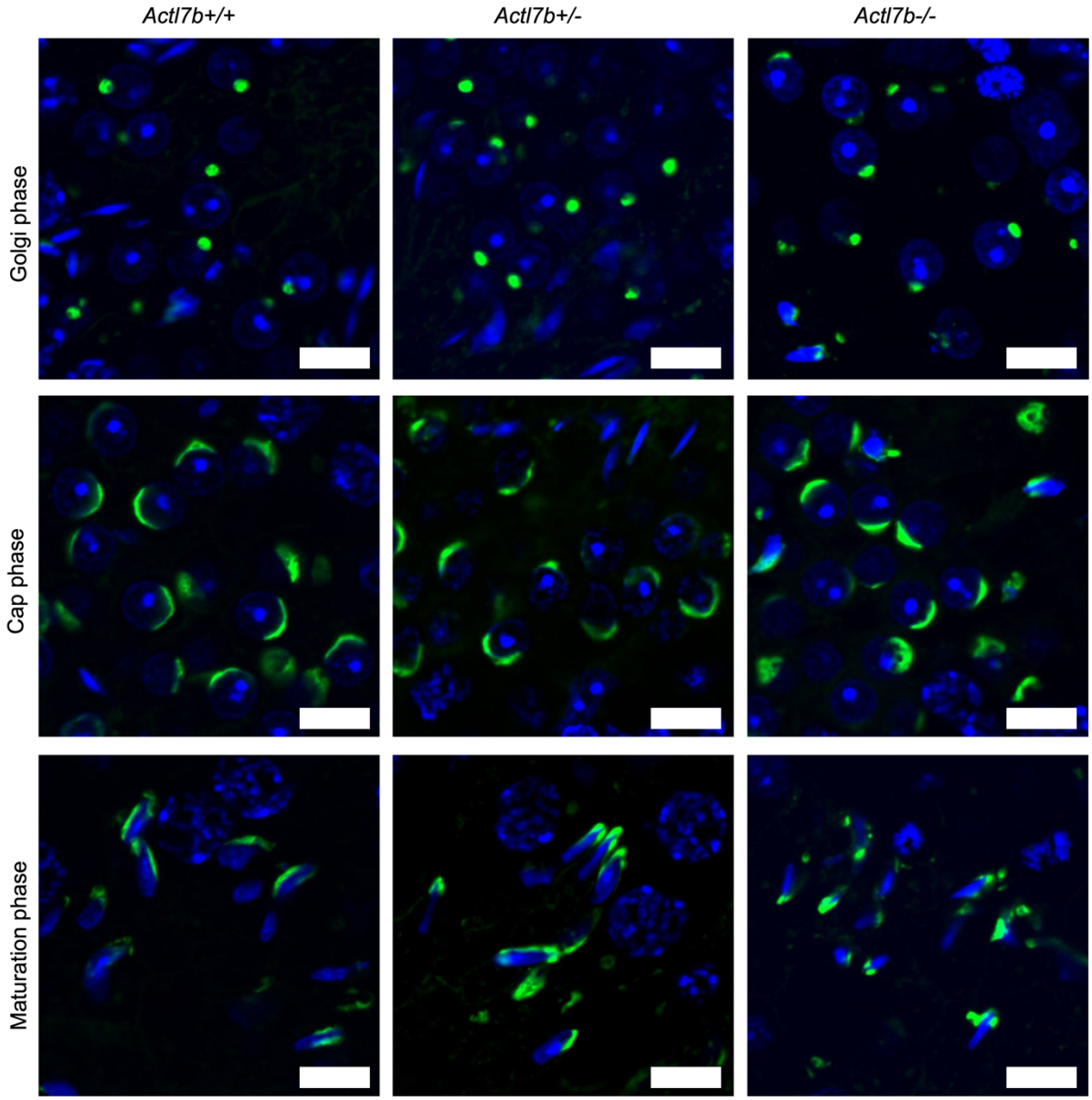


**Figure 45: Acrosome biogenesis in *Actl7b*-deficient mice.** Representative images of PNA-stained acrosomal structures in Golgi, Cap and Maturation phase of acrosome biogenesis in *Actl7b+/+, Actl7b+/-* and *Actl7b-/-* mice (counterstain: DAPI). Scale: 10 µm. Confocal microscopy was performed together with Anđela Kovacevic.

To evaluate chromatin remodeling in *Actl7b*-deficient mice, major chromatin remodeling proteins were stained on testis sections. After TNPs are loaded onto the DNA (Figure 46A), protamines are detected in elongating spermatids in *Actl7b-/-*, *Actl7b+/-* and *Actl7b+/+* mice (Figure 46B). Staining against the cleaved domain of PRM2 (cP2) showed that PRM2 localizes to the nuclei of *Actl7b+/+*, *Actl7b+/-* and *Actl7b+/+* elongating spermatids. Finally, in *Actl7b+/+* and *Actl7b+/-* mice remaining full-length unprocessed PRM2 is evicted in residual bodies as described in literature (Arévalo et al., 2022a) (Figure 46C). *Actl7b-/-* testis sections show enlarged, cP2-stained residual bodies that are less clearly separated from spermatid nuclei. This could be indicative of impaired cytoplasmic eviction in *Actl7b-/-* mice.

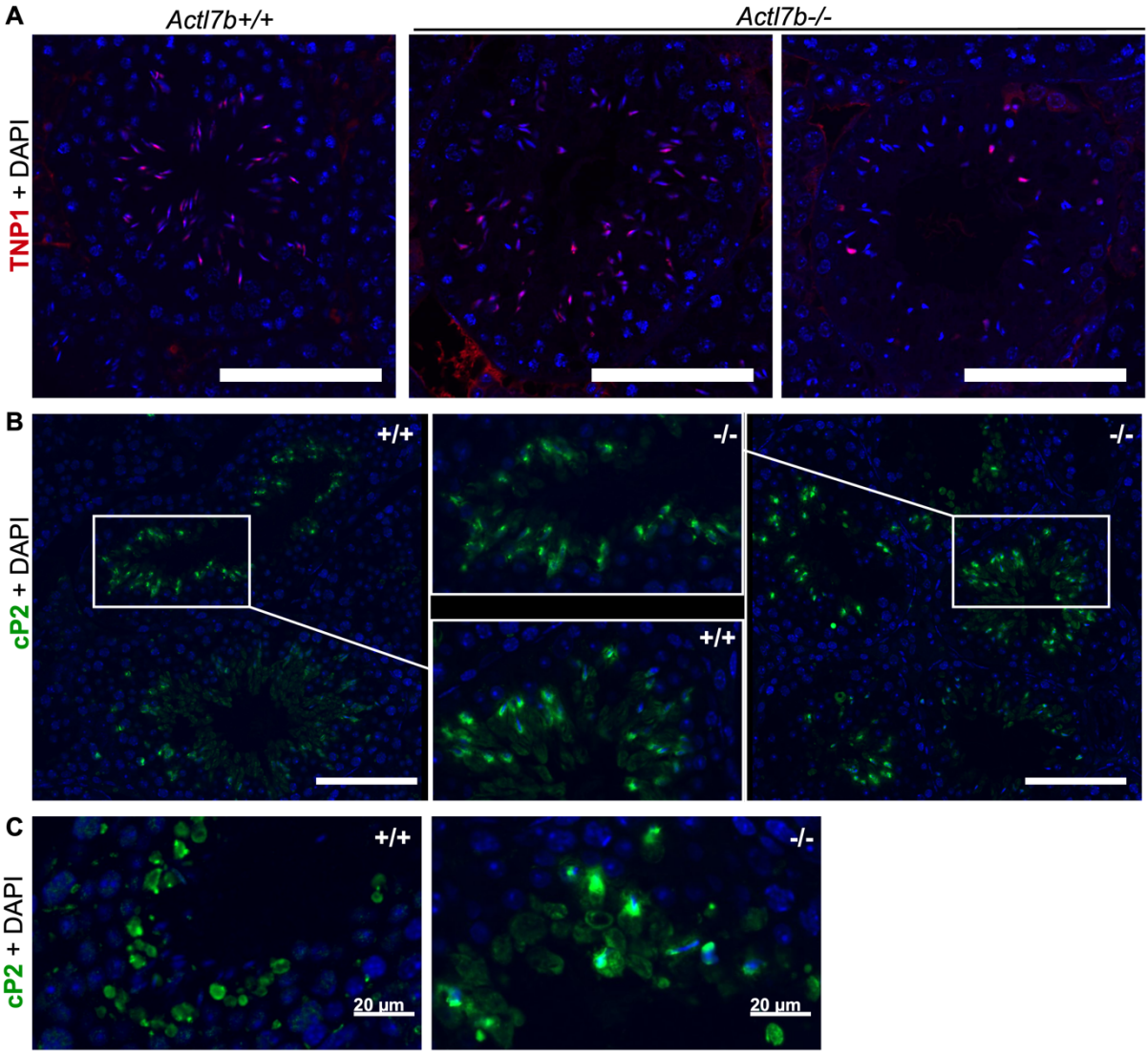


**Figure 46: Chromatin remodeling in *Actl7b*-deficient mice. (A)** IHC stainings against TNP1 on testis sections from *Actl7b+/+, Actl7b+/-* and *Actl7b-/-* mice (counterstain: DAPI). Scale: 100 µm **(B)** IHC stainings against cP2 on testis sections from *Actl7b+/+, Actl7b+/-* and *Actl7b-/-* mice (counterstain: DAPI). Scale: 100 µm **(C)** IHC stainings against cP2 on caput epididymal sections from *Actl7b+/+* and *Actl7b-/-* mice (counterstain: DAPI). Scale: 20 µm. Confocal microscopy was performed together with Anđela Kovacevic.

Indeed, we found immature spermatids with retained cytoplasm lining the lumen of *Actl7b-/-* seminiferous tubules (Figure 47A). In comparison, mature spermatozoa, ready to be spermiated, line the lumen in *Actl7b+/+* mice. Next, staining against cleaved PRM2 (cP2) was performed on caput epididymal sections (Figure 47B). Large numbers of cP2-stained cells were detected in *Actl7b-/-* caput epididymides (Figure 47C), again indicative of failed eviction of cytoplasm and release of immature spermatids from testis.

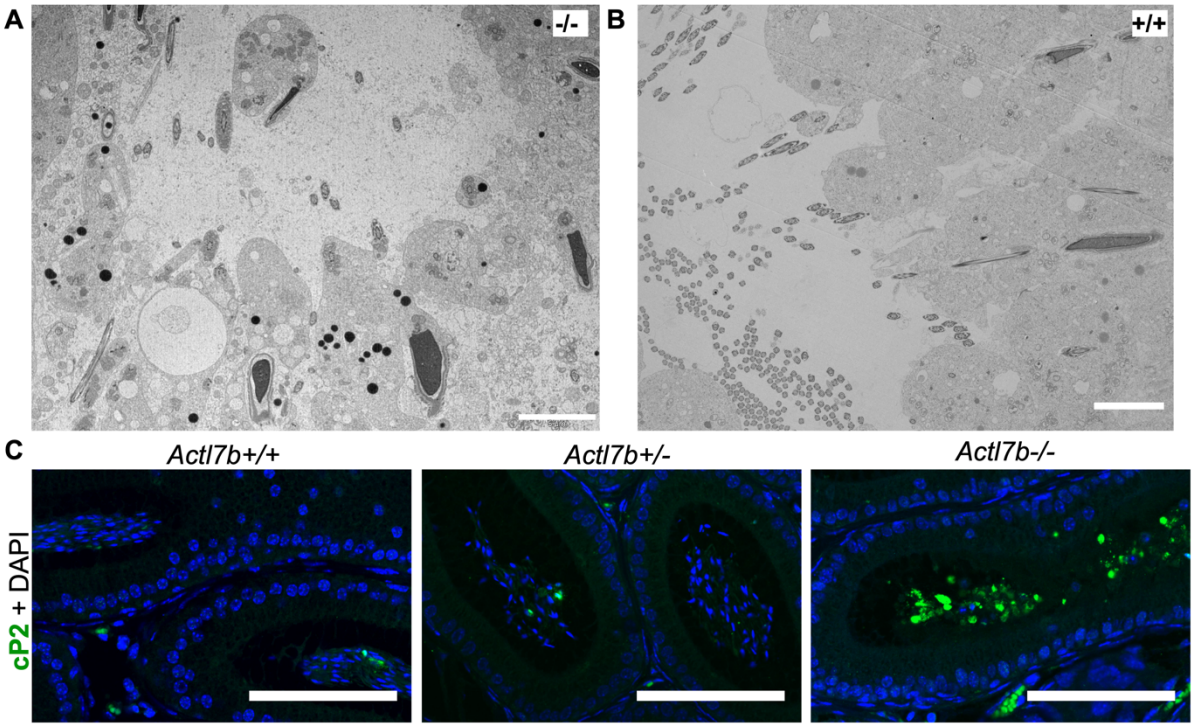


**Figure 47: Eviction of cytoplasm in *Actl7b-/-* mice. (A-B)** Transmission micrograph of a lumen of an **(A)** *Actl7b-/-* and **(B)** *Actl7b+/+* seminiferous tubule. Scale: 5 µm **(C)** IHC staining against cP2 on caput epididymal sections from *Actl7b+/+, Actl7b+/-* and *Actl7b-/-* mice (counterstain: DAPI). Confocal microscopy was performed together with Anđela Kovacevic. Modified from (Merges et al., 2022a).

Next, staining against ODF2, an outer dense fiber protein of sperm flagella, was used to visualize flagella formation. Flagella are formed less frequently in *Actl7b-/-* testis compared to *Actl7b+/+* and *Actl7b+/-* testis (Figure 48A-B). Further, disorganization of sperm within the epithelium in *Actl7b-/-* mice can be seen. Flagellated sperm were detected close to the basal membrane in *Actl7b-/-* testis (encircled in white, Figure 48C). This suggests, that abnormal sperm are drawn towards the basal membrane to be degraded.

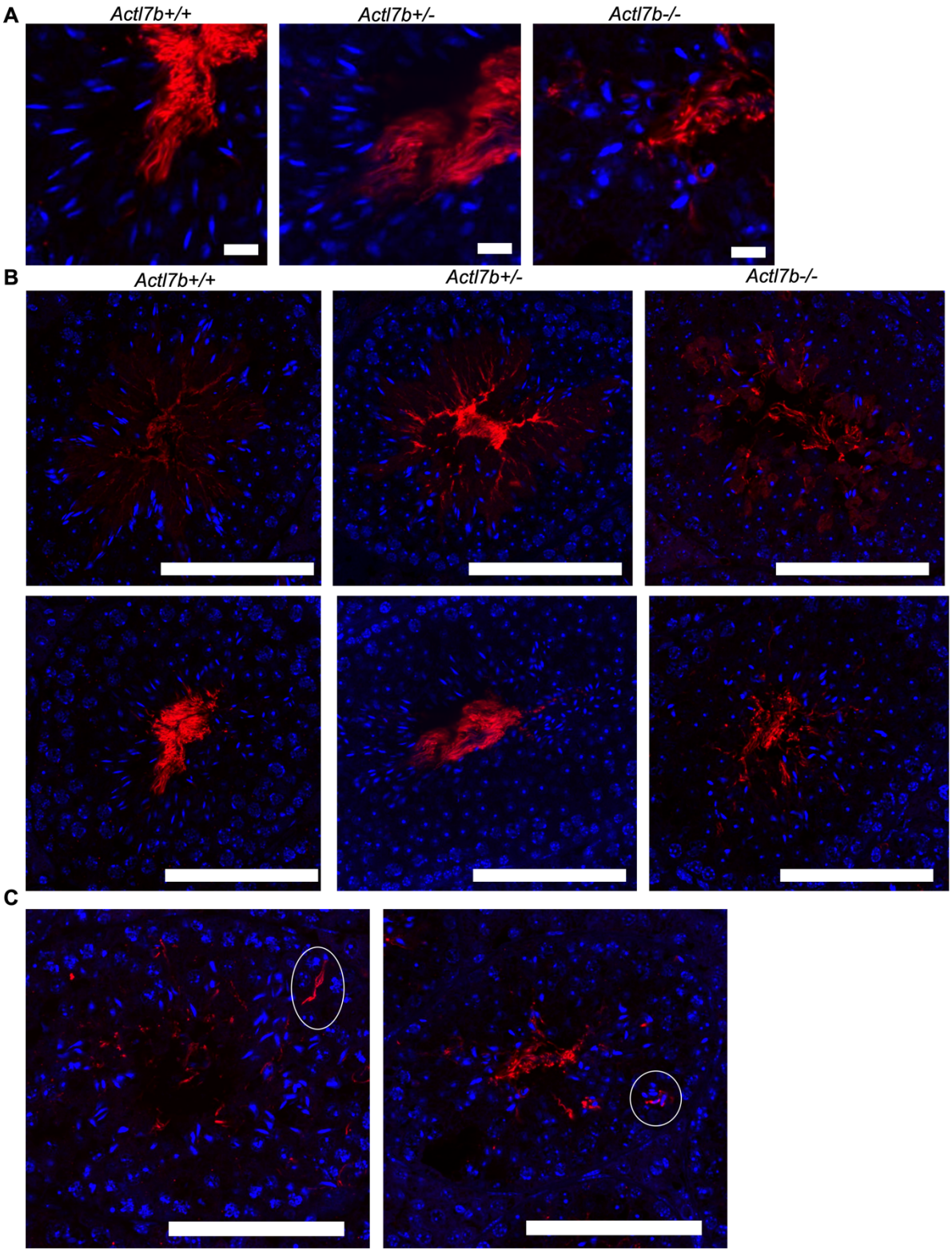


**Figure 48: Sperm flagella formation in *Actl7b*-deficient mice. (A-B)** IHC staining against ODF2 on *Actl7b+/+*, *Actl7b+/-* and *Actl7b-/-* testis sections (counterstain: DAPI). Note, that *Actl7b+/+* and *Actl7b+/-* images in **(A)** are zoomed in cut-outs from **(B)**. Scales: **(A)** 10 µm, **(B)** 100 µm **(C)** IHC staining against ODF2 on *Actl7b-/-* testis sections (counterstain: DAPI). Flagellated sperm close to basal membrane are encircled. Scales: 100 µm. Confocal microscopy was performed together with Anđela Kovacevic.

After detailed description of spermatid abnormalities in *Actl7b-/-* mice, we used transmission electron micrographs of spermatids in testis to determine exactly the step of spermiogenesis after which spermatid deformities can be detected. Until step 9, spermiogenesis appears normal in *Actl7b-/-* mice (Figure 49). Proacrosomal vesicles were formed, fuse and later form an acrosomal cap. Manchette were formed and spermatids started to elongate.

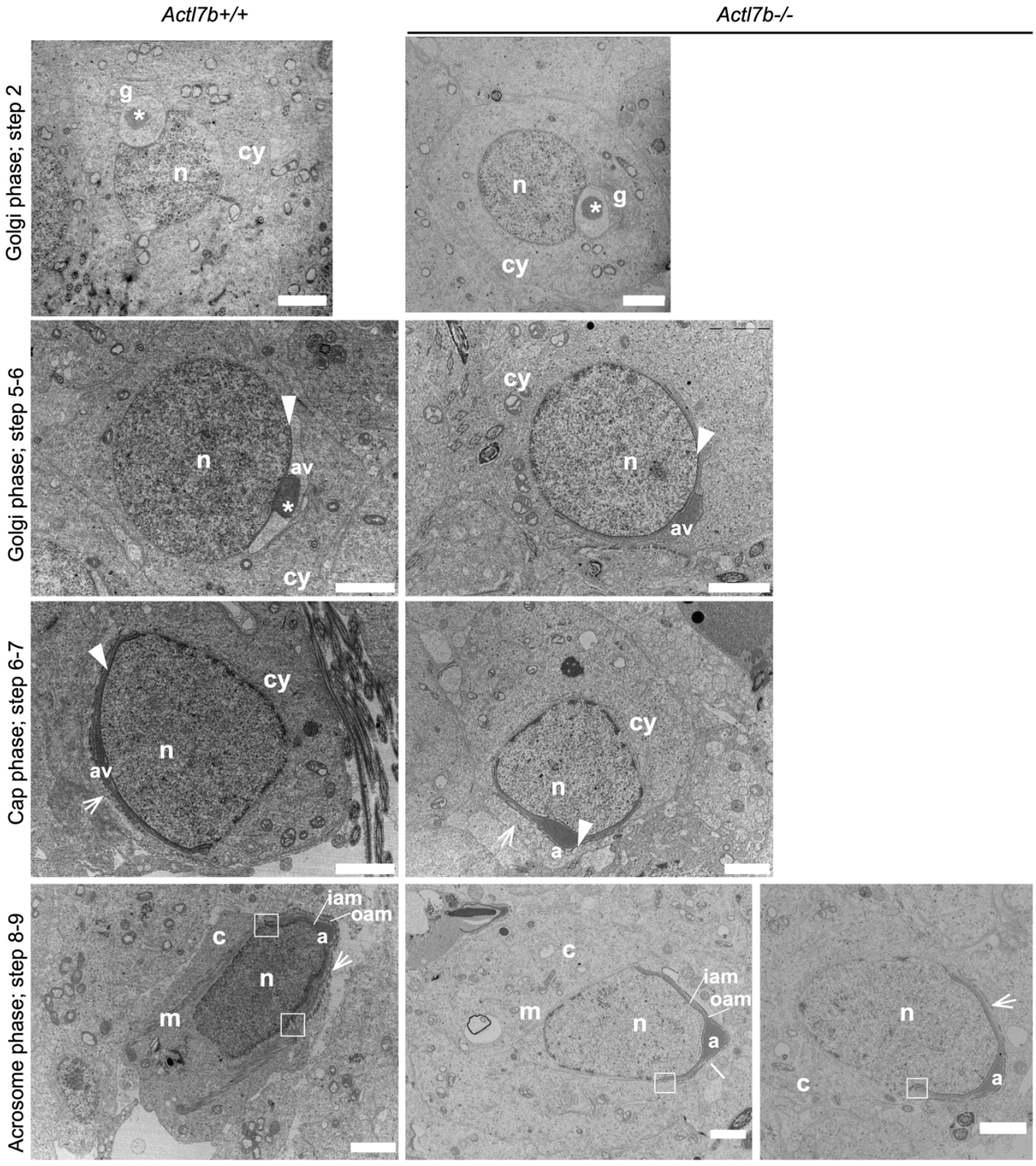


**Figure 49: Developmental steps 2-9 of spermiogenesis in *Actl7b+/+* and *Actl7b-/-* mice**. Representative transmission electron micrographs of spermatids. n: nucleus; cy: cytoplasm; boxes: marginal ring region; white *: acrosomal granule/acrosomal vesicle; av: acrosomal vacuole; a: acrosome; m: manchette microtubules; iam: inner acrosomal membrane; oam: outer acrosomal membrane; white arrow: ectoplasmic F-actin bundles. Scale: 2 µm. Modified from (Merges et al., 2022a).

After step 9 of spermiogenesis, sperm deformities became visible (Figure 50). Sperm nuclear head shapes appeared abnormal and nicked to one side. Nuclei were less electron dense suggestive partly degraded DNA in *Actl7b-/-* step 12 spermatids. Membranes and acrosomes became detached and flagella formation fails in part of *Actl7b-/-* sperm.

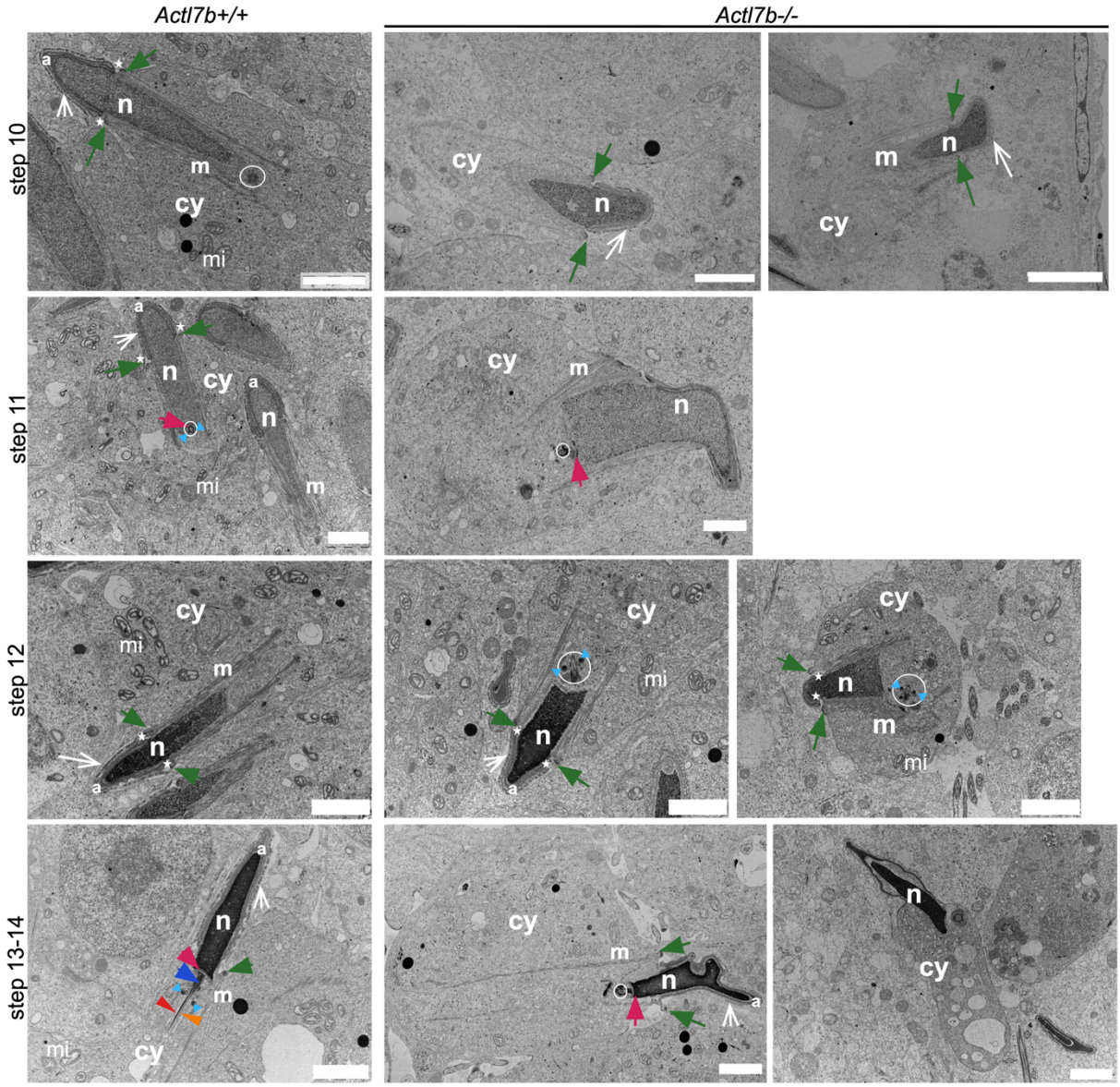


**Figure 50: Developmental steps 10-14 of spermiogenesis in *Actl7b+/+* and *Actl7b-/-* mice.** Representative transmission electron micrographs of spermatids. n: nucleus; cy: cytoplasm; boxes: marginal ring region; white *: acrosomal granule/acrosomal vesicle; a: acrosome; m: manchette microtubules; white arrow: ectoplasmic F-actin bundles; star: groove belt region; mi: mitochondria; encircled: proximal centriole; light blue arrow heads: annulus; green arrow: perinuclear ring; fuchsia arrow: basal plate; blue arrow: segmented column; red arrow head: axoneme; orange arrow heads: outer dense fibers. Scale: 2 µm. Modified from (Merges et al., 2022a).

Thereafter, sperm were isolated from cauda epididymides of *Actl7b-/-*, *Actl7b+/-* and *Actl7b+/+* mice. Of note, low sperm numbers hindered some staining procedures used on *Actl7b-/-* swim-out solutions. The percentage of viable sperm was comparable in *Actl7b+/-* and *Actl7b+/+* samples (Figure 51A). Further, staining with PNA and Mitored to visualize sperm acrosomes and mitochondria lining the flagellum revealed, that acrosomes and flagella are intact in

*Actl7b+/-* mice (Figure 51B-C). In contrast, acrosomes and flagella were disorganized in *Actl7b-/-* sperm. Most sperm stained positive for PNA and Mitored in the whole sperm head and tail region.

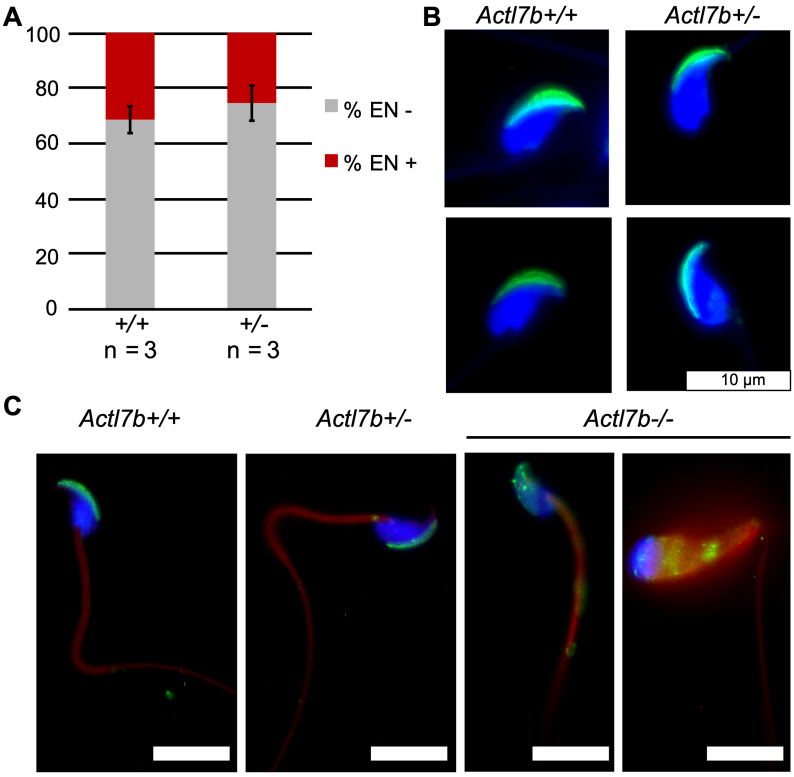


**Figure 51: Morphology of *Actl7b*-deficient epididymal sperm. (A)** Percentage of Eosin-Nigrosin positive/negative epididymal sperm from *Actl7b+/+* and *Actl7b+/-* mice. **(B)** Representative images of *Actl7b+/-* and *Actl7b+/+* sperm isolated from cauda epididymis and stained with PNA and DAPI. **(C)** Representative images of *Actl7b+/+, Actl7b+/-* and *Actl7b-/-* sperm isolated from cauda epididymis and stained with PNA, Mitotracker and DAPI. Parts modified from (Merges et al., 2022a).

### 4.5.2. Proteomic changes in *Actl7b*-deficient testes

In order to get further insight in the molecular basis of the defects detected in *Actl7b-/-* mice, analysis of the testicular proteome was performed. Protein samples obtained from complete testes of five *Actl7b-/-*, *Actl7b+/-*, *and Aclt7b+/+* mice were utilized for mass spectrometric analysis. *Actl7b-/-* samples clustered apart from *Actl7b+/-* and *Actl7b+/+* samples as shown by principle component analysis (Figure 52A). Differential abundance (DA) analysis indicated no significant variation in protein abundances identified in *Actl7b+/+* and *Actl7b+/-* samples (Figure 52B, Figure 53A). In *Actl7b-/-* compared to *Actl7b+/+* and *Actl7b+/-* samples, however, DA proteins were identified. More proteins were found to be higher abundant in *Actl7b-/-* vs. *Actl7b+/+* and *Actl7b+/-* testes. DA proteins were analyzed utilizing a strict log fold change (LFC) of ≥1 to look into specific proteins and a less stringent LFC of ≥0.5 to examine enrichment of biological processes.

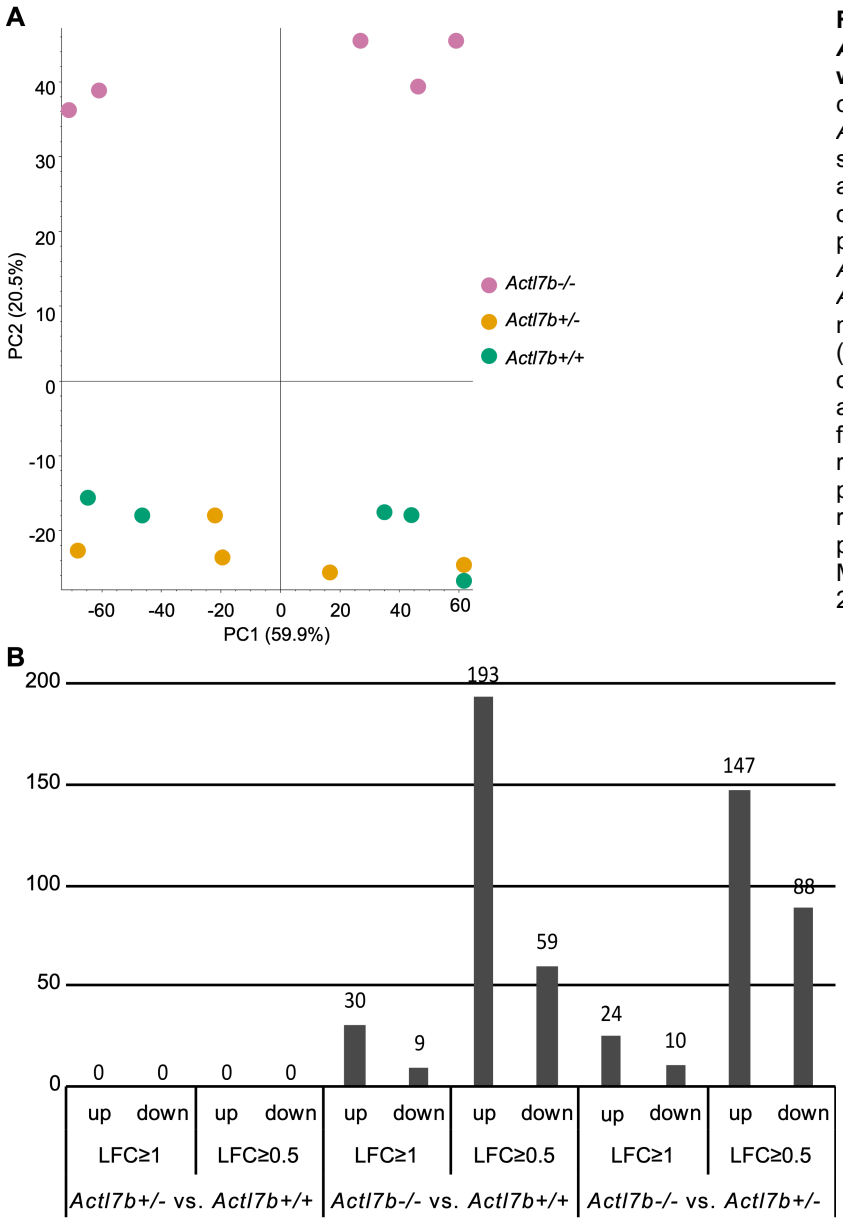


**Figure 52: Proteomic analysis of *Actl7b-/-*, *Actl7b+/-* and *Actl7b+/+* whole testis. (A)** Principal component analysis (PCA) of *Actl7b+/+*, *Actl7b+/-* and *Actl7b-/-* samples used for proteomic analysis (n = 5). **(B)** Number of differentially abundant (DA) proteins in *Actl7b+/-* vs. *Actl7b+/+*, *Actl7b-/-* vs. *Actl7b+/+* and *Actl7b-/-* vs. *Actl7b+/-* testis. The number of higher (up) and lower (down) abundant proteins are depicted. Results are given with an adjusted p-value ≤ 0.05 and a log2-fold change (LFC) of ≥ 1 and ≥ 0.05, respectively. The number of DA proteins are given above the respective bars. Analysis was performed by Dr. Lena Arévalo. Modified from (Merges et al., 2022a).

DA analysis applying a LCF of ≥1 revealed that 30 proteins were higher abundant in *Aclt7b-/-* vs. *Actl7b+/+* samples and 24 proteins were higher abundant in *Aclt7b-/-* vs. *Actl7b+/-* samples (Figure 53B-D). 19 of these proteins were identified in both comparisons (Figure 53D). On the other hand, 9 and 10 proteins were identified to be lower abundant in *Actl7b-/-* compared to *Actl7b+/+* and *Actl7b+/-* samples, respectively. The majority (8 proteins) was shown to be lower abundant in both comparisons (Figure 53E).

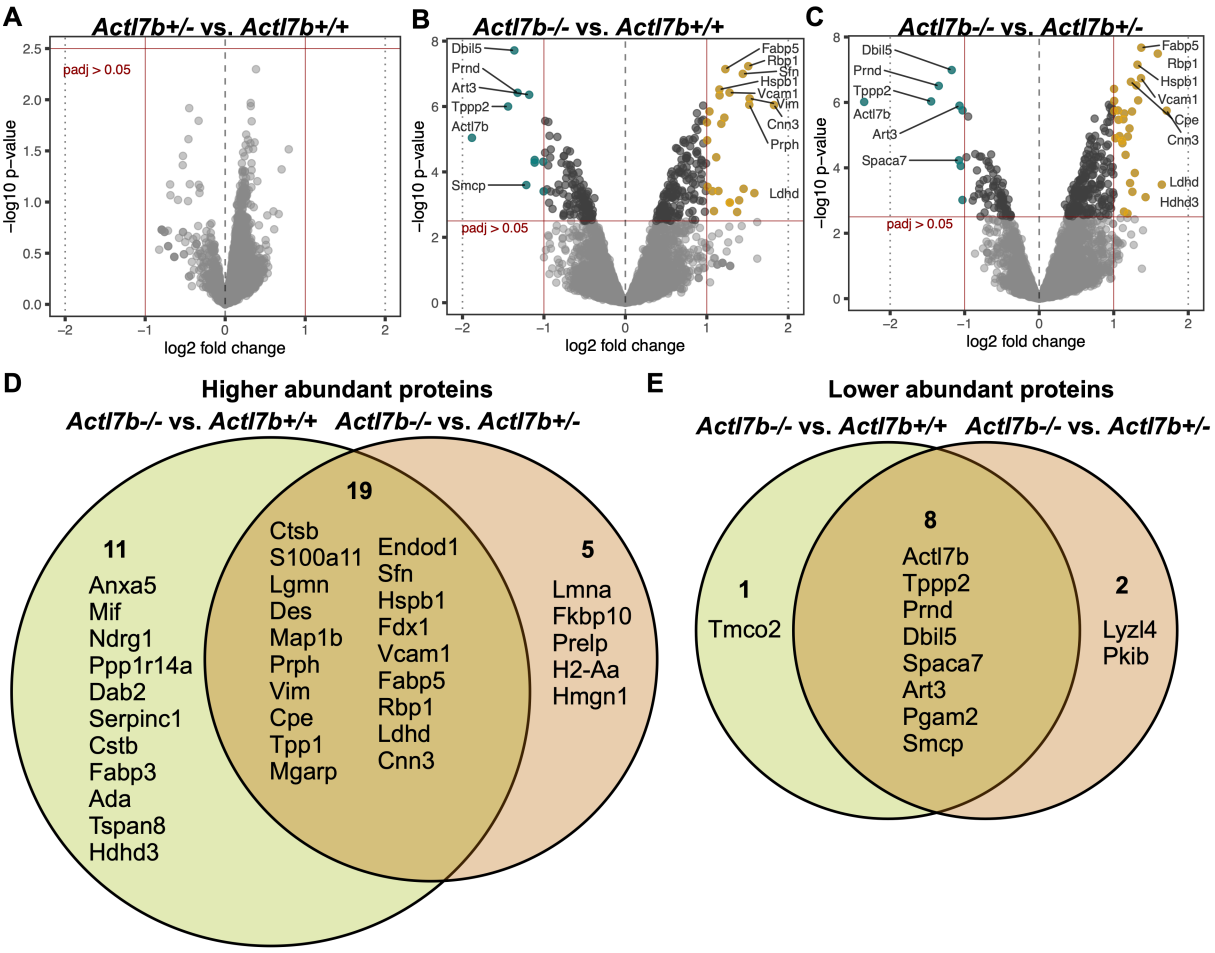


**Figure 53: Differentially abundant (DA) proteins in *Actl7b*-deficient testis. (A-C)** Volcano plots depicting DA proteins in *Actl7b+/-* vs. *Actl7b+/+, Actl7b+/-* vs. *Actl7b+/+* and *Actl7b+/-* vs. *Actl7b+/+* testis samples. Significantly lower abundant proteins are labeled in teal, significantly higher abundant proteins are labeled in yellow (adjusted p-value > 0.05). Top DA proteins are indicated with their corresponding gene symbol. **(D-E)** Venn diagrams showing the overlap of significantly higher and lower abundant proteins in the comparisons of *Actl7b-/-* vs. *Actl7b+/+* and *Actl7b-/-* vs. *Actl7b+/-* testis samples (adjusted p-value ≤ 0.05, LFC ≤ 1). Proteins are labeled with their gene symbol. Analysis was performed by Dr. Lena Arévalo. Modified from (Merges et al., 2022a).

Spermatocyte and spermatid related proteins were found to be lower abundant in *Actl7b-/-* compared to *Actl7b+/+* and *Actl7b+/-* samples (ACTL7B, ART3, SPACA7, SMCP, TPPP2, TMCO2, PGAM2, LYZL4, PRND, PKIB). As expected, ACTL7B was identified as one of them. Another example, is the prion-like protein doppel (PRND), which is expressed in both Sertoli cells and spermatids during the last stages of spermiogenesis (Allais-Bonnet and Pailhoux, 2014). Male PRND KO mice have been shown to be infertile (Behrens et al., 2002, Paisley et al., 2004). Staining of PNRD on *Actl7b-/-* testis sections showed lack of PRND in whole areas of the seminiferous epithelium (Figure 54).

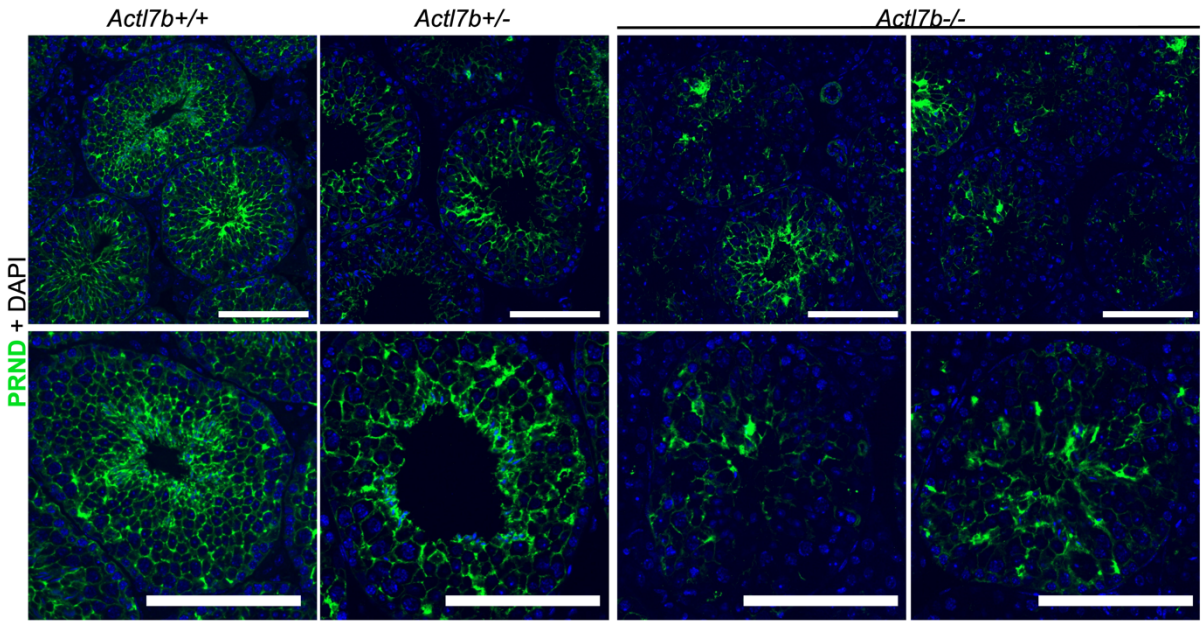


**Figure 54: IHC staining against PRND on *Actl7b*-deficient testis sections.** Representative images of IHC staining against PRND on *Actl7b+/+, Actl7b+/-* and *Actl7b-/-* testis sections (counterstain: DAPI). Scale: 100 µm. Confocal microscopy was performed together with Anđela Kovacevic.

Among the higher abundant proteins, several were found to be involved in protein or nucleic acid degradation as well as early apoptosis (ANXA5, CTSB, LGMN, TPP1, ENDOD1) (Figure 53D). Of note, CTSB, which was already shown to be higher abundant in western blot (Figure 42C), was also detected with mass spectrometric analysis. Furthermore, VCAM-1, which has been postulated to operate as an adhesion protein in testicular immunoregulation, was found to be higher abundant in *Actl7b-/-* testis (Sainio-Pollanen et al., 1997).

Additionally, type III intermediate filament proteins vimentin, desmin and peripherin (Mruk and Cheng, 2004, Vogl et al., 2008), as well as fatty acid-binding protein 5 (FABP5) and intracellular retinol-binding protein 1 (RBP1) (Oresti et al., 2013, Griswold, 2022), were found to be more abundant in *Actl7b-/-* testicular samples. The differential abundance of these proteins, which are predominantly found in Sertoli cells, could imply a secondary effect induced by stalled spermiogenesis and degrading/apoptotic germ cells.

Next, a less stringent LFC of ≥0.5 was applied to evaluate enrichment in biological processes in *Actl7b-/-* testes compared to *Actl7b+/+* samples (Table S2). 193 proteins were determined to be higher abundant in *Actl7b-/-* vs. *Actl7b+/+* testes. Proteins found in *Actl7b-/-* testes were found to be more frequently involved in protein degradation pathways, apoptosis, oxidative stress response, cell motility, and localization (Figure 55). Of note, the autophagy-related protein LC3B, which has been detected in western blot before (Figure 42C), was also identified to be higher abundant when applying a LFC of ≥0.5 (gene symbol: Map1lc3b; Table S2).

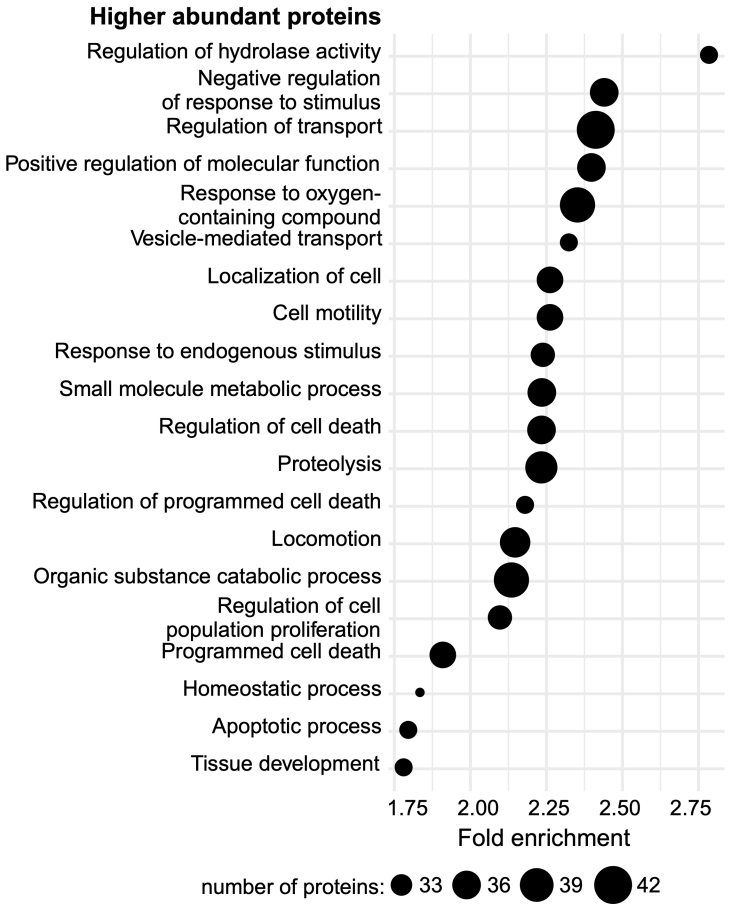


**Figure 55: Biological processes enriched in higher abundant proteins in *Actl7b*-deficient mice.** Dot plot showing the top twenty gene ontology (GO)- biological process terms significantly enriched in higher abundant proteins in *Actl7b-/-* vs. *Actl7b+/+* samples ($p \leq 0.05$, LFC ≤ 0.05). Dot sizes show the number of proteins contributing to the GO-term. Analysis and visualization were performed by Dr. Lena Arévalo. Modified from (Merges et al., 2022a).

Further, ezrin was higher abundant in *Actl7b-/-* samples. It affects Sertoli cell-spermatid adhesion, influences spermatid polarity, and is implicated in residual body/phagosome transit (Gungor-Ordueri et al., 2014). Additionally, ezrin has been demonstrated to interact with VCAM-1, which was also higher abundant in *Actl7b-/-* samples, *in vitro* (Barreiro et al., 2002). While ezrin was only found around the seminiferous tubules in *Actl7b +/-* and *Actl7b+/+* testis and below the detection level of IHC in the epithelial tissue, extensive concentrations of ezrin was found around germ cells and tissue vacuolations in *Actl7b-/-* sections (Figure 56). This suggests enhanced germ cell transport and clearance.

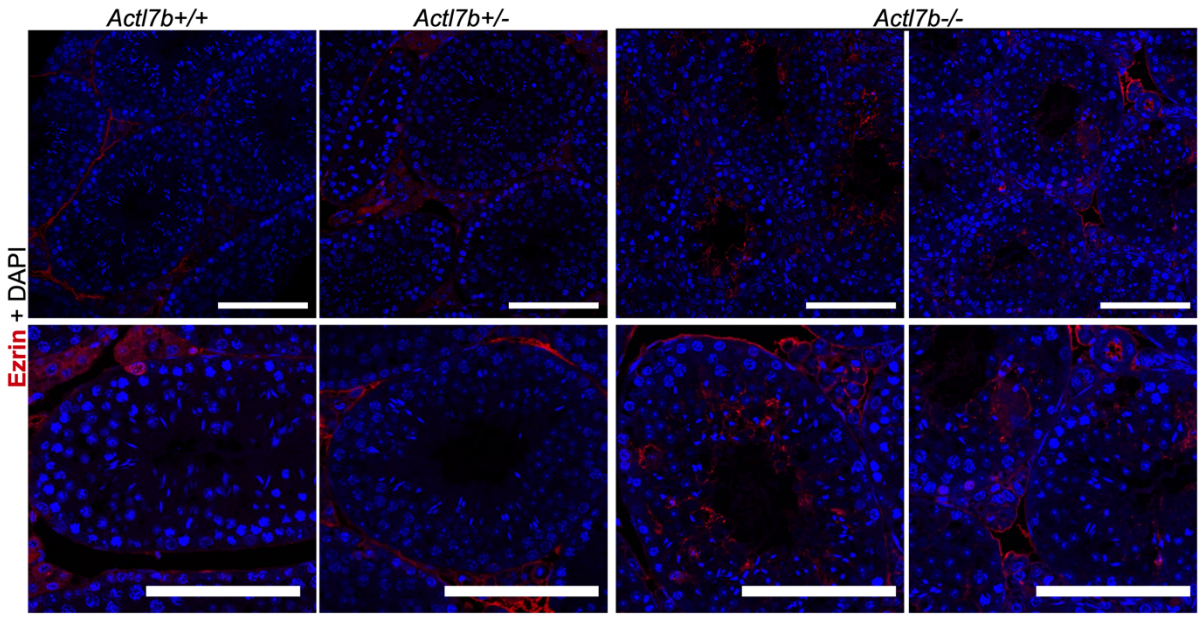


**Figure 56: IHC staining against Ezrin on *Actl7b*-deficient testis sections.** Representative images of IHC staining against Ezrin on *Actl7b+/+*, *Actl7b+/-* and *Actl7b-/-* testis sections (counterstain: DAPI). Scale: 100 µm. Confocal microscopy was performed together with Anđela Kovacevic.

Opposed to that, lower abundant proteins were enriched in gamete development, fertilization, reproduction, microtubule-based motility and cell recognition (Figure 57).

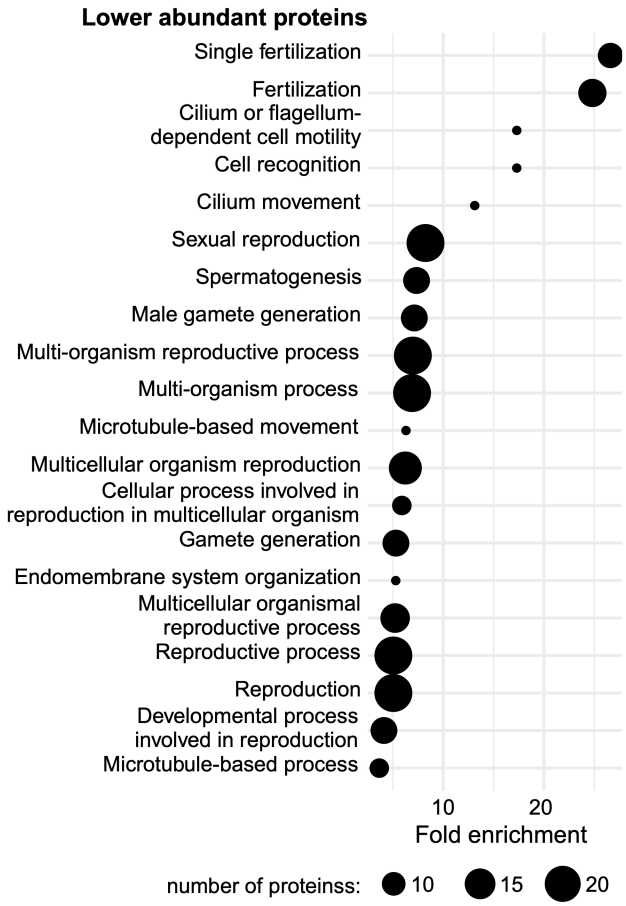


**Figure 57: Biological processes enriched in lower abundant proteins in *Actl7b*-deficient mice.** Dot plot showing the top twenty gene ontology (GO)- biological process terms significantly enriched in lower abundant proteins in *Actl7b-/-* vs. *Actl7b+/+* samples ($p \leq 0.05$, $LFC \leq 0.05$). Dot sizes show the number of proteins contributing to the GO-term. Analysis and visualization were performed by Dr. Lena Arévalo. Modified from (Merges et al., 2022a)

### 4.5.3. ACTL7B protein interactions

Analysis of spermatogenesis and DA proteins in *Actl7b*-deficient mice allowed us to describe the consequences of lack of ACTL7B in detail. However, the primary effect of ACTL7B-deficiency on molecular level remained elusive.

To find ACTL7B protein interaction partners, we applied co-immunoprecipitation (Co-IP) after using anti-ACTL7B antibody coupled Dynabeads on protein extract from whole WT testis. Of note, the experiment was performed once on one WT sample and needs to be repeated. Proteins in the eluate were identified with mass spectrometry and uncoupled beads were used as control. Peptides identified in the "beads only" control were excluded from further analyses. Additionally, contaminating peptides like keratins were filtered out and a published bead proteome from HeLa cells was utilized to exclude additional peptides, which non-specifically bind Dynabeads (Trinkle-Mulcahy et al., 2008). Among those have been various histone H2B variants. After filtering of the data and excluding ribonucleoproteins and ribosomal proteins from further analysis we identified LC8 dynein light chains DYNLL1 and DYNLL2 in similar abundance as ACTL7B.

Next, western blot against ACTL7B, DYNLL1 and DYNLL2 was performed on the protein input as well as in the non-bound fraction of both the IP using ACTL7B-coupled and uncoupled beads (Figure 58A). DYNLL1 and DYNLL2 present as bands of around 12 kDa in the input. For DYNLL2 weaker bands of larger size are visible as well, indicating that DYNLL2 forms complexes with other proteins. ACTL7B presents as a band of approximately 49 kDa in the input.

None of the proteins was detected in the IP of the "beads-only" control. In the IP using ACTL7B-coupled beads, bands of approximately 60 kDa were identified with all three antibodies. Weak bands of similar size were already detected in the input utilizing the anti-DYNLL2 antibody. For now, these results are inconclusive, since denaturing SDS PAGE should separate potential ACTL7B-DYNLL1/2 protein complexes.

To further investigate ACTL7B-DYNLL binding, anti-DYNLL1 and anti-DYNLL2 were coupled to Dynabeads. Co-IP on whole testis protein eluate was performed and western blots were used to identify proteins. Of note, no DYNLL1 was detected in the eluate (not shown), so we concluded that the anti-DYNLL1 antibody was not suitable for coupling and/or Co-IP. In the IP using DYNLL2-coupled beads, ACTL7B was identified as a weak band of around 60 kDa in size (Figure 58B). DYNLL2 was detected as a band of 12 kDa in the IP eluate. These first results suggest that ACTL7B might interact with the dynein cytoskeletal network. Noteworthy, again a band with a size of 60 kDa was detected. Despite the fact, that this is a denaturing PAGE, it lets to the speculation, that the proteins form complexes which might not be resolved by the conditions.

Next, HEK cells stably expressing ACTL7B fused to eGFP (HEK$^{Actl7b\text{-}eGFP}$) were used to identify ACTL7B interaction partners *in vitro*. GFP nanobody-coupled beads were used followed by western blots. WT HEK cells served as control. As expected, ACTL7B was identified in the HEK$^{Actl7b\text{-}eGFP}$ protein input, but not the WT control (Figure 58C). DYNLL2 again presented as multiple bands in both protein inputs, indicating DYNLL2 to be present alone but also as part of protein complexes. Using anti-ACTL7B and anti-DYNLL2 on the IP from the HEK$^{Actl7b\text{-}eGFP}$ cells, identified bands of approximately 60 kDa. No bands were detected in the IP of the WT HEK cells. Again, native DYNLL2 has not been detected after denaturing SDS PAGE. Hence, the experiments need to be repeated. Noteworthy, it needs to be considered that mass spectrometry is more sensitive compared to WB.

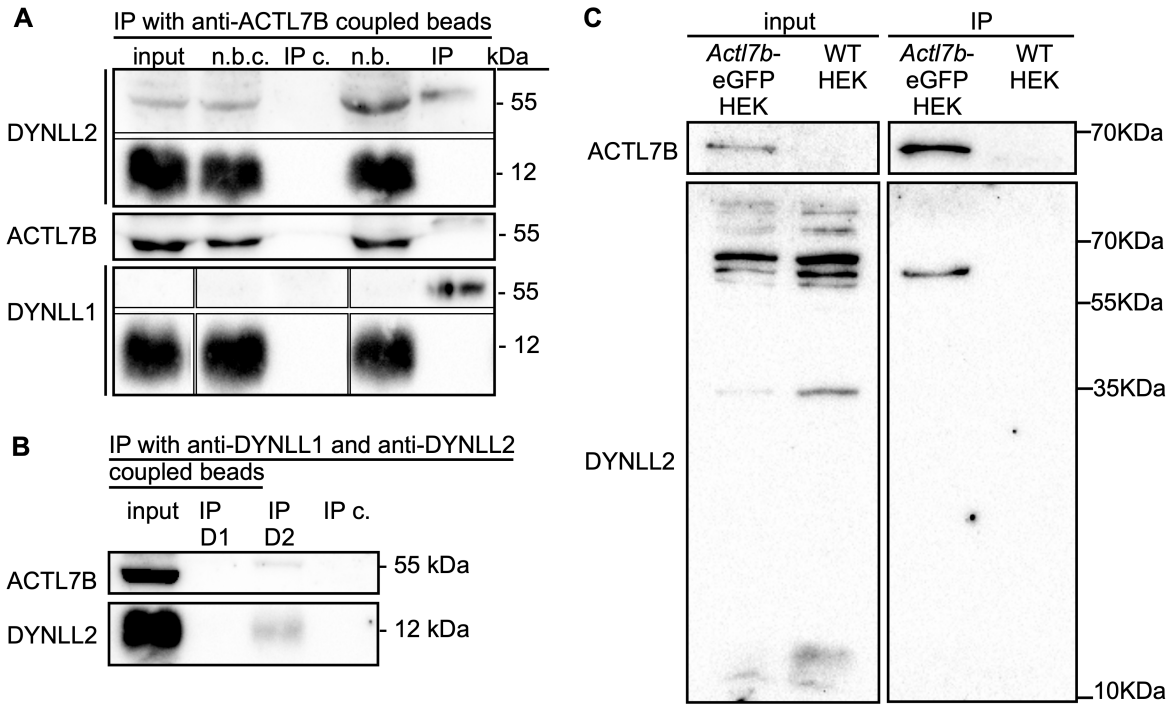


**Figure 58: ACTL7B protein interaction with DYNLL1 and DYNLL2. (A)** Western blots on the protein input (whole WT testis), the non-bound fraction of the beads only control (n.b. c.), the IP eluate of the beads only control (IP c.), non-bound fraction of the anti-ACTL7B-coupled beads (n.b.), the IP eluate of the anti-ACTL7B-coupled beads (IP). Anti-DYNLL2, anti-DYNLL1 and anti-ACTL7B were used. **(B)** Western blots on the protein input (whole WT testis), the IP eluate of the anti-DYNLL1-coupled beads (IP D1), the IP eluate of the anti-DYNLL2-coupled beads (IP D2), the IP eluate of the beads only control (IP c.). Anti-ACTL7B and anti-DYNLL2 were used for western blots. **(C)** Western blots on the protein input (HEK cell protein extraction) and the IP eluate using GFP-trap beads. Anti-DYNLL2 and anti-ACTL7B were used. HEK cell experiments were performed by Dr. Lena Arévalo. Stable cell lines were generated by Carla Simon, with aid from Pietro Pilo Boyl. Parts modified from (Merges et al., 2022a).

Western blots on proteins isolated from whole testis, again showed that ACTL7B amounts are reduced in *Actl7b+/-* testis (Figure 59). No ACTL7B was detected in *Actl7b-/-* testis. DYNLL1 and DYNLL2 protein amounts were similar in *Actl7b+/+, Actl7b+/-* and *Actl7b-/-* testis.

The abundance of ACTL7A was determined using western blot to assess potential compensation of ACTL7B by ACTL7A. ACTL7A levels were lower in *Actl7b-/-* testes compared to *Actl7b+/-* and *Actl7b+/+* testes, indicating that ACTL7A has no compensatory function. Furthermore, *Actl7b-/-* testis had lower levels of HOOK1, a protein produced late in spermiogenesis.

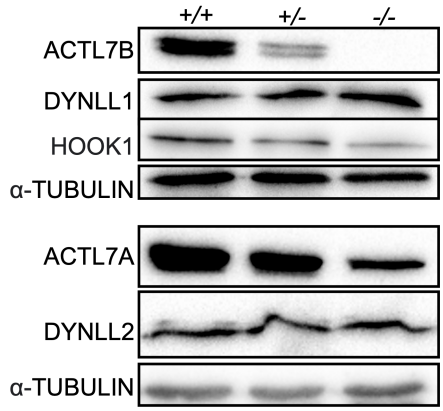


**Figure 59: Quantification of DYNLL1 and DYNLL2 in *Actl7b*-deficient testis.** Western blots on whole testis protein extracts. Anti-ACTL7B, anti-DYNLL1, anti-HOOK1, anti-ACTL7A and anti-DYNLL2 were used. Anti-α-tubulin was used as loading control. Modified from (Merges et al., 2022a).

We hypothesize that *Actl7b-/-* animals have fewer spermatids reaching later stages of spermiogenesis, resulting in lower relative protein levels.

Since, DYNLL1 and DYNLL2 protein amounts were unaltered in *Actl7b-/-* testis, DYNLL1 and DYNLL2 localization was analyzed. DYNLL1 is described to be localized first to the nucleus of elongating spermatids and later in the cytoplasm and residual bodies of elongated spermatids (Figure 60A) (Wang et al., 2005). Noteworthy, expression of DYNLL1 correlates to the onset of defects seen in *Act7b-/-* spermatids described here. IF staining of DYNLL1 and DYNLL2 followed by confocal microscopy revealed that both proteins show the same localization in WT and *Actl7b+/-* testis (Figure 60B-C, Figure S7, Figure S8). In *Actl7b-/-* testis, however, DYNLL1 and DYNLL2 are mislocalized starting from stage I-III of the seminiferous cycle. While DYNLL1 and DYNLL2 are homogenously present in the cytoplasm of *Actl7b+/+* and *Actl7b+/-* elongating spermatids, it is heterogeneously localized in *Actl7b-/-* spermatids. The cytoplasm of *Actl7b-/-* spermatids seem to arrange in roundish sacs, rather than in the stream-like fashion towards the tubule lumen. Additionally, vacuolations in the staining as well as intense foci of DYNLL1 and DYNLL2 accumulations can be seen in *Actl7b-/-* spermatids. This suggests that the localization and the distribution of DYNLL1 and DYNLL2 changes, when ACTL7B is absent.

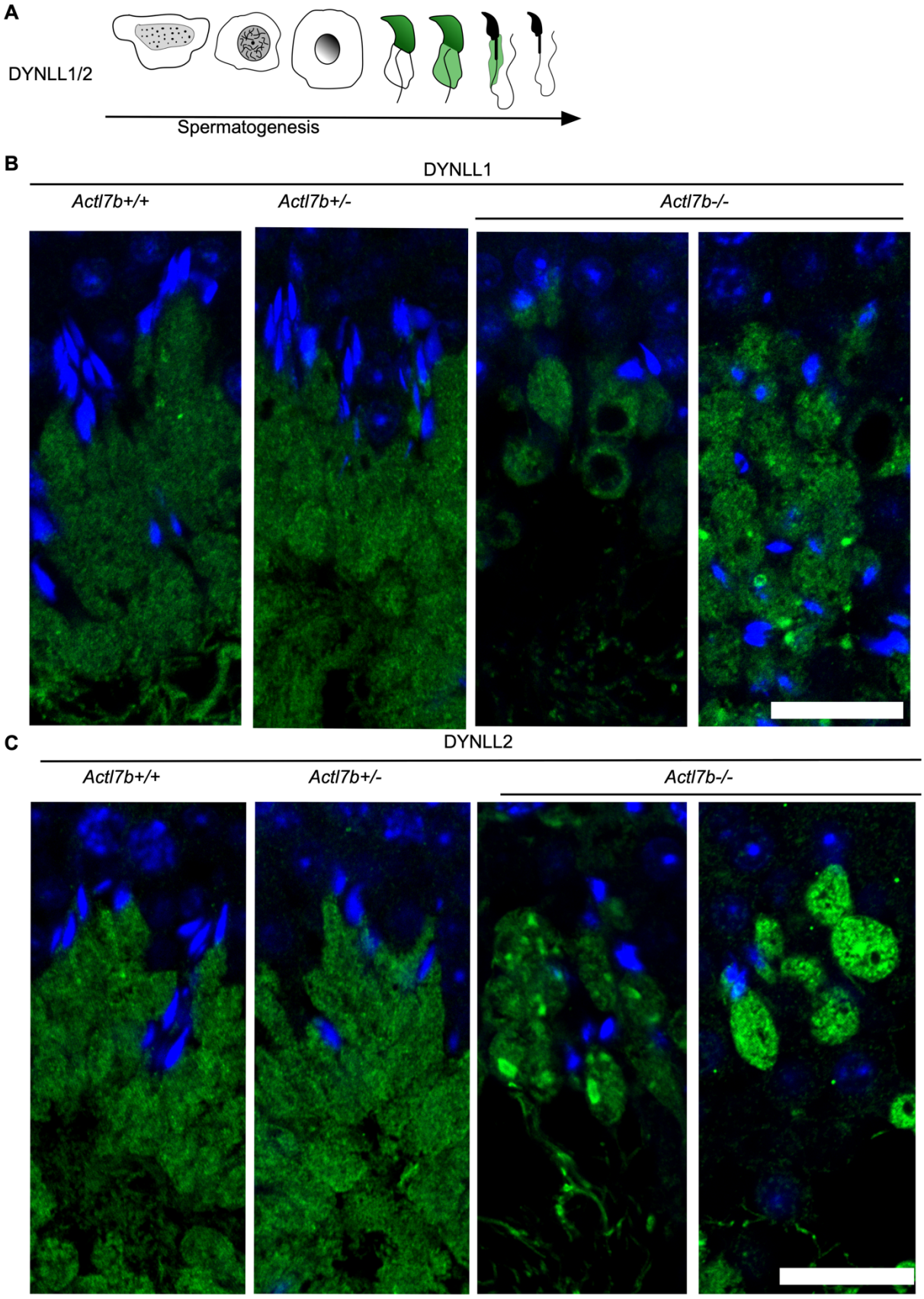


**Figure 60: Mislocalization of DYNLL1 and DYNLL2 in *Actl7b*-deficient spermatids. (A)** Graphical representation of DYNLL1 and DYNLL2 immunolocalization during spermiogenesis based on literature (Wang et al., 2005) and IHC stainings. **(B-C)** IHC stainings against DYNLL1 and DYNLL2 on *Actl7b+/+, Actl7b+/-* and *Actl7-/-* testis sections (counterstain: DAPI). Of note, images are cut-outs from overviews shown in Figures S7 and S8. Scale: 20 µm. Confocal microscopy was performed together with Keerthika Lohanadan. Modified from (Merges et al., 2022a).

IC staining of DYNLL1 and DYNLL2 in HEK$^{Actl7b\text{-}eGFP}$ cells, showed that DYNLL1 and DYNLL2 are differentially localized compared WT HEK cells (Figure 61). Whereas, DYNLL1 and DYNLL2 are localized mainly to the nuclei of WT HEK cells and only weakly in the cytoplasm, both proteins are localized in a fibrous fashion throughout the whole cytoplasm when ACTL7B is present. ACTL7B localizes mainly to the cytoplasm.

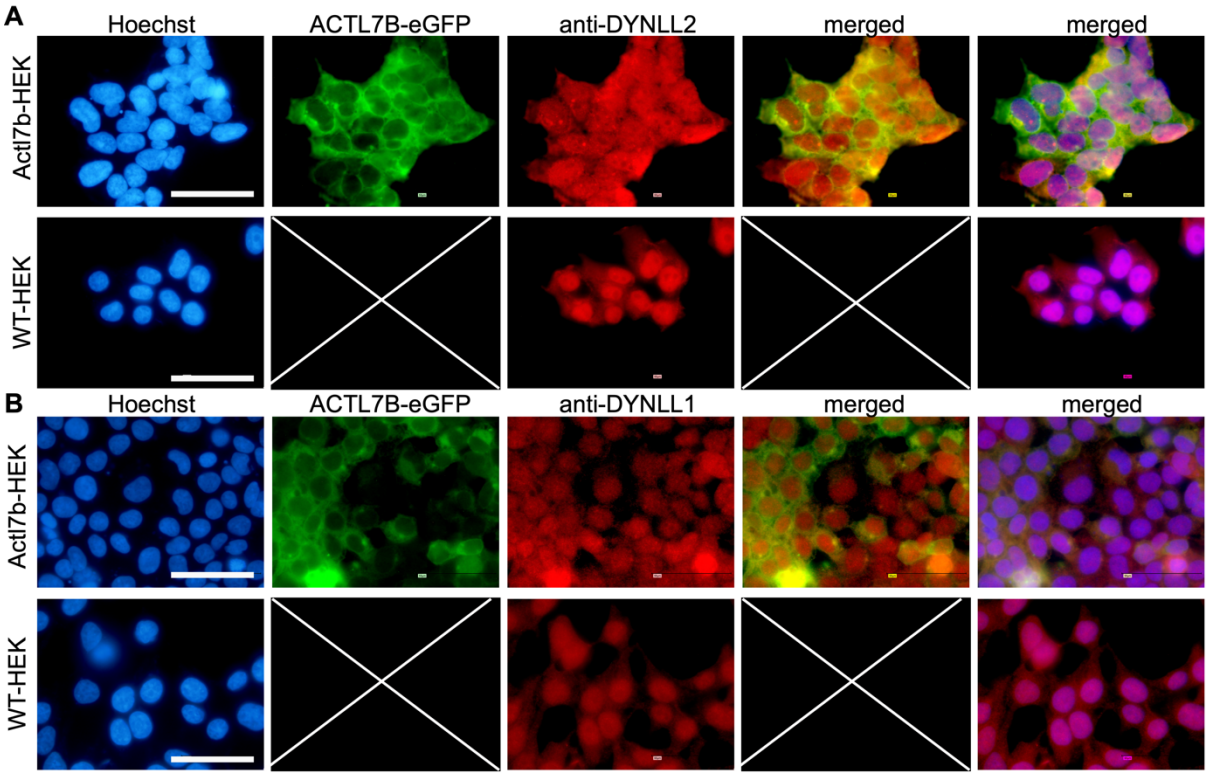


**Figure 61: ACTL7B and DYNLL1 and DYNLL2 *in vitro*. (A)** Representative images of IC staining against DYNLL2 in a ACTL7B-eGFP expressing HEK cell line and WT HEK cells (counterstain: Hoechst). **(B)** Representative images of IC staining against DYNLL1 in a ACTL7B-eGFP expressing HEK cell line and WT HEK cells (counterstain: Hoechst). Scale: 50 µm. HEK cell experiments were performed by Dr. Lena Arévalo. Stable cell lines were generated by Carla Simon, with aid from Pietro Pilo Boyl.

Next, HEK$^{Actl7b\text{-}eGFP}$ and WT HEK cells were transfected with expression plasmids containing murine DYNLL1 and DYNLL2 coupled to mCherry. Similar changes in DYNLL1 and DYNLL2 localization were detected (Figure 62). Taken together these results suggest that LC8 dynein light chain localization is altered in the absence of ACTL7B, while DYNLL1 and DYNLL2 protein amounts are unchanged.

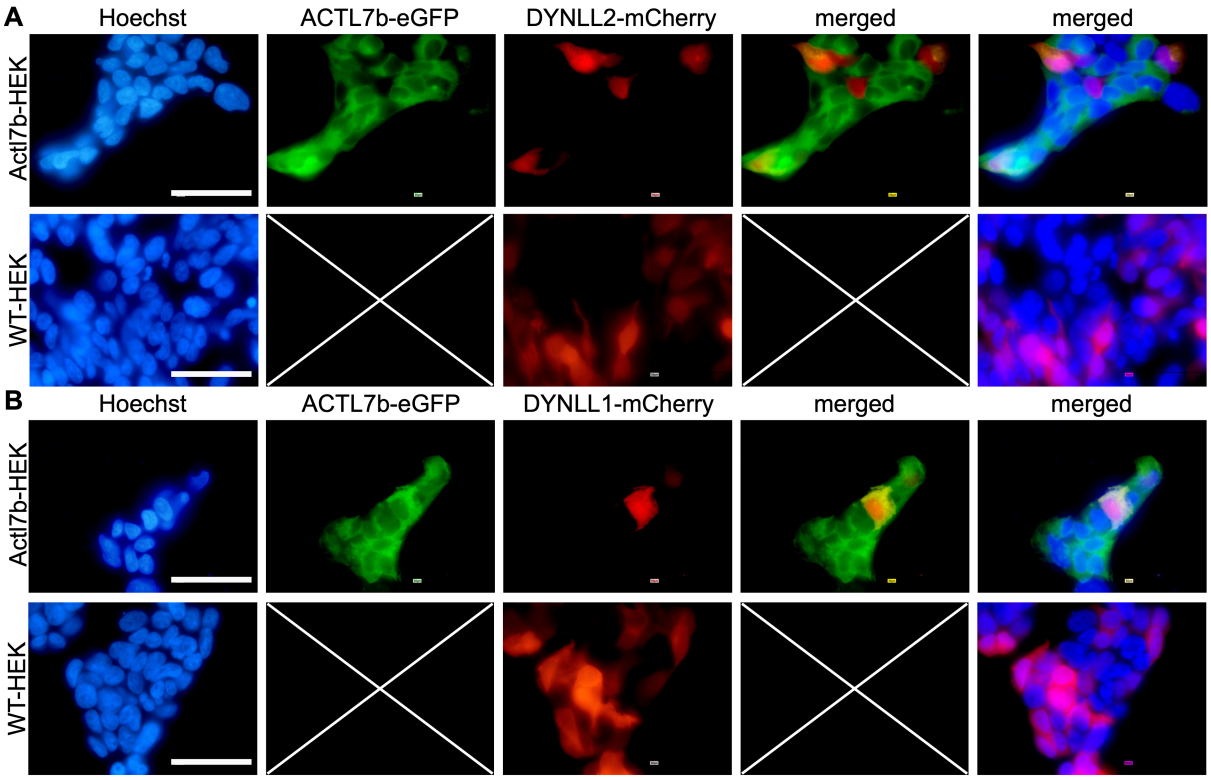


**Figure 62: ACTL7B and murine DYNLL1 and DYNLL2 *in vitro*. (A)** Representative images of mCherry-tagged DYNLL2 in an ACTL7B-eGFP expressing HEK cell line and WT HEK cells (counterstain: Hoechst). **(B)** Representative images of mCherry-tagged DYNLL1 in an ACTL7B-eGFP expressing HEK cell line and WT HEK cells (counterstain: Hoechst). Scale: 50 µm. HEK cell experiments were performed by Dr. Lena Arévalo. Stable cell lines were generated by Carla Simon, with aid from Pietro Pilo Boyl.

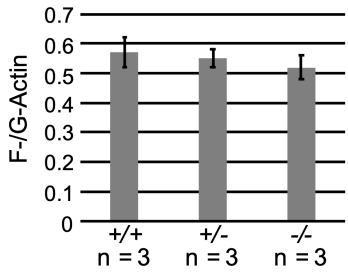


**Figure 63: F-/G-Actin ratio in *Actl7b*-deficient testis.** F-/G-Actin ratio in *Actl7b+/+, Actl7b+/-* and *Actl7b-/-* testes based on western blots. Data are mean ± s.d. and were analyzed using a two-tailed, unpaired Student's t-test. Analysis was performed by Melanie Jokwitz. Modified from (Merges et al., 2022a).

Lastly, even though Co-IP did not reveal ACTL7B-Actin protein interactions, we decided to evaluate actin turnover and localization in *Actl7b*-deficient mice. The F- to G-Actin ratio, which gives indirect information on actin-based cytoskeletal organization and actin filament turnover, was not significantly different in *Actl7b-/-* testes compared to *Actl7b+/-* and *Actl7b+/+* testes, indicating no disturbances in actin filament turnover when ACTL7B is lacking (Figure 63).

IF staining, however, showed that actin filament arrangement is disorganized in part of *Actl7b*-deficient testis (Figure 64). Lack of ACTL7B seems to disturb cytoskeletal organization. While the studies clearly suggest, that ACTL7B is essential for proper spermiogenesis, further studies are required to decipher the molecular interactions of ACTL7B.

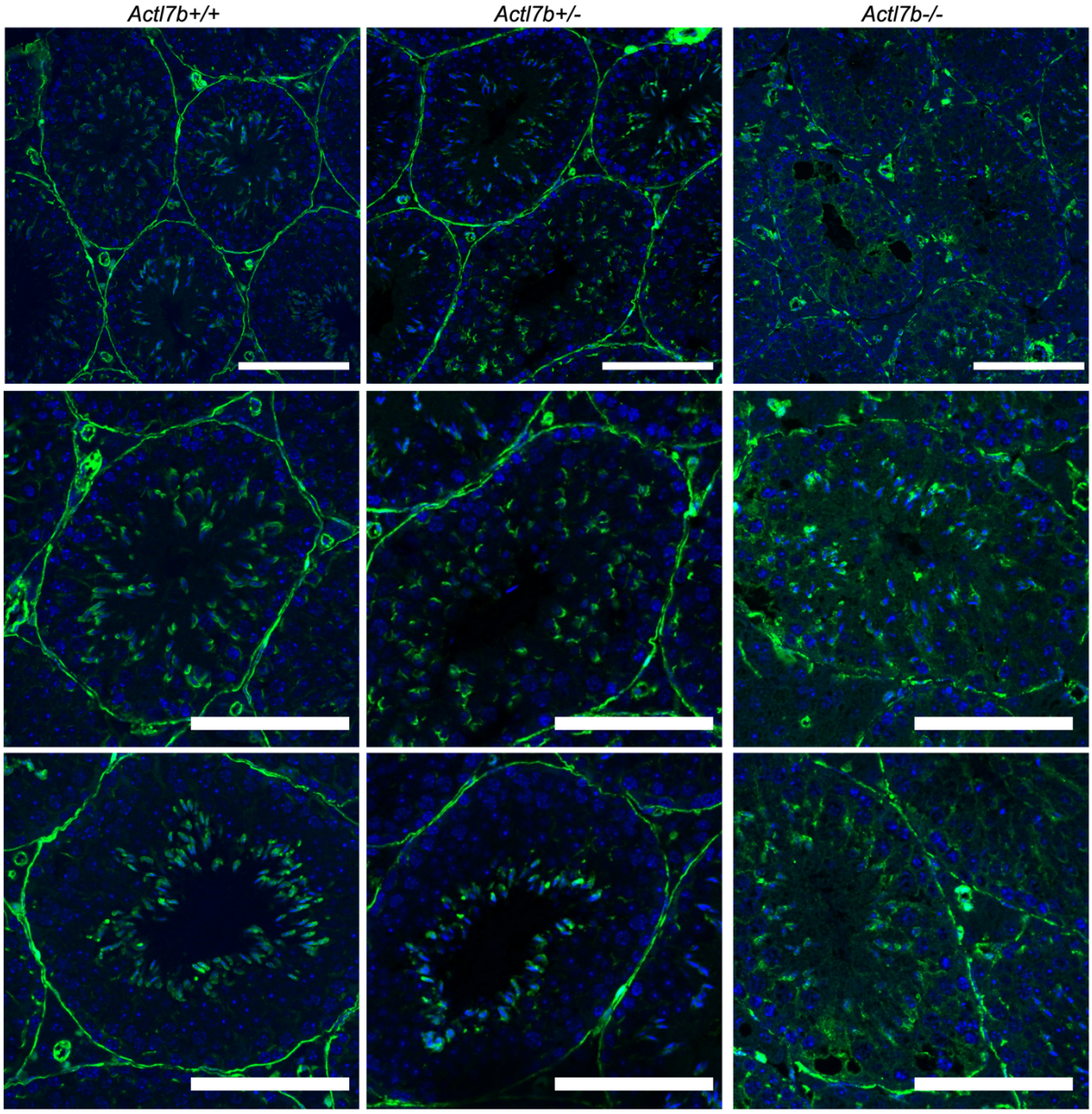


**Figure 64: Localization of filamentous actin in *Actl7b*-deficient seminiferous tubules.** IHC staining against F-actin on testis sections from *Actl7b+/+, Actl7b+/-* and *Actl7b-/-* mice (counterstain: DAPI). Scale: 100 µm. Confocal microscopy was performed together with Anđela Kovacevic.

Part of these data were published in:

Gina Esther Merges, Lena Arévalo, Keerthika Lohanadan, Dirk G. de Rooij, Melanie Jokwitz, Walter Witke, Hubert Schorle (2022) *Actl7b*-deficiency leads to mislocalization of LC8 type dynein light chains and disruption of murine spermatogenesis. *BioRxiv.* DOI: 10.1101/2022.12.19.520998 (currently in revision with Development)

# 5. Discussion

**Parts of the discussion sections have been discussed and published in:**

Gina Esther Merges, Julia Meier, Simon Schneider, Alexander Kruse, Andreas Christian Fröbius, Klaus Steger, Lena Arévalo, Hubert Schorle (2022) Loss of *Prm1* leads to defective chromatin protamination, impaired PRM2 processing, reduced sperm motility and subfertility in male mice. *Development.* DOI: 10.1242/dev.200330

Gina Esther Merges, Lena Arévalo, Keerthika Lohanadan, Dirk G. de Rooij, Melanie Jokwitz, Walter Witke, Hubert Schorle (2022) *Actl7b*-deficiency leads to mislocalization of LC8 type dynein light chains and disruption of murine spermatogenesis. *BioRxiv.* DOI: 10.1101/2022.12.19.520998 (currently in revision with Development)

In this study the roles of different genes, important in spermatogenesis, have been analyzed based on gene-edited mouse models. Mice are still the model of choice, since cell culture or organoid based models for investigating sperm development are still scarce and inefficient. Additionally, the examination of tissue or cell-type specific expressed genes eases the generation of knockout models. Although differences between human and mouse spermatogenesis exist, mouse models have been invaluable for studying sperm formation and spermatogenic defects. Here, the roles of protamines have been studied based on a *Prm1*-deficient mouse model, which has been compared to a *Prm2*-defcient mouse model. Additionally, the examination of a *Prm1-Prm2* fusion model gave new insights into the role of the protamine ratio, protamine-protamine interactions and the PRM2 protein domains and gave rise to new hypotheses currently under investigation. Lastly, the analysis of an *Actl7b*-deficient model helped to understand essential role of ACTL7B in spermiogenesis and provided information on its interaction partners.

## 5.1. Protamine-deficient and protamine mutated mice

The analysis of *Prm1*-deficient mice revealed, that *Prm1+/-* mice were subfertile, while *Prm1-/-* mice were infertile. *Prm1-/-* epididymal sperm were inviable and showed fragmentation of DNA, severe membrane and flagella damage, high levels of 8-OHdG and immotility. *Prm1+/-* sperm, on the other hand, only showed moderate levels of DNA damage and low levels of 8-OHdG. Sperm motility was severely reduced. Moreover, analysis of nuclear proteins revealed that both *Prm1-/-* and *Prm1+/-* sperm contain high levels of unprocessed PRM2 and

that the protamine ratio is shifted in *Prm1+/-* sperm. The analysis of mice carrying a *Prm1-Prm2* fusion showed, that both $Prm^{+/mut}$ and $Prm^{mut/mut}$ mice are subfertile, suggesting that the PRM1-PRM2 fusion protein is able to condense and protect the paternal chromatin. Noteworthy, the fusion protein still contains one cleavage site of cP2, but is not cleaved. $Prm^{mut/mut}$ sperm showed reduced DNA condensation levels, whereas $Prm^{+/mut}$ sperm DNA was condensed comparable to WT. Interestingly, data suggests that the PRM1-PRM2 fusion protein can effectively aid histone eviction, whereas $Prm^{+/mut}$ sperm show high levels of incompletely processed PRM2 and retained histone H3.

The role of protamines have been extensively studied based on mutant mouse models examining protamine-deficiency and protamine modifications (Cho et al., 2003, Cho et al., 2001, Takeda et al., 2016, Mashiko et al., 2013, Schneider et al., 2016, Schneider et al., 2020, Itoh et al., 2019, Arévalo et al., 2022a, Moritz et al., 2023). *Prm1*-deficiency has been associated with male factor infertility in studies by Cho *et al.*, Takeda *et al.* and Mashiko *et al.* (Cho et al., 2003, Cho et al., 2001, Takeda et al., 2016, Mashiko et al., 2013). *Prm1*-deficient chimeras and *Prm1+/-* males have been reported to be infertile in all previous studies, which prevented mouse line establishment and in-depth analysis of *Prm1*-deficiency. Contrary in the current study we reported *Prm1+/-* males to be subfertile. Takeda *et al.* applied embryonic stem cell (ESC)-targeting technology and established a *Prm1*-deficient mouse line (Takeda et al., 2016). We hypothesized, that eventually the expression of the G418 (neomycin) resistance cassette introduced by classical gene targeting could have silenced the neighboring *Prm2* as well as *Tnp2*. So, differences in the methodology, might have caused the differences in fertility of *Prm1+/-* mice. *Prm1*-deficient mice by Mashiko *et al.* were generated utilizing CRISPR/Cas9-mediated gene editing and backcrossed to C57BL/6J (Mashiko et al., 2013). Since the focus of the study was on techniques to generate gene-edited mice, rather than detailed phenotypical analysis of such, we hypothesized that they might not have performed a sufficiently exhaustive backcrossing and analysis to observe subfertility.

*Prm1-/-* mice were like *Prm2-/-* mice infertile, showing that loss of one protamine cannot be compensated by the other (Schneider et al., 2016). *Prm1-/-* mice showed severe DNA fragmentation, membrane and flagella damage as well as high levels of 8-OHdG. Similar pathomorphological effects have been described for *Prm2-/-* sperm (Schneider et al., 2016, Schneider et al., 2020). Schneider *et al.* showed that an oxidative stress-mediated destruction cascade is initiated during epididymal transit resulting in elevated ROS leading to widespread destruction of sperm. While it is well known that certain levels of ROS are required for sperm function, high levels of ROS cause sperm damage (de Lamirande et al., 1997). Spermatogenesis in *Prm2-/-* mice appeared overtly normal and sperm damage accumulated during sperm maturation in the epididymis. Likewise, spermatogenesis in *Prm1-/-* mice seemed overtly normal. Testicular sperm head shapes were unaltered and transmission

electron micrographs appeared inconspicuous. Epididymal sperm from *Prm1-/-* and *Prm2-/-* mice were DAPI weak, the DNA less condensed and sperm nuclei were smaller in size. We hypothesize that DNA fragmentation caused by ROS prevented proper staining. In *Prm1-/-* males, elevated levels of 8-OHdG positive sperm were already detected in the testis, even though testicular sperm appeared morphologically normal, was already seen in testicular sperm. For *Prm2-/-* sperm 8-OHdG is detected from caput epididymis on. Hence, loss of PRM1 leads to a more widespread disturbance of DNA protamination, which triggers the ROS-mediated destruction at an earlier time point.

Differential abundance analysis of basic sperm proteins showed that levels of proteins related to translation and apoptotic processes were elevated in *Prm1-/-* and *Prm2-/-* epididymal sperm. This matches the secondary effects described for both sperm populations. In contrast, only small differences were detected in *Prm1+/-* sperm, suggesting that changes in the basic sperm protein abundances are not contributing to the phenotype.

Histones were retained in *Prm1-/-* and *Prm2-/-* sperm as shown by mass spectrometry and IF staining, suggesting impairments in histone eviction. Additionally, increased levels of HSPA2 were found in *Prm1-/-* and *Prm2-/-* sperm. HSPA2 was proposed as TNP chaperone (Govin et al., 2006). This could be indicative of remaining HSAP2-TNP complexes and defects in TNP unloading. Indeed, slight TNP retention was detected in *Prm1-/-* sperm. Of note, protamines and transition proteins are, due to methodical limitations, not detected by the mass spectrometry analysis used. Also, $Prm^{+/mut}$ sperm show increased histone H3 retention. Interestingly, this is not the case for $Prm^{mut/mut}$ sperm. This suggests on one hand, that the fusion protein is able to effectively evict histones, but on the other hand interferes with histone eviction, when endogenous PRM1 and PRM2 are present. Hence, $PRM^{MUT}$ seems to interfere with PRM1-PRM2 dynamics and proper histone eviction. Alternatively, if histones bind to unprocessed PRM2 and are evicted together with it, high amounts of retained unprocessed PRM2 might correlate to levels of retained histones. However, no apparent increase in histones H3 and H4 were detected in $Prm2^{+/\Delta c}$ and $Prm2^{-/\Delta c}$ sperm (Arévalo et al., 2022a), which indicated that the cP2 domain is not necessary for histone eviction. This is supported by the fact that histone H3 levels were not elevated in $Prm^{mut/mut}$ sperm, which lack the cP2 domain. So, if histones bind unprocessed PRM2, it would be dependent on the full length pre-PRM2 being present and not the cP2 domain alone. TNP1, however, was retained in $Prm2^{+/\Delta c}$ and $Prm2^{-/\Delta c}$ sperm (Arévalo et al., 2022a), which implied that the cP2 domain plays a role in TNP eviction. If this holds true, elevated TNP levels are expected in $Prm^{mut/mut}$ sperm. The fact that the basic sperm protein content detected via mass spectrometry did not significantly differ between *Prm1+/-* and WT sperm and that *Prm1+/-* sperm nuclei appear electron dense in TEM, indicative of condensed chromatin, raised the question as to why *Prm1+/-* males are subfertile. Noteworthy, *Prm2+/-* males are fertile (Schneider et al., 2016),

which suggests that loss of one allele of *Prm2* can be tolerated, while loss of one allele of *Prm1* cannot.

One difference detected when comparing *Prm1+/-* and *Prm2+/-* sperm, was that *Prm1+/-* sperm show a slight increase in 8-OHdG positive sperm compared to WT, while *Prm2+/-* sperm did not (Schneider et al., 2020). Additionally, low levels of DNA fragmentation were detected in *Prm1+/-* sperm, while *Prm2+/-* sperm DNA was intact comparable to DNA isolated from WT sperm. This again suggests that loss of PRM1 triggers the ROS system than loss of PRM2. Slight ROS-mediated sperm damage could contribute to the subfertility in *Prm1+/-* mice.

Indeed, it has been shown that redox imbalance in sperm can be associated not only to DNA damage, but also reduced sperm motility (Alahmar, 2019). Sperm mitochondria have been found to be a substantial source of ROS in defective sperm (Koppers et al., 2008). In human, it has been shown that defective sperm produce mitochondrial ROS spontaneously, which damages the sperm midpiece and reduces sperm motility. Loss of one allele of *Prm1* resulted in a noticeable decrease in sperm motility, with only approx. 23% of sperm being motile. In human, this would, according to WHO criteria, qualify as asthenozoospermic (Alahmar, 2019, Cooper et al., 2010, World Health Organization, 2010). In line with this data, TEM revealed flagella defects in *Prm1+/-* sperm. Similar sperm tail deformities and motility defects have been described for *Prm1+/-* mice by Takeda *et al.* (Takeda et al., 2016). Additionally, they showed that *Prm1+/-* sperm display a reduction in the mitochondrial membrane potential, which has been correlated to a reduction in sperm motility (Gawlik et al., 2008). This suggests that reduced motility in *Prm1+/-* sperm is at least partially caused by ROS and contributes to the subfertility of *Prm1+/-* mice. Of note, *Prm2+/-* sperm showed no significant reduction in sperm motility compared to WT sperm (Schneider et al., 2016).

Whereas $Prm2^{+/\Delta c}$ and $Prm2^{-/\Delta c}$ sperm were described to be completely inviable and immotile, $Prm^{+/mut}$ and $Prm^{mut/mut}$ sperm appeared motile and did not show significantly increased membrane damage compared to WT. However slightly reduced sperm count analyzed by swim-out assay could indicate a slight reduction in $Prm^{mut/mut}$ sperm motility. A detailed computer assisted semen analysis (CASA) might help to assess these differences. These results again show, that the secondary effects described in $Prm^{+/mut}$ and $Prm^{mut/mut}$ sperm are less drastic compared to $Prm2^{+/\Delta c}$ and $Prm^{-/\Delta c}$ sperm. Accordingly, cauda epididymal sperm from $Prm2^{+/\Delta c}$ and $Prm^{-/\Delta c}$ males stained for 8-OHdG. Also here, oxidative damage accumulated during epididymal transit as it has been described for *Prm1-/-* and *Prm2-/-* mice. Therefore, we expect to see only a slight increase of 8-OHdG-positive sperm in $Prm^{+/mut}$ and $Prm^{mut/mut}$ mice.

The aberrant chromatin protamination identified by CMA3 staining, was another distinguishing feature between *Prm1+/-* and *Prm2+/-* sperm. CMA3 is a chromatin intercalating dye, which cannot bind protaminated DNA (Sadeghi et al., 2019). While only around 2% of WT sperm

stained with CMA3, approx. 98% of *Prm1+/-* and 29% of *Prm2+/-* sperm stained with CMA3. Hence, *Prm1+/-* and *Prm2+/-* sperm chromatin is either not fully or not correctly protaminated. Surprising was that one third of *Prm2+/-* sperm stained with CMA3, but seemingly had no effect on fertility. A study by Lolis *et al.* showed that the percentage of CMA3-positive sperm varies considerably in human ejaculates (Lolis et al., 1996). Other studies monitored up to 30% CMA3-positive sperm in semen samples of fertile men (Sakkas et al., 1996, Zandemami et al., 2012). Hence, similar to the situation in human, the 29% of CMA3-positive sperm seen in *Prm2+/-* males seem to be tolerated and do not influence the overall fertility of *Prm2+/-* mice. In *Prm1+/-* mice, on the other hand, nearly all sperm stained with CMA3. While a correlation between CMA3 levels and histone retention in sperm has been described (Ihara et al., 2014), other studies showed that defects in protamination analyzed via CMA3 staining did not correlate with increased histone retention monitored via aniline blue staining (Jahmani et al., 2021). Increased CMA3 staining in *Prm1+/-* sperm could not be correlated to increased histone retention as shown by mass spectrometry and IF staining. Thus, we hypothesize that protamination defects in *Prm1+/-* sperm is caused by vast amounts of unprocessed PRM2 bound to DNA. Loading of pre-PRM2 onto DNA, which is subsequently not processed, might cause protamination defects and allows CMA3 to intercalate. Lower amounts of unprocessed PRM2 were detected in *Prm2+/-* sperm, correlating to lower percentage of CMA3-positive sperm. If the hypothesis, that increased CMA3 staining correlates with levels of unprocessed PRM2 rather than histone retention, holds true we would expect higher percentages of CMA3-positive sperm in $Prm^{+/mut}$ compared to $Prm^{mut/mut}$ samples, since unprocessed PRM2 was detected in $Prm^{+/mut}$ sperm. In fact, CMA3 staining performed by Ilse Hamers revealed only a slight increase in CMA3-positive sperm in both genotypes compared to WT sperm. Unknown, however, is how the fusion protein binds and condenses chromatin, which might also influence CMA3 staining.

Presence of unprocessed PRM2 has been described in various mouse models displaying fertility problems (Takeda et al., 2016, Zhao et al., 2001, Shirley et al., 2004, Arévalo et al., 2022a, Barral et al., 2017, Moritz et al., 2023). Moreover, presence of incompletely processed PRM2 has been described in subfertile men (de Yebra et al., 1998) and pre-PRM2 retention in human sperm has been correlated to poor ICSI outcome (Rezaei-Gazik et al., 2022). Takeda *et al.* described defects in PRM2 processing in their *Prm1+/-* mice (Takeda et al., 2016). Further, presence of unprocessed PRM2 has been described in histone variant *H2A.L.2*-knockout (KO), *TNP1/TNP2*-double KO, *TNP2*-KO and $Prm2^{+/\Delta C}$ mice (Zhao et al., 2001, Shirley et al., 2004, Arévalo et al., 2022a, Barral et al., 2017). Hence, various disturbances in nuclear remodeling protein content can lead to impairments in PRM2 processing. Interestingly, a recent study showed that mice carrying a single non-arginine residue mutation (K49A) in PRM1 ($P1^{K49A/K49A}$), are subfertile and display defects in PRM2 processing (Moritz et al., 2023).

The fact that the relative amount of unprocessed PRM2 was significantly larger in *Prm1+/-* sperm compared to *Prm2+/-* sperm, shows the importance of species-specific PRM1 levels for correct PRM2 processing.

Another parameter, which could be correlated to the fertility differences seen in *Prm1+/-* compared to *Prm2+/-* mice, was the protamine ratio. In human, multiple studies have associated alterations of the species-specific protamine ratio (1:1) to male sub- and infertility (Aoki et al., 2005b, Balhorn et al., 1988, Belokopytova et al., 1993, Bench et al., 1998, de Yebra et al., 1998, Garcia-Peiro et al., 2011, Khara et al., 1997, Ni et al., 2016, Oliva, 2006, Steger et al., 2008, Steger et al., 2003, Steger et al., 2001, Torregrosa et al., 2006). While the protamine ratio is shifted to 1:5 in *Prm1+/-* mice, the species-specific protamine ratio (1:2) is maintained in *Prm2+/-* sperm comparable to WT sperm. Also, mice carrying the *Prm2Δ* allele, where the cP2 domain has been deleted, were shown to have altered protamine ratios (Arévalo et al., 2022a). While $Prm2^{+/\Delta c}$ sperm display a ratio of 2:1, $Prm^{-/\Delta c}$ sperm show a ratio of 5:1. Both mouse lines are infertile, while *Prm1+/-* mice are subfertile, suggesting that a shift towards lower amounts of PRM2 is less tolerated compared to lower PRM1 levels. The relative amounts of protamines in $Prm^{+/mut}$ sperm has not been assessed. In $Prm^{mut/mut}$ samples, however 100% of the protamine content should be made up by the PRM1-PRM2 fusion protein. This would in principle mean a 1:1 ratio of the N-terminal part of PRM1 and the mPRM2 domain, reflecting a humanized protamine ratio. Thus, since fertility is partially retained, mice seem to tolerate a 1:1 ratio of the protamine domains. Interestingly, an evolutionary study on sexual selection in mice and voles found, that sperm competition in mice seems to drive sexual selection towards an equilibrium in *Prm1/Prm2* expression (1:1).

Interestingly, the protamine ratio in $P1^{K49A/K49A}$ mice published by Moritz *et al.* were shifted from the expected 1:2 towards a 1:1 ratio (Moritz et al., 2023). The subfertile phenotype in $P1^{K49A/K49A}$ mice could, however, also be correlated to increased histone retention similar to *Prm1-/-* and *Prm2-/-* mice. Our results gathered with the *Prm1+/-* mice demonstrate, that one allele of intact/ not mutated *Prm1* is sufficient for histone eviction even if the protamine ratio is severely shifted.

In summary the analysis of *Prm1*-deficient and *Prm1-Prm2*-fusion mice and the comparison to other *Prm*-deficient or *Prm*-modified mouse models revealed, that both protamines are essential for proper sperm chromatin condensation and that the species-specific protamine ratio as well as correct protamine-protamine interaction is crucial for male fertility. Loss of *Prm1* or *Prm2* let to histone retention and severe sperm damage during epididymal transit. While loss of one allele of *Prm2* did not influence male mice fertility, *Prm1+/-* males are subfertile. In contrast to *Prm2+/-* sperm, *Prm1+/-* sperm show low but increased levels of ROS and DNA damage. Loss of one allele of *Prm1* let to a shift in the protamine ratio, while loss of one allele of *Prm2* did not. Mice carrying a mutated *Prm1-Prm2* fusion allele were subfertile. The PRM1-PRM2 fusion protein, lacking the cP2 domain, is able to condense the paternal chromatin and

support the production of functional sperm. Seemingly, the cP2 domain, although proven to be essential as such, is not needed if the N-terminal part of PRM1 and the mP2 domain are fused together. This suggests that cP2 is necessary for PRM1-mP2 interaction or binding.

### 5.2. *Actl7b*-deficient mice

For the second part of this thesis, I established *Actl7b*-deficient mice to analyze the role of ACTL7B in spermatogenesis. Loss of ACTL7B led to male infertility, due to severe defects in spermiogenesis. Starting after step 9 of spermiogenesis, various morphological abnormalities were detected, like detached acrosomes and membranes and malformed flagella. In part of the spermatids eviction of cytoplasm seems not to work properly. The majority of spermatids were subsequently degraded and seem to become engulfed by Sertoli cells. Autophagy marker proteins were elevated in *Actl7b*-deficient testis. Remaining immature spermatids were released into the lumen of seminiferous tubules. As a consequence, the synchronization of the seminiferous cycle appeared disrupted. While *Actl7b-/-* mice displayed complete spermatogenic failure, *Actl7b+/-* mice were fertile, producing viable sperm at concentrations comparable to WT males, albeit showing reduced ACTL7B levels. Interestingly, I found indications that ACTL7B interacts with the LC8 Dynein Light chains DYNLL1 and DYNLL2, suggesting a role in the microtubule network, rather than actin cytoskeleton dynamics.

Not much is known about ACTL7B. It is expressed in haploid male germ cells in human and mice, starting at round spermatid stage (Chadwick et al., 1999, Hisano et al., 2003b, Tanaka et al., 2003). The protein localizes to the cytoplasm of round and elongating spermatids and is later evicted from the mature sperm together with excess cytoplasm to residual bodies. Evolutionary analysis showed that *ACTL7B* is under purifying selection in both primates and rodents. Of note, human and mouse ACTL7B show high pairwise amino acid identity. Selection against changes in the gene sequence suggested that ACTL7B is essential for spermatogenesis in both clades.

The phenotypic alterations upon loss of *Actl7b* described here, are highly similar to those described in a recently published study by Clement *et al.* (Clement et al., 2023). Clement et al. utilized homologous recombination in ESC to generate an *Actl7b*-KO mouse model. Like in the model used for this study, the whole coding sequence of *Actl7b* has been deleted. *Actl7b*-KO mice were described to be infertile. In both models multifaceted morphological sperm abnormalities were discovered and immature germ cell release from the testis was described. Similar to the mice described here, *Actl7b*-KO mice generated by Clement *et al.* showed severely reduced epididymal sperm counts, even though the reduction we saw was more severe (1000-fold reduction vs. 10-fold reduction). One marked difference in mouse line generation was that Clement *et al.* generated their mice on C57BL/6N, while we used

C57Bl/6J. A difference in strain, which is known to be able to cause differences in phenotype (Simon et al., 2013). This might explain the difference in epididymal sperm counts.

Another phenomenon detected in both mouse models, was testicular germ cell loss. However, while Clement *et al.* describe the presence of TUNEL positive, i.e. apoptotic, roundish cells being shed into the lumen of *Actl7b*-KO seminiferous tubules, we did not detect an increase in TUNEL-positive cells. Although apoptosis related proteins were found to be higher abundant in *Actl7b-/-* testis compared to *Actl7b+/-* and *Actl7b+/+* testis using mass spectrometry, we also detected higher abundance of autophagy related proteins both in mass spectrometry and with western blot. Based on our results we favor autophagy to be the main cause of spermatid degradation. Additionally, mass spectrometry analysis of whole testicular protein, revealed higher abundance of Sertoli cell associated proteins in *Actl7b-/-* testis compared to *Actl7b+/-* and *Actl7b+/+* testis. This indicates a Sertoli cell-mediated reaction to defective and damaged spermatids. Higher abundancies were discovered for intermediate filaments (vimentin, desmin, and peripherin), ezrin, N-cadherin, and VCAM-1. The Sertoli cell nucleus is typically surrounded by intermediate filaments, which from there extend to desmosome junctions, which are found between Sertoli cells and between Sertoli cells and germ cells (Johnson, 2014). In *Actl7b-/-* testes tissue, ezrin accumulated around germ cells and vacuolations indicating recent germ cell loss. In rat testis, ezrin has been shown to interact with actin microfilaments, mostly at the basal ectoplasmic specialization (Gungor-Ordueri et al., 2014). It controls phagosome trafficking as well as Sertoli cell-spermatid adhesion. Further, it has been shown to colocalize with N-cadherin at the basal ectoplasmic specialization. N-cadherin, which interacts with both intermediate filaments and actin, localizes to ectoplasmic specializations between Sertoli cells and germ cells (Jiang et al., 2015). It has been shown to play a crucial role in blood-testis-barrier integrity. Ezrin was further shown to interact with the vascular adhesion molecule VCAM-1 *in vitro* (Barreiro et al., 2002). VCAM-1 expression can be triggered by a variety of stimuli, including pro-inflammatory cytokines and ROS, under inflammatory or chronic circumstances (Kong et al., 2018). Sertoli cell exposure to inflammatory mediators has been demonstrated to increase VCAM-1 expression *in vitro* (Riccioli et al., 1995). Together, these secondary consequences of ACTL7B loss indicate that Sertoli cells quickly degrade aberrant, developing spermatids. In agreement with this, spermatid, male gamete, and fertility-related proteins were found to be lower abundant in *Actl7b-/-* testes compared to *Actl7b+/-* and *Actl7b+/+* testes.

Interestingly, spermatogenesis in *Actl7b+/-* mice appeared inconspicuous, albeit showing reduced ACTL7B levels. Hence, there is a dosage effect, which seems to have no consequences on the phenotype. Since *ACTL7A* and *ACTL7B* show a high level of identity and are both expressed specifically in the testes of mice and human (Chadwick et al., 1999, Hisano et al., 2003b, Tanaka et al., 2003), we wanted to investigate for compensatory roles

for each other. First, evolutionary analysis showed that both genes are under purifying selection in primates and rodents, suggesting that both genes are essential and not redundant in function. Further, cellular localization of the proteins differs. While ACTL7B is present in the cytoplasm of round and elongating spermatids and is later evicted from sperm, ACTL7A localizes to the acrosome and tail of murine sperm and is later present in the acrosome of mature sperm (Tanaka et al., 2003, Fu et al., 2012). This supports the idea that both genes have acquired different functions. Accordingly, the phenotype described for *Actl7a*-mutant mice and humans carrying *Actl7a* variants differ from those described for *Actl7b*-deficient mice. In human and mice, a homozygous *ACTL7A* missense mutation induced sperm acrosomal abnormalities and infertility (Xin et al., 2020). PLCζ, a sperm-borne oocyte activation factor, was found to be reduced in *ACTL7A*-deficient sperm and infertility induced by *ACTL7A*-deficiency was overcome by artificial oocyte activation. Another recent study described a teratozoospermic patient with a homozygous missense variation of *ACTL7A* (Dai et al., 2022). Analysis of a mouse model carrying an equivalent mutation, revealed that acrosomes and acroplaxomes detach during spermiogenesis and sperm failed to activate the oocyte. Taken together these studies show that ACTL7A is crucial for acrosome biogenesis and unlike ACTL7B-deficiency does not lead to a disruption of spermiogenesis. Additionally, we showed that ACTL7A levels are not elevated in *Actl7b*-deficient mice, further arguing against a compensatory or redundant role of ACTL7A.

After detailed analysis of the secondary effects caused by *Actl7b*-deficiency, we aimed to find ACTL7B interaction partners. Utilizing Co-IP and mass spectrometry, first results suggest that ACTL7B might interact with DYNLL1 and DYNLL2. *DYNLL1* and *DYNLL2* are highly conserved orthologs among mammals and ubiquitously expressed (Rapali et al., 2011). The LC8 family light chains DYNLL1 and its paralog DYNLL2 are hub proteins that form homodimers with high conformational dynamics of binding grooves. They are presumably involved in dynein complex assembly, thereby indirectly affecting cargo binding. By binding intrinsically disordered proteins as dimers they link subunits in multiprotein complexes (Reardon et al., 2020, Asthana et al., 2012). For instance, DYNLL1 was shown to facilitate dissociation of dynactin from dynein, regulating cargo release (Jin et al., 2014). Their ability to interact with a wide variety of proteins and function in multiple cellular processes complicates predictions about their specific function during spermiogenesis. They have been shown to function in processes like mitosis, intracellular transport, the stabilization of microtubules, nuclear transport, apoptosis, postsynaptic density and regulation of transcription (Rapali et al., 2011, Nyarko et al., 2011, Jespersen and Barbar, 2020, Hall et al., 2008). DYNLL1 and DYNLL2 can be detected first in step 9 spermatids (this study and (Wang et al., 2005)). Thus, the defects monitored during spermiogenesis in *Actl7b-/-* mice started to appear directly after DYNLL1 and DYNLL2 synthesis. ACTL7B synthesis precedes that of DYNLL1 and DYNLL2 and DYNLL1/2

localization is changed when ACTL7B is absent *in vivo*. Further, expression of ACTL7B changed DYNLL1 and DYNLL2 localization in eukaryotic cells *in vitro*. These results indicate that ACTL7B-DYNLL1/2 interaction is crucial for proper sperm development and lack of it leads to defects in DYNLL1/2 localization and consequently spermiogenesis. We hypothesize that ACTL7B dimerization and/or stability in multiprotein complexes is promoted by DYNLL1 and DYNLL2. Alternatively, due to mislocalization of DYNLL1/2 in absence of ACTL7B, ACTL7B might be involved in LC8 light chain transport, activation or directing. Nevertheless, effects of DYNLL1/2 on the microtubule network could explain the defects seen in spermiogenesis in *Actl7b*-deficient mice.

Consequences of loss of other dynein complex components in spermatogenesis have been described previously. For instance, in rat it has been shown that knockdown of the cytoplasmic dynein 1 heavy chain DYNC1H1 causes a disruption of the microtubule structure and polymerization in Sertoli cells (Wen et al., 2018). The F-actin organization was perturbed and spermatid polarity, transport as well as release affected. Additionally, phagosome transport was affected and spermatogenesis disrupted. These results demonstrate that there is a cross talk between F-actin- and microtubule-based cytoskeleton. The results described for DYNC1H1 knockdown in rat are similar to what was described for *Actl7b*-deficient mice here. Although we did not detect direct interaction between ACTL7B and F-actin, F-actin structure was perturbed in part of *Actl7b-/-* seminiferous tubules. DYNC1H1 was found to interact with SPEF2 (Lehti et al., 2017). *Spef2* knockout in germ cells caused various spermatid differentiation abnormalities, substantially reduced sperm counts, and male mice infertility. SPEF2 was proposed to act as a linker protein by interacting with dynein 1 to enhance cargo transport along microtubules during spermatid development. Based on the described phenotype, ACTL7B might have similar functions.

Also, in human, functions of dynein light chains have been described. Absence or lower levels of dynein light chain tctex-type 1 (DNLT1), have been associated with male infertility (Indu et al., 2015). Further, 40 different interaction partners of another dynein light chain, dynein light chain tctex-type 4 (DNLT4), have been identified, clearly demonstrating the functional variety of dynein light chains (Freitas et al., 2014). Unraveling the roles of the LC8 dynein light chains in spermatogenesis would considerably aid in understanding the role of ACTL7B.

Studies on *ACTL7B* in humans is as up to now limited to correlative approaches. Ahn *et al.* described *ACTL7B* levels to be significantly lower in a cohort of teratozoospermic patients compared to healthy controls (Ahn et al., 2017). Others identified single nucleotides polymorphisms (SNPs) in the ACTL7B coding sequence in cohorts of infertile patients (Tanaka et al., 2019, Tanaka et al., 2007). Additionally, on both the protein and transcript level, *ACTL7B* has been found to have a strong discriminating power between obstructive and non-obstructive azoospermia subtypes, implying that it could be used to screen patients (Davalieva et al.,

2022). Although these studies have been retrospective and correlative, links of *ACTL7B* to fertility problems have been established. Taken together with the high level of amino acid identity between mice and human and the fact that the gene is under purifying selection in both clades, lets us surmise that ACTL7B variants can lead to failed spermatogenesis and infertility in humans. Hence, further studies on *ACTL7B* in human are mandatory.

# 6. Bibliography


Agarwal, A., Mulgund, A., Hamada, A. & Chyatte, M. R. (2015). A unique view on male infertility around the globe. *Reprod Biol Endocrinol* **13,** 37.

Ahlmann-Eltze, C. & Anders, S. (2021). proDA: Probabilistic dropout analysis for identifying differentially abundant proteins in label-free mass spectrometry. *Biorxiv*

Ahn, J., Park, Y. J., Chen, P., Lee, T. J., Jeon, Y. J., Croce, C. M., Suh, Y., Hwang, S., Kwon, W. S., Pang, M. G., et al. (2017). Comparative expression profiling of testis-enriched genes regulated during the development of spermatogonial cells. *PLoS One* **12,** e0175787.

Alahmar, A. T. (2019). Role of Oxidative Stress in Male Infertility: An Updated Review. *J Hum Reprod Sci* **12,** 4-18.

Allais-Bonnet, A. & Pailhoux, E. (2014). Role of the prion protein family in the gonads. *Front Cell Dev Biol* **2,** 56.

Allen, M. J., Bradbury, E. M. & Balhorn, R. (1996). The chromatin structure of well-spread demembranated human sperm nuclei revealed by atomic force microscopy. *Scanning Microsc* **10,** 989-94; discussion 994-6.

Allen, M. J., Bradbury, E. M. & Balhorn, R. (1997). AFM analysis of DNA-protamine complexes bound to mica. *Nucleic Acids Res* **25,** 2221-6.

Allen, M. J., Lee, C., Lee, J. D. T., Pogany, G. C., Balooch, M., Siekhaus, W. J. & Balhorn, R. (1993). Atomic force microscopy of mammalian sperm chromatin. *Chromosoma* **102,** 623-30.

Amann, R. P. (2008). The cycle of the seminiferous epithelium in humans: a need to revisit? *J Androl* **29,** 469-87.

Aoki, V. W., Emery, B. R., Liu, L. & Carrell, D. T. (2006a). Protamine levels vary between individual sperm cells of infertile human males and correlate with viability and DNA integrity. *J Androl* **27,** 890-8.

Aoki, V. W., Liu, L. & Carrell, D. T. (2005a). Identification and evaluation of a novel sperm protamine abnormality in a population of infertile males. *Hum Reprod* **20,** 1298-306.

Aoki, V. W., Liu, L. & Carrell, D. T. (2006b). A novel mechanism of protamine expression deregulation highlighted by abnormal protamine transcript retention in infertile human males with sperm protamine deficiency. *Mol Hum Reprod* **12,** 41-50.

Aoki, V. W., Liu, L., Jones, K. P., Hatasaka, H. H., Gibson, M., Peterson, C. M. & Carrell, D. T. (2006c). Sperm protamine 1/protamine 2 ratios are related to in vitro fertilization pregnancy rates and predictive of fertilization ability. *Fertil Steril* **86,** 1408-15.

Aoki, V. W., Moskovtsev, S. I., Willis, J., Liu, L., Mullen, J. B. & Carrell, D. T. (2005b). DNA integrity is compromised in protamine-deficient human sperm. *J Androl* **26,** 741-8.

Arévalo, L., Merges, G. E., Schneider, S., Oben, F. E., Neumann, I. S. & Schorle, H. (2022a). Loss of the cleaved-protamine 2 domain leads to incomplete histone-to-protamine exchange and infertility in mice. *PLoS Genet* **18,** e1010272.

Arévalo, L., Merges, G. E., Schneider, S. & Schorle, H. (2022b). Protamines: lessons learned from mouse models. *Reproduction* **164,** R57-R74.

Arévalo, L., Tourmente, M., Varea-Sanchez, M., Garcia, D. O. & Roldan, E. R. S. (2021). Sexual selection towards a protamine expression ratio optimum in two rodent groups? *Evolution*

Asthana, J., Kuchibhatla, A., Jana, S. C., Ray, K. & Panda, D. (2012). Dynein light chain 1 (LC8) association enhances microtubule stability and promotes microtubule bundling. *J Biol Chem* **287,** 40793-805.

Avidor-Reiss, T., Carr, A. & Fishman, E. L. (2020). The sperm centrioles. *Mol Cell Endocrinol* **518,** 110987.

Azhar, M., Altaf, S., Uddin, I., Cheng, J., Wu, L., Tong, X., Qin, W. & Bao, J. (2021). Towards Post-Meiotic Sperm Production: Genetic Insight into Human Infertility from Mouse Models. *Int J Biol Sci* **17,** 2487-2503.

Balhorn, R. (1982). A model for the structure of chromatin in mammalian sperm. *J Cell Biol* **93,** 298-305.

Balhorn, R. (2007). The protamine family of sperm nuclear proteins. *Genome Biol* **8,** 227.

Balhorn, R., Brewer, L. & Corzett, M. (2000). DNA condensation by protamine and arginine-rich peptides: analysis of toroid stability using single DNA molecules. *Mol Reprod Dev* **56,** 230-4.

Balhorn, R., Corzett, M. & Mazrimas, J. A. (1992). Formation of intraprotamine disulfides in vitro. *Arch Biochem Biophys* **296,** 384-93.

Balhorn, R., Reed, S. & Tanphaichitr, N. (1988). Aberrant protamine 1/protamine 2 ratios in sperm of infertile human males. *Experientia* **44,** 52-5.

Balhorn, R., Steger, K., Bergmann, M., Schuppe, H. C., Neuhauser, S. & Balhorn, M. C. (2018). New monoclonal antibodies specific for mammalian protamines P1 and P2. *Syst Biol Reprod Med* **64,** 424-447.

Barral, S., Morozumi, Y., Tanaka, H., Montellier, E., Govin, J., De Dieuleveult, M., Charbonnier, G., Coute, Y., Puthier, D., Buchou, T., et al. (2017). Histone Variant H2A.L.2 Guides Transition Protein-Dependent Protamine Assembly in Male Germ Cells. *Mol Cell* **66,** 89-101 e8.

Barreiro, O., Yanez-Mo, M., Serrador, J. M., Montoya, M. C., Vicente-Manzanares, M., Tejedor, R., Furthmayr, H. & Sanchez-Madrid, F. (2002). Dynamic interaction of VCAM-1 and ICAM-1 with moesin and ezrin in a novel endothelial docking structure for adherent leukocytes. *J Cell Biol* **157,** 1233-45.

Baudat, F. & De Massy, B. (2007). Regulating double-stranded DNA break repair towards crossover or non-crossover during mammalian meiosis. *Chromosome Res* **15,** 565-77.

Behrens, A., Genoud, N., Naumann, H., Rulicke, T., Janett, F., Heppner, F. L., Ledermann, B. & Aguzzi, A. (2002). Absence of the prion protein homologue Doppel causes male sterility. *EMBO J* **21,** 3652-8.

Belokopytova, I. A., Kostyleva, E. I., Tomilin, A. N. & Vorob'ev, V. I. (1993). Human male infertility may be due to a decrease of the protamine P2 content in sperm chromatin. *Mol Reprod Dev* **34,** 53-7.

Bench, G., Corzett, M. H., De Yebra, L., Oliva, R. & Balhorn, R. (1998). Protein and DNA contents in sperm from an infertile human male possessing protamine defects that vary over time. *Mol Reprod Dev* **50,** 345-53.

Bench, G., Corzett, M. H., Kramer, C. E., Grant, P. G. & Balhorn, R. (2000). Zinc is sufficiently abundant within mammalian sperm nuclei to bind stoichiometrically with protamine 2. *Mol Reprod Dev* **56,** 512-9.

Bench, G. S., Friz, A. M., Corzett, M. H., Morse, D. H. & Balhorn, R. (1996). DNA and total protamine masses in individual sperm from fertile mammalian subjects. *Cytometry* **23,** 263-71.

Braun, R. E. (1990). Temporal translational regulation of the protamine 1 gene during mouse spermatogenesis. *Enzyme* **44,** 120-8.

Braun, R. E., Peschon, J. J., Behringer, R. R., Brinster, R. L. & Palmiter, R. D. (1989). Protamine 3'-untranslated sequences regulate temporal translational control and subcellular localization of growth hormone in spermatids of transgenic mice. *Genes Dev* **3,** 793-802.

Brewer, L., Corzett, M. & Balhorn, R. (2002). Condensation of DNA by spermatid basic nuclear proteins. *J Biol Chem* **277,** 38895-900.

Brewer, L. R., Corzett, M. & Balhorn, R. (1999). Protamine-induced condensation and decondensation of the same DNA molecule. *Science* **286,** 120-3.

Brykczynska, U., Hisano, M., Erkek, S., Ramos, L., Oakeley, E. J., Roloff, T. C., Beisel, C., Schubeler, D., Stadler, M. B. & Peters, A. H. (2010). Repressive and active histone methylation mark distinct promoters in human and mouse spermatozoa. *Nat Struct Mol Biol* **17,** 679-87.

Bunick, D., Johnson, P. A., Johnson, T. R. & Hecht, N. B. (1990). Transcription of the testis-specific mouse protamine 2 gene in a homologous in vitro transcription system. *Proc Natl Acad Sci U S A* **87,** 891-5.

Carrell, D. T., Emery, B. R. & Hammoud, S. (2007). Altered protamine expression and diminished spermatogenesis: what is the link? *Hum Reprod Update* **13,** 313-27.

Carrell, D. T. & Liu, L. (2001). Altered protamine 2 expression is uncommon in donors of known fertility, but common among men with poor fertilizing capacity, and may reflect other abnormalities of spermiogenesis. *J Androl* **22,** 604-10.

Chadwick, B. P., Mull, J., Helbling, L. A., Gill, S., Leyne, M., Robbins, C. M., Pinkett, H. W., Makalowska, I., Maayan, C., Blumenfeld, A., et al. (1999). Cloning, mapping, and expression of two novel actin genes, actin-like-7A (ACTL7A) and actin-like-7B (ACTL7B), from the familial dysautonomia candidate region on 9q31. *Genomics* **58,** 302-9.

Chandley, A. C. & Kofman-Alfaro, S. (1971). "Unscheduled" DNA synthesis in human germ cells following UV irradiation. *Exp Cell Res* **69,** 45-8.

Chauviere, M., Martinage, A., Debarle, M., Sautiere, P. & Chevaillier, P. (1992). Molecular characterization of six intermediate proteins in the processing of mouse protamine P2 precursor. *Eur J Biochem* **204,** 759-65.

Cho, C., Jung-Ha, H., Willis, W. D., Goulding, E. H., Stein, P., Xu, Z., Schultz, R. M., Hecht, N. B. & Eddy, E. M. (2003). Protamine 2 deficiency leads to sperm DNA damage and embryo death in mice. *Biol Reprod* **69,** 211-7.

Cho, C., Willis, W. D., Goulding, E. H., Jung-Ha, H., Choi, Y. C., Hecht, N. B. & Eddy, E. M. (2001). Haploinsufficiency of protamine-1 or -2 causes infertility in mice. *Nat Genet* **28,** 82-6.

Clement, T. M., Geyer, C. B., Willis, W. D., Goulding, E. H., Upadhyay, S. & Eddy, E. M. (2023). Actin-related protein ACTL7B ablation leads to OAT with multiple morphological abnormalities of the flagellum and male infertility in mice. *Biol Reprod*

Cooper, T. G., Noonan, E., Von Eckardstein, S., Auger, J., Baker, H. W., Behre, H. M., Haugen, T. B., Kruger, T., Wang, C., Mbizvo, M. T., et al. (2010). World Health Organization reference values for human semen characteristics. *Hum Reprod Update* **16,** 231-45.

Corzett, M., Mazrimas, J. & Balhorn, R. (2002). Protamine 1: protamine 2 stoichiometry in the sperm of eutherian mammals. *Mol Reprod Dev* **61,** 519-27.

Dacheux, J. L. & Dacheux, F. (2014). New insights into epididymal function in relation to sperm maturation. *Reproduction* **147,** R27-42.

Dai, J., Chen, Y., Li, Q., Zhang, T., Zhou, Q., Gong, F., Lu, G., Zheng, W. & Lin, G. (2022). Pathogenic variant in ACTL7A causes severe teratozoospermia characterized by bubble-shaped acrosomes and male infertility. *Mol Hum Reprod*

Dai, J., Zhang, T., Guo, J., Zhou, Q., Gu, Y., Zhang, J., Hu, L., Zong, Y., Song, J., Zhang, S., et al. (2021). Homozygous pathogenic variants in ACTL9 cause fertilization failure and male infertility in humans and mice. *Am J Hum Genet* **108,** 469-481.

Davalieva, K., Rusevski, A., Velkov, M., Noveski, P., Kubelka-Sabit, K., Filipovski, V., Plaseski, T., Dimovski, A. & Plaseska-Karanfilska, D. (2022). Comparative proteomics analysis of human FFPE testicular tissues reveals new candidate biomarkers for distinction among azoospermia types and subtypes. *J Proteomics* 104686.

De Lamirande, E., Jiang, H., Zini, A., Kodama, H. & Gagnon, C. (1997). Reactive oxygen species and sperm physiology. *Rev Reprod* **2,** 48-54.

De Mateo, S., Gazquez, C., Guimera, M., Balasch, J., Meistrich, M. L., Ballesca, J. L. & Oliva, R. (2009). Protamine 2 precursors (Pre-P2), protamine 1 to protamine 2 ratio (P1/P2), and assisted reproduction outcome. *Fertil Steril* **91,** 715-22.

De Yebra, L., Ballesca, J. L., Vanrell, J. A., Corzett, M., Balhorn, R. & Oliva, R. (1998). Detection of P2 precursors in the sperm cells of infertile patients who have reduced protamine P2 levels. *Fertil Steril* **69,** 755-9.

De Yebra, L. & Oliva, R. (1993). Rapid analysis of mammalian sperm nuclear proteins. *Anal Biochem* **209,** 201-3.

Erkek, S., Hisano, M., Liang, C. Y., Gill, M., Murr, R., Dieker, J., Schubeler, D., Van Der Vlag, J., Stadler, M. B. & Peters, A. H. (2013). Molecular determinants of nucleosome retention at CpG-rich sequences in mouse spermatozoa. *Nat Struct Mol Biol* **20,** 868-75.

Fajardo, M. A., Haugen, H. S., Clegg, C. H. & Braun, R. E. (1997). Separate elements in the 3' untranslated region of the mouse protamine 1 mRNA regulate translational repression and activation during murine spermatogenesis. *Dev Biol* **191,** 42-52.

Fawcett, D. W. & Phillips, D. M. (1969). The fine structure and development of the neck region of the mammalian spermatozoon. *Anat Rec* **165,** 153-64.

Francis, S., Yelumalai, S., Jones, C. & Coward, K. (2014). Aberrant protamine content in sperm and consequential implications for infertility treatment. *Hum Fertil (Camb)* **17,** 80-9.

Freitas, M. J., Korrodi-Gregorio, L., Morais-Santos, F., Cruz E Silva, E. & Fardilha, M. (2014). TCTEX1D4 interactome in human testis: unraveling the function of dynein light chain in spermatozoa. *OMICS* **18,** 242-53.

Fu, J., Song, W., Zong, S., Koide, S. S., Miao, S. & Wang, L. (2013). Dynamic alterations in the expression and localization of ACTL7a during capacitation in mouse spermatozoa. *Fertil Steril* **99,** 882-8.

Fu, J., Wang, Y., Fok, K. L., Yang, D., Qiu, Y., Chan, H. C., Koide, S. S., Miao, S. & Wang, L. (2012). Anti-ACTL7a antibodies: a cause of infertility. *Fertil Steril* **97,** 1226-33 e1-8.

Fukuda, N., Fukuda, T., Sinnamon, J., Hernandez-Hernandez, A., Izadi, M., Raju, C. S., Czaplinski, K. & Percipalle, P. (2013). The transacting factor CBF-A/Hnrnpab binds to the A2RE/RTS element of protamine 2 mRNA and contributes to its translational regulation during mouse spermatogenesis. *PLoS Genet* **9,** e1003858.

Garcia-Peiro, A., Martinez-Heredia, J., Oliver-Bonet, M., Abad, C., Amengual, M. J., Navarro, J., Jones, C., Coward, K., Gosalvez, J. & Benet, J. (2011). Protamine 1 to protamine 2 ratio correlates with dynamic aspects of DNA fragmentation in human sperm. *Fertil Steril* **95,** 105-9.

Gawlik, V., Schmidt, S., Scheepers, A., Wennemuth, G., Augustin, R., Aumuller, G., Moser, M., Al-Hasani, H., Kluge, R., Joost, H. G., et al. (2008). Targeted disruption of Slc2a8 (GLUT8) reduces motility and mitochondrial potential of spermatozoa. *Mol Membr Biol* **25,** 224-35.

Gazquez, C., Oriola, J., De Mateo, S., Vidal-Taboada, J. M., Ballesca, J. L. & Oliva, R. (2008). A common protamine 1 promoter polymorphism (-190 C->A) correlates with abnormal sperm morphology and increased protamine P1/P2 ratio in infertile patients. *J Androl* **29,** 540-8.

Gervasi, M. G. & Visconti, P. E. (2017). Molecular changes and signaling events occurring in spermatozoa during epididymal maturation. *Andrology* **5,** 204-218.

Giorgini, F., Davies, H. G. & Braun, R. E. (2002). Translational repression by MSY4 inhibits spermatid differentiation in mice. *Development* **129,** 3669-79.

Gou, L. T., Lim, D. H., Ma, W., Aubol, B. E., Hao, Y., Wang, X., Zhao, J., Liang, Z., Shao, C., Zhang, X., et al. (2020). Initiation of Parental Genome Reprogramming in Fertilized Oocyte by Splicing Kinase SRPK1-Catalyzed Protamine Phosphorylation. *Cell* **180,** 1212-1227 e14.

Goudarzi, A., Shiota, H., Rousseaux, S. & Khochbin, S. (2014). Genome-scale acetylation-dependent histone eviction during spermatogenesis. *J Mol Biol* **426,** 3342-9.

Govin, J., Caron, C., Escoffier, E., Ferro, M., Kuhn, L., Rousseaux, S., Eddy, E. M., Garin, J. & Khochbin, S. (2006). Post-meiotic shifts in HSPA2/HSP70.2 chaperone activity during mouse spermatogenesis. *J Biol Chem* **281,** 37888-92.

Govin, J., Escoffier, E., Rousseaux, S., Kuhn, L., Ferro, M., Thevenon, J., Catena, R., Davidson, I., Garin, J., Khochbin, S., et al. (2007). Pericentric heterochromatin reprogramming by new histone variants during mouse spermiogenesis. *J Cell Biol* **176,** 283-94.

Griswold, M. D. (2016). Spermatogenesis: The Commitment to Meiosis. *Physiol Rev* **96,** 1-17.

Griswold, M. D. (2022). Cellular and molecular basis for the action of retinoic acid in spermatogenesis. *J Mol Endocrinol* **69,** T51-T57.

Gungor-Ordueri, N. E., Tang, E. I., Celik-Ozenci, C. & Cheng, C. Y. (2014). Ezrin is an actin binding protein that regulates sertoli cell and spermatid adhesion during spermatogenesis. *Endocrinology* **155,** 3981-95.

Guo, J., Grow, E. J., Mlcochova, H., Maher, G. J., Lindskog, C., Nie, X., Guo, Y., Takei, Y., Yun, J., Cai, L., et al. (2018). The adult human testis transcriptional cell atlas. *Cell Res* **28,** 1141-1157.

Gusse, M., Sautiere, P., Belaiche, D., Martinage, A., Roux, C., Dadoune, J. P. & Chevaillier, P. (1986). Purification and characterization of nuclear basic proteins of human sperm. *Biochim Biophys Acta* **884,** 124-34.

Hall, J., Hall, A., Pursifull, N. & Barbar, E. (2008). Differences in dynamic structure of LC8 monomer, dimer, and dimer-peptide complexes. *Biochemistry* **47,** 11940-52.

Hamad, M., Shelko, N., Montenarh, M. & Hammadeh, M. E. (2019). The impact of cigarette smoking on protamines 1 and 2 transcripts in human spermatozoa. *Hum Fertil (Camb)* **22,** 104-110.

Hamada, A., Esteves, S. C., Nizza, M. & Agarwal, A. (2012). Unexplained male infertility: diagnosis and management. *Int Braz J Urol* **38,** 576-94.

Hammadeh, M. E., Hamad, M. F., Montenarh, M. & Fischer-Hammadeh, C. (2010). Protamine contents and P1/P2 ratio in human spermatozoa from smokers and non-smokers. *Hum Reprod* **25,** 2708-20.

Hammoud, S. S., Nix, D. A., Hammoud, A. O., Gibson, M., Cairns, B. R. & Carrell, D. T. (2011). Genome-wide analysis identifies changes in histone retention and epigenetic modifications at developmental and imprinted gene loci in the sperm of infertile men. *Hum Reprod* **26,** 2558-69.

He, X. J., Ruan, J., Du, W. D., Chen, G., Zhou, Y., Xu, S., Zuo, X. B., Cao, Y. X. & Zhang, X. J. (2012). PRM1 variant rs35576928 (Arg>Ser) is associated with defective spermatogenesis in the Chinese Han population. *Reprod Biomed Online* **25,** 627-34.

Hecht, N. B., Bower, P. A., Waters, S. H., Yelick, P. C. & Distel, R. J. (1986a). Evidence for haploid expression of mouse testicular genes. *Exp Cell Res* **164,** 183-90.

Hecht, N. B., Kleene, K. C., Yelick, P. C., Johnson, P. A., Pravtcheva, D. D. & Ruddle, F. H. (1986b). Mapping of haploid expressed genes: genes for both mouse protamines are located on chromosome 16. *Somat Cell Mol Genet* **12,** 203-8.

Heller, C. G. & Clermont, Y. (1963). Spermatogenesis in man: an estimate of its duration. *Science* **140,** 184-6.

Heller, C. H. & Clermont, Y. (1964). Kinetics of the Germinal Epithelium in Man. *Recent Prog Horm Res* **20,** 545-75.

Henricks, D. M. & Mayer, D. T. (1965). Isolation and characterization of a basic keratin-like protein from mammalian spermatozoa. *Exp Cell Res* **40,** 402-12.

Hisano, M., Ohta, H., Nishimune, Y. & Nozaki, M. (2003a). Methylation of CpG dinucleotides in the open reading frame of a testicular germ cell-specific intronless gene, Tact1/Actl7b, represses its expression in somatic cells. *Nucleic Acids Res* **31,** 4797-804.

Hisano, M., Yamada, S., Tanaka, H., Nishimune, Y. & Nozaki, M. (2003b). Genomic structure and promoter activity of the testis haploid germ cell-specific intronless genes, Tact1 and Tact2. *Mol Reprod Dev* **65,** 148-56.

Hsu, P. D., Scott, D. A., Weinstein, J. A., Ran, F. A., Konermann, S., Agarwala, V., Li, Y., Fine, E. J., Wu, X., Shalem, O., et al. (2013). DNA targeting specificity of RNA-guided Cas9 nucleases. *Nat Biotechnol* **31,** 827-32.

Huang, Y. L., Zhang, P. F., Fu, Q., He, W. T., Xiao, K. & Zhang, M. (2020). Novel targets identified by integrated proteomic and phosphoproteomic analysis in spermatogenesis of swamp buffalo (Bubalus bubalis). *Sci Rep* **10,** 15659.

Hud, N. V., Allen, M. J., Downing, K. H., Lee, J. & Balhorn, R. (1993). Identification of the elemental packing unit of DNA in mammalian sperm cells by atomic force microscopy. *Biochem Biophys Res Commun* **193,** 1347-54.

Hud, N. V., Downing, K. H. & Balhorn, R. (1995). A constant radius of curvature model for the organization of DNA in toroidal condensates. *Proc Natl Acad Sci U S A* **92,** 3581-5.

Huerta-Cepas, J., Serra, F. & Bork, P. (2016). ETE 3: Reconstruction, Analysis, and Visualization of Phylogenomic Data. *Mol Biol Evol* **33,** 1635-8.

Ihara, M., Meyer-Ficca, M. L., Leu, N. A., Rao, S., Li, F., Gregory, B. D., Zalenskaya, I. A., Schultz, R. M. & Meyer, R. G. (2014). Paternal poly (ADP-ribose) metabolism modulates retention of inheritable sperm histones and early embryonic gene expression. *PLoS Genet* **10,** e1004317.

Imken, L., Rouba, H., El Houate, B., Louanjli, N., Barakat, A., Chafik, A. & Mcelreavey, K. (2009). Mutations in the protamine locus: association with spermatogenic failure? *Mol Hum Reprod* **15,** 733-8.

Indu, S., Sekhar, S. C., Sengottaiyan, J., Kumar, A., Pillai, S. M., Laloraya, M. & Kumar, P. G. (2015). Aberrant Expression of Dynein light chain 1 (DYNLT1) is Associated with Human Male Factor Infertility. *Mol Cell Proteomics* **14,** 3185-95.

Itoh, K., Kondoh, G., Miyachi, H., Sugai, M., Kaneko, Y., Kitano, S., Watanabe, H., Maeda, R., Imura, A., Liu, Y., et al. (2019). Dephosphorylation of protamine 2 at serine 56 is crucial for murine sperm maturation in vivo. *Sci Signal* **12,**

Iuso, D., Czernik, M., Toschi, P., Fidanza, A., Zacchini, F., Feil, R., Curtet, S., Buchou, T., Shiota, H., Khochbin, S., et al. (2015). Exogenous Expression of Human Protamine 1 (hPrm1) Remodels Fibroblast Nuclei into Spermatid-like Structures. *Cell Rep* **13,** 1765-71.

Jahmani, M. Y., Hammadeh, M. E., Al Smadi, M. A. & Baller, M. K. (2021). Label-Free Evaluation of Chromatin Condensation in Human Normal Morphology Sperm Using Raman Spectroscopy. *Reprod Sci* **28,** 2527-2539.

Jespersen, N. & Barbar, E. (2020). Emerging Features of Linear Motif-Binding Hub Proteins. *Trends Biochem Sci* **45,** 375-384.

Jiang, X., Ma, T., Zhang, Y., Zhang, H., Yin, S., Zheng, W., Wang, L., Wang, Z., Khan, M., Sheikh, S. W., et al. (2015). Specific deletion of Cdh2 in Sertoli cells leads to altered meiotic progression and subfertility of mice. *Biol Reprod* **92,** 79.

Jin, M., Yamada, M., Arai, Y., Nagai, T. & Hirotsune, S. (2014). Arl3 and LC8 regulate dissociation of dynactin from dynein. *Nat Commun* **5,** 5295.

Jodar, M., Oriola, J., Mestre, G., Castillo, J., Giwercman, A., Vidal-Taboada, J. M., Ballesca, J. L. & Oliva, R. (2011). Polymorphisms, haplotypes and mutations in the protamine 1 and 2 genes. *Int J Androl* **34,** 470-85.

Johnson, K. J. (2014). Testicular histopathology associated with disruption of the Sertoli cell cytoskeleton. *Spermatogenesis* **4,** e979106.

Johnson, P. A., Peschon, J. J., Yelick, P. C., Palmiter, R. D. & Hecht, N. B. (1988). Sequence homologies in the mouse protamine 1 and 2 genes. *Biochim Biophys Acta* **950,** 45-53.

Juma, A. R., Grommen, S. V. H., O'bryan, M. K., O'connor, A. E., Merriner, D. J., Hall, N. E., Doyle, S. R., Damdimopoulou, P. E., Barriga, D., Hart, A. H., et al. (2017). PLAG1 deficiency impairs spermatogenesis and sperm motility in mice. *Sci Rep* **7,** 5317.

Jung, Y. H., Sauria, M. E. G., Lyu, X., Cheema, M. S., Ausio, J., Taylor, J. & Corces, V. G. (2017). Chromatin States in Mouse Sperm Correlate with Embryonic and Adult Regulatory Landscapes. *Cell Rep* **18,** 1366-1382.

Kall, L., Storey, J. D., Maccoss, M. J. & Noble, W. S. (2008). Assigning significance to peptides identified by tandem mass spectrometry using decoy databases. *J Proteome Res* **7,** 29-34.

Khara, K. K., Vlad, M., Griffiths, M. & Kennedy, C. R. (1997). Human protamines and male infertility. *J Assist Reprod Genet* **14,** 282-90.

Khawar, M. B., Gao, H. & Li, W. (2019). Mechanism of Acrosome Biogenesis in Mammals. *Front Cell Dev Biol* **7,** 195.

Kierszenbaum, A. L. & Tres, L. L. (1975). Structural and transcriptional features of the mouse spermatid genome. *J Cell Biol* **65,** 258-70.

Kim, D., Langmead, B. & Salzberg, S. L. (2015). HISAT: a fast spliced aligner with low memory requirements. *Nat Methods* **12,** 357-60.

Klaus, E. S., Gonzalez, N. H., Bergmann, M., Bartkuhn, M., Weidner, W., Kliesch, S. & Rathke, C. (2016). Murine and Human Spermatids Are Characterized by Numerous, Newly Synthesized and Differentially Expressed Transcription Factors and Bromodomain-Containing Proteins. *Biol Reprod* **95,** 4.

Kleene, K. C. (1989). Poly(A) shortening accompanies the activation of translation of five mRNAs during spermiogenesis in the mouse. *Development* **106,** 367-73.

Kleene, K. C., Distel, R. J. & Hecht, N. B. (1984). Translational regulation and deadenylation of a protamine mRNA during spermiogenesis in the mouse. *Dev Biol* **105,** 71-9.

Kong, D. H., Kim, Y. K., Kim, M. R., Jang, J. H. & Lee, S. (2018). Emerging Roles of Vascular Cell Adhesion Molecule-1 (VCAM-1) in Immunological Disorders and Cancer. *Int J Mol Sci* **19,**

Koppers, A. J., De Iuliis, G. N., Finnie, J. M., Mclaughlin, E. A. & Aitken, R. J. (2008). Significance of mitochondrial reactive oxygen species in the generation of oxidative stress in spermatozoa. *J Clin Endocrinol Metab* **93,** 3199-207.

Kotaja, N., Kimmins, S., Brancorsini, S., Hentsch, D., Vonesch, J. L., Davidson, I., Parvinen, M. & Sassone-Corsi, P. (2004). Preparation, isolation and characterization of stage-specific spermatogenic cells for cellular and molecular analysis. *Nat Methods* **1,** 249-54.

Krawetz, S. A. & Dixon, G. H. (1988). Sequence similarities of the protamine genes: implications for regulation and evolution. *J Mol Evol* **27,** 291-7.

Kwon, Y. K. & Hecht, N. B. (1991). Cytoplasmic protein binding to highly conserved sequences in the 3' untranslated region of mouse protamine 2 mRNA, a translationally regulated transcript of male germ cells. *Proc Natl Acad Sci U S A* **88,** 3584-8.

Kwon, Y. K. & Hecht, N. B. (1993). Binding of a phosphoprotein to the 3' untranslated region of the mouse protamine 2 mRNA temporally represses its translation. *Mol Cell Biol* **13,** 6547-57.

Leduc, F., Maquennehan, V., Nkoma, G. B. & Boissonneault, G. (2008). DNA damage response during chromatin remodeling in elongating spermatids of mice. *Biol Reprod* **78,** 324-32.

Lee, K., Fajardo, M. A. & Braun, R. E. (1996). A testis cytoplasmic RNA-binding protein that has the properties of a translational repressor. *Mol Cell Biol* **16,** 3023-34.

Lee, K., Haugen, H. S., Clegg, C. H. & Braun, R. E. (1995). Premature translation of protamine 1 mRNA causes precocious nuclear condensation and arrests spermatid differentiation in mice. *Proc Natl Acad Sci U S A* **92,** 12451-5.

Lehti, M. S. & Sironen, A. (2017). Formation and function of sperm tail structures in association with sperm motility defects. *Biol Reprod* **97,** 522-536.

Lehti, M. S., Zhang, F. P., Kotaja, N. & Sironen, A. (2017). SPEF2 functions in microtubule-mediated transport in elongating spermatids to ensure proper male germ cell differentiation. *Development* **144,** 2683-2693.

Leslie, S. W., Soon-Sutton, T. L. & Khan, M. a. B. 2023. Male Infertility. Available: https://www.ncbi.nlm.nih.gov/books/NBK562258/.

Letunic, I. & Bork, P. (2021). Interactive Tree Of Life (iTOL) v5: an online tool for phylogenetic tree display and annotation. *Nucleic Acids Res* **49,** W293-W296.

Lolis, D., Georgiou, I., Syrrou, M., Zikopoulos, K., Konstantelli, M. & Messinis, I. (1996). Chromomycin A3-staining as an indicator of protamine deficiency and fertilization. *Int J Androl* **19,** 23-7.

Louie, A. J. & Dixon, G. H. (1972). Kinetics of enzymatic modification of the protamines and a proposal for their binding to chromatin. *J Biol Chem* **247,** 7962-8.

Love, M. I., Huber, W. & Anders, S. (2014). Moderated estimation of fold change and dispersion for RNA-seq data with DESeq2. *Genome Biol* **15,** 550.

Loytynoja, A. & Goldman, N. (2010). webPRANK: a phylogeny-aware multiple sequence aligner with interactive alignment browser. *BMC Bioinformatics* **11,** 579.

Luense, L. J., Donahue, G., Lin-Shiao, E., Rangel, R., Weller, A. H., Bartolomei, M. S. & Berger, S. L. (2019). Gcn5-Mediated Histone Acetylation Governs Nucleosome Dynamics in Spermiogenesis. *Dev Cell* **51,** 745-758 e6.

Lukassen, S., Bosch, E., Ekici, A. B. & Winterpacht, A. (2018). Single-cell RNA sequencing of adult mouse testes. *Sci Data* **5,** 180192.
Lüke, L., Tourmente, M., Dopazo, H., Serra, F. & Roldan, E. R. (2016). Selective constraints on protamine 2 in primates and rodents. *BMC Evol Biol* **16,** 21.
Lüke, L., Vicens, A., Tourmente, M. & Roldan, E. R. (2014). Evolution of protamine genes and changes in sperm head phenotype in rodents. *Biol Reprod* **90,** 67.
Lung, B. (1972). Ultrastructure and chromatin disaggregation of human sperm head with thioglycolate treatment. *J Cell Biol* **52,** 179-86.
Mahi, C. A. & Yanagimachi, R. (1975). Induction of nuclear decondensation of mammalian spermatozoa in vitro. *J Reprod Fertil* **44,** 293-6.
Marcon, L. & Boissonneault, G. (2004). Transient DNA strand breaks during mouse and human spermiogenesis new insights in stage specificity and link to chromatin remodeling. *Biol Reprod* **70,** 910-8.
Mashiko, D., Fujihara, Y., Satouh, Y., Miyata, H., Isotani, A. & Ikawa, M. (2013). Generation of mutant mice by pronuclear injection of circular plasmid expressing Cas9 and single guided RNA. *Sci Rep* **3,** 3355.
Mcpherson, S. M. & Longo, F. J. (1993). Nicking of rat spermatid and spermatozoa DNA: possible involvement of DNA topoisomerase II. *Dev Biol* **158,** 122-30.
Meier, J. (2020). Investigating the role of protamine 1 for fertility, by establishing and analysis of a gene edited mouse line.
Mellacheruvu, D., Wright, Z., Couzens, A. L., Lambert, J. P., St-Denis, N. A., Li, T., Miteva, Y. V., Hauri, S., Sardiu, M. E., Low, T. Y., et al. (2013). The CRAPome: a contaminant repository for affinity purification-mass spectrometry data. *Nat Methods* **10,** 730-6.
Mengual, L., Ballesca, J. L., Ascaso, C. & Oliva, R. (2003). Marked differences in protamine content and P1/P2 ratios in sperm cells from percoll fractions between patients and controls. *J Androl* **24,** 438-47.
Merges, G. (2018). Gene edited mice as model to study infertility caused by alterations in the protamine ratio.
Merges, G. E., Arévalo, L., Lohanadan, K., De Rooij, D. G., Jokwitz, M., Witke, W. & Schorle, H. (2022a). Actl7b-deficiency leads to mislocalization of LC8 type dynein light chains and disruption of murine spermatogenesis. *Biorxiv*
Merges, G. E., Meier, J., Schneider, S., Kruse, A., Frobius, A. C., Kirfel, G., Steger, K., Arévalo, L. & Schorle, H. (2022b). Loss of Prm1 leads to defective chromatin protamination, impaired PRM2 processing, reduced sperm motility and subfertility in male mice. *Development* **149**
Mi, H., Huang, X., Muruganujan, A., Tang, H., Mills, C., Kang, D. & Thomas, P. D. (2017). PANTHER version 11: expanded annotation data from Gene Ontology and Reactome pathways, and data analysis tool enhancements. *Nucleic Acids Res* **45,** D183-D189.
Montellier, E., Boussouar, F., Rousseaux, S., Zhang, K., Buchou, T., Fenaille, F., Shiota, H., Debernardi, A., Hery, P., Curtet, S., et al. (2013). Chromatin-to-nucleoprotamine transition is controlled by the histone H2B variant TH2B. *Genes Dev* **27,** 1680-92.

Moritz, L., Schon, S. B., Rabbani, M., Sheng, Y., Agrawal, R., Glass-Klaiber, J., Sultan, C., Camarillo, J. M., Clements, J., Baldwin, M. R., et al. (2023). Sperm chromatin structure and reproductive fitness are altered by substitution of a single amino acid in mouse protamine 1. *Nat Struct Mol Biol* **30,** 1077-1091.

Mruk, D. D. & Cheng, C. Y. (2004). Sertoli-Sertoli and Sertoli-germ cell interactions and their significance in germ cell movement in the seminiferous epithelium during spermatogenesis. *Endocr Rev* **25,** 747-806.

Muciaccia, B., Boitani, C., Berloco, B. P., Nudo, F., Spadetta, G., Stefanini, M., De Rooij, D. G. & Vicini, E. (2013). Novel stage classification of human spermatogenesis based on acrosome development. *Biol Reprod* **89,** 60.

Nasr-Esfahani, M. H., Salehi, M., Razavi, S., Mardani, M., Bahramian, H., Steger, K. & Oreizi, F. (2004). Effect of protamine-2 deficiency on ICSI outcome. *Reprod Biomed Online* **9,** 652-8.

Ni, K., Spiess, A. N., Schuppe, H. C. & Steger, K. (2016). The impact of sperm protamine deficiency and sperm DNA damage on human male fertility: a systematic review and meta-analysis. *Andrology* **4,** 789-99.

Nyarko, A., Hall, J., Hall, A., Hare, M., Kremerskothen, J. & Barbar, E. (2011). Conformational dynamics promote binding diversity of dynein light chain LC8. *Biophys Chem* **159,** 41-7.

Oakberg, E. F. (1956a). A description of spermiogenesis in the mouse and its use in analysis of the cycle of the seminiferous epithelium and germ cell renewal. *Am J Anat* **99,** 391-413.

Oakberg, E. F. (1956b). Duration of spermatogenesis in the mouse and timing of stages of the cycle of the seminiferous epithelium. *Am J Anat* **99,** 507-16.

Oakberg, E. F. (1971a). A new concept of spermatogonial stem-cell renewal in the mouse and its relationship to genetic effects. *Mutat Res* **11,** 1-7.

Oakberg, E. F. (1971b). Spermatogonial stem-cell renewal in the mouse. *Anat Rec* **169,** 515-31.

Oliva, R. (2006). Protamines and male infertility. *Hum Reprod Update* **12,** 417-35.

Oresti, G. M., Garcia-Lopez, J., Aveldano, M. I. & Del Mazo, J. (2013). Cell-type-specific regulation of genes involved in testicular lipid metabolism: fatty acid-binding proteins, diacylglycerol acyltransferases, and perilipin 2. *Reproduction* **146,** 471-80.

Paisley, D., Banks, S., Selfridge, J., Mclennan, N. F., Ritchie, A. M., Mcewan, C., Irvine, D. S., Saunders, P. T., Manson, J. C. & Melton, D. W. (2004). Male infertility and DNA damage in Doppel knockout and prion protein/Doppel double-knockout mice. *Am J Pathol* **164,** 2279-88.

Pertea, M., Pertea, G. M., Antonescu, C. M., Chang, T. C., Mendell, J. T. & Salzberg, S. L. (2015). StringTie enables improved reconstruction of a transcriptome from RNA-seq reads. *Nat Biotechnol* **33,** 290-5.

Peschon, J. J., Behringer, R. R., Brinster, R. L. & Palmiter, R. D. (1987). Spermatid-specific expression of protamine 1 in transgenic mice. *Proc Natl Acad Sci U S A* **84,** 5316-9.

Phillips, B. T., Gassei, K. & Orwig, K. E. (2010). Spermatogonial stem cell regulation and spermatogenesis. *Philos Trans R Soc Lond B Biol Sci* **365,** 1663-78.

Pilo Boyl, P., Di Nardo, A., Mulle, C., Sassoe-Pognetto, M., Panzanelli, P., Mele, A., Kneussel, M., Costantini, V., Perlas, E., Massimi, M., et al. (2007). Profilin2 contributes to synaptic vesicle exocytosis, neuronal excitability, and novelty-seeking behavior. *EMBO J* **26,** 2991-3002.

Pirhonen, A., Linnala-Kankkunen, A. & Maenpaa, P. H. (1994). Identification of phosphoseryl residues in protamines from mature mammalian spermatozoa. *Biol Reprod* **50,** 981-6.

Pogany, G. C., Corzett, M., Weston, S. & Balhorn, R. (1981). DNA and protein content of mouse sperm. Implications regarding sperm chromatin structure. *Exp Cell Res* **136,** 127-36.

Rapali, P., Szenes, A., Radnai, L., Bakos, A., Pal, G. & Nyitray, L. (2011). DYNLL/LC8: a light chain subunit of the dynein motor complex and beyond. *FEBS J* **278,** 2980-96.

Ravel, C., Chantot-Bastaraud, S., El Houate, B., Berthaut, I., Verstraete, L., De Larouziere, V., Lourenco, D., Dumaine, A., Antoine, J. M., Mandelbaum, J., et al. (2007). Mutations in the protamine 1 gene associated with male infertility. *Mol Hum Reprod* **13,** 461-4.

Reardon, P. N., Jara, K. A., Rolland, A. D., Smith, D. A., Hoang, H. T. M., Prell, J. S. & Barbar, E. J. (2020). The dynein light chain 8 (LC8) binds predominantly "in-register" to a multivalent intrinsically disordered partner. *J Biol Chem* **295,** 4912-4922.

Retief, J. D. & Dixon, G. H. (1993). Evolution of pro-protamine P2 genes in primates. *Eur J Biochem* **214,** 609-15.

Rezaei-Gazik, M., Vargas, A., Amiri-Yekta, A., Vitte, A. L., Akbari, A., Barral, S., Esmaeili, V., Chuffart, F., Sadighi-Gilani, M. A., Coute, Y., et al. (2022). Direct visualization of pre-protamine 2 detects protamine assembly failures and predicts ICSI success. *Mol Hum Reprod* **28,**

Riccioli, A., Filippini, A., De Cesaris, P., Barbacci, E., Stefanini, M., Starace, G. & Ziparo, E. (1995). Inflammatory mediators increase surface expression of integrin ligands, adhesion to lymphocytes, and secretion of interleukin 6 in mouse Sertoli cells. *Proc Natl Acad Sci U S A* **92,** 5808-12.

Robinson, J. T., Thorvaldsdottir, H., Winckler, W., Guttman, M., Lander, E. S., Getz, G. & Mesirov, J. P. (2011). Integrative genomics viewer. *Nat Biotechnol* **29,** 24-6.

Rogenhofer, N., Dansranjavin, T., Schorsch, M., Spiess, A., Wang, H., Von Schonfeldt, V., Cappallo-Obermann, H., Baukloh, V., Yang, H., Paradowska, A., et al. (2013). The sperm protamine mRNA ratio as a clinical parameter to estimate the fertilizing potential of men taking part in an ART programme. *Hum Reprod* **28,** 969-78.

Russell, L. D., Ettlin, R. A., Sinha-Hikim, A. P. & Clegg, E. D. 1990. *Histological and Histopathological Evaluation of the Testis*, Cache River Press.

Sadeghi, S., Talebi, A. R., Shahedi, A., Moein, M. R. & Abbasi-Sarcheshmeh, A. (2019). Effects of Tamoxifen on DNA Integrity in Mice. *J Reprod Infertil* **20,** 10-15.

Sainio-Pollanen, S., Sundstrom, J., Erkkila, S., Hanninen, A., Vainiopaa, M., Martikainen, M., Salminen, E., Verajankorva, E., Antola, H., Nikula, H., et al. (1997). CD106 (VCAM-1) in testicular immunoregulation. *J Reprod Immunol* **33,** 221-38.

Sakkas, D., Urner, F., Bianchi, P. G., Bizzaro, D., Wagner, I., Jaquenoud, N., Manicardi, G. & Campana, A. (1996). Sperm chromatin anomalies can influence decondensation after intracytoplasmic sperm injection. *Hum Reprod* **11,** 837-43.

Schafer, D. A. & Schroer, T. A. (1999). Actin-related proteins. *Annu Rev Cell Dev Biol* **15,** 341-63.

Schneider, C. A., Rasband, W. S. & Eliceiri, K. W. (2012). NIH Image to ImageJ: 25 years of image analysis. *Nat Methods* **9,** 671-5.

Schneider, S. (2015). Establishment of the CRISPR/Cas9 gene editing for the production of genetically altered mice.

Schneider, S. (2019). Functional analysis of genes relevant for spermatogenesis by CRISPR/Cas9-mediated gene editing in mice.

Schneider, S., Balbach, M., Jan, F. J., Fietz, D., Nettersheim, D., Jostes, S., Schmidt, R., Kressin, M., Bergmann, M., Wachten, D., et al. (2016). Re-visiting the Protamine-2 locus: deletion, but not haploinsufficiency, renders male mice infertile. *Sci Rep* **6,** 36764.

Schneider, S., Shakeri, F., Trotschel, C., Arévalo, L., Kruse, A., Buness, A., Poetsch, A., Steger, K. & Schorle, H. (2020). Protamine-2 Deficiency Initiates a Reactive Oxygen Species (ROS)-Mediated Destruction Cascade during Epididymal Sperm Maturation in Mice. *Cells* **9,**

Shinagawa, T., Huynh, L. M., Takagi, T., Tsukamoto, D., Tomaru, C., Kwak, H. G., Dohmae, N., Noguchi, J. & Ishii, S. (2015). Disruption of Th2a and Th2b genes causes defects in spermatogenesis. *Development* **142,** 1287-92.

Shirley, C. R., Hayashi, S., Mounsey, S., Yanagimachi, R. & Meistrich, M. L. (2004). Abnormalities and reduced reproductive potential of sperm from Tnp1- and Tnp2-null double mutant mice. *Biol Reprod* **71,** 1220-9.

Simon, L., Castillo, J., Oliva, R. & Lewis, S. E. (2011). Relationships between human sperm protamines, DNA damage and assisted reproduction outcomes. *Reprod Biomed Online* **23,** 724-34.

Simon, M. M., Greenaway, S., White, J. K., Fuchs, H., Gailus-Durner, V., Wells, S., Sorg, T., Wong, K., Bedu, E., Cartwright, E. J., et al. (2013). A comparative phenotypic and genomic analysis of C57BL/6J and C57BL/6N mouse strains. *Genome Biol* **14,** R82.

Skinner, B. M., Rathje, C. C., Bacon, J., Johnson, E. E. P., Larson, E. L., Kopania, E. E. K., Good, J. M., Yousafzai, G., Affara, N. A. & Ellis, P. J. I. (2019). A high-throughput method for unbiased quantitation and categorization of nuclear morphologydagger. *Biol Reprod* **100,** 1250-1260.

Snustad, D. P. & Simmons, M. J. 2016. Meiosis. *Principles of Genetics.* 7th ed.: John Wiley & Sons, Inc.

Soler-Ventura, A., Castillo, J., De La Iglesia, A., Jodar, M., Barrachina, F., Ballesca, J. L. & Oliva, R. (2018). Mammalian Sperm Protamine Extraction and Analysis: A Step-By-Step Detailed Protocol and Brief Review of Protamine Alterations. *Protein Pept Lett* **25,** 424-433.

Soler-Ventura, A., Gay, M., Jodar, M., Vilanova, M., Castillo, J., Arauz-Garofalo, G., Villarreal, L., Ballesca, J. L., Vilaseca, M. & Oliva, R. (2020). Characterization of

Human Sperm Protamine Proteoforms through a Combination of Top-Down and Bottom-Up Mass Spectrometry Approaches. *J Proteome Res* **19,** 221-237.

**Steger, K., Failing, K., Klonisch, T., Behre, H. M., Manning, M., Weidner, W., Hertle, L., Bergmann, M. & Kliesch, S.** (2001). Round spermatids from infertile men exhibit decreased protamine-1 and -2 mRNA. *Hum Reprod* **16,** 709-16.

**Steger, K., Fink, L., Failing, K., Bohle, R. M., Kliesch, S., Weidner, W. & Bergmann, M.** (2003). Decreased protamine-1 transcript levels in testes from infertile men. *Mol Hum Reprod* **9,** 331-6.

**Steger, K., Wilhelm, J., Konrad, L., Stalf, T., Greb, R., Diemer, T., Kliesch, S., Bergmann, M. & Weidner, W.** (2008). Both protamine-1 to protamine-2 mRNA ratio and Bcl2 mRNA content in testicular spermatids and ejaculated spermatozoa discriminate between fertile and infertile men. *Hum Reprod* **23,** 11-6.

**Stewart, K. S., Kramer, J. A., Evans, M. I. & Krawetz, S. A.** (1999). Temporal expression of the transgenic human protamine gene cluster. *Fertil Steril* **71,** 739-45.

**Stewart, T. A., Hecht, N. B., Hollingshead, P. G., Johnson, P. A., Leong, J. A. & Pitts, S. L.** (1988). Haploid-specific transcription of protamine-myc and protamine-T-antigen fusion genes in transgenic mice. *Mol Cell Biol* **8,** 1748-55.

**Tachiwana, H., Kagawa, W., Osakabe, A., Kawaguchi, K., Shiga, T., Hayashi-Takanaka, Y., Kimura, H. & Kurumizaka, H.** (2010). Structural basis of instability of the nucleosome containing a testis-specific histone variant, human H3T. *Proc Natl Acad Sci U S A* **107,** 10454-9.

**Takeda, N., Yoshinaga, K., Furushima, K., Takamune, K., Li, Z., Abe, S., Aizawa, S. & Yamamura, K.** (2016). Viable offspring obtained from Prm1-deficient sperm in mice. *Sci Rep* **6,** 27409.

**Tanaka, H., Hirose, M., Tokuhiro, K., Matsuoka, Y., Miyagawa, Y., Tsujimura, A., Okuyama, A. & Nishimune, Y.** (2007). Single nucleotide polymorphisms: discovery of the genetic causes of male infertility. *Soc Reprod Fertil Suppl* **65,** 531-4.

**Tanaka, H., Iguchi, N., Egydio De Carvalho, C., Tadokoro, Y., Yomogida, K. & Nishimune, Y.** (2003). Novel actin-like proteins T-ACTIN 1 and T-ACTIN 2 are differentially expressed in the cytoplasm and nucleus of mouse haploid germ cells. *Biol Reprod* **69,** 475-82.

**Tanaka, H., Miyagawa, Y., Tsujimura, A. & Wada, M.** (2019). Genetic Polymorphisms within The Intronless ACTL7A and ACTL7B Genes Encoding Spermatogenesis-Specific Actin-Like Proteins in Japanese Males. *Int J Fertil Steril* **13,** 245-249.

**Tao, L., He, X. Y., Wang, F. Y., Pan, L. X., Wang, X. Y., Gan, S. Q., Di, R. & Chu, M. X.** (2021). Identification of genes associated with litter size combining genomic approaches in Luzhong mutton sheep. *Anim Genet* **52,** 545-549.

**The, M., Maccoss, M. J., Noble, W. S. & Kall, L.** (2016). Fast and Accurate Protein False Discovery Rates on Large-Scale Proteomics Data Sets with Percolator 3.0. *J Am Soc Mass Spectrom* **27,** 1719-1727.

**Torregrosa, N., Dominguez-Fandos, D., Camejo, M. I., Shirley, C. R., Meistrich, M. L., Ballesca, J. L. & Oliva, R.** (2006). Protamine 2 precursors, protamine 1/protamine 2 ratio, DNA integrity and other sperm parameters in infertile patients. *Hum Reprod* **21,** 2084-9.

Trinkle-Mulcahy, L., Boulon, S., Lam, Y. W., Urcia, R., Boisvert, F. M., Vandermoere, F., Morrice, N. A., Swift, S., Rothbauer, U., Leonhardt, H., et al. (2008). Identifying specific protein interaction partners using quantitative mass spectrometry and bead proteomes. *J Cell Biol* **183,** 223-39.

Truett, G. E., Heeger, P., Mynatt, R. L., Truett, A. A., Walker, J. A. & Warman, M. L. (2000). Preparation of PCR-quality mouse genomic DNA with hot sodium hydroxide and tris (HotSHOT). *Biotechniques* **29,** 52, 54.

Tuttelmann, F., Krenkova, P., Romer, S., Nestorovic, A. R., Ljujic, M., Stambergova, A., Macek, M., Jr., Macek, M., Sr., Nieschlag, E., Gromoll, J., et al. (2010). A common haplotype of protamine 1 and 2 genes is associated with higher sperm counts. *Int J Androl* **33,** e240-8.

Vogl, A. W., Vaid, K. S. & Guttman, J. A. (2008). The Sertoli cell cytoskeleton. *Adv Exp Med Biol* **636,** 186-211.

Wang, R. A., Zhao, M., Meistrich, M. L. & Kumar, R. (2005). Stage-specific expression of dynein light chain-1 and its interacting kinase, p21-activated kinase-1, in rodent testes: implications in spermiogenesis. *J Histochem Cytochem* **53,** 1235-43.

Wen, Q., Tang, E. I., Lui, W. Y., Lee, W. M., Wong, C. K. C., Silvestrini, B. & Cheng, C. Y. (2018). Dynein 1 supports spermatid transport and spermiation during spermatogenesis in the rat testis. *Am J Physiol Endocrinol Metab* **315,** E924-E948.

Wen, Z., Zhu, H., Wu, B., Zhang, A., Wang, H., Cheng, Y., Zhao, H., Li, J., Liu, M. & Gao, J. (2022). Cathepsin B plays a role in spermatogenesis and sperm maturation through regulating autophagy and apoptosis in mice. *PeerJ* **10,** e14472.

Weyrich, A. (2012). Preparation of genomic DNA from mammalian sperm. *Curr Protoc Mol Biol* **98,** Chapter 2 Unit 2 13 1-3.

Wickham, H. (2011). ggplot2. *Wiley Interdisciplinary Reviews: Computational Statistics*

World Health Organization 2010. WHO laboratory manual for the examination and processing of human semen. 5th ed. Geneva: World Health Organization.

World Health Organization. 2023. *Infertility* [Online]. Available: https://www.who.int/news-room/fact-sheets/detail/infertility#:~:text=Key%20facts,on%20their%20families%20and%20communities. [Accessed 07.2023].

Wu, J. Y., Ribar, T. J., Cummings, D. E., Burton, K. A., Mcknight, G. S. & Means, A. R. (2000). Spermiogenesis and exchange of basic nuclear proteins are impaired in male germ cells lacking Camk4. *Nat Genet* **25,** 448-52.

Wykes, S. M. & Krawetz, S. A. (2003). Conservation of the PRM1 --> PRM2 --> TNP2 domain. *DNA Seq* **14,** 359-67.

Xin, A., Qu, R., Chen, G., Zhang, L., Chen, J., Tao, C., Fu, J., Tang, J., Ru, Y., Chen, Y., et al. (2020). Disruption in ACTL7A causes acrosomal ultrastructural defects in human and mouse sperm as a novel male factor inducing early embryonic arrest. *Sci Adv* **6,** eaaz4796.

Yamaguchi, K., Hada, M., Fukuda, Y., Inoue, E., Makino, Y., Katou, Y., Shirahige, K. & Okada, Y. (2018). Re-evaluating the Localization of Sperm-Retained Histones Revealed the Modification-Dependent Accumulation in Specific Genome Regions. *Cell Rep* **23,** 3920-3932.

Yan, W., Ma, L., Burns, K. H. & Matzuk, M. M. (2003). HILS1 is a spermatid-specific linker histone H1-like protein implicated in chromatin remodeling during mammalian spermiogenesis. *Proc Natl Acad Sci U S A* **100,** 10546-51.

Yang, Z. (1997). PAML: a program package for phylogenetic analysis by maximum likelihood. *Comput Appl Biosci* **13,** 555-6.

Yang, Z. (2007). PAML 4: phylogenetic analysis by maximum likelihood. *Mol Biol Evol* **24,** 1586-91.

Yelick, P. C., Balhorn, R., Johnson, P. A., Corzett, M., Mazrimas, J. A., Kleene, K. C. & Hecht, N. B. (1987). Mouse protamine 2 is synthesized as a precursor whereas mouse protamine 1 is not. *Mol Cell Biol* **7,** 2173-9.

Yu, B., Qi, Y., Liu, D., Gao, X., Chen, H., Bai, C. & Huang, Z. (2014). Cigarette smoking is associated with abnormal histone-to-protamine transition in human sperm. *Fertil Steril* **101,** 51-57 e1.

Yu, Q. F., Yang, X. X., Li, F. X., Ye, L. W., Wu, Y. S. & Mao, X. M. (2012). [Association of PRM1-190C- > A polymorphism with teratozoospermia]. *Zhonghua Nan Ke Xue* **18,** 314-7.

Zandemami, M., Qujeq, D., Akhondi, M. M., Kamali, K., Raygani, M., Lakpour, N., Shiraz, E. S. & Sadeghi, M. R. (2012). Correlation of CMA3 Staining with Sperm Quality and Protamine Deficiency. *Lab Med* **43,**

Zhao, M., Shirley, C. R., Yu, Y. E., Mohapatra, B., Zhang, Y., Unni, E., Deng, J. M., Arango, N. A., Terry, N. H., Weil, M. M., et al. (2001). Targeted disruption of the transition protein 2 gene affects sperm chromatin structure and reduces fertility in mice. *Mol Cell Biol* **21,** 7243-55.

Zhong, J., Peters, A. H., Kafer, K. & Braun, R. E. (2001). A highly conserved sequence essential for translational repression of the protamine 1 messenger rna in murine spermatids. *Biol Reprod* **64,** 1784-9.

# 7. Appendix

**Parts of the supplement section have been published in:**

Gina Esther Merges, Julia Meier, Simon Schneider, Alexander Kruse, Andreas Christian Fröbius, Klaus Steger, Lena Arévalo, Hubert Schorle (2022) Loss of *Prm1* leads to defective chromatin protamination, impaired PRM2 processing, reduced sperm motility and subfertility in male mice. *Development.* DOI: 10.1242/dev.200330

Gina Esther Merges, Lena Arévalo, Keerthika Lohanadan, Dirk G. de Rooij, Melanie Jokwitz, Walter Witke, Hubert Schorle (2022) *Actl7b*-deficiency leads to mislocalization of LC8 type dynein light chains and disruption of murine spermatogenesis. *BioRxiv.* DOI: 10.1101/2022.12.19.520998 (currently in revision with Development)

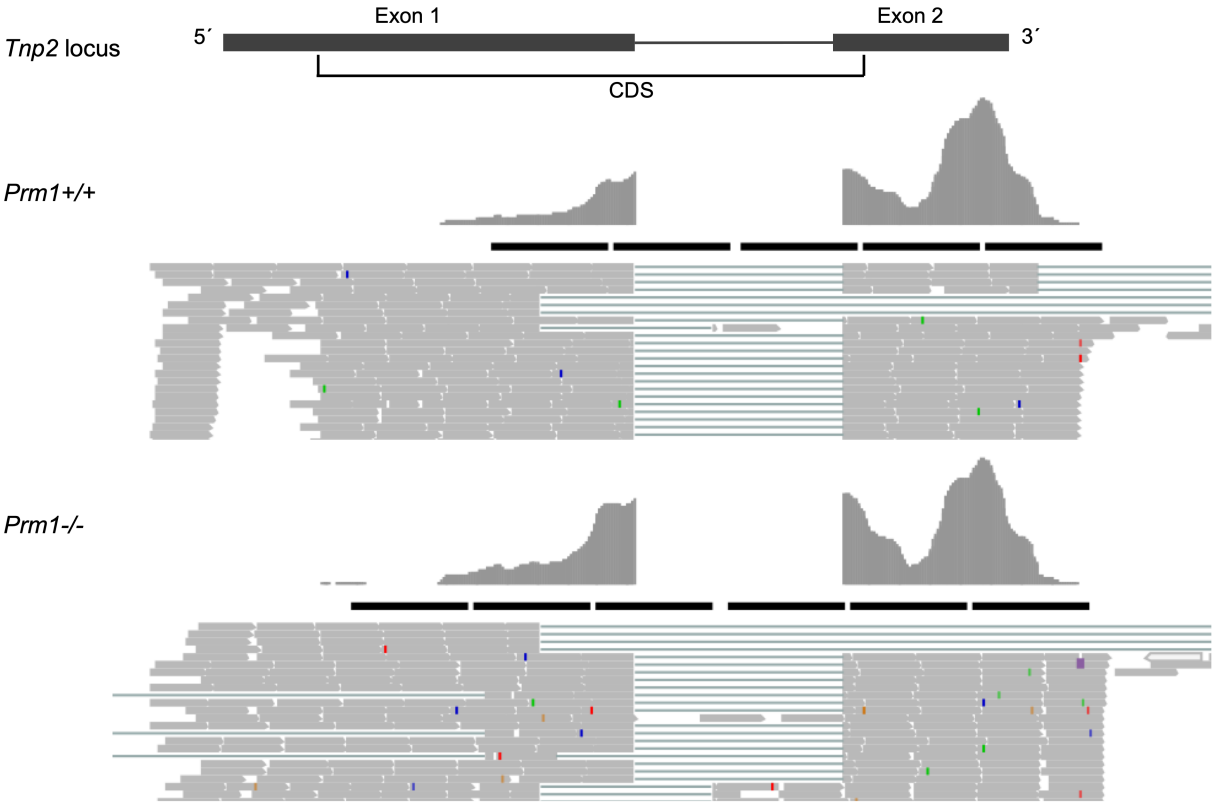


**Figure S1: Analysis of *Tnp2* expression in *Prm1*-deficient mice.** Representative cut-out of RNAseq reads mapping to the *Tnp2* locus from whole testis RNAseq of *Prm1+/+* and *Prm1-/-* mice. Modified from (Merges et al., 2022b). RNAseq analysis was performed by Dr. Lena Arévalo.

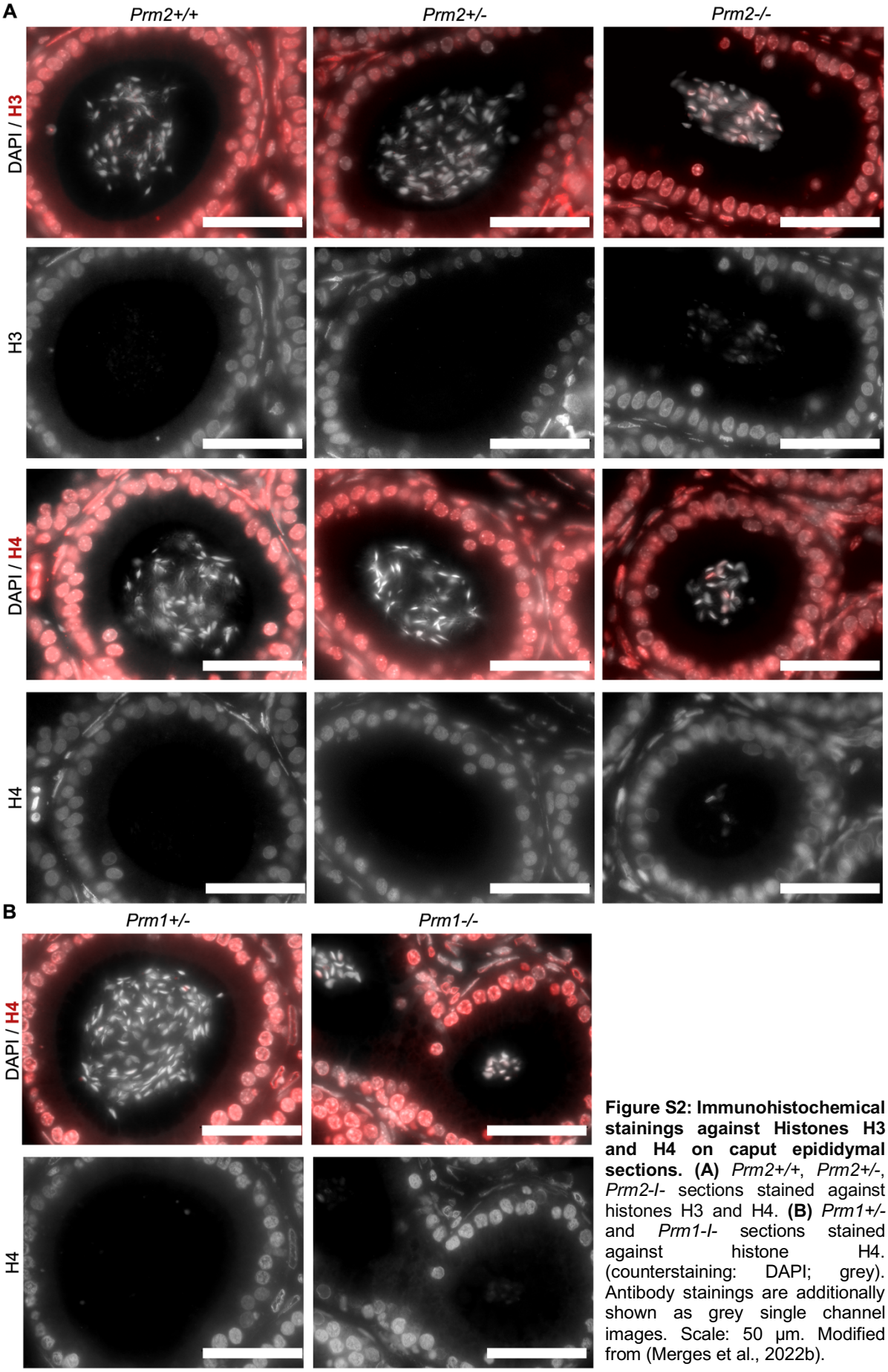


**Figure S2: Immunohistochemical stainings against Histones H3 and H4 on caput epididymal sections. (A)** *Prm2+/+*, *Prm2+/-*, *Prm2-/-* sections stained against histones H3 and H4. **(B)** *Prm1+/-* and *Prm1-/-* sections stained against histone H4. (counterstaining: DAPI; grey). Antibody stainings are additionally shown as grey single channel images. Scale: 50 µm. Modified from (Merges et al., 2022b).

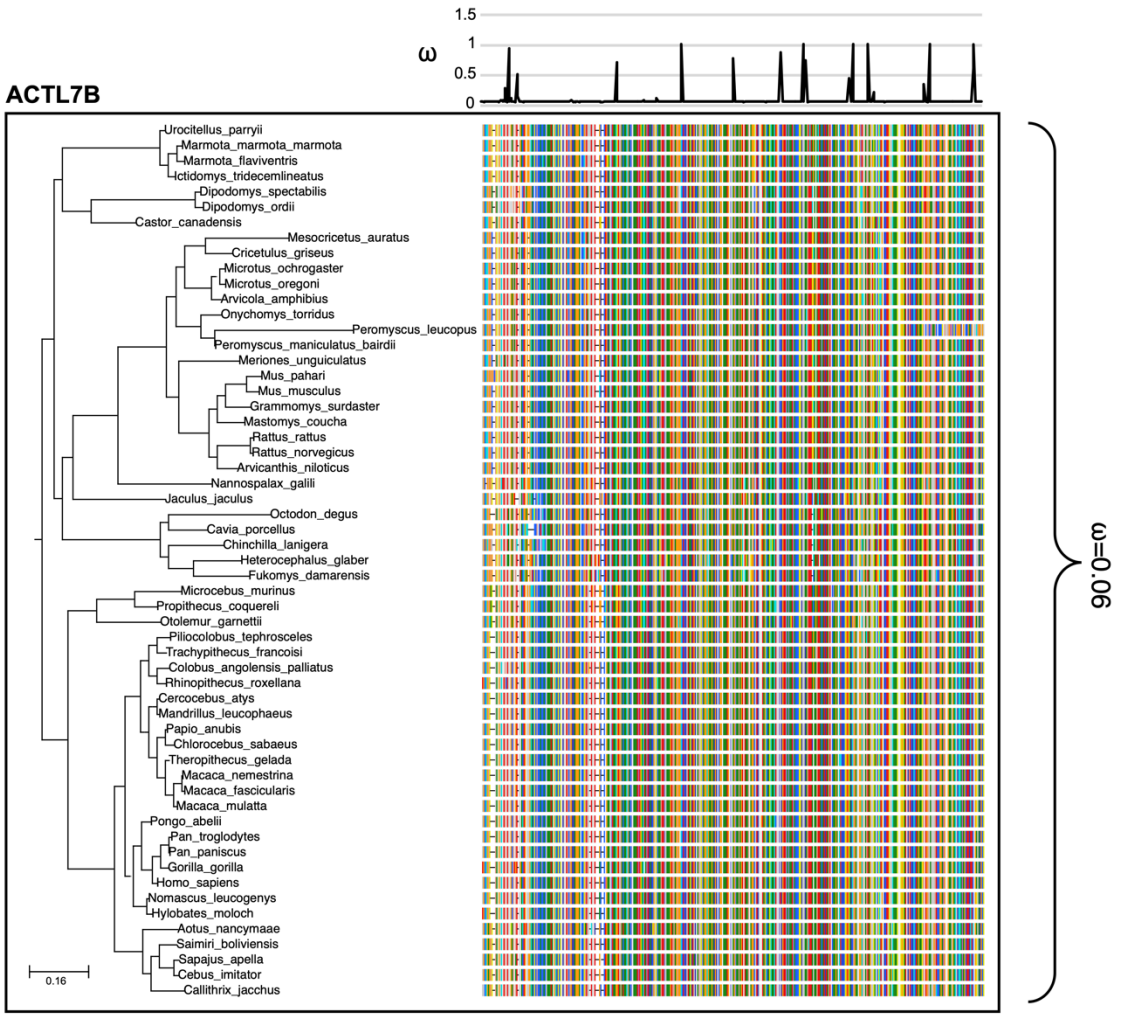


**Figure S3: Species phylogeny with branch length representing number of nucleotide substitutions per codon with schematic representation of ACTL7B amino acid alignment used in the PAML CodeML analysis.** Evolutionary rate (ω) obtained by CodeML models M0 is shown for the whole alignment. The graph on top shows the evolutionary rate (ω) per codon sites across the whole tree (CodeML model M1a). See also: Table 1. Modified from (Merges et al., 2022a). Analysis was performed by Dr. Lena Arévalo.

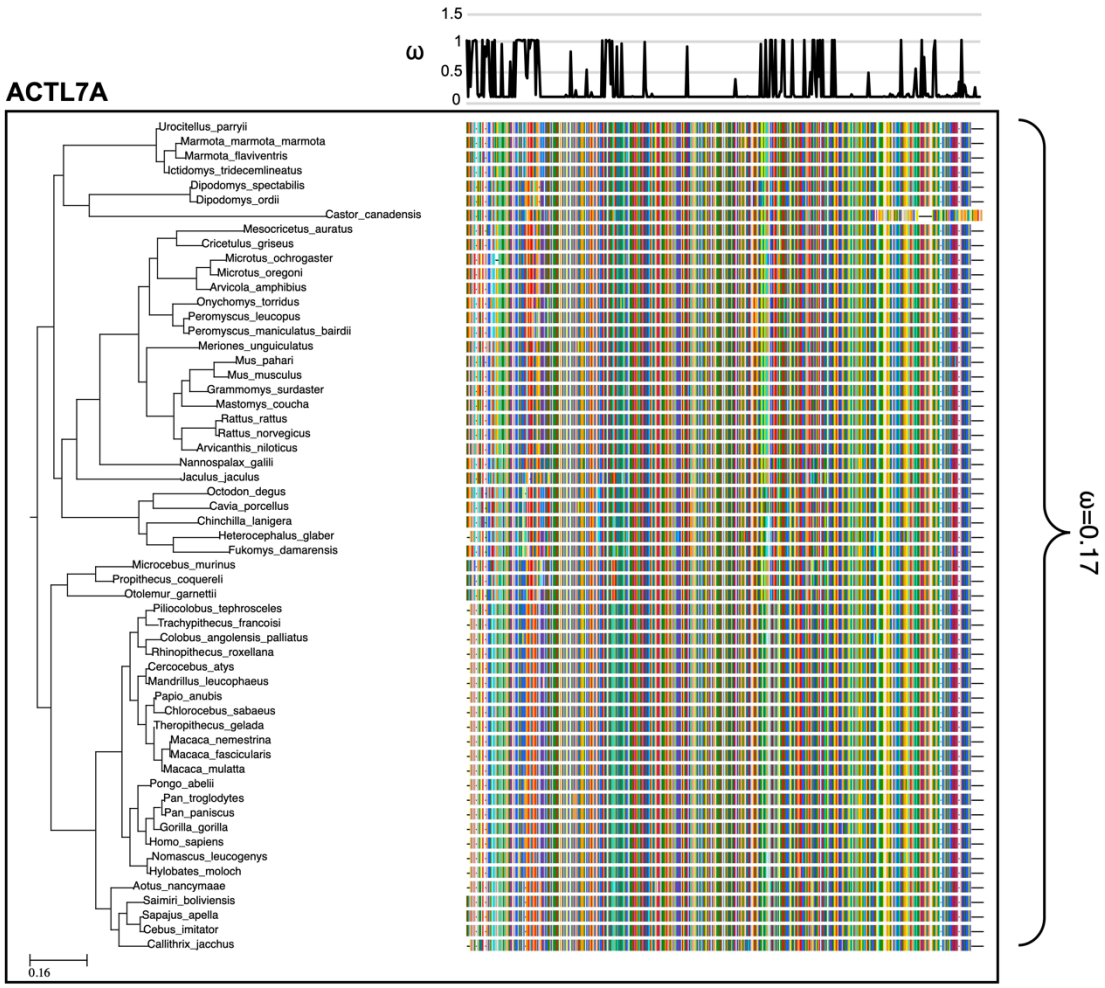


**Figure S4: Species phylogeny with branch length representing number of nucleotide substitutions per codon with schematic representation of ACTL7A amino acid alignment used in the PAML CodeML analysis.** Evolutionary rate (ω) obtained by CodeML models M0 is shown for the whole alignment. The graph on top shows the evolutionary rate (ω) per codon sites across the whole tree (CodeML model M1a). See also: Table S1. Modified from (Merges et al., 2022a). Analysis was performed by Dr. Lena Arévalo..

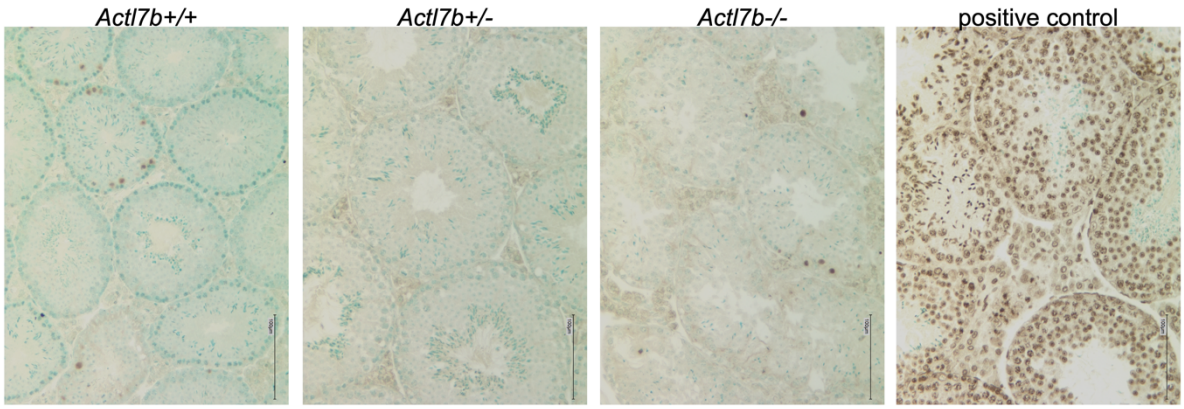


**Figure S5: TUNEL staining on *Actl7b*-deficient testis sections** TUNEL staining on *Actl7b+/+*, *Actl7b+/-* and *Actl7b-/-* testis sections. DNase treated sections were used as positive control. Scale: 100 µm

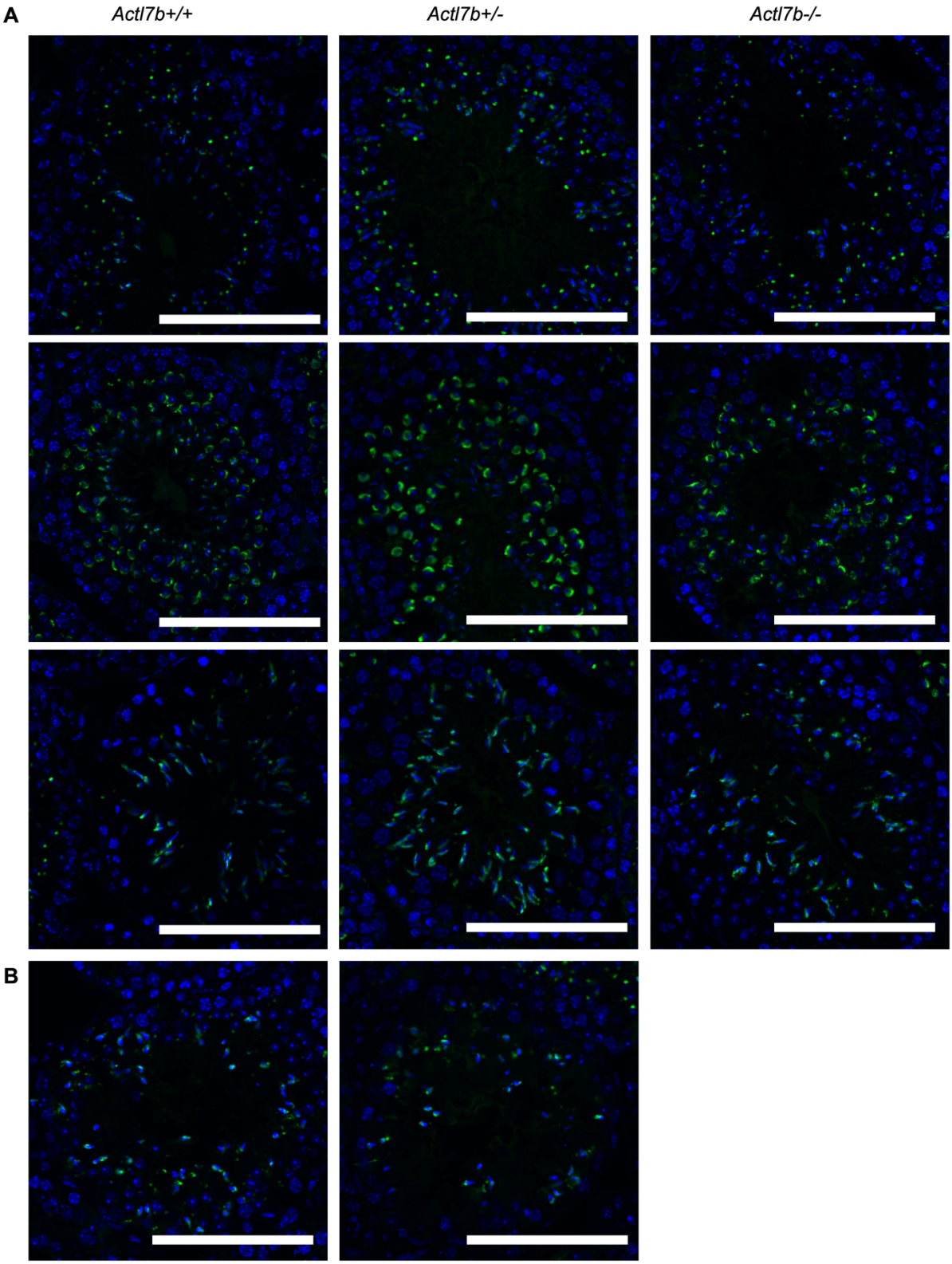


**Figure S6: PNA staining on *Actl7b*-deficient testis sections. (A)** PNA staining on *Actl7b+/+*, *Actl7b+/-* and *Actl7b-/-* testis sections. **(B)** PNA staining on *Actl7b-/-* testis sections. Confocal microscopy was performed together with Anđela Kovacevic. Scale: 100 µm

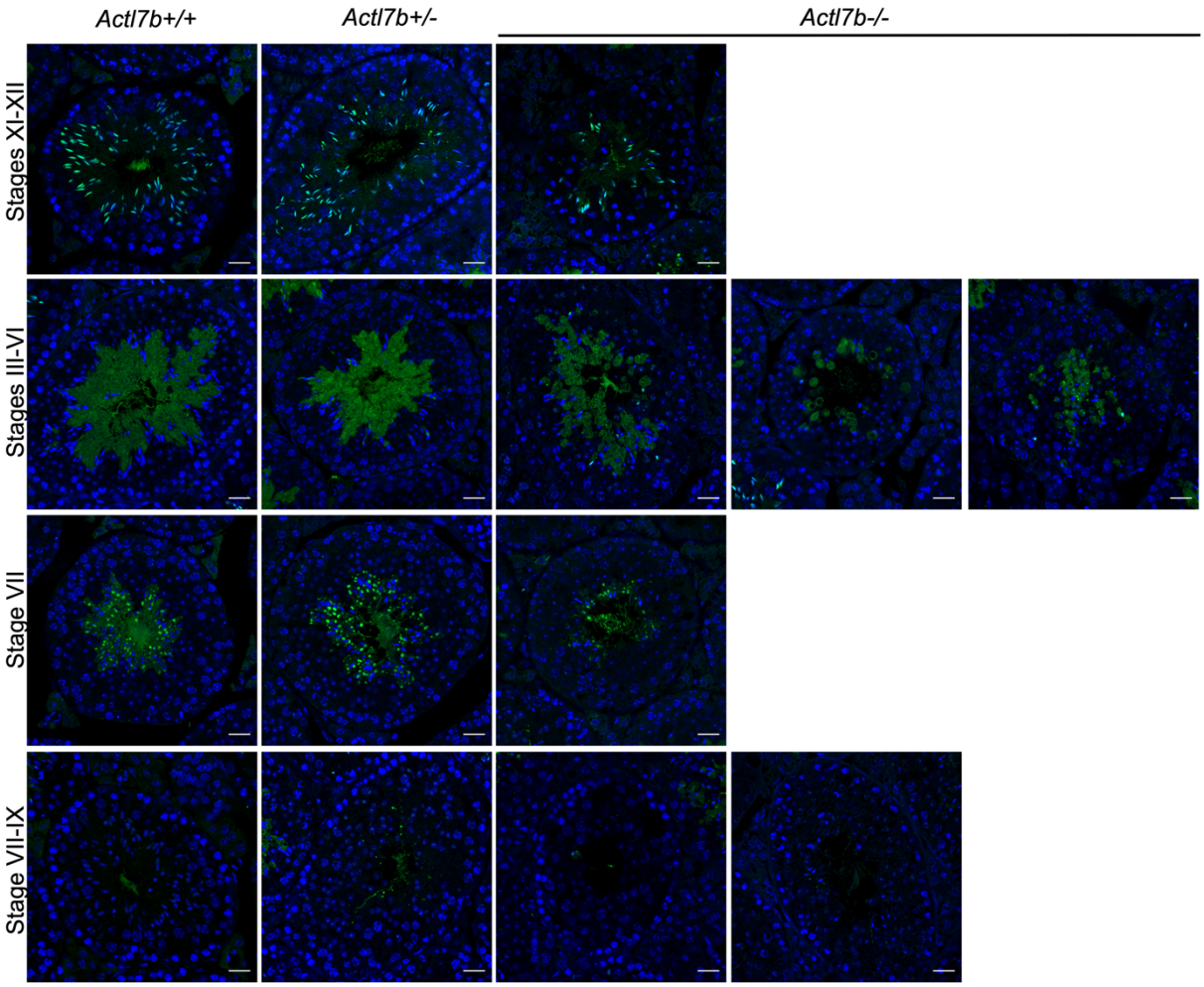


**Figure S7: DYNLL1 in *Actl7b*-deficient seminiferous tubules.** Representative images of IHC staining against DYNLL1 on *Actl7b+/+*, *Actl7b+/-* and *Actl7b-/-* testis sections (counterstain: DAPI). Scale: 20 µm. Confocal microscopy was performed together with Keerthika Lohanadan. Modified from (Merges et al., 2022a).

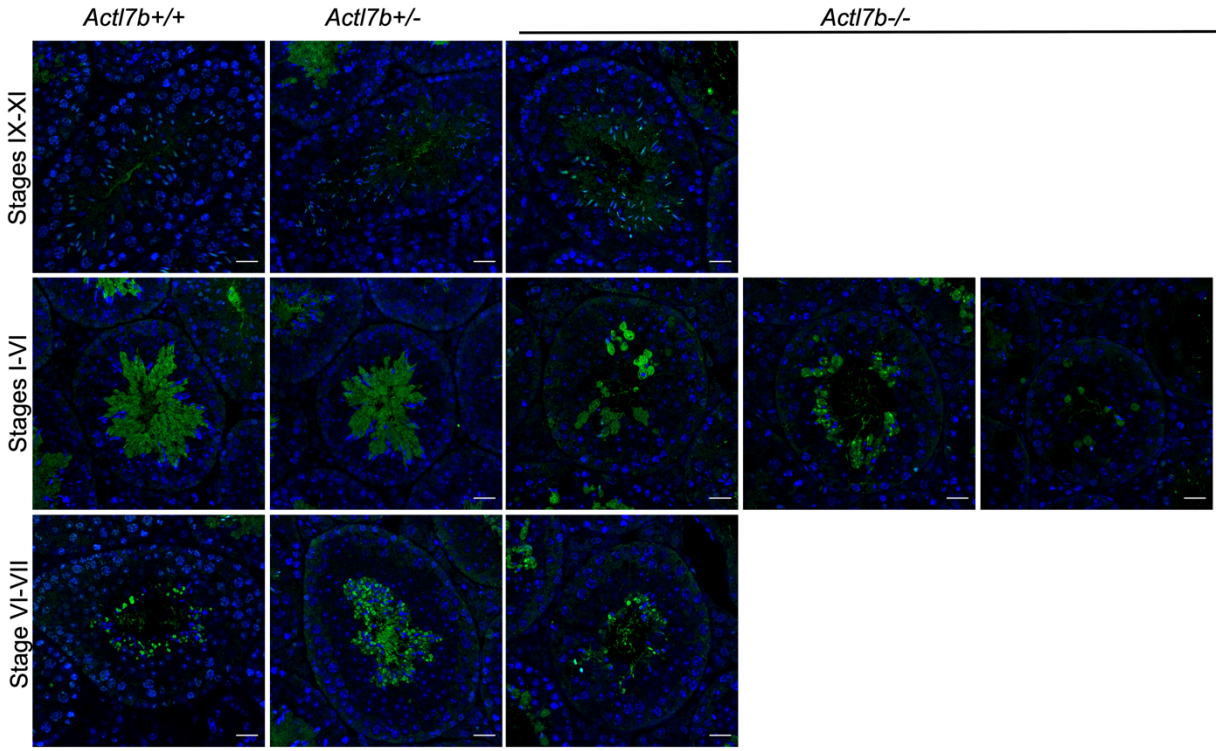


**Figure S8: DYNLL2 in *Actl7b*-deficient seminiferous tubules.** Representative images of IHC staining against DYNLL1 on *Actl7b+/+*, *Actl7b+/-* and *Actl7b-/-* testis sections (counterstain: DAPI). Scale: 20 µm. Confocal microscopy was performed together with Keerthika Lohanadan. Modified from (Merges et al., 2022a).

**Table S1: Evolutionary analysis of *ACTL7A*.** Values of selective constrains acting on *ACTL7B* across the whole phylogenetic tree, on the clades primates and rodentia, and the codon sites across the whole tree.

Results of the evolutionary analysis using CodeML (PAML4.9).

***ACTL7A***

| **Selection on:** | | **LnL null model** | **LnL alternative model** | **LRT** | **p** | **ω** | **interpretation** | | | |
|---|---|---|---|---|---|---|---|---|---|---|
| whole sequence, whole tree | | 12123.91 (M0fix) | 12510.29 (M0) | -772.77 | >0.001 | 0.17 (M0) | ω sign. different from 1 | | overall conserved | |
| whole sequence, clades / lineages | Primates | 12510.29 (M0) | 12507.93 (MCfree) | 4.72 | n.s. | 0.20 (M0) | ω not group specific | | both lineages equally conserved | |
| | Rodentia | | | | | 0.16 (M0) | | | | |
| codon sites, whole tree | | 12281.27 (M1a) | 12281.27 (M2a) | 0.00 | n.s. | n.a. | purifying selection on sites | | sequence is 97% conserved | |
| | | | | | | | prop 0 | prop 1 | prop 2a | PSS |
| | | | | | | | 0.83 | 0.17 | n.a. | n.a. |

LnL = log Likelihood value of the model; LRT = Likelihood Ratio Test; p = p-value of the LRT; ω = evolutionary rate (dN/dS); sign. = sigificantly; prop = proportion of sites assigned to the respective site class; PSS = positively selected sites; for explanation of the models see M&M.

Modified from (Merges et al., 2022a). Analysis was performed by Lena Arévalo.

**Table S2: List of higher and lower abundant proteins in *Actl7b-/-* compared to *Actl7b+/+* whole testis samples.** (p ≤ 0.05, LFC ≤ 0.05) DA proteins are labeled with their corresponding gene symbol.

| *Actl7b-/-* vs. *Actl7b+/+* | | | | | | |
|---|---|---|---|---|---|---|
| higher abundant | | | | | lower abundant | |
| n = 193 | | | | | n = 59 | |
| Commd8 | Azgp1 | Rnf181 | Enpp5 | Tppp3 | Actl7b | Spaca9 |
| Mdp | Cnn1 | Naaa | Ptms | Ctnna1 | Tppp2 | Rpgrip1 |
| Syap1 | Serpinf2 | P0C913 | Ctsl | Hmgcl | Prnd | Glipr1l1 |
| Golim4 | Fkbp14 | Snx12 | Clic1 | Txn | Dbil5 | Fbxo2 |
| Maged1 | Map1lc3b | Dnajc1 | Ftl1 | Insl3 | Spaca7 | Creld2 |
| Kng1 | Cobll1 | Lgals3 | Rbpms | Ak3 | Art3 | Tex33 |
| Fam89b | Fnbp1l | Cycs | Lsr | Ctsa | Pgam2 | Q8VCE4 |
| Cdh2 | Palm | F2 | Rcn3 | Ezr | Smcp | Habp4 |
| Nt5e | Ywhab | Prdx3 | Tpm4 | Gstp1 | Tmco2 | Ment |
| Hook3 | Arpc5 | Tgoln2 | Efnb1 | Prxl2b | Cabs1 | Cyct |
| Ctsz | Vtn | Scrn1 | Lmna | Sr | Dpep3 | Haqh |
| Entpd2 | Vapb | Pdlim1 | Ldhd | Ifi35 | Pkib | Calml3 |
| Pir | Cr1l | Ndrg2 | Cnn3 | Zyx | Hspb9 | Ccdc91 |
| Dnajc5 | Itga6 | Lmnb2 | Fdx1 | Spon1 | Acrbp | Spaca1 |
| Scarb2 | Gyg1 | Fam114a1 | Scarb1 | Glrx | Prss39 | Prss55 |
| Hpcal1 | S100a10 | Serping1 | Asah1 | Gstp2 | Prm3 | Asrgl1 |
| Hpca | Gng5 | Tf | Hmox1 | Prelp | H2al1a | Ropn1 |
| Grb2 | Sorbs2 | Serpina1d | Natd1 | Ctsd | Ak1 | Prss21 |
| Rsu1 | Arsb | Tmed5 | Echdc3 | Scp2 | Txndc2 | Tmod2 |
| Ctsh | Mme | Glul | Cgnl1 | Sh3bgrl | Anxa13 | Spata21 |
| Ccdc90b | Tppp | Serpina1b | S100a1 | Mavs | Crisp2 | |
| Col18a1 | Ahsg | Ech1 | Idh1 | Cyb5a | Lyzl4 | |
| Washc2 | Prdx2 | Psme1 | Cat | Sncb | Tcp11 | |
| Commd6 | Hint2 | F12 | Cox7a1 | Plin2 | Cetn4 | |
| Wipf3 | Ptges2 | Rhoa | Etfa | Fkbp10 | Dkkl1 | |
| H2.Q8 | Cox6b1 | Vsig10 | Hdhd3 | Anxa5 | Spesp1 | |
| Ostf1 | Vamp8 | Cd63 | Rbp1 | Mif | Tex101 | |
| Atf7ip | Psap | Plin3 | Hspb1 | Ctsb | Eqtn | |
| Cavin1 | Txndc17 | Scpep1 | Rcn1 | Ndrg1 | Bpgm | |
| Capg | Fkbp7 | Mfge8 | Cd36 | S100a11 | Spaca5 | |
| Slirp | Otud6b | Psme2 | Fxyd1 | Ppp1r14a | Fscb | |
| Gba | C9 | Ppt1 | Ctsf | Dab2 | Ubl4b | |
| Akap2 | Gamt | Apoe | Vcam1 | Serpinc1 | Q9CPS8 | |
| Ppp1r12a | Bin1 | Arhgdib | Fabp5 | Cstb | Tmsb10 | |
| P33monox | Tgoln1 | Arhgap17 | Sfn | Lgmn | Izumo1 | |
| Prph | Ftl2 | Cgn | Cpe | Des | Knstrn | |
| Vim | Sparc | Stim1 | Tpp1 | Fabp3 | Acyp1 | |
| Tspan8 | Emb | Comt | Mgarp | | Pbp2 | |
| Tubb3 | Endod1 | Map1b | Ada | | Nectin3 | |

Modified from (Merges et al., 2022a).

# 8. Acknowledgment

An dieser Stelle möchte ich allen voran meinem Doktorvater Prof. Dr. Hubert Schorle danken, der mir nach Anfertigung meiner Masterarbeit in seiner Arbeitsgruppe die Möglichkeit geboten hat für meine Promotion zu bleiben. Er hat mich auf dem ganzen Weg wissenschaftlich gefördert und mir das Vertrauen entgegengebracht meine Projekte selbstverantwortlich zu bearbeiten. Ich hatte das Gefühl, alle Höhen und Tiefen dieser Zeit teilen und diskutieren zu können.

Darüber hinaus gilt mein Dank Prof. Dr. Oliver Gruß für die freundliche Bereitschaft das 2.-Gutachten dieser Arbeit zu übernehmen. PD Dr. Reinhard Bauer und Prof. Dr. Dagmar Wachten danke ich für die Zusage zur Prüfungskommission als fachnahes und fachfremdes Mitglied.

Weiterhin danke ich Prof. Dr. Klaus Steger, Dr. Andreas C. Fröbius, Alexander Kruse, Prof. Dr. Walter Witke, PD Dr. Gregor Kirfel und Prof. Dr. Dirk G. de Rooij für erfolgreiche Kooperationen und fachlich hilfreiche Dialoge.

Ich möchte mich bei einigen ehemaligen und derzeitigen Mitarbeitern der AG Schorle bedanken. Für das freundliche Arbeitsklima und viele schöne Erlebnisse sowohl innerhalb wie auch außerhalb des Laboralltags.
Ein ganz besonderer Dank gilt hier Dr. Simon Schneider, welcher meine Masterarbeit betreut und den Grundstein für diese Arbeit gelegt hat. Er mein Interesse an der Thematik geweckt und die fachlichen Diskussionen mit ihm haben das Vorangehen dieser Arbeit maßgeblich gefördert.
Ferner möchte ich mich herzlich bei Dr. Lena Arévalo bedanken, ohne welche diese Arbeit nicht die wäre, die sie heute ist. Enge Zusammenarbeit im Labor und kontinuierliche Diskussion mit ihr haben die Projekte, wie auch meinen wissenschaftlichen Werdegang entscheidend vorangebracht.
Mein Dank gilt Dr. Jan Langkabel, Dr. Kai Funke, Dr. Sina Jostes, Dr. Franziska Kaiser, Anđela Kovacevic, Aylin Hansen und Greta Zech. Leidenschaftliche Diskussionen konnten meist jedes experimentelle Problem lösen und jegliche Erfolge wurden begeistert als Team gefeiert. Mein spezieller Dank geht an Gaby Beine, welche alles zusammenhält und mir immer mit Rat und Tat zur Seite stand.
Andrea Jäger, Angela Egert und dem gesamten Tierstallteam danke ich für tatkräftige Unterstützung und die Einarbeitung in die Mausarbeit. Anna Pehlke und Irina Kosterin danke ich für exzellente technische Unterstützung bei Sequenzierungen und der Arbeit mit dem Elektronen Mikroskop. Ich möchte mich bei Julia Meier, Christoph Wiesejahn, Simone Welz und Ilse Hamers bedanken. Gerne habe ich ihre Bachelor- und Masterarbeiten mit betreut und ihre Leistungen haben ausschlaggebend zu diesen Projekten beigetragen.

Nicht zuletzt möchte ich meiner Familie, meinen Freunden und meinem Partner für ihr Verständnis und ihre Liebe danken. Ihr Rückhalt war während dieser spannenden Phase meines Lebens unabdingbar und absolut. Insbesondere meinen Eltern und Großeltern danke ich für ihr grenzenloses Vertrauen und ihre bedingungslose Unterstützung.